

1. Report No. FHWA/TX-04/1855-2		2. Government Accession No.		3. Recipient's Catalog No.	
4. Title and Subtitle Anchorage of Headed Reinforcement in CCT Nodes				5. Report Date May 2002 <i>Revised June 2003</i>	
				6. Performing Organization Code	
7. Author(s) M. K. Thompson, M. J. Young, J. O. Jirsa, J. E. Breen, and R. E. Klingner				8. Performing Organization Report No. Research Report 1855-2	
9. Performing Organization Name and Address Center for Transportation Research The University of Texas at Austin 3208 Red River, Suite 200 Austin, TX 78705-2650				10. Work Unit No. (TRAIS)	
				11. Contract or Grant No. Research Project 0-1855	
12. Sponsoring Agency Name and Address Texas Department of Transportation Research and Technology Implementation Office P.O. Box 5080 Austin, TX 78763-5080				13. Type of Report and Period Covered Research Report (9/99-8/01)	
				14. Sponsoring Agency Code	
15. Supplementary Notes Project conducted in cooperation with the U.S. Department of Transportation, Federal Highway Administration, and the Texas Department of Transportation.					
16. Abstract The behavior of headed reinforcement in concrete was studied using full-scale tests of CCT nodes. The mechanics of the anchorage behavior were observed and recorded to evaluate the manner in which the capacity of a headed bar is developed. The measured data were used to evaluate existing models of headed reinforcement anchorage as well as the ultimate limit state for anchored bars in CCT nodes. Observations from the CCT node tests provided information on the stages of truss development in a simple strut-and-tie model as well as the stress state of the concrete in the node and adjacent struts. Observations of headed bar anchorage have shown that the final anchorage capacity consists of peak head bearing and reduced bond. A model for anchorage capacity was produced based on this concept.					
17. Key Words headed reinforcement, concrete reinforcement, strut-and-tie modeling, CCT nodes, bearing			18. Distribution Statement No restrictions. This document is available to the public through the National Technical Information Service, Springfield, Virginia 22161.		
19. Security Classif. (of report) Unclassified		20. Security Classif. (of this page) Unclassified		21. No. of pages 160	22. Price

ANCHORAGE OF HEADED REINFORCEMENT IN CCT NODES

by

*M. K. Thompson, M. J. Young, J. O. Jirsa,
J. E. Breen, and R. E. Klingner*

Research Report 1855-2

Research Project 0-1855

*EXPLORE NEW USES FOR T-HEADED BARS IN STRUCTURAL
CONCRETE REINFORCEMENT APPLICATIONS*

conducted for the

Texas Department of Transportation

in cooperation with the

**U.S. Department of Transportation
Federal Highway Administration**

by the

**CENTER FOR TRANSPORTATION RESEARCH
BUREAU OF ENGINEERING RESEARCH
THE UNIVERSITY OF TEXAS AT AUSTIN**

May 2002

Revised June 2003

Research performed in cooperation with the Texas Department of Transportation and the U.S. Department of Transportation, Federal Highway Administration.

ACKNOWLEDGEMENTS

We greatly appreciate the financial support from the Texas Department of Transportation that made this project possible. The support and guidance of the Project Director, Dean VanLanduyt, (BRG) and Project Coordinator, Richard Wilkison, (BRG) is also very much appreciated.

DISCLAIMER

The contents of this report reflect the views of the authors, who are responsible for the facts and the accuracy of the data presented herein. The contents do not necessarily reflect the view of the Federal Highway Administration or the Texas Department of Transportation. This report does not constitute a standard, specification, or regulation.

NOTICE

The United States Government and the state of Texas do not endorse products or manufacturers. Trade or manufacturers' names appear herein solely because they are considered essential to the object of this report.

NOT INTENDED FOR CONSTRUCTION,
PERMIT, OR BIDDING PURPOSES

J. O. Jirsa, P.E., Texas #31360

J. E. Breen, P.E., Texas #18479

R. E. Klingner, P.E., Texas #42483

Research Supervisors

TABLE OF CONTENTS

CHAPTER 1: INTRODUCTION.....	1
1.1 OVERVIEW	1
1.2 PROJECT DIRECTION AND SCOPE	1
CHAPTER 2: CCT NODES: SPECIMEN FABRICATION AND TESTING PROCEDURES	3
2.1 INTRODUCTION	3
2.2 SPECIMEN DETAILS	3
2.3 SPECIMEN INSTRUMENTATION.....	9
2.4 LOAD SETUP.....	11
2.5 TESTING PROCEDURE.....	13
2.6 CCT NODE VARIABLES	14
2.6.1 <i>Bar Size</i>	14
2.6.2 <i>Strut Angle</i>	14
2.6.3 <i>Head Size/Type</i>	15
2.6.4 <i>Confinement</i>	16
2.7 NOMENCLATURE AND LIST OF SPECIMENS.....	16
CHAPTER 3: CCT NODES: BEHAVIOR DURING TESTING.....	21
3.1 UNCONFINED SPECIMEN BEHAVIOR	21
3.1.1 <i>Cracking Behavior</i>	21
3.1.2 <i>Stress/Strain Development in the Bar</i>	31
3.1.3 <i>Equilibrium of the Truss Mechanism</i>	35
3.1.4 <i>Head Slip</i>	36
3.1.5 <i>Load-Deflection Response</i>	39
3.1.6 <i>Modes of Failure</i>	41
3.1.7 <i>Special Test Results</i>	48
3.2 CONFINED SPECIMEN BEHAVIOR.....	52
3.2.1 <i>Cracking Behavior</i>	53
3.2.2 <i>Stress/Strain Development in the Bar</i>	58
3.2.3 <i>Stress/Strain Development in the Stirrups</i>	60
3.2.4 <i>Head Slip</i>	72
3.2.5 <i>Load-Deflection Response</i>	72
3.2.6 <i>Modes of Failure</i>	73
3.3 SUMMARY OF BEHAVIORAL OBSERVATIONS	75
CHAPTER 4: CCT NODES: COMPARISON TO FAILURE MODELS AND FORMULATION OF DESIGN METHODOLOGY	79
4.1 INTRODUCTION	79
4.2 TRENDS IN THE DATA	79
4.2.1 <i>Effect of Relative Head Area</i>	79

4.2.2	<i>Effect of Strut Angle</i>	79
4.2.3	<i>Effect of Head Shape and Orientation</i>	80
4.2.4	<i>Effect of Bar Size</i>	83
4.2.5	<i>Effect of Confinement</i>	84
4.2.6	<i>Comparison to Hooked Bars</i>	84
4.3	COMPARISON OF HEAD CAPACITY TO THEORETICAL MODELS.....	85
4.3.1	<i>Comparison to ACI STM Procedures</i>	85
4.3.2	<i>Comparison to Modified CCD Approach</i>	88
4.3.3	<i>Comparison to ACI Bearing Capacity Model</i>	91
4.4	DEVELOPMENT OF A CAPACITY MODEL FOR HEAD BEARING.....	93
4.4.1	<i>Effect of Cover/Head Bearing Area Ratio</i>	97
4.4.2	<i>Effect of the Secondary Cover</i>	98
4.4.3	<i>Effect of Concrete Strength</i>	99
4.4.4	<i>Effect of Aspect Ratio</i>	101
4.4.5	<i>Aggregate Size Effect</i>	102
4.4.6	<i>Regression Analysis of Proposed Models</i>	103
4.5	CONTRIBUTION FROM BOND.....	107
4.6	SUMMARY	112
CHAPTER 5: SUMMARY AND CONCLUSIONS		113
5.1	SUMMARY	113
5.2	CONCLUSIONS	113
5.2.1	<i>Anchorage Behavior of Headed Reinforcement</i>	113
5.2.2	<i>CCT Node Behavior</i>	114
APPENDIX A: INSTRUMENTATION AND MECHANICAL PROPERTIES OF REINFORCING BARS		117
APPENDIX B: DISTRIBUTION PLOTS FOR BEARING CAPACITY DATABASE		131
APPENDIX C: SUMMARY OF CCT NODE DATA		141
REFERENCES		145

LIST OF FIGURES

Figure 2-1: A typical CCT node test.....	3
Figure 2-2: Reinforcement layouts for unconfined specimens.....	4
Figure 2-3: Reinforcement layouts for confined specimens	5
Figure 2-4: Widths of unconfined specimens	6
Figure 2-5: Cross section of confined specimen and stirrup geometry	6
Figure 2-6: Alignment of heads with bearing plate.....	7
Figure 2-7: Placement of miscellaneous details in the CCT node specimens	9
Figure 2-8: Placement of instrumentation for a typical specimen.....	10
Figure 2-9: Placement of instrumentation in the nodal region of a typical specimen	10
Figure 2-10: Details of the reinforcement and instrumentation for hooked bar specimens	11
Figure 2-11: Placement of instrumentation on stirrups of confined specimens	12
Figure 2-12: Equilibrium of CCT node panel with a horizontal reaction at the bearing plate (45° strut angle).....	12
Figure 2-13: Free roller detail used for the final CCT node test setup.....	13
Figure 3-1: Development of cracks in a representative test with a large head (CCT-08-45-10.39-2)	22
Figure 3-2: Failure of Specimen CCT-08-45-10.39-2	23
Figure 3-3: Crack width measurements from Specimen CCT-08-45-10.39-2	24
Figure 3-4: Development of cracks in a representative test with a small head (CCT-08-45-01.85-2).....	25
Figure 3-5: Development of cracks in the hooked bar test (CCT-08-45-Hook2-1)	26
Figure 3-6: CCT node height in headed bar and hooked bar tests	27
Figure 3-7: Development of cracks in a steep strut angle test (CCT-08-55-10.39-1)	28
Figure 3-8: Development of cracks in a shallow strut angle test (CCT-08-30-10.39-1).....	29
Figure 3-9: Top and bottom fiber strains of the tie bar in Specimen CCT-08-45-10.39-2.....	31
Figure 3-10: “Kinking” of reinforcement caused by dowel action across diagonal shear cracks	32
Figure 3-11: Development of bar stress in Specimen CCT-08-45-10.39-2	33
Figure 3-12: Measured bond stresses in CCT-08-45-10.39-2.....	34
Figure 3-13: Development of stress for headed and non-headed bars	34
Figure 3-14: Components of bar stress provided by bond and head bearing in CCT-11-45-02.85(V)-1	35
Figure 3-15: Equilibrium of CCT node (45° strut angle).....	35
Figure 3-16: Equilibrium plot of bar force versus bearing reaction in Specimen CCT-08-45-10.39-2	36
Figure 3-17: Bar stress versus head slip for CCT node specimens with #11 bars	37
Figure 3-18: Bar stress versus head slip for CCT node specimens with #8 bars	38
Figure 3-19: Load-deflection and load-slip data for specimens with small and large heads.....	39
Figure 3-20: Assumed and possible equilibrium geometries for 30° CCT node specimens	40
Figure 3-21: Assumed and possible stress states of CCC nodes.....	41
Figure 3-22: Pullout failure of a non-headed bar (specimen CCT-08-55-00.00-1).....	42

Figure 3-23: Patterns of strut/node rupture	43
Figure 3-24: Side view of a failed specimen with a vertically oriented head (CCT-08-55-02.80(V)-1) demonstrating splitting of the diagonal compression strut	43
Figure 3-25: Front view of a failed specimen with a vertically oriented head (CCT-08-55-02.80(V)-1) demonstrating splitting of diagonal compression strut	44
Figure 3-26: Splitting failure of a specimen with a small head (CCT-11-55-01.10-1)	45
Figure 3-27: Zone of crushed concrete in a specimen with a horizontally oriented head (CCT-08-45-04.70(H)-1) after failure (top view)	45
Figure 3-28: Zone of crushed concrete in a specimen with a horizontally oriented head (CCT-11-45-04.13(H)-1) after failure (side view)	46
Figure 3-29: Specimen CCT-08-55-02.80(H)-1 after failure	46
Figure 3-30: Special instrumentation in Specimen CCT-08-45-04.70(V)-1-S2	49
Figure 3-31: Transverse splitting strains in specimen CCT-08-45-04.70(V)-1-S2	49
Figure 3-32: Special instrumentation in Specimen CCT-08-45-04.70(H)-1-S3	51
Figure 3-33: In-plane splitting strains in specimen CCT-08-45-04.70(H)-1-S3	51
Figure 3-34: Spiral confinement detail attempted in specimen CCT-08-45-04.70(V)-1-S1	52
Figure 3-35: Development of cracks in a heavily confined, headed bar specimen (CCT-08-45-04.70(V)-1-C0.012)	53
Figure 3-36: Crack patterns overlaid onto probable truss mechanisms for the heavily confined, headed bar specimen (CCT-08-45-04.70(V)-1-C0.012)	55
Figure 3-37: Crack width measurements from the heavily confined, headed bar specimen (CCT-08-45-04.70(V)-1-C0.012)	56
Figure 3-38: Development of cracks in a lightly confined, headed bar specimen (CCT-08-45-04.70(V)-1-C0.006)	57
Figure 3-39: Development of cracks in a heavily confined, hooked bar specimen (CCT-08-45-Hook2-1-C0.012) ..	58
Figure 3-40: Strain at 5" vs. bearing reaction in unconfined and confined specimens	59
Figure 3-41: Components of bar stress provided by bond and head bearing in CCT-08-45-04.70(V)-1-C0.012	59
Figure 3-42: Development of vertical tensile strain in the stirrup confinement of the heavily confined, headed bar specimen (CCT-08-45-04.70(V)-1-C0.012)	61
Figure 3-43: Development of vertical tensile strain in the stirrup confinement of the lightly confined, headed bar specimen (CCT-08-45-04.70(V)-1-C0.006)	62
Figure 3-44: Vertical tensile strains along the tie in the heavily confined, headed bar specimen (CCT-08-45-04.70(V)-1-C0.012)	63
Figure 3-45: Vertical tensile strains along the tie in the heavily confined, non-headed bar specimen (CCT-08-45-00.00-1-C0.012)	64
Figure 3-46: Vertical tensile strains along the tie in the heavily confined, hooked bar specimen (CCT-08-45-Hook2-1-C0.012)	65
Figure 3-47: State of stress around the CCT node	66
Figure 3-48: Development of transverse tensile strain in the stirrup confinement of the heavily confined, headed bar specimen (CCT-08-45-04.70(V)-1-C0.012)	67
Figure 3-49: Development of transverse tensile strain in the stirrup confinement of the lightly confined, headed bar specimen (CCT-08-45-04.70(V)-1-C0.006)	68

Figure 3-50: Transverse strains along the underside of the tie in the heavily confined, headed bar specimen (CCT-08-45-04.70(V)-1-C0.012).....	69
Figure 3-51: Transverse strains along the underside of the tie in the heavily confined, non-headed bar specimen (CCT-08-45-00.00-1-C0.012).....	70
Figure 3-52: Transverse strains along the underside of the tie in the heavily confined, hooked bar specimen (CCT-08-45-Hook2-1-C0.012).....	71
Figure 3-53: Bar stress versus head slip for unconfined and confined specimens.....	72
Figure 3-54: Load-deflection data for specimens unconfined and confined specimens.....	73
Figure 3-55: Failure cracking patterns for non-headed and headed specimens with varying degrees of confinement.....	74
Figure 4-1: Effect of relative head area on head capacity.....	79
Figure 4-2: Approximate development lengths for 45° and 30° strut angles.....	80
Figure 4-3: Minimum head size necessary to achieve yield of the tie bar.....	80
Figure 4-4: Head slip plots for circular and square heads.....	81
Figure 4-5: Effect of head orientation and aspect ratio on head capacity.....	82
Figure 4-6: Shallow and steep faces of the wedge for a rectangular head.....	82
Figure 4-7: Transverse splitting components of shallow and steep wedge face bearing.....	83
Figure 4-8: Horizontal versus vertical head orientation in a CCT node.....	83
Figure 4-9: Effect of bar size on head capacity.....	83
Figure 4-10: Effect of confinement on head capacity.....	84
Figure 4-11: Bar stress from hooked bars compared with headed bars (#8 sizes).....	85
Figure 4-12: Critical node faces for STM stresses.....	85
Figure 4-13: Efficiency factors for node bearing at the face adjacent to the head.....	86
Figure 4-14: Distribution of efficiency factors for CCT node bearing results.....	86
Figure 4-15: Geometry of the strut/node intersection at the CCT node.....	87
Figure 4-16: Distribution of efficiency factors for strut bearing at the face adjacent to the CCT node.....	88
Figure 4-17: Definition of embedment depth and project breakout area for application of concrete breakout model.....	89
Figure 4-18: Correlation of measured and calculated values for concrete breakout model.....	89
Figure 4-19: Projected side blow-out areas for various CCT specimen series.....	90
Figure 4-20: Correlation of measured and calculated values for side blow-out model.....	91
Figure 4-21: Notional areas for bearing analysis of CCT nodes.....	92
Figure 4-22: Correlation of measured and calculated values for bearing model.....	92
Figure 4-23: Distribution plot of measured/calculated ratios for bearing model.....	93
Figure 4-24: Relation of concrete power to $2c_1/\sqrt{A_{nh}}$ ratio.....	96
Figure 4-25: Normalized bearing capacity versus $2c_1/\sqrt{A_{nh}}$ ratio.....	98
Figure 4-26: Normalized bearing capacity versus cover ratio, c_2/c_1	99

Figure 4-27: Normalized bearing capacity versus concrete strength, f_c' , with trend lines for relationships to f_c' and $\sqrt{f_c'}$	100
Figure 4-28: Normalized bearing capacity versus concrete strength, f_c' , with trend lines for the proposed concrete exponent term	101
Figure 4-29: Effect of head aspect ratio on capacity	102
Figure 4-30: Size effect on capacity	103
Figure 4-31: Distribution of measured/calculated values for bearing model 1	104
Figure 4-32: Distribution of measured/calculated values for bearing model 2	105
Figure 4-33: Probability of unsafe test outcome as a function of exclusion factor	106
Figure 4-34: Distribution plot of measured/calculated ratios for model 1 (CCT node tests)	107
Figure 4-35: Distribution plot of measured/predicted ratios for model 2 (CCT node tests)	107
Figure 4-36: Measured failure bond stress versus relative head area.....	108
Figure 4-37: Measured peak bond stress versus vertical compression stress.....	109
Figure 4-38: Measured peak bond stress versus relative head area.....	110
Figure 4-39: Distribution plot of measured/calculated ratios for failure bond.....	111
Figure 4-40: Distribution plot of measured/calculated ratios for peak bond.....	112
Figure 5-1: Typical CCT node from the test program.....	113
Figure 5-2: Critical development point for a CCT node	115
Figure 5-3: The state of stress at the CCT node.....	115

LIST OF TABLES

Table 2-1: Concrete mix proportions.....	8
Table 2-2: Hardened concrete properties.....	8
Table 2-3: Measured head dimensions for Xtender bars.....	15
Table 2-4: Nomenclature of CCT node test identifiers.....	17
Table 2-5: List of all CCT node tests.....	18
Table 3-1: Specimen information for data plotted in Figure 3-17.....	36
Table 3-2: Specimen information for data plotted in Figure 3-18.....	42
Table 3-3: Failure modes of unconfined CCT node specimens.....	47
Table 3-4: Capacities of companion CCT node specimens with and without the ladder detail.....	50
Table 3-5: Capacities of companion CCT node specimens with and without the strut detail.....	52
Table 3-6: Failure modes of confined CCT node specimens.....	75
Table 4-1: Companion specimens for effect of head shape.....	81
Table 4-2: Companion specimens for effect of head orientation.....	82
Table 4-3: Statistical data for accuracy of side blow-out model.....	91
Table 4-4: Statistical data for accuracy of ACI bearing model.....	92
Table 4-5: Summary of sources for collected database of headed bar, anchor bolt, and bearing tests.....	94
Table 4-6: Various models for head capacity.....	97
Table 4-7: Statistical data for proposed models of bearing capacity.....	104
Table 4-8: Statistical data for accuracy of model 1 (CCT node tests).....	106
Table 4-9: Statistical data for accuracy of model 2 (CCT node tests).....	106
Table 4-10: Statistical data for accuracy of ACI bond equation in predicting the failure bond.....	111
Table 4-11: Statistical data for accuracy of ACI bond equation in predicting the peak bond.....	111

SUMMARY

The behavior of headed reinforcement in concrete was studied using full-scale tests of CCT nodes. The mechanics of the anchorage behavior were observed and recorded to evaluate the manner in which the capacity of a headed bar is developed. The measured data were used to evaluate existing models of headed reinforcement anchorage as well as the ultimate limit state for anchored bars in CCT nodes. Observations from the CCT node tests provided information on the stages of truss development in a simple strut-and-tie model as well as the stress state of the concrete in the node and adjacent struts. Observations of headed bar anchorage have shown that the final anchorage capacity consists of peak head bearing and reduced bond. A model for anchorage capacity was produced based on this concept.

CHAPTER 1: INTRODUCTION

1.1 OVERVIEW

In structural concrete, the provisions for anchorage of straight bars and hooks sometimes present detailing problems due to the long development lengths and large bend diameters that are required, particularly when large-diameter reinforcing bars are used. Occasionally, the requirements for straight bar anchorage and lap splices cannot be provided within the available dimensions of elements. Hooked bars can be used to shorten anchorage length, but in many cases, the bend of the hook will not fit within the dimensions of a member or the hooks create congestion and make an element difficult to construct. Similarly, mechanical anchorage devices can be used to shorten lap splice lengths, but they frequently require special construction operations and careful attention to tolerances.

To address the problems that arise from the use of conventional anchorages (straight bar development length and hooks), headed bars were developed for use in the construction of concrete platforms for the offshore oil industry. Headed bars (Figure 1-1) are formed by the attachment of a plate or the forging of an upset bearing surface at the end of a straight reinforcing bar. Such bars are anchored by a combination of bond along the straight bar length and direct bearing at the head. Like a hooked bar, they can develop within a short distance, but they do not create as much congestion. Headed reinforcement has been used in the construction of platforms for the offshore oil industry. However, headed bars have not been widely used in other structures such as bridges, buildings, or other traditional concrete structures. There is little guidance currently available for the design of headed bar anchorage either in the form of code provisions or published research.

Project 1855 was funded by the Texas Department of Transportation (TxDOT) to examine the behavior of headed bars in bridge details and to evaluate the feasibility of using headed bars for Texas transportation structures. Additionally, the findings of an extensive literature review and experimental program are to be reported and design guidelines for the use of headed bars are to be developed.

1.2 PROJECT DIRECTION AND SCOPE

After several meetings between the research team and TxDOT bridge design engineers to identify bridge details for which headed bars showed the most promise, two experimental directions were decided upon. TxDOT representatives expressed the most interest in the use of headed bars to reduce lap lengths and to replace hooked bars in congested discontinuity regions. Two specimen types were selected: lap splices and compression-compression-tension (CCT) nodes. These specimens were designed to be as general as possible so that the behavior of the headed bars in these details could be extrapolated to a variety of specific applications in which lap splices and CCT nodes occur.

A CCT node specimen was developed to test the anchorage of a single headed bar in a CCT node. Companion specimens with non-headed bars and hooked bars were also tested. Other variables of the test program included the angle of the compression strut, head size and shape, bar size, and the presence of confinement in the nodal zone. A total of 64 CCT node specimens were tested. In addition to studying the anchorage performance of headed bars, these specimens were used to determine the behavior of CCT nodes and the current provisions related to strut-and-tie modeling (STM) were evaluated against the results.

A lap splice specimen was developed to test the anchorage of multiple headed bars anchored within a single layer lap splice. Companion specimens with non-headed bars were also tested. Other variables of the lap splice test program included the lap length, the head size and shape, the bar spacing, contact versus non-contact laps, and the presence of confinement in the lap zone. A total of 27 lap splices were tested.

This report, CTR 1855-2, contains a description of the CCT node test program, presentation of CCT results, and evaluation of the CCT data against various behavioral models. Chapter 2 describes the test program. Chapter 3 describes behavioral observations from the tests. Chapter 4 contains an analysis of the trends in the data and the development of a model for headed bar anchorage capacity. Chapter 5 is a brief summary of the material from this report. Additional reports in this project include:

CTR 1855-1 *"Anchorage Behavior of Headed Reinforcement: Literature Review"* [19]

CTR 1855-3 *"Anchorage of Headed Reinforcement in Lap Splices"* [20]

CHAPTER 2: CCT NODES: SPECIMEN FABRICATION AND TESTING PROCEDURES

2.1 INTRODUCTION

This chapter briefly discusses the details of the CCT node specimens and of the test setup and procedures used in the testing of the CCT nodes. A total of 64 CCT node specimens were tested in the course of the project. Figure 2-1 shows a photo of a test specimen and the test frame. The basic test was essentially as shown in Figure 2-1, however, many small details of the test specimens and the testing procedure evolved over the course of the project.

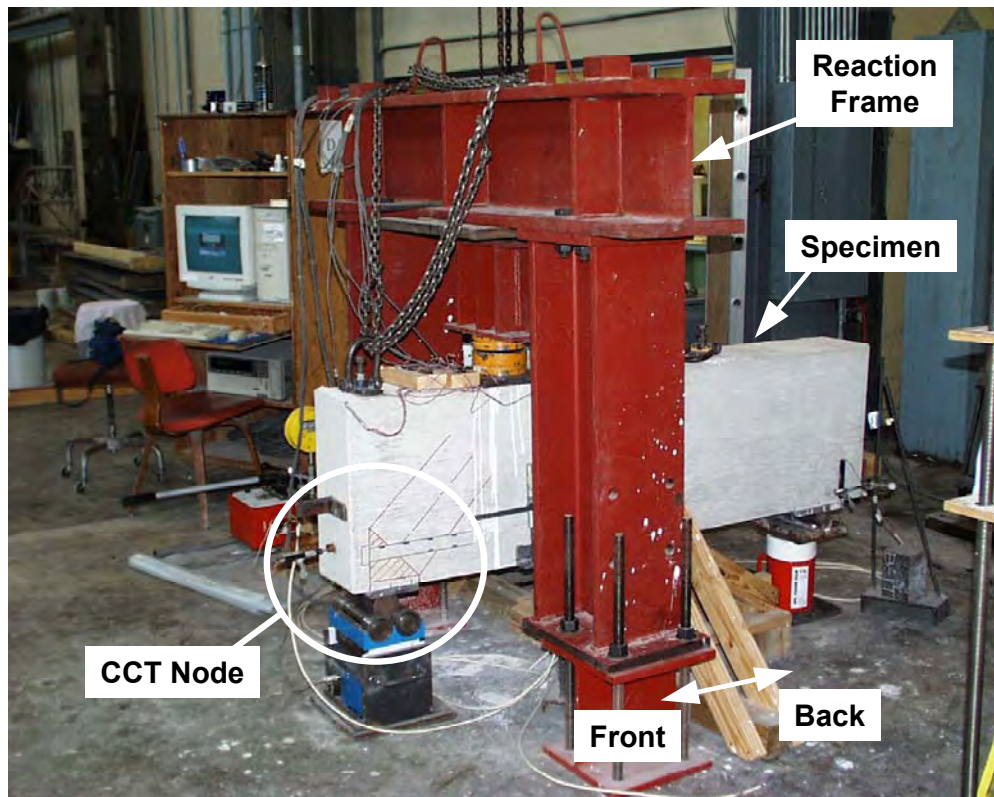


Figure 2-1: A typical CCT node test

2.2 SPECIMEN DETAILS

Both unconfined and confined CCT node specimens were tested. Confined specimens contained stirrup reinforcement through the nodal zone while unconfined specimens contained nothing but the tensile tie steel in the nodal zone region. Figure 2-2 shows the basic reinforcement layout for the unconfined specimens. No stirrups were placed in the region through which the nodal zone and the primary diagonal strut pass. In the unconfined specimen series, three strut angles were tested: 30° , 45° , and 55° . Changes in strut angle were accomplished by moving the location of the top reaction frame. All CCT node specimens were 20" deep and 72" long. The width of the specimens was changed depending on the size bar used in the primary tension tie. The width was generally $6d_b$, where d_b was the diameter of the tension tie bar. #8 and #11 size bars were tested with corresponding specimen widths of 6" and 8.5" respectively (Figure 2-4). The tension tie was always centered at 4" from the bottom of the specimen. The yield strength (f_y) of the ties was between 61 - 68 ksi (refer to Table A-1 in Appendix A for further details).

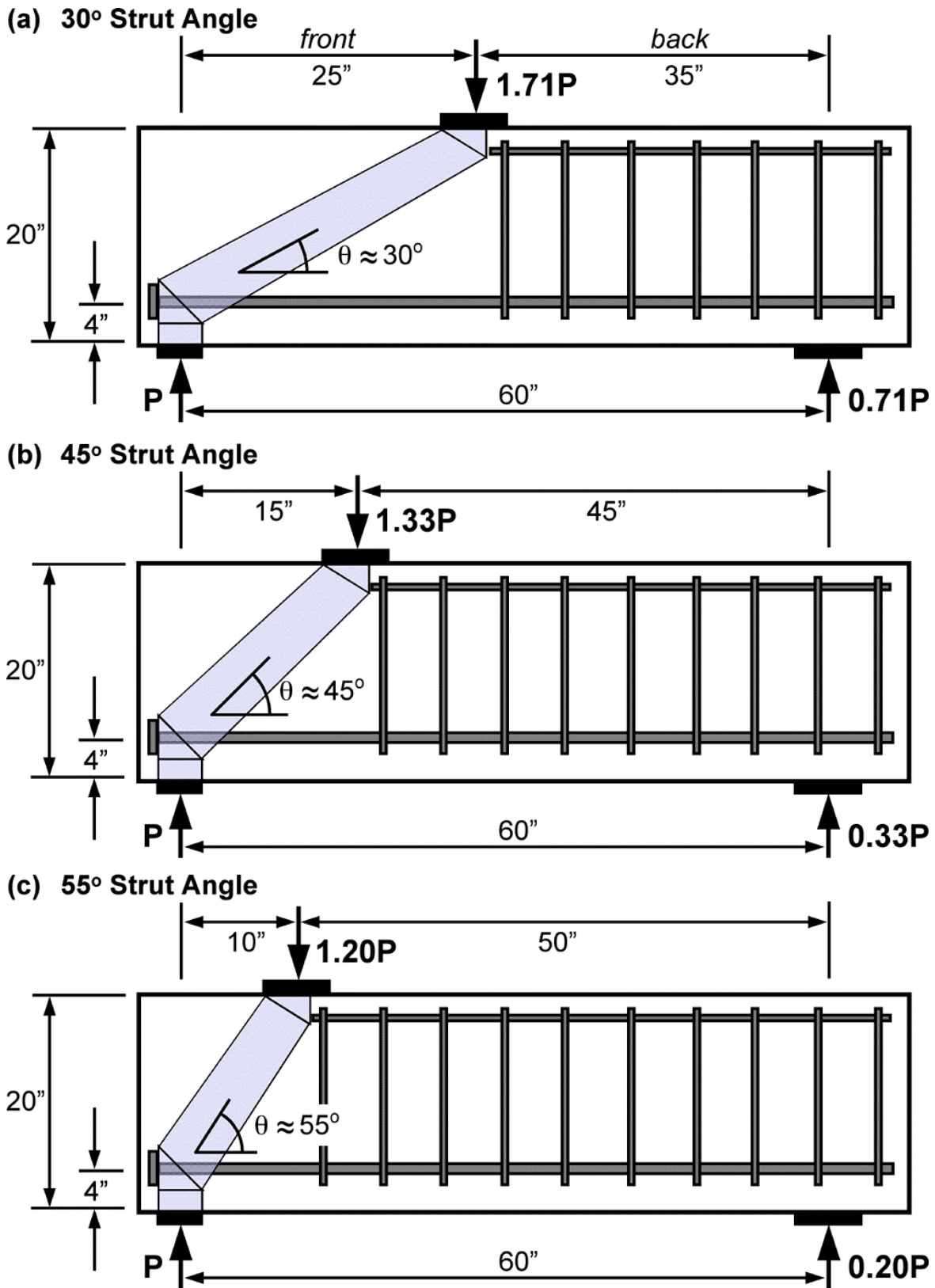


Figure 2-2: Reinforcement layouts for unconfined specimens

The first 8 specimens of the CCT node test program differed from the final layout described above. The first four specimens were cast with 5500 psi concrete, $8d_b$ width (#8 bars with 8" width), and no stirrup reinforcement. Originally it was thought that node failure would occur before shear dominated the capacity of the specimen, thus stirrups were omitted as an unnecessary detail. However, the nodes achieved higher capacities than expected and shear failure occurred in the back section of the specimens (Front" and "back" are labeled in Figure 2-2(a). The "front" of the specimen refers to the end containing the CCT node region. The "back" refers to the other end of the specimen.). Thereafter, stirrups were placed in the back portions of all specimens. Stirrups were either #3 or #4 closed hoops. Additionally, the concrete mix used in the CCT node specimens was changed to reduce the strength of the concrete to make node failure more likely. The second group of CCT node specimens was cast with 3000-4000 psi concrete that was used throughout the rest of the test program. Seven specimens were cast in that batch: 4 with an $8d_b$ specimen width and 3 with a $6d_b$ width. Following the test of those specimens, the $6d_b$ width was used throughout the rest of the testing to allow more specimens to be cast in a single batch while still producing the failure modes of interest.

The reinforcement layout for the confined specimens is shown in Figure 2-3. Five confined CCT node specimens were tested. Confinement was provided by extending the stirrup reinforcement across the full length of the specimen. #3 hoop stirrups ($f_y = 63$ ksi) were used. Spacing was at 3" and 6" within the nodal zone and 6" along the rest of the specimen. Figure 2-5 shows the geometry of the stirrups used in the confined specimens.

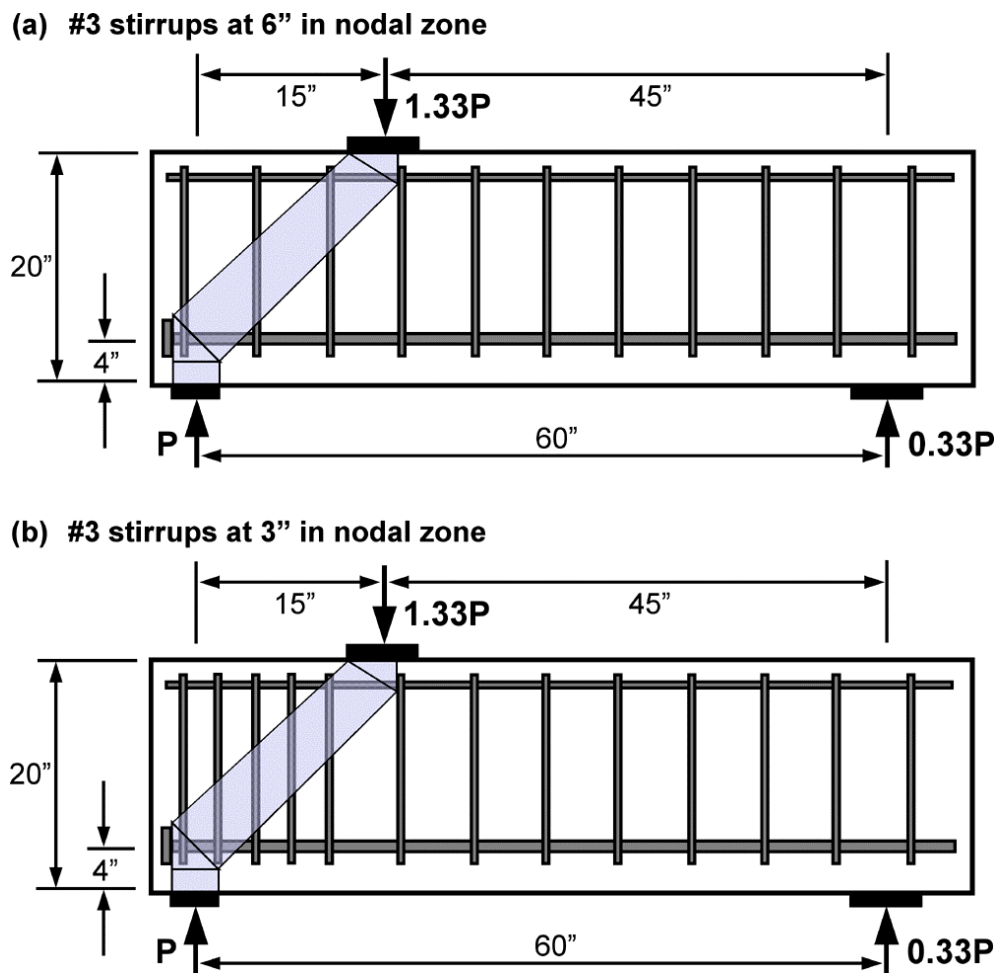


Figure 2-3: Reinforcement layouts for confined specimens

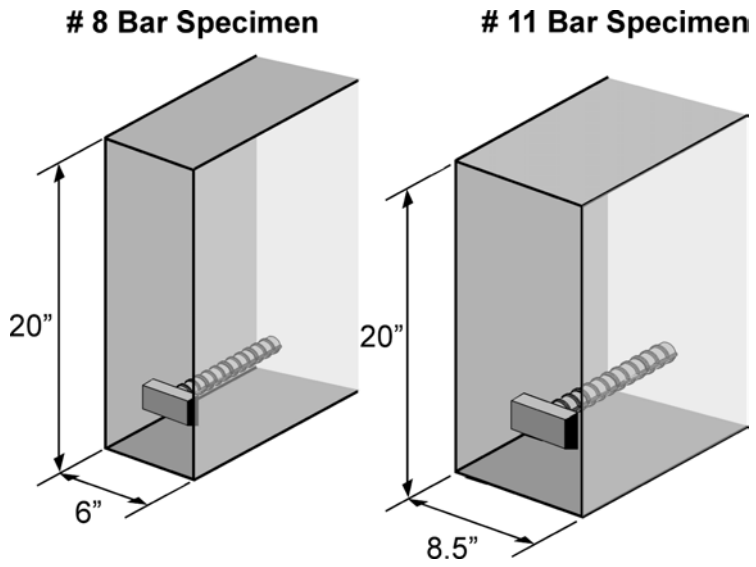


Figure 2-4: Widths of unconfined specimens

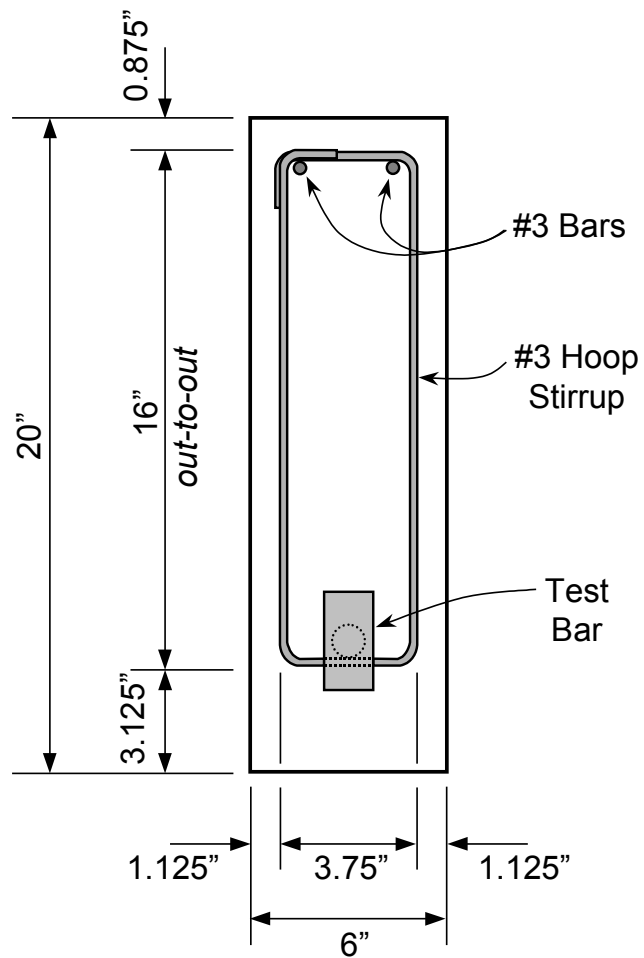


Figure 2-5: Cross section of confined specimen and stirrup geometry

The tensile tie reinforcement of the CCT nodes was generally anchored by a mechanical head. The tensile bars were always placed so that the bearing face of the head aligned with the front edge of the CCT node bearing plate (Figure 2-6). Non-headed bars were aligned such that the end of the bar lined up with the edge of the bearing plate. Xtender headed bars were aligned such that the point where the maximum head diameter began lined up with the front edge of the bearing plate. Stirrups in confined specimens began 1” from the front edge of the bearing plate. Two details were used for hooked bar specimens: either the point of horizontal tangency of the bend was aligned with the front edge of the bearing plate (detail 1) or the inside bend of the hook was aligned with the front edge of the bearing plate (detail 2). The details of the hooked bar specimens are shown in Figure 2-10.

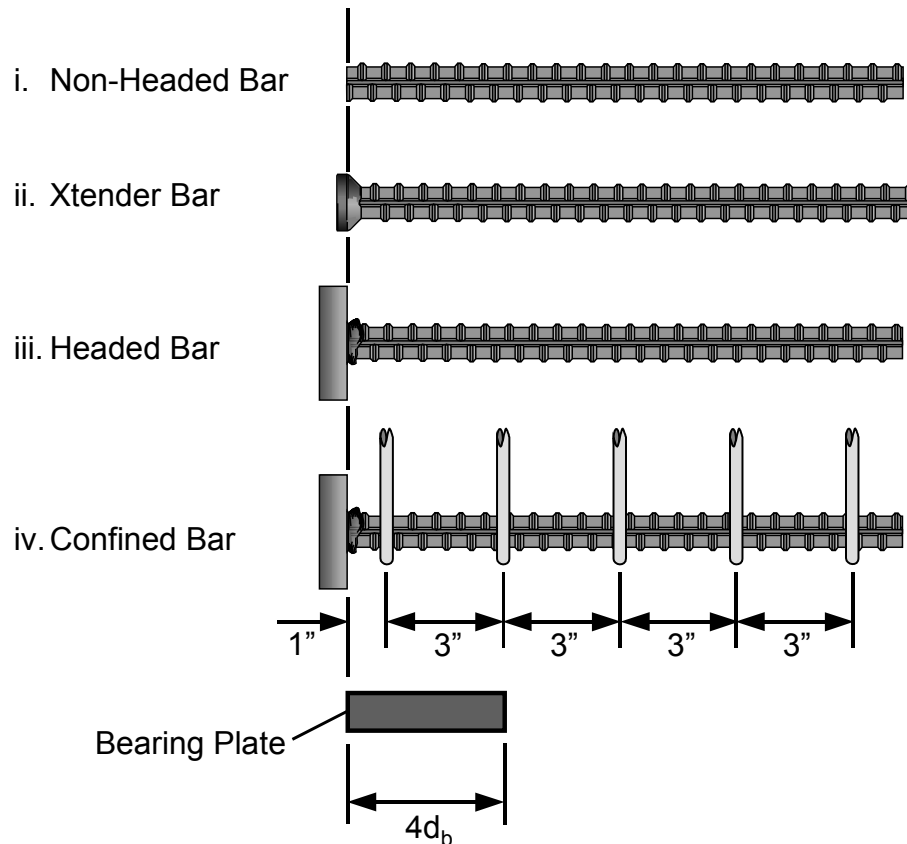


Figure 2-6: Alignment of heads with bearing plate

All but two specimens were cast upright. Concrete was placed from above and vibrated into position. Formwork was constructed of standard lumber ($\frac{3}{4}$ " plywood and 2 x 4 lumber). The formwork for the CCT nodes could accommodate up to eight specimens in one cast. The formwork was reused several times. Two unconfined hooked bar specimens were cast on their sides.

Three concrete mixes (A, B, and C) were used in CCT node specimen casting. The concrete was supplied by a local company. Table 2-1 lists the concrete mix proportions. A nominal maximum aggregate size of 0.75" was specified. Mechanical properties of the hardened concrete were determined using standard 6" diameter cylinders. Compression strength, splitting tensile strength, and modulus of elasticity were measured just prior to and just following tests of a group of specimens with the same concrete. Initially, only compression strength was measured. Tests were performed according to ASTM standards C39 (compressive strength), C496 (splitting tensile strength), and C469 (modulus of elasticity) [3, 4, 5]. Table 2-2 lists the measured properties from each cast.

Table 2-1: Concrete mix proportions

Mix Proportions by Weight						
Mix	Coarse Aggregate	Sand	Water	Portland Cement	Flyash	w/c Ratio
A	45.7%	37.2%	6.4%	7.7%	3.0%	0.60
B	48.0%	36.6%	6.8%	6.7%	2.0%	0.78
C	47.5%	36.3%	6.8%	7.3%	2.2%	0.72

Table 2-2: Hardened concrete properties

Concrete Batch	Cast Date	Age (days)	f'_c (psi)	f_{ct} (psi)	E_c (ksi)
A1	7/12/99	42	5700	-	-
B1	9/23/99	39	3000	-	-
B2	1/21/00	28	4000	-	-
B3	5/16/00	55	3900	-	-
B4	10/6/00	63	4100	460	4300
B5	11/16/00	33	4000	430	3700
B6	1/25/01	41	3100	350	3300
B7	2/8/01	35	4100	420	4000
C6	5/17/01	35	3800	360	4000

All specimens included miscellaneous details such as lifting inserts and bar chair spacers. Placement of these details was avoided in the critical nodal zone and surrounding concrete. Figure 2-7 shows the typical placement of these extra details within an unconfined specimen. Individual chair spacers were used on the bottom and sides of the primary tension tie to maintain its position during the cast. The same details were included in confined specimens in the same locations.

In addition to the specimens listed above, three specimens with special details were tested. These specimens were not typical and were fabricated to study some special aspects of CCT node behavior and are discussed in Section 3.1.7.

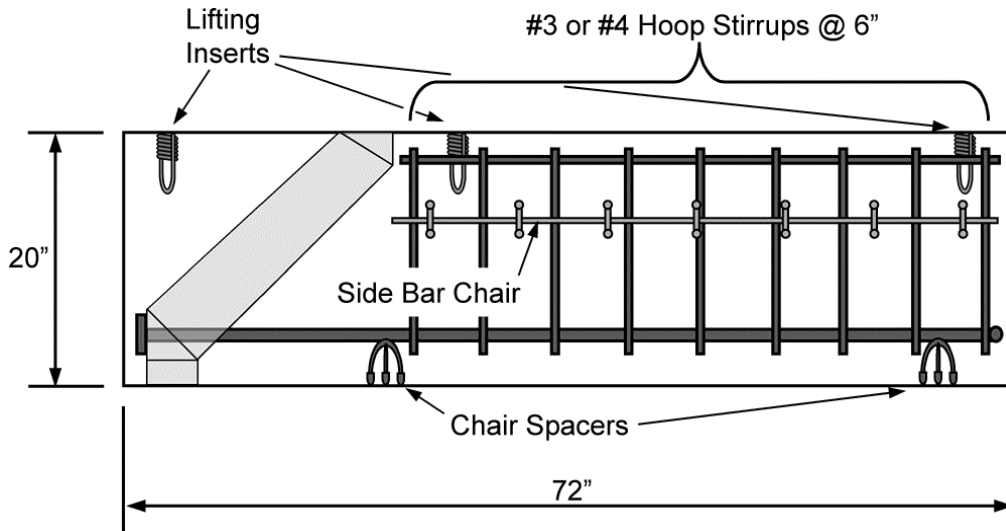


Figure 2-7: Placement of miscellaneous details in the CCT node specimens

2.3 SPECIMEN INSTRUMENTATION

Three types of instrumentation were used during the testing. Below is a list of the different instrumentation types and their purpose in the testing:

- **Strain gages** were used on the tie bar surface to provide information on the development of force in the tie bar in the nodal zone and in the confining reinforcement. Use of the strain gages is discussed in detail in Appendix A.
- **Linear potentiometers** were used to measure horizontal slip of the head relative to the outside face of the concrete and to measure deflection of the specimen under the top load point.
- A **load transducer (load cell)** was used to measure the load directly underneath the CCT node bearing pad.

The placement of this instrumentation is shown in Figure 2-8. Figure 2-9 shows a close-up of the node region and the details of the strain gage placement for the standard specimens. A hollow tube was cast into every specimen to allow access to the head for slip measurements. The linear potentiometers were spring-loaded and required no special attachment to the head. Slip potentiometers were connected to hooked bars through a small diameter hollow tube to determine slip at the point of bend tangency. However, the particular slip potentiometers used for those tests provided very unreliable data. A later test of a confined hooked bar specimen was performed with a linear potentiometer connected to the point at which the hook bend is vertical, treating that portion of the hook in the same manner as the head was treated for all of the other tests. Slip measurements of non-headed bars were simply made against the termination point of the bar. Strain gage layouts for the hooked bars are shown in Figure 2-10. Strain gage layouts on the confined specimen stirrups are shown in Figure 2-11.

The arrangement of strain gages shown in Figure 2-9 was the layout used for most of the CCT tests. As with the reinforcement detailing, the placement of strain gages evolved as the testing progressed. The first two groups of CCT node specimens (indicated as the 1st and 2nd trial groups in Table 2-5) contained strain gages on only the bottom side of the tie bar. Furthermore, the spacing of the gages was at $4d_b$ rather than $2d_b$ as used in the later specimens. Data from these first two casts of CCT node specimens was problematic for many reasons, and those specimens are not included in any of the data presentation. In the third group of CCT node specimens, a layout very similar to the one shown in Figure 2-9 was used,

except that the top gage that is placed at a distance of $7d_b$ from the face of the head was placed on the bottom of the bar at $9d_b$. Following the tests of those specimens, it was realized that little of interest was occurring at that location and the gage was moved up to the top to give redundancy to the other top gage. The layout of the strain gages was then finalized for the remaining casts of specimens with the exception of one specimen. One unconfined specimen was cast with 22 strain gages placed at $2d_b$ on the top and bottom of the tie bar so that the complete strain profile of a bar at a CCT node could be determined.

As mentioned in the last section, three specimens with special reinforcing details were cast. Each of these three specimens contained strain gage instrumentation on the special reinforcing details. The details of the instrumentation of these specimens will be with the test results.

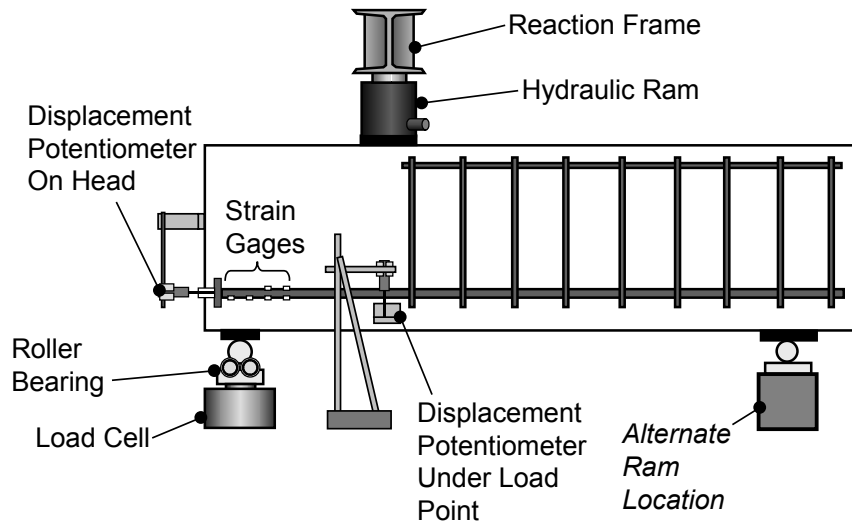


Figure 2-8: Placement of instrumentation for a typical specimen

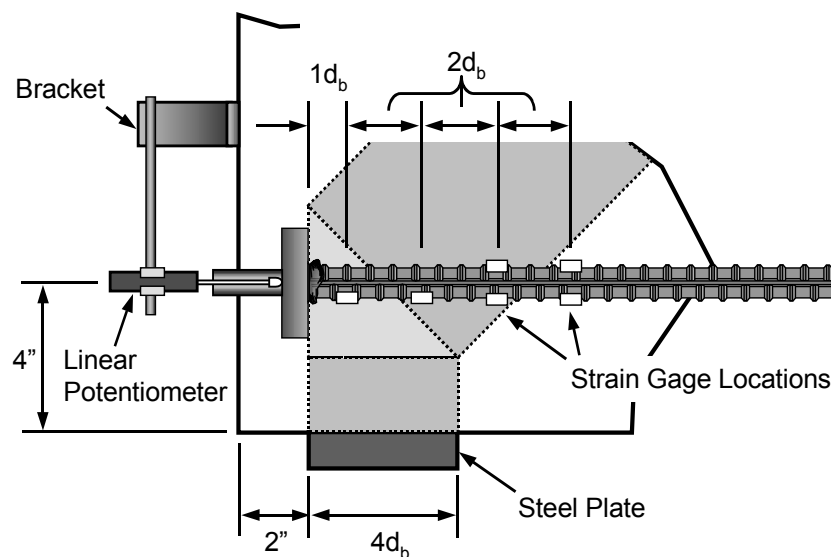
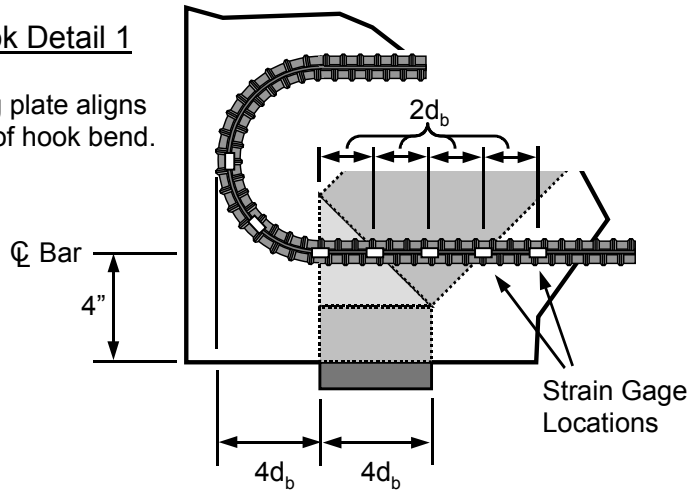


Figure 2-9: Placement of instrumentation in the nodal region of a typical specimen

Standard Hook Detail 1

Edge of bearing plate aligns with beginning of hook bend.



Standard Hook Detail 2

Edge of bearing plate aligns with inside of hook bend.

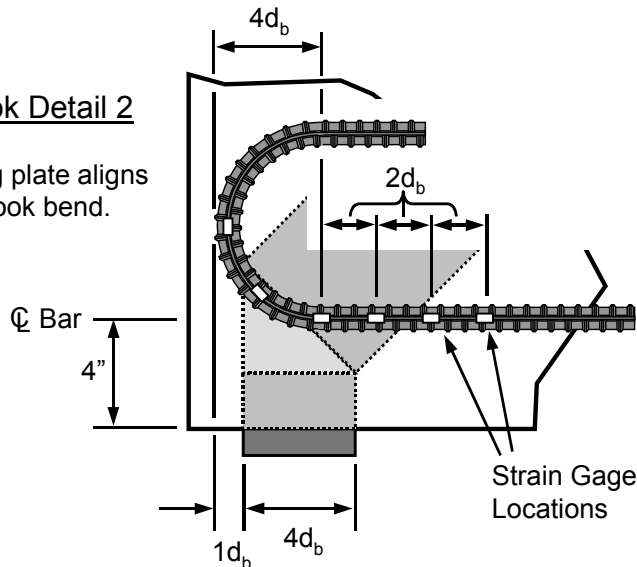


Figure 2-10: Details of the reinforcement and instrumentation for hooked bar specimens

2.4 LOAD SETUP

The basic load setup for the CCT node specimens is pictured in Figures 2-1 and 2-8. Essentially, the CCT node specimen was a deep beam that rested on two bearing supports. A hydraulic ram exerted load through a top bearing plate. The ram reacted against a steel cross-frame that was tied into the floor. The reaction frame was composed of heavy steel W-sections and exhibited no discernible deformation during the loading of any of the test specimens. A hemispherical head was placed in series with the load ram to ensure that load was exerted uniformly from the ram into the specimen.

For the CCT node specimens with #11 bars, the capacity of the specimen exceeded the capacity of the ram. In order to load these specimens, the ram was moved to the back bearing plate and a rigid steel piece was placed between the specimen and the reaction frame (the hemispherical head was left in place). Figure 2-1 shows a photograph of this arrangement. The alternate location of the ram is indicated in Figure 2-8. The placement of the ram at the back bearing plate provided more leverage for the application of load and required less ram force. The disadvantage of this arrangement was that more stroke was required in order to load the specimen and an additional linear potentiometer had to be placed at that

location in order account for deflection at that point. This change in the load arrangement did not affect the behavior of the specimens in any way.

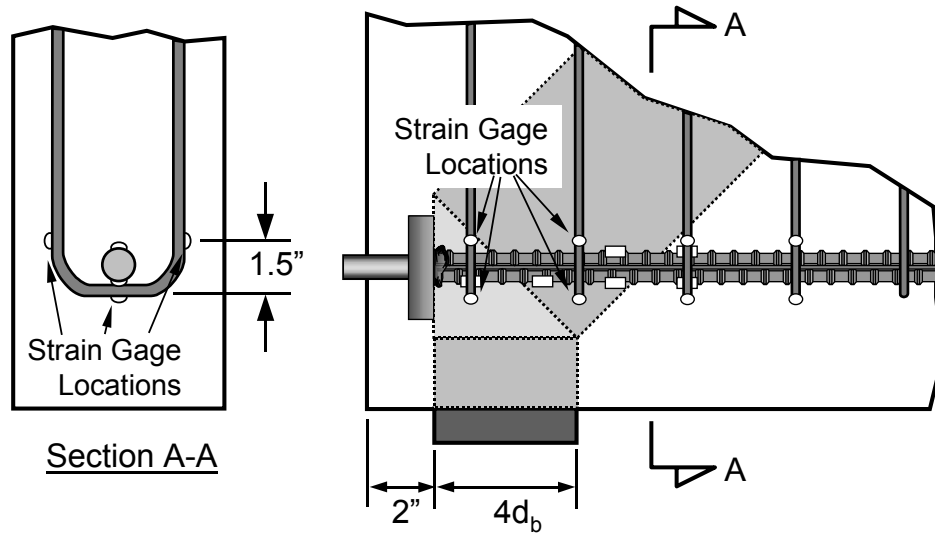


Figure 2-11: Placement of instrumentation on stirrups of confined specimens

Changes in the strut angle required changes in the loading geometry. The reaction frame remained stationary, but the supports and the specimen had to be moved either forward or backward in order to change the placement of the load.

As with the reinforcement layout and the strain gage instrumentation, the configuration of the load setup went through several steps before it was finalized. For the testing of the first two groups of CCT node specimens, the load cell was placed in line with the hydraulic ram at the top of the specimen and the magnitude of the reaction at the node was calculated. Initially, neoprene pads were used to support the beam. However, the distribution of load through the bearing plate was uneven under this configuration. To permit rotation of the bearing plate, a pin was added. However, the pin did not allow horizontal movement of the bearing plate and analysis of subsequent test results indicated that a significant horizontal reaction might occur due to friction. The presence of a horizontal reaction in the CCT node region can seriously affect the equilibrium of the assumed truss (Figure 2-12). The force in the bar, F_b , should be related to the force in the bearing pad, P , by equilibrium of the CCT node and the geometry of the strut angle. If a horizontal reaction, H , is introduced at the bearing plate, the truss mechanism becomes indeterminate. For a 45° strut, the horizontal reaction also makes the vertical reaction, P , larger than the bar force, F_b . Normally the capacity of the specimen, P , should be limited by the force that can develop in the tie bar, but if a horizontal force, H , is introduced, the specimen can reach higher than expected capacities and, unless it can be measured, loads calculated for the bar are not correct. The higher bearing plate reaction causes greater compression in the CCT node region which may affect the CCT anchorage capacity. After the trial groups were tested, a roller bearing was placed under the CCT

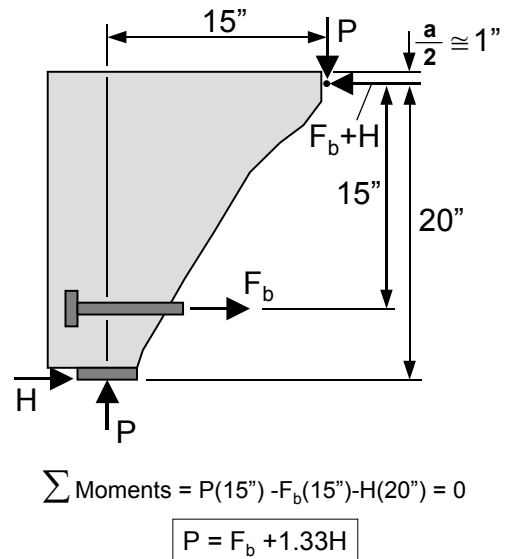


Figure 2-12: Equilibrium of CCT node panel with a horizontal reaction at the bearing plate (45° strut angle)

node (see Figure 2-13). The roller was designed to eliminate any horizontal force development at the bearing plate. Additionally, the load cell was moved underneath the CCT node in order to have an exact measure of the reaction. The development of this support arrangement at the CCT node was an important advance in the accuracy and consistency of the CCT testing process.

Young [24] reported on the first CCT node tests. Her thesis contains a more detailed discussion of the evolution of the CCT fabrication and testing process. By the fourth group of CCT node specimens, all of the reinforcement, instrumentation, and loading details of the CCT node specimens had been finalized (There were 9 groups of CCT node specimens which were separated by casts.).

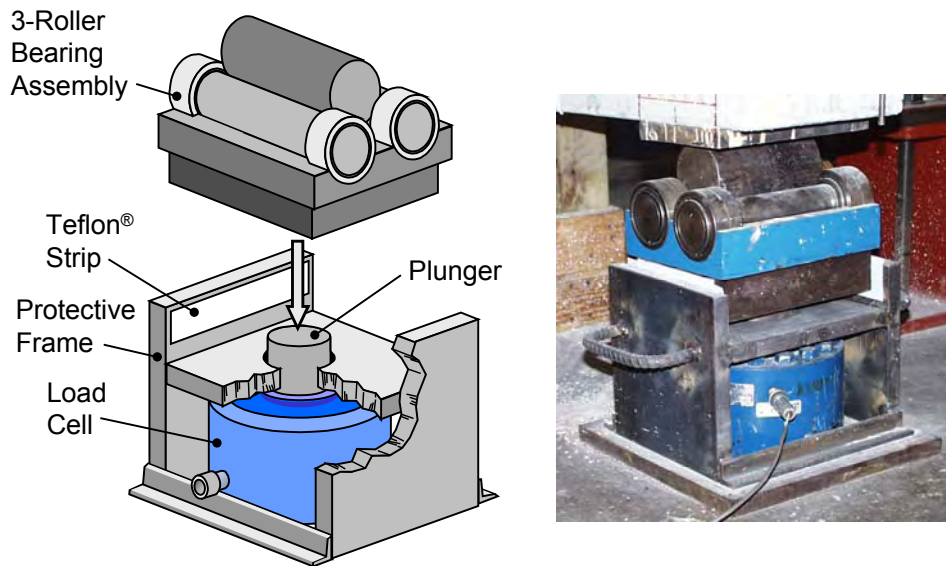


Figure 2-13: Free roller detail used for the final CCT node test setup

2.5 TESTING PROCEDURE

Preparation of the specimen for testing involved the attachment of the top and bottom bearing plates, the front bracket used to hold the linear potentiometer for slip measurements of the head, the attachment of the side bracket used for deflection measurements, and drawing of the reinforcement layout and node geometry on the sides of the specimen (The drawing of those details facilitated in understanding the cracking patterns and provided a reference for picture taking.). $\frac{3}{4}$ " to 1" thick steel bearing plates were used. The plates were the full width of the specimen. The top and rear-bottom plates were each $6d_b$ long for all tests. The front-bottom plate (the critical CCT node plate) was either $4d_b$ or $6d_b$ in length for all tests. Initially the $6d_b$ length was used, but, by the third group of specimens, most tests were carried out with the $4d_b$ length. The smaller bearing area made the node region more likely to fail and thus provided insight into the failure modes. The bearing plates were attached to the specimen with Hydrostone® plaster. The plaster provided a uniform bearing between the plate and the concrete surface allowing for an even transfer of stress. The slip and deflection potentiometer brackets were simply epoxied to the concrete surface.

After the pre-test preparation, the specimen was placed into position within the load frame (the top cross-piece was removable for this purpose) and the load ram and hemispherical head were placed into position on the top of the specimen. Next, all instrumentation was connected to the data acquisition equipment and a computerized check of the circuits was conducted. Once the instrumentation was deemed to be working properly, the test was begun.

Load was controlled in the specimen via a hand-controlled pump. The data acquisition equipment allowed for instantaneous reading of the load cell data. A hydraulic dial gage was also used as an alternative check

on the specimen load. Load was generally applied in 3-5 kip increments up to the cracking point of the specimen. Thereafter, load was applied in 1-2 kip increments with data acquisition after each load increment. Load increments were generally once every 15-30 seconds. Loading was halted at intervals of 5-10 kips to check the specimen for cracking and take pictures if necessary. On some specimens crack widths were measured. These breaks in loading usually took around 5 minutes or less. Once the ultimate load of the specimen was approached, the load increment was reduced to about 0.2-0.5 kips until failure. Failure was generally sudden and brittle (frequently explosive). Photographs were then taken of the failed specimen and the load setup was cleaned up for the next test.

The complete testing process generally took 3-4 hours with loading taking only one hour or less of that time. Two CCT node tests could easily be performed in a day. At the peak of testing activity, three tests were performed on some days. The specimen fabrication process was much longer. Usually, three workweeks were required to build and cast 8 CCT node specimens. The testing of these 8 specimens could be performed in one week.

2.6 CCT NODE VARIABLES

As stated at the beginning of this chapter, 64 CCT node test specimens were fabricated and tested. The first 11 of these tests (from the first two specimen casts) must be discounted in the final analysis because the reinforcement layout and/or load setup were flawed. These tests were valuable in the information they provided on construction and testing procedures. However, the data can not be compared with other test results. Two other specimens in the later casts were also flawed due to poor concrete consolidation and the results were omitted in the final analysis. The study is based on 51 specimens that provided reliable test data. This section outlines the variables tested in the CCT node series and finally provides a master list of all the CCT node specimens.

Four basic variables were tested in the CCT node tests: the bar size, the strut angle, the head size and type, and the amount of confining steel.

2.6.1 Bar Size

Two bar sizes were tested: #8 bars and #11 bars. These sizes were chosen as being of the most interest to the project sponsors, TxDOT. #8's and #11's are at the larger end of the bar size spectrum (though not at the extreme end with #14's and #18's). Anchorage of smaller size bars in nodal zones is not of much concern because the smaller development lengths required for those bars are usually easier to fit into the tight nodal zone space restrictions. Larger bars are frequently more difficult to incorporate into disturbed regions because of their correspondingly larger development lengths. Typical Texas bridge projects typically do not use bars larger than #11 size. #8's were chosen to represent the smaller end of the spectrum and because their area is almost exactly half that of the #11's.

2.6.2 Strut Angle

Three strut angles were tested in the CCT test series: 30°, 45°, and 55°. The 45° strut angle was chosen as the baseline for testing because it provided a convenient equilibrium solution and represented a median strut angle that is believed to be very realistic for strut-and-tie modeling. The 30° angle was chosen as an extreme lower bound for possible strut angles. The debate over reasonable strut angles in ACI code committee work has surfaced the question of whether or not the 30° angle is a realistic limit. Specimens with 30° angles were included in the test series in order to answer questions regarding the lower bounds of strut angle limits. A 60° degree strut angle has been considered as an upper limit for strut-and-tie modeling. Specimens with a 55° strut angle were tested as an upper limit. The geometry of the 60° strut configuration placed the top load plate too close to the front of the specimen, so a slightly shallower angle was used for the upper limit of the test program.

2.6.3 Head Size/Type

Head size will be defined by a term called the relative head area, A_{nh}/A_b . The relative head area is the ratio of net head area to bar area:

$$\text{Relative Head Area} = \frac{A_{nh}}{A_b} = \frac{A_{gh} - A_b}{A_b} \quad (2-1)$$

- A_{nh} = the net head area (in²)
- A_{gh} = the gross head area (in²)
- A_b = the nominal bar area (in²)

Several different head types were tested in the program as well as standard hooks. Though the different head types frequently had different geometric shapes (square, rectangular, circular) they can usually be distinguished by their size alone. The hooks have no reasonable geometry to define as a head area. Head/anchorage types consisted of non-headed bars, standard 180° hooked bars, Xtender headed bars, Lenton Terminator headed bars, and HRC headed bars. The HRC headed bars were frequently cut down in size to provide a variety of head sizes and proportions. For most of the discussion in this report, heads will be distinguished by their relative head area alone. Only in sections that discuss the effect of head shape will the type and shape of the head be distinguished. The relative head areas of the various head types ranged from 0.00 (no head) to 10.39. Most of the heads had very consistent dimensions except the Xtender heads supplied by HRC. This head type is created by a forging process that is not very precise. Micrometer measurements were made of the Xtender heads supplied by HRC and the relative head areas of the bars were calculated. These results are summarized in Table 2-3. The mean head sizes from these measurements were used for all data reduction related to the Xtender headed bar tests. Headed bars that were made by cutting down HRC heads were accomplished by first torch cutting the head to slightly over-size dimensions, then by grinding the excess material off until the head had reasonable proportions. Cut-down heads were rejected if either side dimension was off by more than 0.1” or if the total head area was off by more than 5%.

Table 2-3: Measured head dimensions for Xtender bars

		Bar Size		
		# 5	# 8	# 11
Number of Bars Measured		11	35	20
Head Diameter, d_h (in)	Minimum	0.916	1.447	2.019
	Maximum	1.016	1.512	2.107
	Average	0.970	1.479	2.041
	Std. Deviation	0.034	0.016	0.021
Gross Head Area, A_{gh} (in ²)	Minimum	0.66	1.64	3.20
	Maximum	0.81	1.80	3.49
	Average	0.74	1.72	3.27
	Std. Deviation	0.05	0.04	0.07
Relative Head Area, $\frac{A_{nh}}{A_b}$	Range	1.13 - 1.61	1.08 - 1.28	1.05 - 1.24
	Average	1.39	1.18	1.10
	Std. Deviation	0.17	0.05	0.04

2.6.4 Confinement

Only a few confined CCT node specimens were tested. Confinement consisted of #3 hoops stirrups. The only variable with respect to confinement was the spacing of the stirrups. Stirrups spacing was 3" or 6". It is also reasonable to define the analogous unconfined CCT node specimens as confined specimens with a very large spacing of ties. Confinement was referred to by the confinement ratio: A_s/b_s (the stirrup steel area divided by the specimen width and the stirrup spacing). The three confinement ratios are then 0.000 (unconfined), 0.006 (#3 stirrups at 6"), and 0.012 (#3 stirrups at 3").

2.7 NOMENCLATURE AND LIST OF SPECIMENS

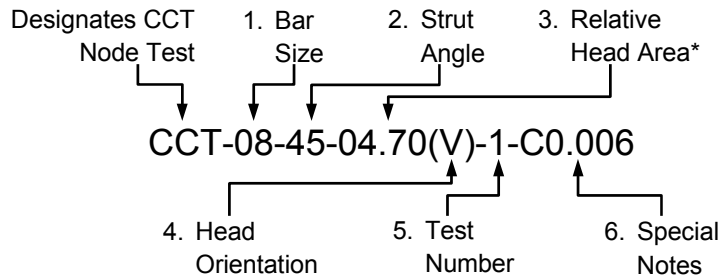
In this section, a standard nomenclature for CCT node specimen identification is presented. Young [24] developed a standard nomenclature in her report on the early CCT node testing that included bar size, head area and shape, specimen width, base plate length, single or multiple bars, confined or unconfined bars, and first or repeat tests. Her nomenclature was extended to include strut angle but symbols for multiple bars were omitted (no multiple bar tests were ever performed). Table 2-4 provides an example of the nomenclature and descriptions of the different identifiers.

The example given in Table 2-4 is for a CCT node specimen with a #8 bar, 45° strut angle, a head with 4.70 relative head area (this happens to be a 1.5" x 3" rectangular head) oriented with the long side parallel to the vertical axis. It is the first test of its kind and has confinement with a stirrup ratio of 0.006 (#3 closed hoops at 6" spacing within a 6" wide specimen). Special notes are included with the id's only when necessary. Some other examples are given below:

CCT-11-45-02.85(H)-1:	#11 bar size, 45° strut angle, relative head area of 2.85; the head is rectangular and oriented horizontally.
CCT-08-45-Hook1-1:	#8 bar size, 45° strut angle, bar anchored by a standard hook with positioning conforming to detail 1 shown in Figure 3-10.
CCT-08-45-00.00-1-E2,W8:	#8 bar size, 45° strut angle, relative head area equal to zero (non-headed); the specimen was an early test from the 2 nd cast with 8d _b width.
CCT-08-45-04.70(V)-1-C0.000:	#8 bar size, 45° strut angle, relative head area equal to 4.7, a rectangular head with vertical orientation; the special note is optional and only included when the specimen is listed next to confined specimens; it indicates that zero confinement was provided

Table 2-5 is a list of all the CCT node specimens. Every specimen that was fabricated and tested is listed in Table 2-5 whether the test was successful or not. The table lists the specimen id's, the head type used, the concrete used in the test (refer to Table 2-2), the date of the test, and special notes not indicated by the id. Square and rectangular heads are referred to by their outer dimensions. Circular heads are referred to by their diameter, d_h. Standard hooks are referred to by name.

Table 2-4: Nomenclature of CCT node test identifiers



Identifier	Description	Choices
1.	Bar Size - the size of the tie bar in standard ASTM sizes.	08..... #8 11..... #11
2.	Strut Angle [†] - given in degrees.	30, 45, or 55
3.	Relative Head Area * -given to four significant digits. <i>or alternatively</i> a designation for a standard hook detail	00.00 - 10.39 <i>or</i> Hook1 or Hook2
4.	Head Orientation - either vertical or horizontal; used only for rectangular head tests.	(H)...Horizontal (V).....Vertical
5.	Test Number - gives the number for repeated tests	1.....1 st Test 2.....2 nd Test
6.	Special Notes - Information for non-standard tests (<i>optional</i>):	
	C - Confined Test; followed by the stirrup reinforcement ratio A_s/bs	C0.000-C0.012
	W - Nonstandard specimen width; followed by the width/ d_b	W8..... $8d_b$ wide W6..... $6d_b$ wide
	B - Nonstandard bearing plate length; followed by the length/ d_b	B6..... $6d_b$ long B4..... $4d_b$ long
	E - Early tests with no stirrups in back region (1 st cast) or without a free roller bearing (2 nd cast)	E1.....1 st cast E2.....2 nd cast
S - Special reinforcement detail (<i>discussed in next chapter</i>)	S1, S2, or S3	

* Relative head area is defined as the ratio of net head area to bar area: $A_{nh}/A_b = (A_{gh} - A_b)/A_b$
with A_{nh} = net head area, A_{gh} = gross head area, &
 A_b = bar area

[†] Strut angle is measured from the horizontal.

Table 2-5(a): List of all CCT node tests

Specimen Identification	Head Type	Concrete	Test Date	Notes
CCT-08-45-00.00-1-E1,W8	no head	A1	08-12-99	1 st Trial Group
CCT-08-45-01.18-1-E1,W8	$d_h = 1.48"$	A1	08-13-99	
CCT-08-45-04.70(H)-1-E1,W8	1.5" x 3.0"	A1	08-14-99	
CCT-08-45-10.39-1-E1,W8	3.0" x 3.0"	A1	08-15-99	
CCT-08-45-00.00-1-E2,W8	no head	B1	10-26-99	2 nd Trial Group
CCT-08-45-01.18-1-E2,W8	$d_h = 1.48"$	B1	10-28-99	
CCT-08-45-04.70(H)-1-E2,W8	1.5" x 3.0"	B1	11-01-99	
CCT-08-45-10.39-1-E2,W8	3.0" x 3.0"	B1	11-03-99	
CCT-08-45-00.00-1-E2,W6	no head	B1	11-05-99	
CCT-08-45-04.70(H)-1-E2,W6	1.5" x 3.0"	B1	11-07-99	
CCT-08-45-10.39-1-E2,W6	3.0" x 3.0"	B1	11-09-99	
CCT-08-45-00.00-1-B6	no head	B2	02-21-00	
CCT-08-45-00.00-1	no head	B2	02-22-00	#8 Bars 45° Strut Angle
CCT-08-45-01.18-1	$d_h = 1.48"$	B2	02-23-00	
CCT-08-45-01.85-1	1.5" x 1.5"	B2	02-23-00	
CCT-08-45-01.85-2	1.5" x 1.5"	B6	03-06-01	
CCT-08-45-02.80(H)-1	1.5" x 2.0"	B2	02-24-00	
CCT-08-45-02.80(H)-2	1.5" x 2.0"	B6	03-07-01	
CCT-08-45-02.80(V)-1	1.5" x 2.0"	B3	07-10-00	
CCT-08-45-04.04-1	$d_h = 2.25"$	B2	02-25-00	
CCT-08-45-04.06-1	2.0" x 2.0"	B6	03-05-01	
CCT-08-45-04.70(H)-1	1.5" x 3.0"	B6	03-06-01	
CCT-08-45-04.70(V)-1	1.5" x 3.0"	B3	07-10-00	
CCT-08-45-10.39-1*	3.0" x 3.0"	B6	03-05-01	
CCT-08-45-10.39-2†	3.0" x 3.0"	C6	06-18-01	
CCT-08-45-Hook1-1‡	Hook Detail 1	B2	02-28-00	
CCT-08-45-Hook2-1‡	Hook Detail 2	B2	02-28-00	
CCT-08-30-00.00-1	no head	B7	03-12-01	#8 Bars 30° Strut Angle
CCT-08-30-01.18-1	$d_h = 1.48"$	B7	03-12-01	
CCT-08-30-01.85-1	1.5" x 1.5"	B7	03-14-01	
CCT-08-30-04.04-1	$d_h = 2.25"$	B7	03-13-01	
CCT-08-30-04.06-1	2.0" x 2.0"	B7	03-13-01	
CCT-08-30-10.39-1	3.0" x 3.0"	B7	03-14-01	

Table 2-5(b): List of all CCT node tests (continued)

Specimen Identification	Head Type	Concrete	Test Date	Notes
CCT-08-55-00.00-1	no head	B3	07-11-00	#8 Bar 55° Strut Angle
CCT-08-55-01.18-1	$d_h = 1.48"$	B3	07-11-00	
CCT-08-55-01.85-1	1.5" x 1.5"	B3	07-12-00	
CCT-08-55-02.80(H)-1	1.5" x 2.0"	B3	07-13-00	
CCT-08-55-02.80(V)-1	1.5" x 2.0"	B3	07-13-00	
CCT-08-55-04.04-1	$d_h = 2.25"$	B6	03-01-01	
CCT-08-55-04.06-1	2.0" x 2.0"	B6	03-01-01	
CCT-08-55-04.70(H)-1	1.5" x 3.0"	B2	03-07-00	
CCT-08-55-04.70(H)-2	1.5" x 3.0"	B6	03-02-01	
CCT-08-55-04.70(V)-1	1.5" x 3.0"	B3	07-14-00	
CCT-08-55-10.39-1	3.0" x 3.0"	B2	03-08-00	
CCT-08-45-00.00-1-C0.006	no head	C6	06-19-01	
CCT-08-45-00.00-1-C0.012	no head	C6	06-20-01	
CCT-08-45-04.70(V)-1-C0.006	1.5" x 3.0"	C6	06-19-01	
CCT-08-45-04.70(V)-1-C0.012	1.5" x 3.0"	C6	06-20-01	
CCT-08-45-Hook2-1-C0.012	Hook Detail 2	C6	06-19-01	
CCT-08-45-04.70(V)-1-S1*	1.5" x 3.0"	B7	03-08-01	Special Details
CCT-08-45-04.70(V)-1-S2	1.5" x 3.0"	B7	03-09-01	
CCT-08-45-04.70(H)-1-S3	1.5" x 3.0"	C6	06-18-01	
CCT-11-45-00.00-1	no head	B4	12-05-00	#11 Bars 45° Strut Angle
CCT-11-45-01.10-1	$d_h = 2.04"$	B4	12-05-00	
CCT-11-45-01.56-1	2.0" x 2.0"	B4	12-06-00	
CCT-11-45-02.85(H)-1	2.0" x 3.0"	B4	12-07-00	
CCT-11-45-02.85(V)-1	2.0" x 3.0"	B4	12-07-00	
CCT-11-45-03.53-1	$d_h = 3.00"$	B5	12-15-00	
CCT-11-45-04.13(H)-1	2.0" x 4.0"	B4	12-08-00	
CCT-11-45-04.13(V)-1	2.0" x 4.0"	B5	12-14-00	
CCT-11-45-04.77-1	3.0" x 3.0"	B5	12-18-00	
CCT-11-45-06.69(H)-1	3.0" x 4.0"	B5	12-17-00	
CCT-11-45-06.69(V)-1	3.0" x 4.0"	B5	12-15-00	
CCT-11-45-09.26-1	4.0" x 4.0"	B5	12-19-00	

* Unsuccessful testing due to poor concrete consolidation.

† Specimen specially outfitted with extensive strain gaging.

‡ Specimen was side-cast.

CHAPTER 3: CCT NODES: BEHAVIOR DURING TESTING

The behavior of the CCT node test specimens as observed during the testing process are discussed in terms of: cracking development, deformation and stress, and failure modes. Results of unconfined CCT node specimens that constitute the majority of the testing are discussed first.

3.1 UNCONFINED SPECIMEN BEHAVIOR

3.1.1 *Cracking Behavior*

Specimen CCT-08-45-10.39-2 represents a typical CCT node test. A large number of strain gages were placed along the length of the bar in this test; 22 as opposed to 6 used in other tests. The additional data are helpful in explaining stress gradients along the length of the headed tie bar. This specimen had a 45° strut angle and used a #8 bar with a standard HRC square head (3" x 3") at its anchorage. The measured concrete compressive strength was 3800 psi and the measured split cylinder tensile strength was 360 psi. Figures 3-1a and 3-1b outline the development of cracking in the specimen during testing.

Every CCT node specimen began cracking in the same manner as the representative test (CCT-08-45-10.39-2). A vertical crack initiated at the bottom of the specimen at the maximum moment point somewhere directly underneath the top bearing plate, the point of load application (Figure 3-1, part i). Following the development of the first crack, the pattern of crack growth then followed one of two distinct patterns. The representative test followed a pattern of crack development in which secondary diagonal cracks formed successively at regular intervals along the headed bar, starting from the initial vertical crack forming underneath the point of load application and forming closer and closer to the node (parts ii, iii, iv). In this pattern of crack development, the closer the crack was to the nodal zone, the higher the load that precipitated its formation. Next, as the headed bar reached peak force in the strut-tie mechanism, bond tended to break down along the length of the bar and horizontal cracks appeared between the vertical/diagonal cracks (part v). It was also not unusual for a longitudinal crack to form along the bar on the bottom of the specimen. Longitudinal cracks along the tie bar usually started away from the node and grew towards the head. Crack development generally stopped well before the capacity of the CCT node was reached (part vi). Failure of the specimen could occur in several ways, but generally involved the explosive cleaving of the triangular portion of concrete above the diagonal compression strut (Figure 3-2).

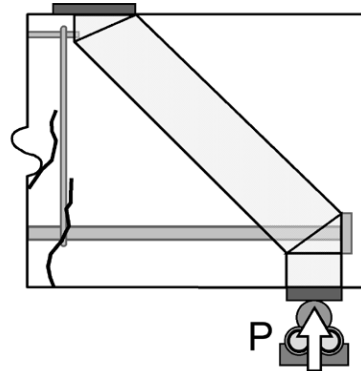
Figure 3-3 illustrates the pattern of crack widening that was observed in Specimen CCT-08-45-10.39-2. Initially the first crack widened until the formation of the second crack closer to the node. Then widening of the first crack ceased and the second crack grew wider than the first. Eventually a third crack formed even closer to the node. After the formation of the third crack, the widening of the second crack halted and the third crack widened to an even greater extent. For every unconfined specimen tested, the crack closest to the node always demonstrated the greatest crack widths and the most rapid growth of crack width.

Specimen CCT-08-45-01.85-2 demonstrated a different pattern of crack development that was typical of a different group of the CCT node specimens. This specimen had a 45° strut angle and a #8 tie bar anchored by an HRC head that was cut down to 1.5" x 1.5" dimensions. This test is representative of the CCT tests with small head sizes. The measured concrete compressive strength was 3100 psi and the tensile strength was 350 psi. Figure 3-4 illustrates the pattern of crack development.

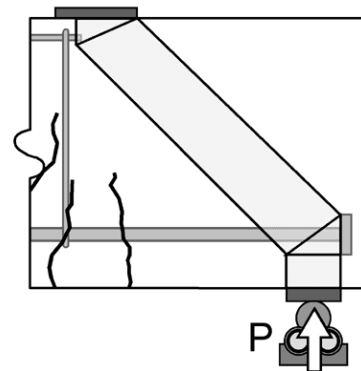
After the initial development of a crack underneath the load point (part i), no new cracks formed until the sudden appearance of a splitting crack along the length of the diagonal compression strut (part ii). The appearance of the splitting crack along the diagonal strut alleviated strain build-up in the concrete adjacent to the nodal zone and very few cracks formed after the development of the splitting crack. A

small vertical crack next to the node was common (part iii) in this cracking behavior. No additional cracks formed prior to failure (part iv).

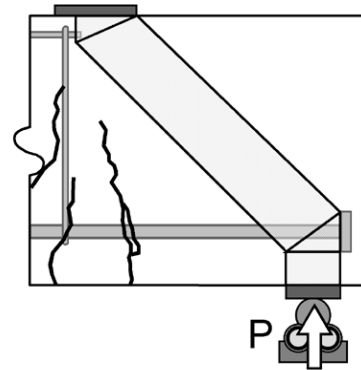
- i. P = 14.5 kips
 First cracking just under load point initiated by presence of front-most stirrup.



- ii. P = 26.1 kips
 A second crack forms closer to the nodal zone.



- iii. P = 29.8 kips
 Growth of the first and second cracks towards the top bearing plate.



- iv. P = 31.6 kips
 Sudden appearance of a third crack even closer to the nodal zone. The third crack grows at an angle parallel to the diagonal strut.

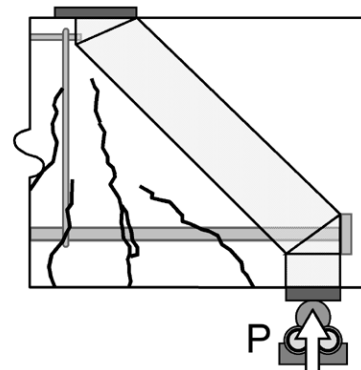
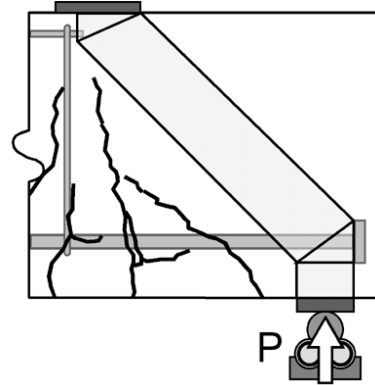


Figure 3-1a: Development of cracks in a representative test with a large head (CCT-08-45-10.39-2)

- v. P = 35.3 kips
A horizontal crack grows from the second to the third crack.



- vi. P = 59.5 kips
No significant growth of the existing cracks until sudden and brittle failure of the specimen. The front portion of the specimen (shaded gray) is split away from the main body.

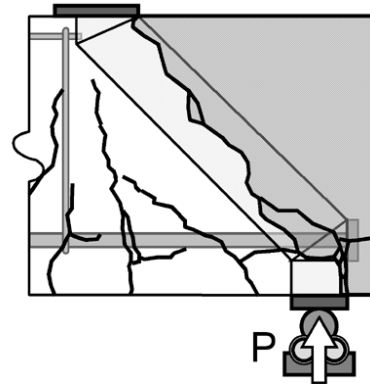


Figure 3-1b: Development of cracks in a representative test with a large head (CCT-08-45-10.39-2) (continued)



Figure 3-2: Failure of Specimen CCT-08-45-10.39-2

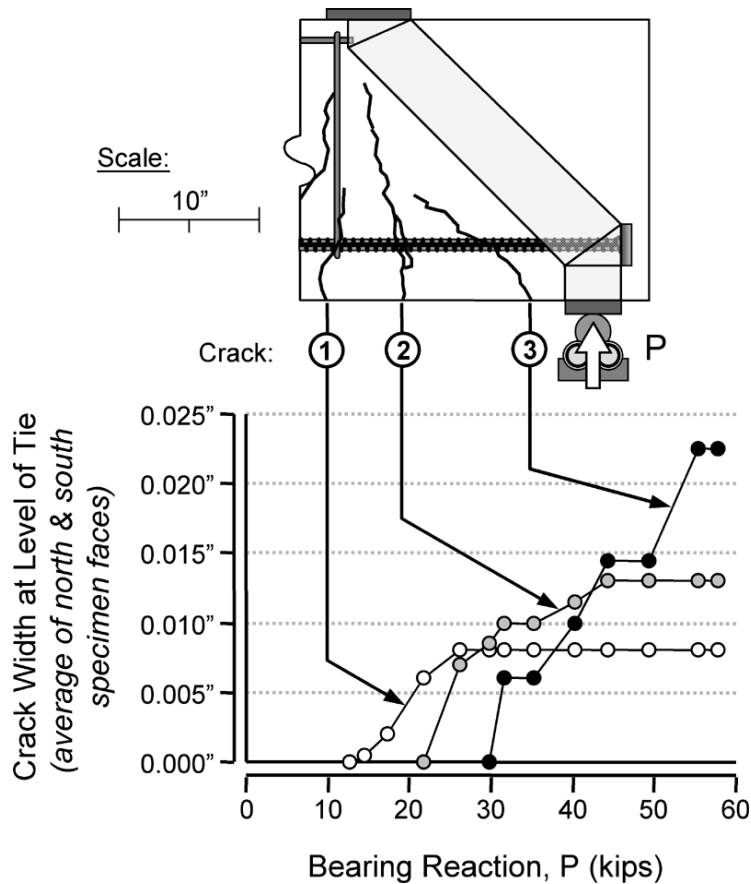


Figure 3-3: Crack width measurements from Specimen CCT-08-45-10.39-2

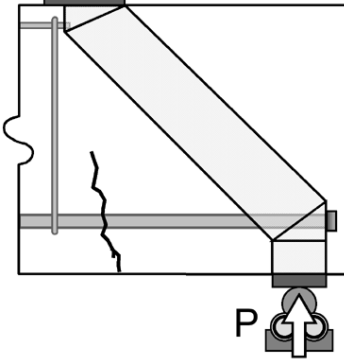
The pattern of crack development in Figure 3-4 differs from the first one described in Figures 3-1a and 3-1b by the occurrence of the large splitting crack along the length of the strut. This type of crack development was more common in specimens that had tie bars anchored by small heads. The bars anchored by small heads experienced more slip at the anchorage point than bars with large heads (see Section 3.1.5) and the cracking behavior may have been influenced by that difference.

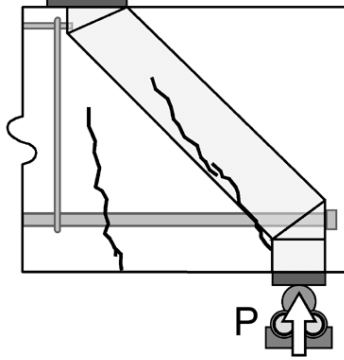
The crack patterns from the previous two specimens are compared to a similar specimen with a tie bar anchored by a standard hook: CCT-08-45-Hook2-1. The measured concrete compressive strength of this specimen was 4000 psi (the tensile strength was not determined by tests, but can be estimated at 400 psi). Figure 3-5 illustrates the development of cracks in the hooked bar test.

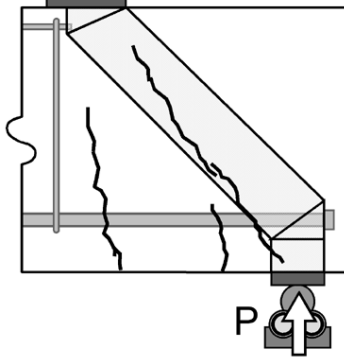
Cracking in the hooked bar test was similar to the cracking pattern in specimens with bars that had large heads. Cracking began with a vertical crack just under the load point (part i). A second crack formed between the first crack and the node. A horizontal crack due to bond failure along the tie bar began shortly after that (part ii). By the time the specimen was near its peak load, a diagonal crack formed in the direction of the strut and several small cracks formed between it and the second crack (part iii). Failure was sudden and brittle. The tail of the hook prevented the concrete above the strut from splitting off. The concrete bulged outward along the diagonal compression strut particularly near the bend of the hook. A crack passed horizontally at this location diverting upward along the bend of the hook. Cracking tended to indicate that the depth of the diagonal compression strut exceeded the presumed dimensions which were more applicable to the headed bar tests (part iv). The increased depth of the diagonal compression strut results because the hooked bar allows a taller CCT node to form (Figure 3-6).

The cracking patterns described in Figures 3-1(a and b), 3-4, and 3-5 were all for specimens with 45° strut angles. Analogous specimens with 30° and 55° struts are examined next.

- i. P = 18.6 kips
 First cracking just under load point.


- ii. P = 29.9 kips
 A second shear/splitting crack suddenly forms within the diagonal compression strut. The crack does not extend to the bottom of the specimen nor to the top.


- iii. P = 37.9 kips
 The strut splitting crack grows towards the top and bottom bearing plates. A third crack forms close to the nodal zone. There is negligible growth of the first crack.


- iv. P = 52.0 kips
 Sudden and brittle failure of the specimen. Side spalling of concrete parallel to the strut. Splitting off of the front-most portions of the specimen.

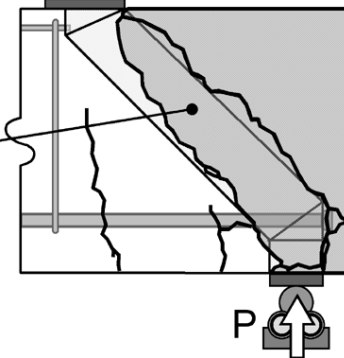


Figure 3-4: Development of cracks in a representative test with a small head (CCT-08-45-01.85-2)

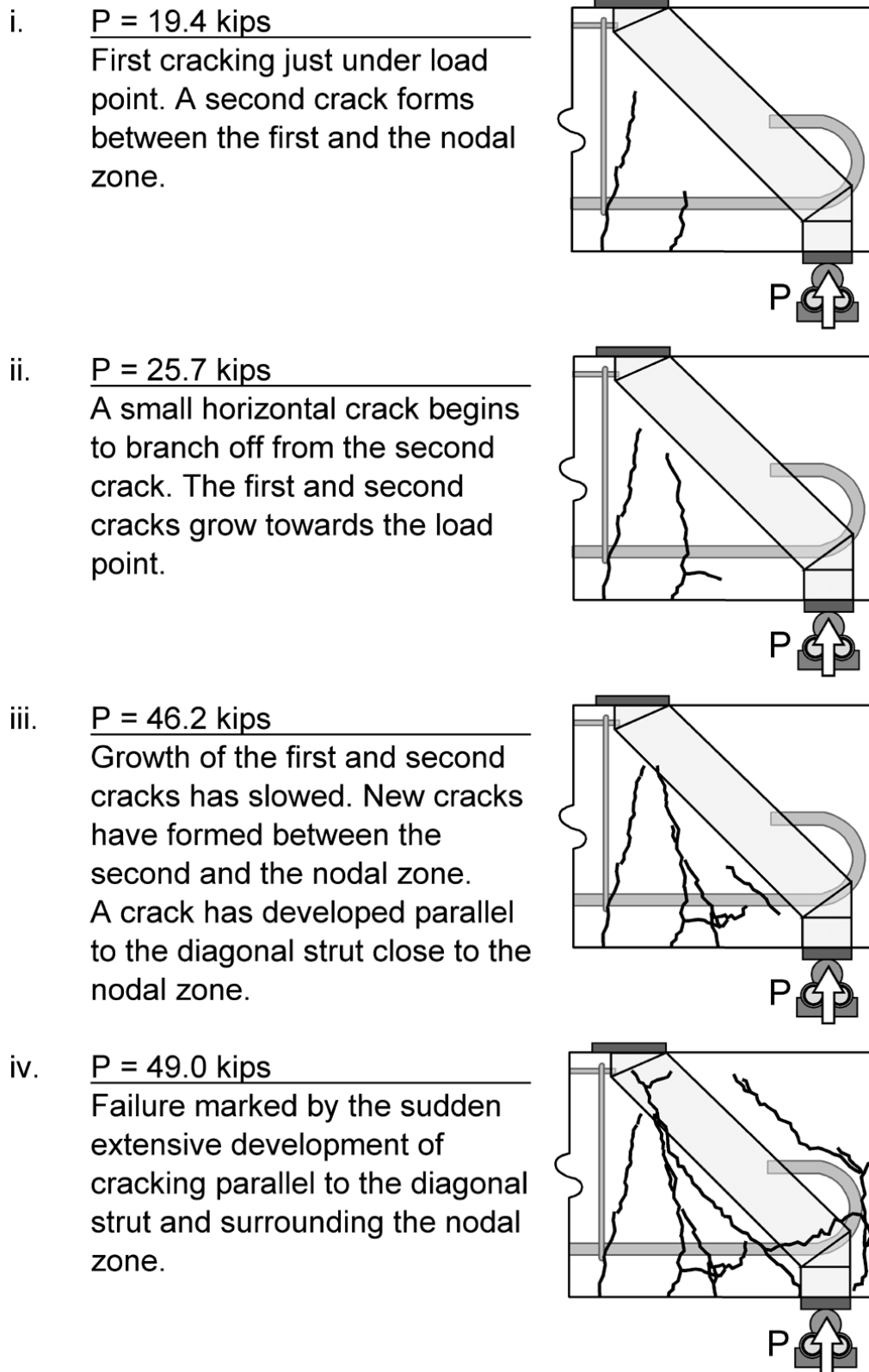


Figure 3-5: Development of cracks in the hooked bar test (CCT-08-45-Hook2-1)

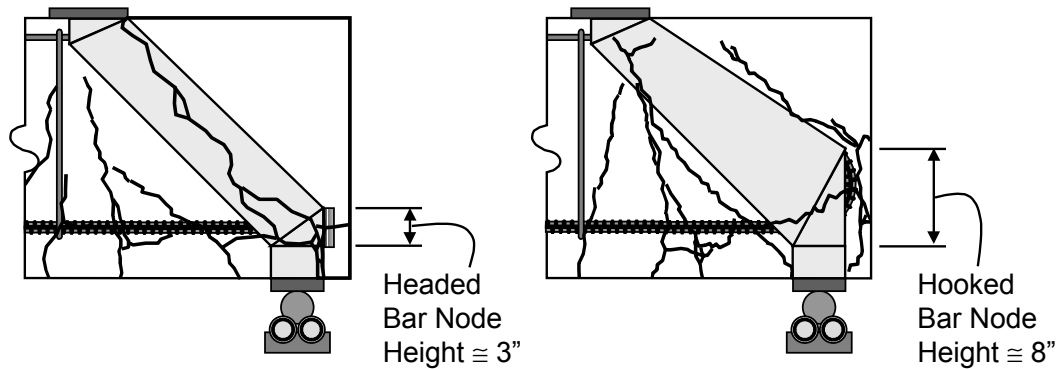


Figure 3-6: CCT node height in headed bar and hooked bar tests

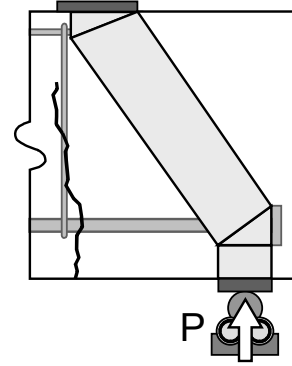
Figure 3-7 shows the cracking pattern for CCT-08-55-10.39-1. This specimen had a 55° strut angle and a #8 tie bar anchored with a standard square HRC head (3" x 3"). The measured concrete compressive strength was 4000 psi (the tensile strength was not measured, but can be estimated at 400 psi). This specimen was directly comparable to the representative test with a large head size (CCT-08-45-10.39-2); the only difference was the strut angle.

As with its 45° counterpart, cracking initiated with a vertical crack just under the load point (part i). A small horizontal crack began to branch off of the first crack and grow towards the node (part ii). Then, like the 45° strut specimen, a second crack formed between the first crack and the node (part iii). A horizontal crack also branched off from the back of the first crack and began to grow away from the node. The horizontal cracks were most likely associated with bond failure of the bar. No new cracking occurred until the load increased by 50% from the load at which the previous cracking had been observed. A long crack occurred along the edge of the strut (part iv). The maximum bearing reaction reached was over 91 kips. Based on presumed equilibrium of the truss mechanism, that load indicated a force that exceeded yield in the tie by almost 12%. The test was halted shortly afterwards due to the fact that the load ram was near ultimate capacity. Unfortunately, the halt in the testing made it impossible to determine the potential ductility of the specimen and its ability to sustain further load. The observed cracking of CCT-08-55-10.39-1 was typical of other specimens with 55° struts.

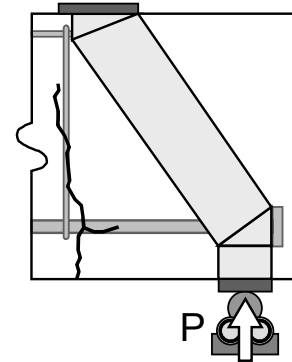
Figures 3-8a and 3-8b illustrate the cracking pattern for Specimen CCT-08-30-10.39-1. This specimen had a 30° strut angle and a #8 tie bar anchored with a standard square HRC head (3" x 3"). The measured concrete compressive strength was 4100 psi and the tensile strength was 420 psi. This specimen was also directly comparable to the representative test with the large head size (CCT-08-45-10.39-2); the only difference being the strut angle.

Cracking in the 30° strut test began with a vertical crack under the load point (part i). This crack was primarily flexural. As bond stresses increased in the tie bar next to this crack, horizontal cracks appeared that grew towards the node (part ii). A diagonal crack eventually connected the horizontal crack to the vertical one (part iii). As more load was applied, second and third diagonal shear cracks appeared between the first crack and the diagonal strut (part iv). The front-most crack eventually grew to the full depth between the bottom fibers and the top of the compression strut as the truss mechanism of the specimen was developed (part v). The top diagonal crack became the primary tensile crack and experienced the most widening. The critical stress location of the tensile tie was at the point where it crossed this crack. The tie began to yield at this point, and after extensive plastic deformation, a fourth diagonal crack began to form next to the node (part vi). The behavior of CCT-08-30-10.39-1 was typical of the 30° strut angle specimens.

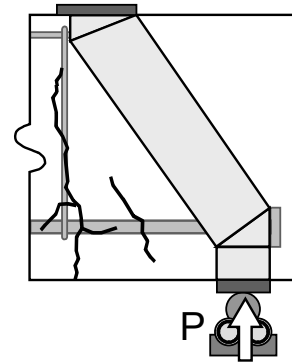
- i. $P = 33.7$ kips
 By this load, there is still only one vertical flexural crack. The path of the crack follows closely to the location of the front-most stirrup.



- ii. $P = 44.4$ kips
 A small horizontal crack begins to branch off of the vertical crack and grows along the depth of the tie bar towards the nodal zone.



- iii. $P = 51.1$ kips
 The first diagonal crack appears halfway between the vertical crack and the path of the diagonal compression strut.



- iv. $P = 76.2$ kips
 Sudden appearance of a second diagonal crack that grows along the edge of the diagonal strut. There is no new crack growth before the test is terminated at a load of 91.9 kips.

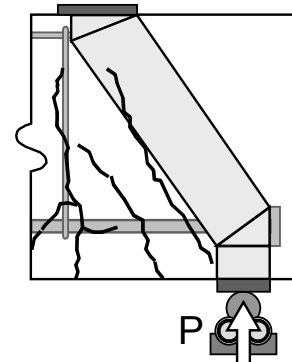
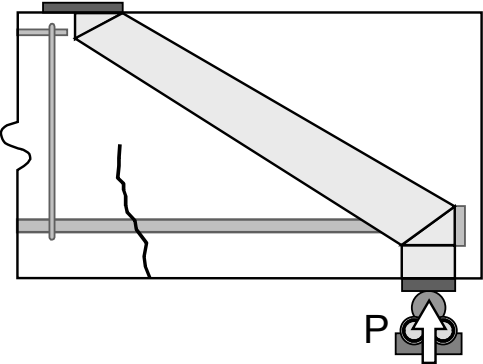


Figure 3-7: Development of cracks in a steep strut angle test (CCT-08-55-10.39-1)

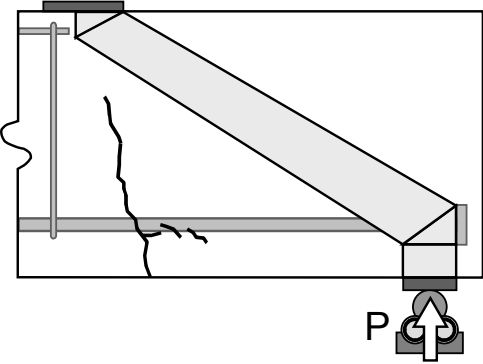
It is apparent from the cracking behaviors of 30°, 45°, and 55° tests that decreases in the strut angle of the specimen increased the anchorage length of the tie bar. For the shallowest angle, 30°, the primary tensile crack was further away from the node boundary than in the cases of the 45° and 55° strut angles. This

allowed more development length for the tie bar at the node. In the 55° strut test, a diagonal crack formed right at the edge of the CCT node and diagonal strut boundary thus reducing the development length of the tie bar to a minimum. As a result, the shallower strut angle specimens tended to show better tie anchorage than specimens with the steeper strut angle (section 4.2.2 discusses this issue further).

- i. P = 12.2 kips
First cracking due to flexure underneath the load point.



- ii. P = 20.5 kips
A small horizontal crack begins to branch off from the first crack.



- iii. P = 25.7 kips
Development of the first diagonal crack. It branches downward from the flexural crack and connects to the horizontal crack.

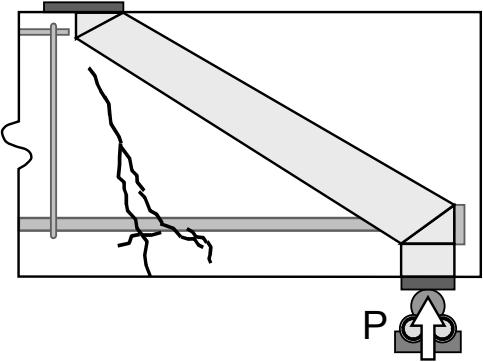
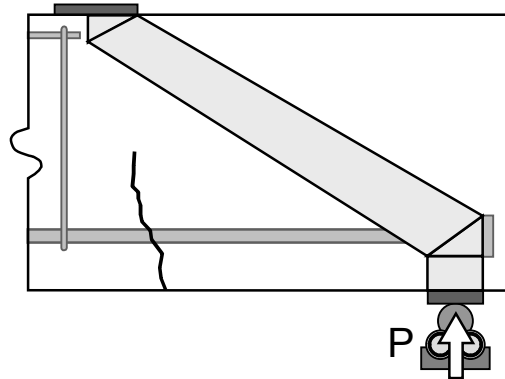
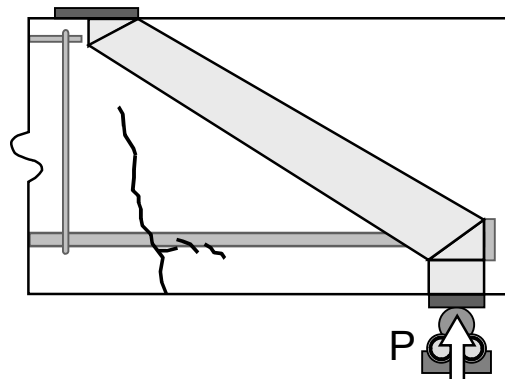


Figure 3-8a: Development of cracks in a shallow strut angle test (CCT-08-30-10.39-1)

- i. $P = 12.2$ kips
First cracking due to flexure underneath the load point.



- ii. $P = 20.5$ kips
A small horizontal crack begins to branch off from the first crack.



- iii. $P = 25.7$ kips
Development of the first diagonal crack. It branches downward from the flexural crack and connects to the horizontal crack.

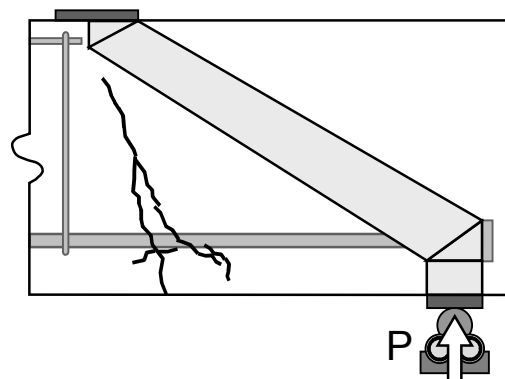


Figure 3-8b: Development of cracks in a shallow strut angle test (CCT-08-30-10.39-1) (continued)

Cracking in the #11 bar specimens resembled the cracking of #8 bar specimens with the same 45° strut angles. In many cases the large bar diameter of the #11 bar resulted in the earlier formation of horizontal cracking along the tie bar. Otherwise, the cracking behaviors shown in Figures 3-1 (a and b) and 3-4 can be regarded as typical for the #11 bar specimens.

3.1.2 Stress/Strain Development in the Bar

The representative test specimen (CCT-08-45-10.39-2) was specially instrumented to fully measure the development of stress in the bar along its length in the CCT node panel region. Strain gages were placed at 2" on the top and bottom of the bar in this specimen. The gages started at 1" from the face of the head and extended for 20". Twenty-two strain gages were used in total. Figure 3-9 is a plot of the measured strains. The distribution of strain along the top and bottom fibers of the bar is plotted for four different load levels (the front reaction, P, is generally used as the indicator of load level for most results presented in this report). Positive strain corresponds to tension. A diagram of the north face of the specimen is drawn to scale at the top of the figure for reference.

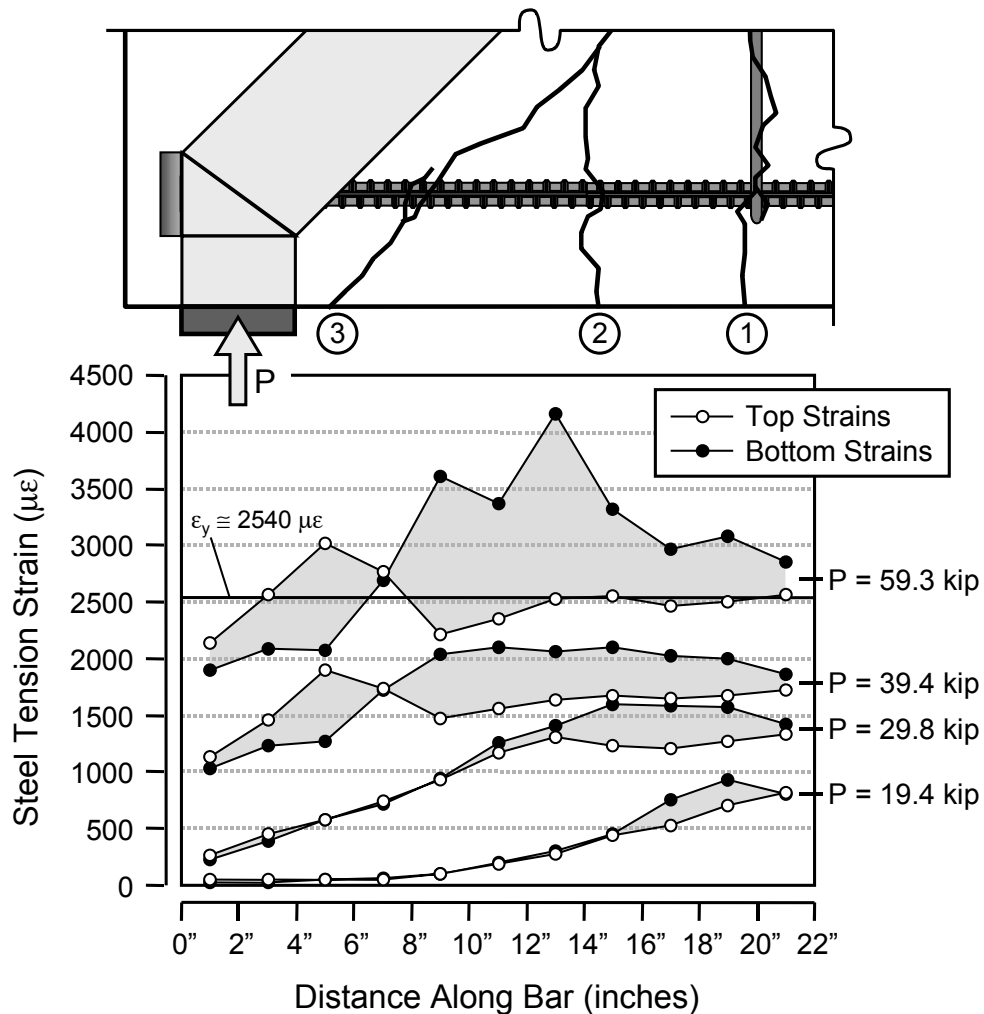


Figure 3-9: Top and bottom fiber strains of the tie bar in Specimen CCT-08-45-10.39-2

No large strains were recorded along the bar until first cracking occurred around a load of 14.5 kips (refer to Figure 3-1 for the progression of cracking in Specimen CCT-08-45-10.39-2). The strain distribution

indicated for a load of 19.4 kips shows that the largest strains in the bar correlate to the position of crack 1. The bottom fiber strains were only slightly greater than the top fiber strains at that load level. The next crack in the specimen, crack 2, occurred around a load of 26.1 kips. The strain distribution at 29.8 kips shows that the zone of large tensile strains in the bar had extended to the location of crack 2. The difference between the top and bottom fiber strains has also grown. This indicates that the bar was in positive curvature (positive curvature equating to larger tensile strains along the bottom of the bar) through the region of maximum tension. The third and last major crack in the specimen appeared at a load of 31.6 kips. The strain distribution at 59.3 kips shows that the bar was strained beyond yield along nearly the entire gaged length. The strain distribution at this load also shows that a situation of reverse curvature had developed in the bar near the location of the third crack (between 6" and 8"). The strain profile indicates that the bar was "kinked" in a manner consistent with dowel action across shear cracks (Figure 3-10). The final strain distribution at a load of 59.3 kips shows that the bar had begun yielding, however, yielding was more pronounced along the bottom fibers of the tie bar. Full yielding of the bar was observed when the load reached 59.8 kips. Large increases in top and bottom strains at a distance of 13" from the head indicated that plastic deformation was concentrated at one location on the tie bar.

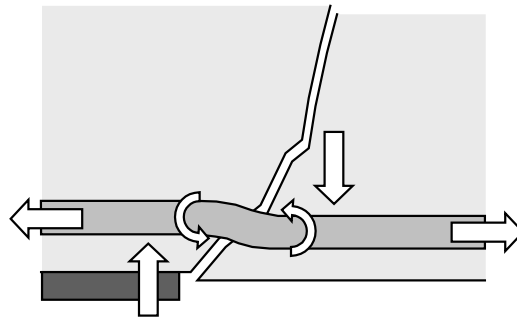


Figure 3-10: "Kinking" of reinforcement caused by dowel action across diagonal shear cracks

Bar stresses are shown in Figure 3-11. The stresses were calculated from the measured strains in accordance with procedures outlined in Appendix A. At a load of 19.4 kips, the maximum stress in the bar was measured at 19" from the face of the head. At a load of 29.8, the maximum stress was reached at 13". At a loads of 39.4 kips and higher, the maximum stress level in the bar was nearly uniform from a point of 7" away from the head. The shortening of the development length corresponded with the formation of cracks closer and closer to the node as the truss mechanism became fully active. Final anchorage of the bar clearly occurred within the first 7", the length roughly from the face of the head to the point where the bar passed out of the diagonal strut. The stresses at 1" in from the head provide an indication of the bar force carried by the head while the stresses at 7" give an indication of the total force in the bar.

The stress data from Figure 3-11 were used to determine bond stress along the bar in Specimen CCT-08-45-10.39-2 as shown in Figure 3-12. At 25.6 kips, the point of maximum bond occurred away from the head, close to the first crack. When the next crack formed at a load of 26.1 kips, the maximum bond shifted to 10" from the head. When the third crack formed, the location of maximum bond moved next to the head. Peak bond stresses increased as the point of maximum bond approached the head. This could be due to the increased vertical compression or platen restraint in the node region next to the head. The bond stress calculated using ACI development length equations is plotted in the figure. The implied understrength factor of 0.9 was removed from the ACI equation. The measured local bond exceeded the ACI value. However, because the ACI equation represents average bond stresses, this is expected.

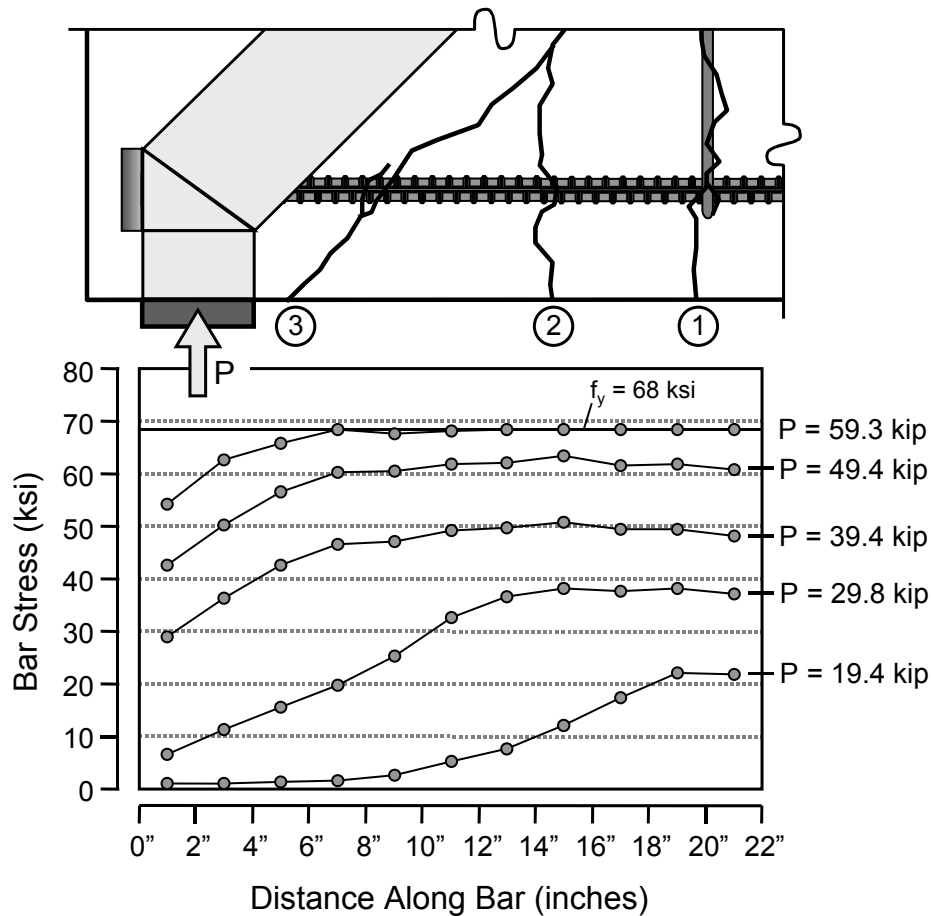


Figure 3-11: Development of bar stress in Specimen CCT-08-45-10.39-2

The development of a non-headed bar is compared to the development of a bar with a small head in Figure 3-13. The strain and stress development at peak capacity for two specimens with 55° struts (CCT-08-55-00.00-1 and CCT-08-55-01.85-1) is plotted. Data from the non-headed bar show that the stress tapered to zero at the end of the bar. Data from the headed bar, on the other hand, show that the stress at the end of the bar was somewhere between 35-40 ksi. The head, even though it is very small, provided a significant boost to the development of the bar. Figure 3-13 also shows that the development of the headed bar was composed of a combination of bond plus a contribution from head bearing. Figure 3-14 shows the contributions to total bar stress provided by bond and head bearing in Specimen CCT-11-45-02.85(V)-1. The stress from bond was measured over the bar length from $1d_b$ to $7d_b$. Figure 3-14 shows that the contribution from bond peaked and then began to decrease before the contribution from head bearing reached its maximum capacity. This behavior was common for many of the CCT node tests with larger head sizes. The bond component of anchorage frequently could not be sustained to the load necessary to achieve full capacity from the larger heads. Thus, anchorage of the headed bars consisted of a two-step process, in which bar force was at first carried by bond, then as the bond reached its maximum level and began to fail, anchorage shifted towards the head. The final development of the bar was comprised of the peak bearing capacity of the head plus a diminished bond contribution.

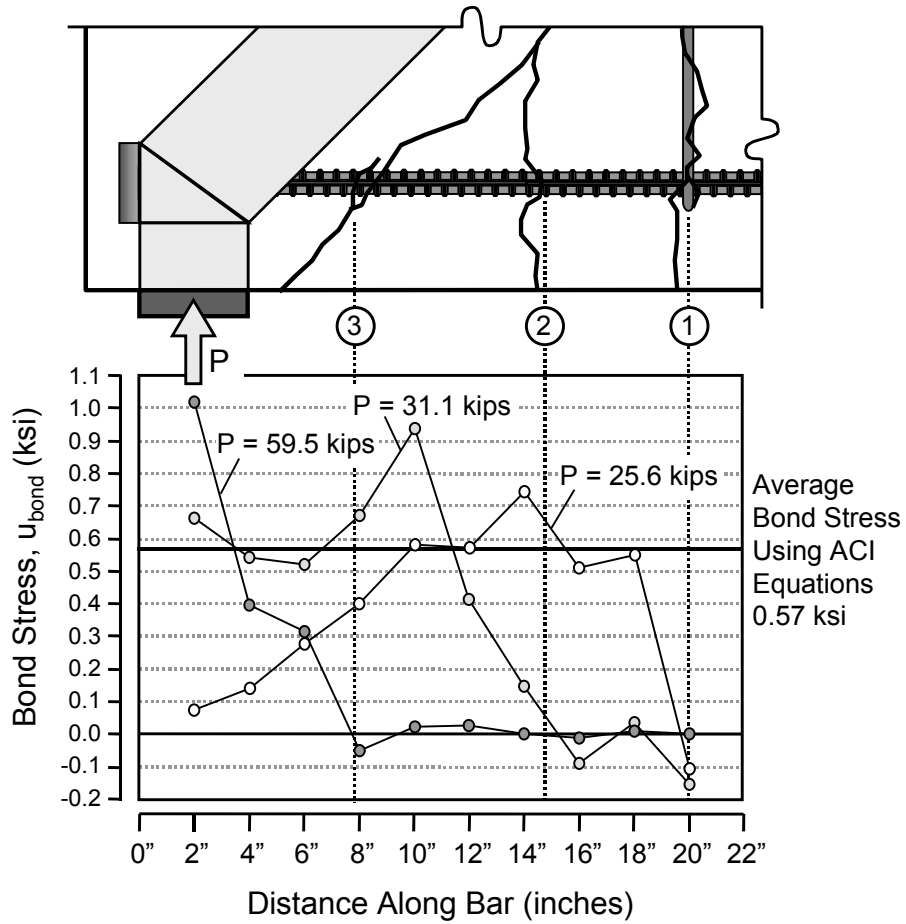


Figure 3-12: Measured bond stresses in CCT-08-45-10.39-2

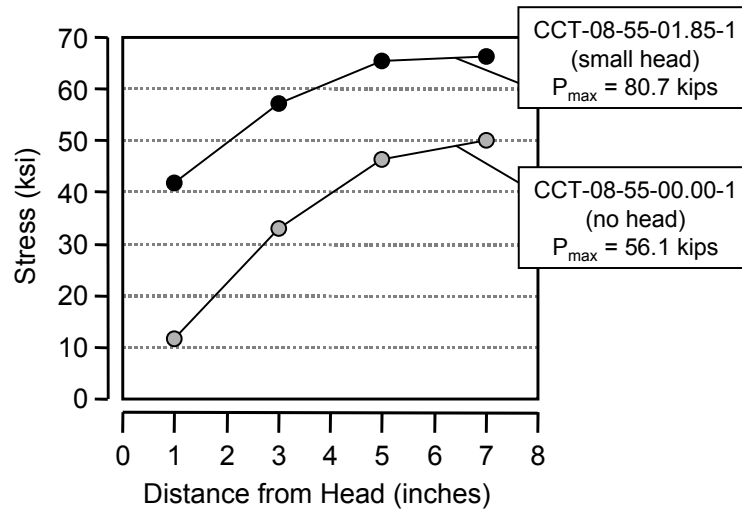


Figure 3-13: Development of stress for headed and non-headed bars

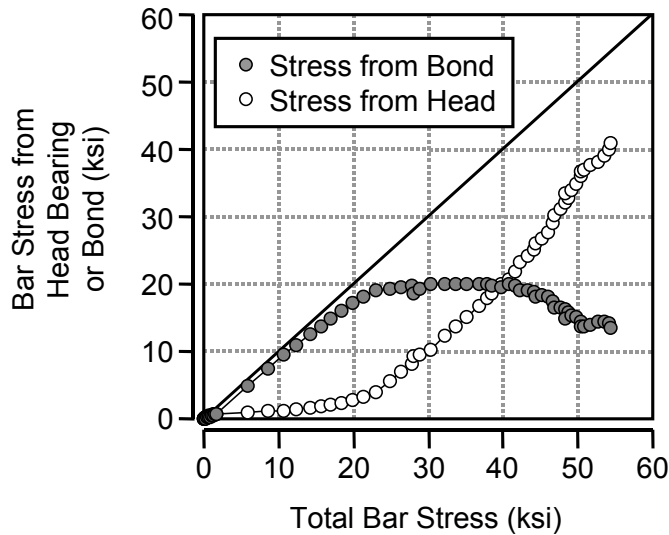


Figure 3-14: Components of bar stress provided by bond and head bearing in CCT-11-45-02.85(V)-1

3.1.3 Equilibrium of the Truss Mechanism

As a check to verify that no horizontal restraint was acting in the load setup and that the strain data for the tie bar were correct, equilibrium of the CCT node was always checked. Figure 3-15 shows a schematic of a CCT node region and the assumed equilibrium solution. A section has been taken through the CCT node specimen and only that portion of the applied load that equilibrates with the front bearing reaction is shown. When analyzed using ACI strut-and-tie provisions [2], the depth of the upper compression block for most of the CCT nodes was between 2.5"-3.5". Thus the approximate lever arm over which the horizontal forces act was about 14.5" on average. The lever arm over which the vertical forces acted changed for the different strut angles. The appropriate values are listed in Figure 3-15.

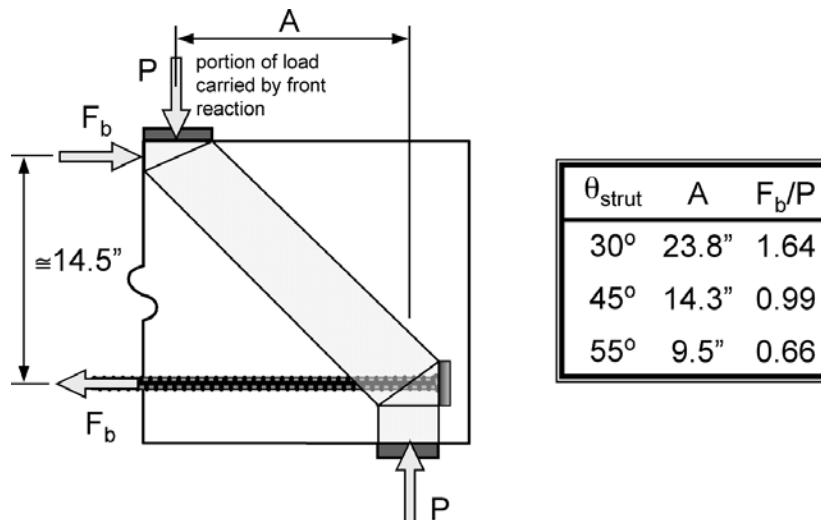


Figure 3-15: Equilibrium of CCT node (45° strut angle)

Figure 3-16 shows a plot of bar force versus bearing reaction for Specimen CCT-08-45-10.39-2. The bar force was calculated from the strain gage readings at a location 7" from the bearing face of the head. For

CCT-08-45-10.39-2, a 45° strut specimen, the equilibrium solution approximates to $F_b = P$. A straight line is plotted in Figure 3-16 that represents the theoretical relationship. Because the bar force was not initially fully developed at 7", the force in the bar near the head does not equal the bearing reaction at low levels of load. However, after the specimen had undergone significant cracking (the formations of the 2nd and 3rd cracks in CCT-08-45-10.39.2 are labeled in the plot), the bar force approached the theoretical value and closely paralleled the expected behavior. The only thing that is surprising about the behavior is the development of load beyond the yield level of the bar. The plot shows that after bar force reached yield of the bar (54 kips) additional load developed at the reaction. The yield level of the reinforcing bar was determined from tensile tests of bar samples. There is no doubt that the bar force was limited to 54 kips for this particular specimen. The reasons for capacity beyond the yield level of the bar are discussed in Section 3.1.5.

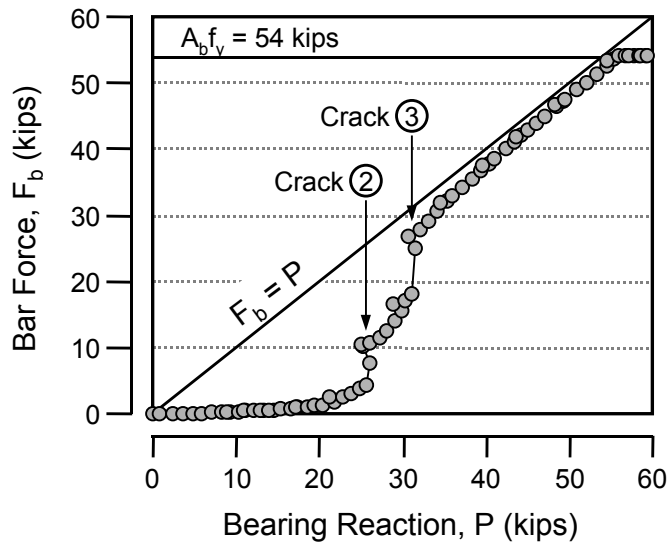


Figure 3-16: Equilibrium plot of bar force versus bearing reaction in Specimen CCT-08-45-10.39-2

3.1.4 Head Slip

Head slip was measured for all of the CCT node tests. In general the results showed that the larger head sizes slipped less. Results for the smaller head sizes tended to be mixed. Some bars began to slip immediately and others did not slip at all until failure was imminent. The most consistent slip results came from the #11 bar tests. Figure 3-17 shows the head slip data for four #11 bar CCT node tests. Information for the four specimens is listed in Table 3-1. The stress at the head is based on data from the strain gage placed a distance d_b from the bearing face of the head.

Table 3-1: Specimen information for data plotted in Figure 3-17

Specimen	Head Dimensions	$\frac{A_{nh}}{A_b}$	f'_c (ksi)	E_c (ksi)
CCT-11-45-00.00-1	no head	0.00	4.1	4300
CCT-11-45-01.56-1	2" x 2"	1.56	4.1	4300
CCT-11-45-04.77-1	3" x 3"	4.77	4.0	3700
CCT-11-45-09.26-1	4" x 4"	9.26	4.0	3700

The characteristics of the stress-slip plots were similar. No measurable slip occurred up to some load level. From that point on, there was little slip resistance until failure was reached especially for small head sizes. The data from the #11 bar tests in Figure 3-17 clearly show that slip resistance improved with increasing head size. As the relative head area increased from 0.00 to 4.77, the bar stress when slip initiated rose from 10 to 30 ksi. An additional area increase in relative head area to 9.26 did not increase the stress at initiation of slip. However, there was improved stiffness of the anchorage beyond that point. The initiation of slip did not seem to be simply related to the level of compression stress applied to the concrete by the bearing face of the head. Larger head sizes began to slip at lower bearing stresses than the smaller head sizes.

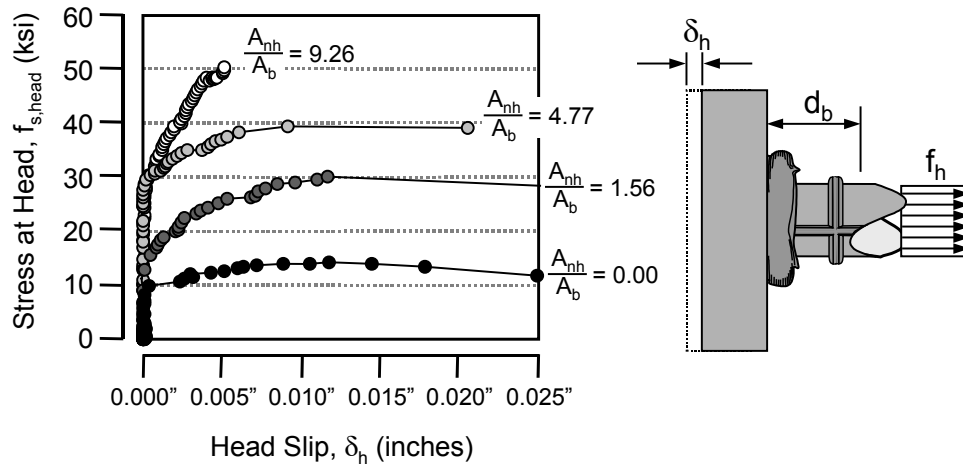


Figure 3-17: Bar stress versus head slip for CCT node specimens with #11 bars

Figure 3-18 shows stress-slip data for analogous #8 bar size tests. Data from 30°, 45°, and 55° strut angle tests are presented. Table 3-2 lists details of the specimens included in Figure 3-18. Slip data from Specimens CCT-08-30-01.85-1 and CCT-08-55-01.85-1 were flawed. The results follow a regular pattern of improved slip resistance with increasing relative head area.

Table 3-2: Specimen information for data plotted in Figure 3-18

θ_{strut}	Specimen	Head Dimensions	$\frac{A_{nh}}{A_b}$	f'_c (ksi)	E_c (ksi)
30°	CCT-08-30-00.00-1	no head	0.00	4.1	4000
	CCT-08-30-01.85-1	1.5" x 1.5"	<i>No slip data</i>		
	CCT-08-30-04.06-1	2" x 2"	4.06	4.1	4000
	CCT-08-30-10.39-1	3" x 3"	10.39	4.1	4000
45°	CCT-08-45-00.00-1	no head	0.00	4.0	4000*
	CCT-08-45-01.85-2	1.5" x 1.5"	1.85	3.1	3300
	CCT-08-45-04.06-1	2" x 2"	4.06	3.1	3300
	CCT-08-45-10.39-2	3" x 3"	10.39	3.8	4000
55°	CCT-08-55-00.00-1	no head	0.00	3.9	4000*
	CCT-08-55-01.85-1	1.5" x 1.5"	<i>No slip data</i>		
	CCT-08-55-04.06-1	2" x 2"	4.06	3.1	3300
	CCT-08-55-10.39-1	3" x 3"	10.39	4.0	4000*

* Estimated modulus of elasticity

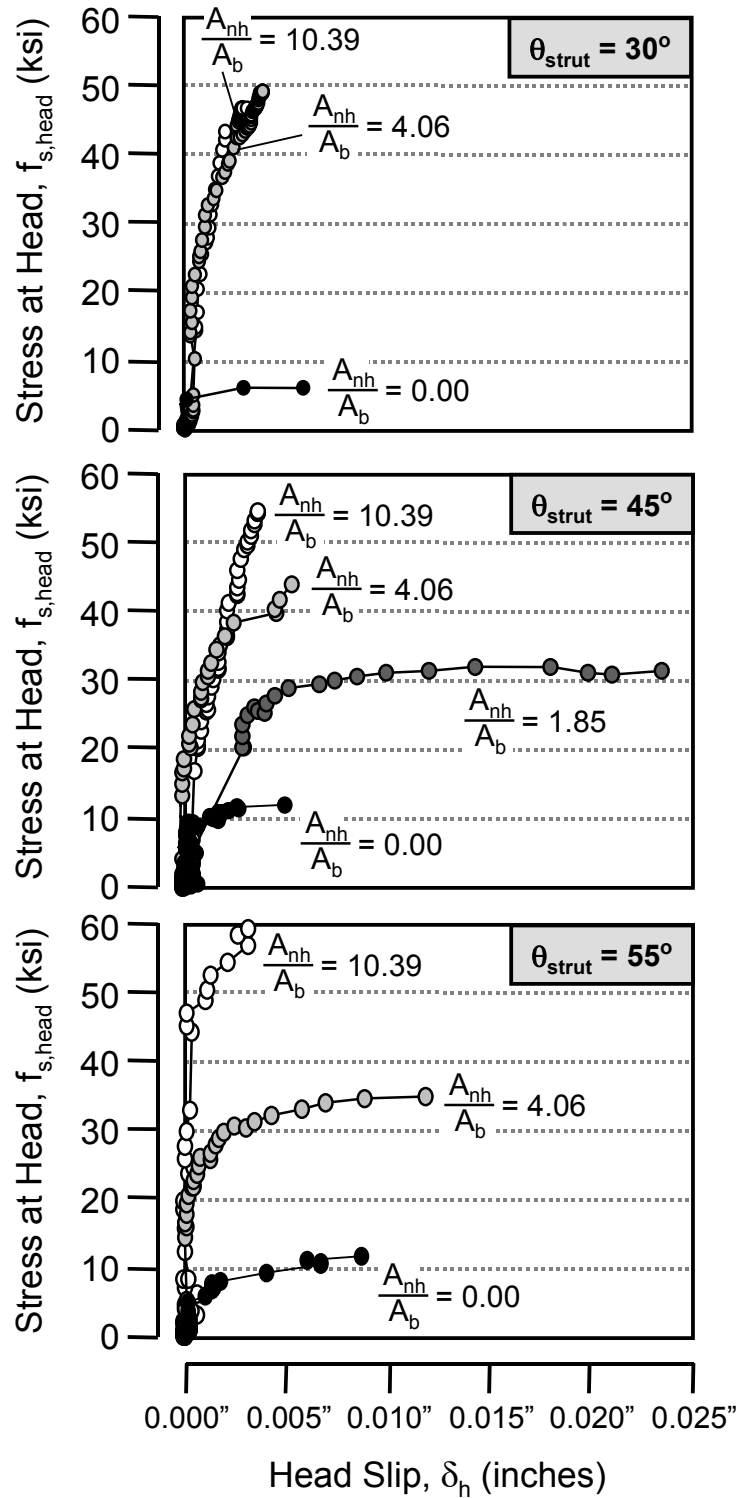


Figure 3-18: Bar stress versus head slip for CCT node specimens with #8 bars

3.1.5 Load-Deflection Response

The deflection of the CCT node specimens was measured underneath the load point for all tests. The deflection data helped to identify key features in the specimen behavior such as changes in stiffness due to head slip or the effects of horizontal restraint at the supports. Figure 3-19 shows the load-deflection response for two 30° strut angle specimens with small and large head sizes: CCT-08-30-01.18-1 and CCT-08-30-04.06-1. Both specimens had the same concrete with $f'_c = 4.1$ ksi and $E_c = 4,000$ ksi. The steel properties of the tie bars were also the same with $f_y = 68$ ksi and $E_s = 27,000$ ksi. Head slip data for the two specimens are presented adjacent to the deflection data. The measured bearing reaction is used as an indication of the load on the specimen.

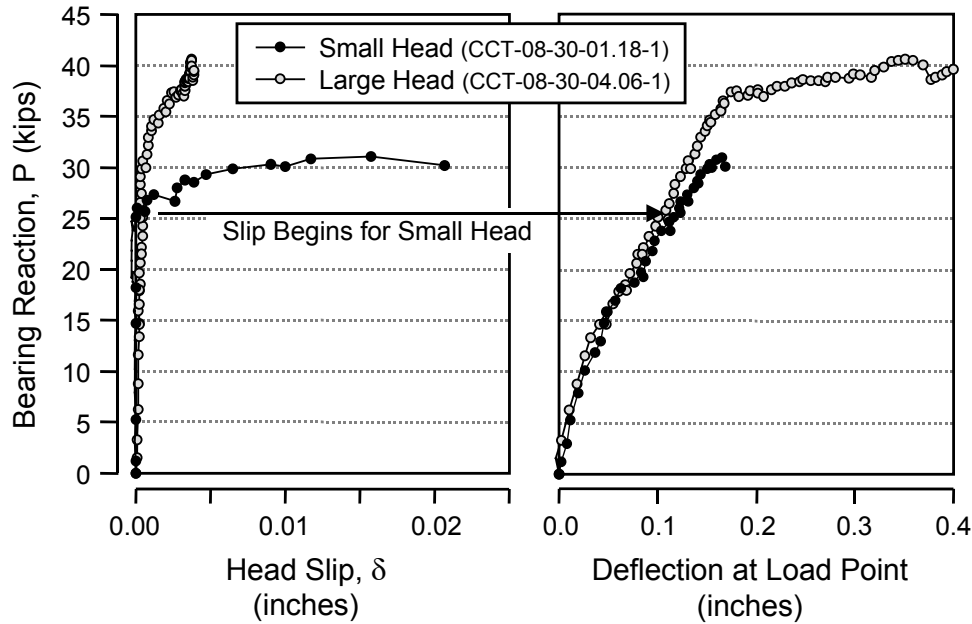


Figure 3-19: Load-deflection and load-slip data for specimens with small and large heads

Head slip data are presented next to the deflection data in Figure 3-19 in order to illustrate the effect of the head slip on the stiffness of the specimen. Initially both specimens had no head slip until a load of about 25 kips was reached. Then, the specimen with the small head began to slip. In the deflection data, a reduction in the stiffness of this specimen can be seen when compared with the specimen that had a larger head. The two load-deflection curves began to diverge around 25 kips. The specimen with a small head failed shortly thereafter at about 31 kips. The specimen with a large head continued to gain load and yielded at about 37 kips. There was a slight gain in strength even after the bar yielded.

The load at which yielding occurs in Figure 3-19 does not coincide with the expected yield load of the specimen. Given the geometry of the specimen, the placement of the loads, and the known yield strength of the tie bar, the yield capacity of the specimen should occur at a load of about 33 kips. However, the specimen with the large head clearly began yielding at a load of 37 kips. This unexpected increase in capacity is difficult to explain. Figure 3-20 shows the expected equilibrium state of the CCT node panel at the front of the specimen. Equilibrium of the moment forces dictates the expected yield capacity, P_y . The yield load of the tie bar, F_y , is known from tensile measurements of bar samples (see Appendix A). Only two other factors could account for an increase in the yield capacity of the specimen: an increase in the vertical lever arm between the horizontal forces or a decrease in the horizontal lever arm between the

vertical forces (as shown in Figure 3-20, part ii). These two distances could change with changes in the dimensions of the top CCC node.

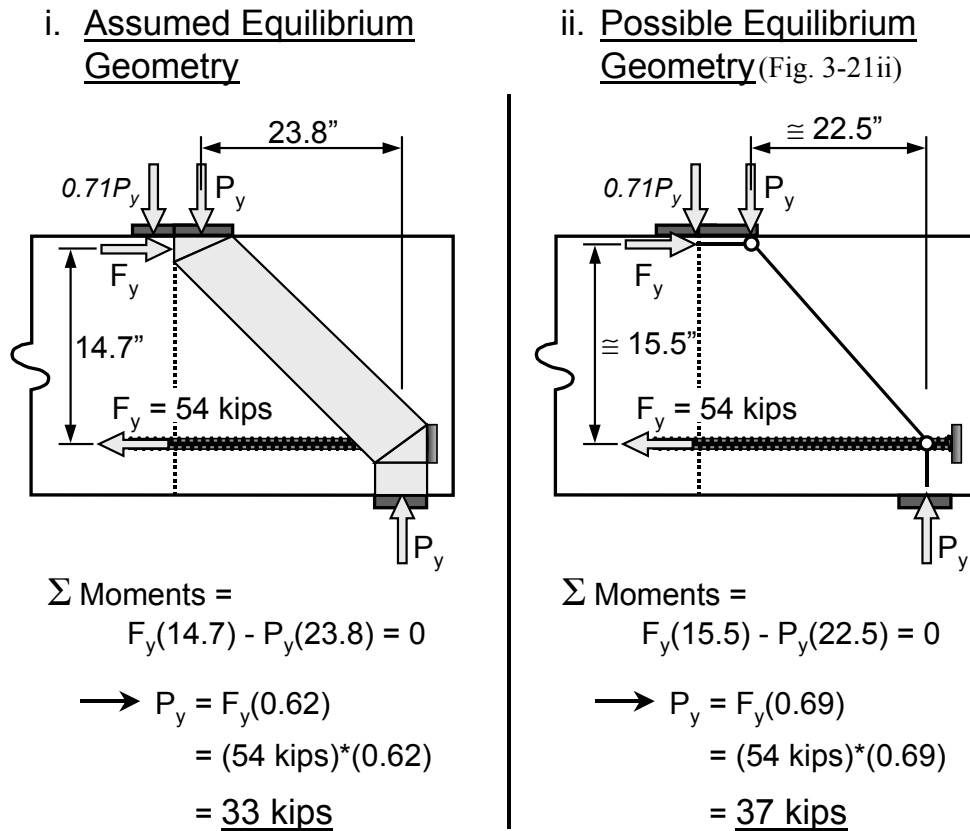


Figure 3-20: Assumed and possible equilibrium geometries for 30° CCT node specimens

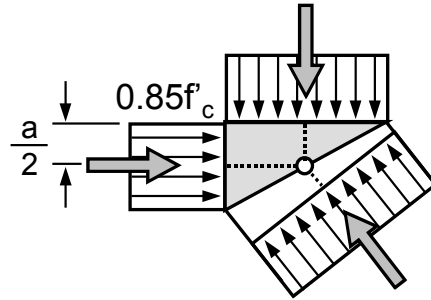
As drawn in Figure 3-20i, the dimensions of the lever arms are based on assumed CCC node dimensions. The assumed dimensions of the top CCC node are dictated by the depth of the concrete compression block at the top of the specimen, a , and a proportional distribution of the load plate length based on the applied load distribution between the front and back reactions of the specimen. The assumed dimensions of the CCC node are also based on uniform stress distributions on all three faces of the node and on a $0.85f'_c$ upper limit for concrete stress. Neither of these two assumptions is necessarily correct. Zeller's tests on corbels showed that the strain distribution of the concrete along the diagonal compression strut is extremely non-uniform near the re-entrant corner of the corbel [10, 19, 25]. Zeller's corbel tests are essentially the same type of test as conducted in this study but oriented differently. The re-entrant corner of his specimens coincides with the location of a CCC node. If non-uniform stress distributions were occurring at the top CCC node in the specimens of this study it would be entirely consistent with Zeller's earlier observations. The latter of the two assumptions that dictate the CCC node dimensions is a stress limit state that is based on an assumption of uniaxial compression behavior in the concrete. However, the state of stress of the top CCC node is biaxial. Experimental studies by Kupfer, Hilsdorf, and Rusch [14] have shown that the biaxial strength of concrete can be as high as $1.2f'_c$ when non-restraining bearing platens (brush type platens) were used to compress the material. When restraining load platens were used (solid steel plates), the strength could reach up to $1.5f'_c$. Since the bearing plates of the CCT node specimens were all solid steel, it is reasonable to propose that the concrete strength at the top CCC node may have reached $1.5f'_c$. Figure 3-21 shows the assumed node condition and the possible node conditions

next to one another. The lever arm dimensions shown in Figure 3-20, ii correspond to the possible dimensions (Fig. 3.21ii) of the CCC node which could account for the higher specimen capacities seen in many CCT node tests.

Though the current node dimensioning assumptions of STM would suggest that large CCC nodes should occur in the test specimens, there is reasonable experimental data to suggest that the actual nodes are much smaller with much higher stresses than have been previously assumed. Smaller node dimensions would allow for changes in the lever arms over which the horizontal and vertical forces act in the CCT node specimens and thus allow the specimens to reach higher than expected capacities. This seems to be the most rational explanation for the results that are demonstrated in Figure 3-19 and earlier in 3-16.

i. Assumed Node Condition

- uniform stress state
- concrete stress limited to $0.85f'_c$



ii. Possible Node Condition

- non-uniform stress state
- concrete stress limit as high as $1.5f'_c$

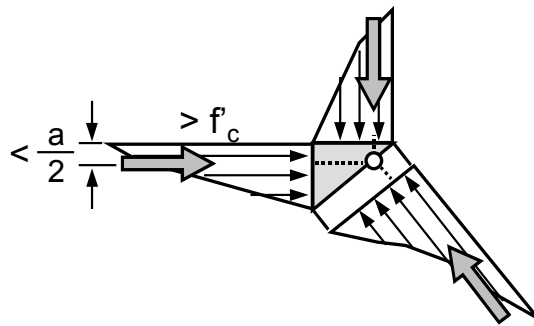


Figure 3-21: Assumed and possible stress states of CCC nodes

3.1.6 Modes of Failure

CCT node specimens failed in three basic ways: pullout of the tie bar from the CCT node, rupture of the concrete strut, or ductile yielding of the tie bar. Most of the discussion in this chapter will deal with the second mode of failure.

Pullout failure was always foreshadowed by extensive slip of the head before the capacity of the anchorage was achieved. It was the mode of failure for all of the non-headed bar specimens. Pullout failure resulted in a loss of load capacity and unrestrained opening of the cracks closest to the node. Generally, extensive slip of the bar resulted in very poor crack distribution with only one primary crack propagating at failure. Pullout is shown in Figure 3-22. Horizontal splitting cracks were sometimes visible in the node region at failure, but typically not beforehand.

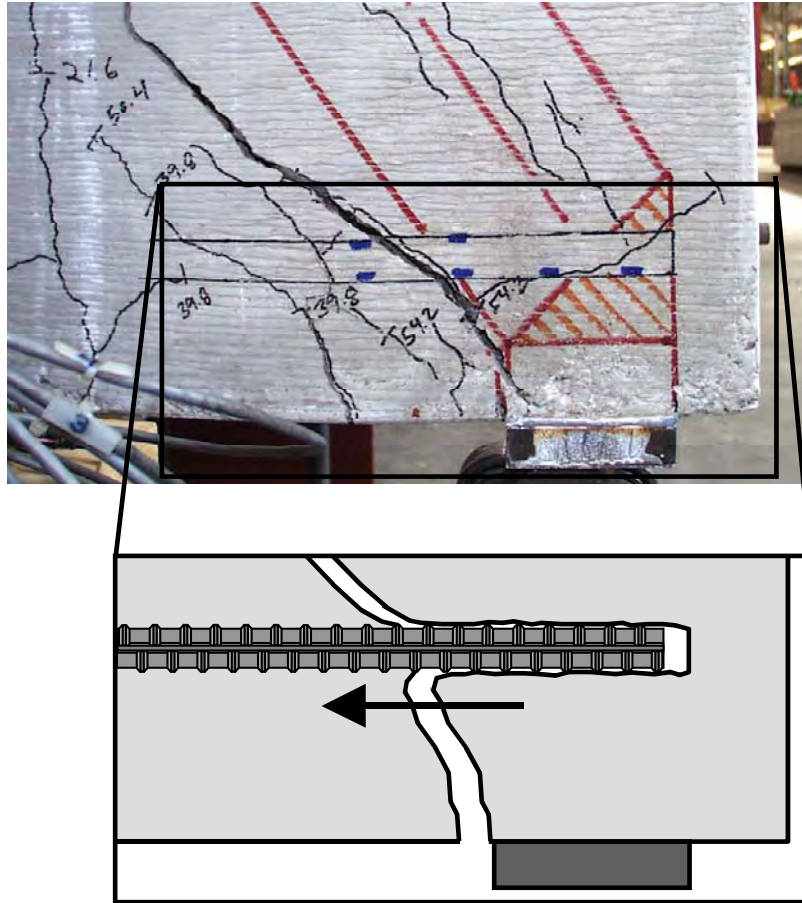
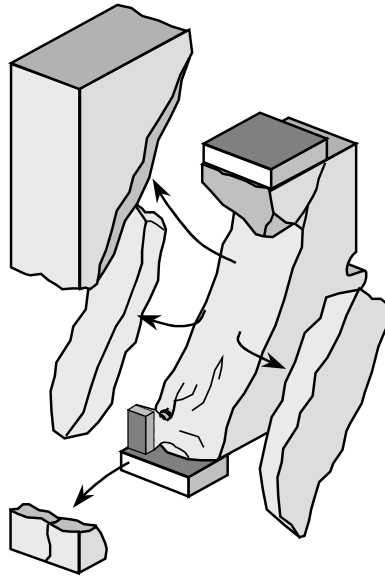


Figure 3-22: Pullout failure of a non-headed bar (specimen CCT-08-55-00.00-1)

All of the headed bar specimens that did not yield experienced rupture of the strut and node region during failure. For smaller heads and vertically oriented rectangular heads, rupture was usually characterized by splitting of the diagonal compression strut along a transverse plane. Larger heads and rectangular heads with horizontal orientations caused a lesser degree of splitting near the node region. A characteristic of the larger head sizes that failed by rupture was extensive crushing of the concrete near the bottom face of the diagonal compression strut. Figure 3-23 shows the two basic failure modes.

Figures 3-24 and 3-25 show post-test photographs of specimen with a vertically oriented head (CCT-08-55-02.80(V)-1) which provide an excellent example of strut rupture with transverse splitting. Figure 3-24 shows a side view of the failed specimen in which the individual pieces of the shattered specimen can be distinguished. Two very clear strips along the path of the diagonal compression strut were blown out laterally from the specimen. The zone between the bottom bearing plate and the headed bar anchorage disintegrated. A very clear cone of concrete was visible on the underside of the headed bar sweeping from the lower head face to the back edge of the bottom bearing plate. On the upper portion of the head face, was a partial wedge of concrete. Figure 3-25 shows a front view of the same specimen. A vertical splitting crack can be seen along the length of the diagonal compression strut. Beneath the head, the zone of disintegrated concrete resembled a pyramid rising up from the lower bearing plate to meet the head.

i. Strut Rupture with Splitting
(vertical head orientation)



ii. Strut Rupture with Crushing
(horizontal head orientation)

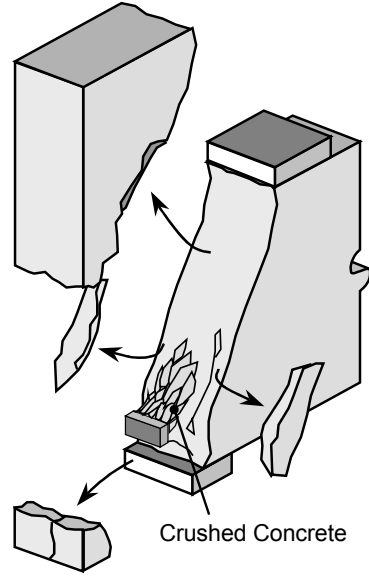


Figure 3-23: Patterns of strut/node rupture



Figure 3-24: Side view of a failed specimen with a vertically oriented head (CCT-08-55-02.80(V)-1) demonstrating splitting of the diagonal compression strut



Figure 3-25: Front view of a failed specimen with a vertically oriented head (CCT-08-55-02.80(V)-1) demonstrating splitting of diagonal compression strut

Figure 3-26 shows the splitting failure of a specimen with a small head (CCT-11-45-01.10-1) which was somewhat different from the splitting failure of the specimen CCT-08-55-02.80(V)-1 (Fig. 3.25). Side and front views clearly indicate a splitting failure with much cleaner edges of cleavage than was seen in the example of the specimen with a larger vertically oriented head. There is much less distress of the concrete between the bottom bearing plate and the head (an Xtender head in this specimen). The differences can be attributed to the much smaller relative head area. More slip of the head occurred in this specimen (CCT-11-45-01.10-1) than in the previous one (CCT-08-55-02.80(V)-1) before failure. Less strain energy was stored in the CCT node region and along the strut before rupture occurred. The result was that there was less distress along the failure surfaces at failure. Thus the final appearance of the specimen was much cleaner with well-defined crack planes.

Transverse splitting at the node tended to occur to some degree in all specimens that did not reach yield or fail by pullout of the tie bar. Splitting was least pronounced in specimens with large head sizes. Also particular to the specimens with larger, horizontally oriented heads was the presence of a distinct zone of crushed concrete progressing from the top of the head up a short distance along the length of the strut. Figures 3-27 and 3-28 show photographs taken of two specimens with horizontally oriented heads (CCT-08-45-04.70(H)-1 and CCT-11-45-04.13(H)-1) after failure. Both photographs show good examples of the type of crushing witnessed during the CCT node testing. Crushing was apparent from the numerous small fragments of destroyed concrete. When the fragments were brushed away, a voided area was apparent at the base of the diagonal strut. Figure 3-29 depicting specimen CCT-08-55-02.80(H)-1 shows this as well as the general appearance of the larger concrete fragments cleaved from the specimen at failure.

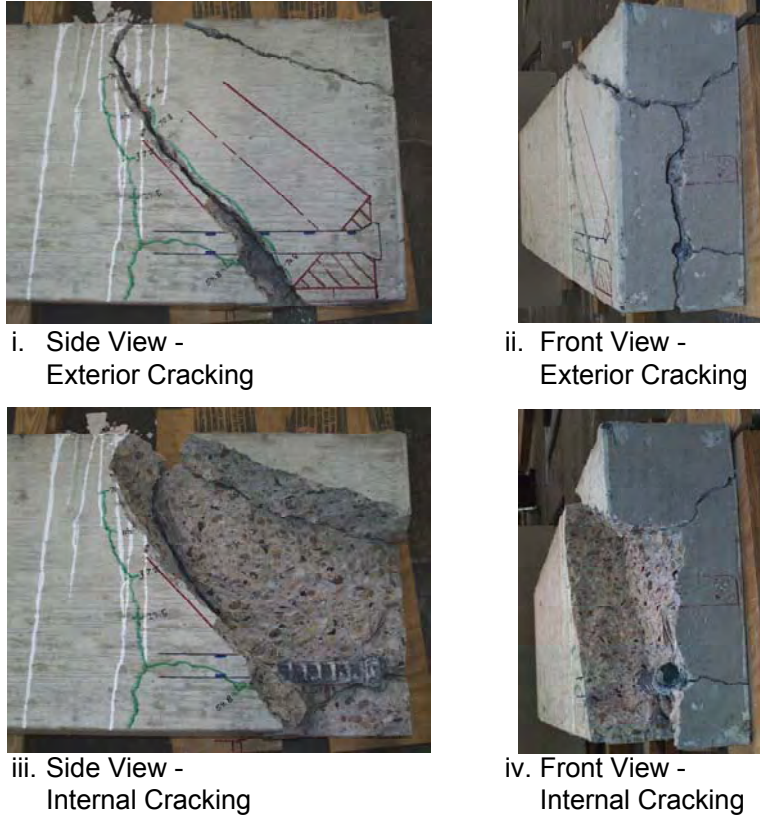


Figure 3-26: Splitting failure of a specimen with a small head (CCT-11-55-01.10-1)

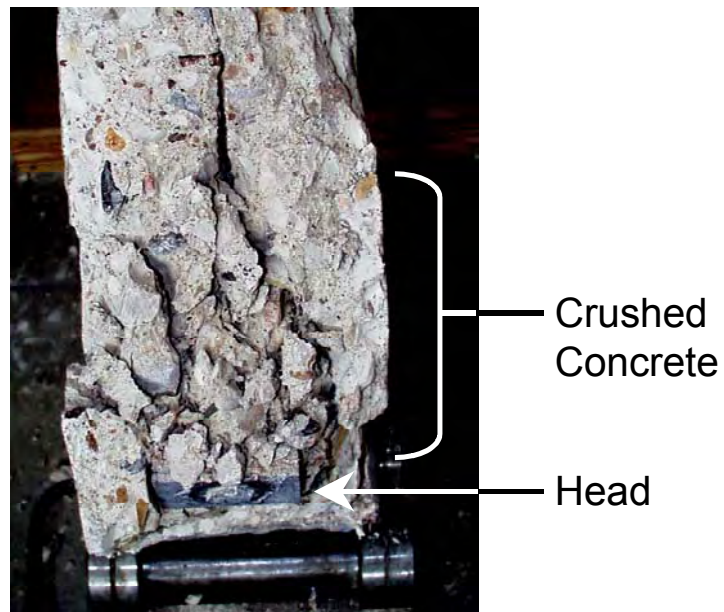


Figure 3-27: Zone of crushed concrete in a specimen with a horizontally oriented head (CCT-08-45-04.70(H)-1) after failure (top view)

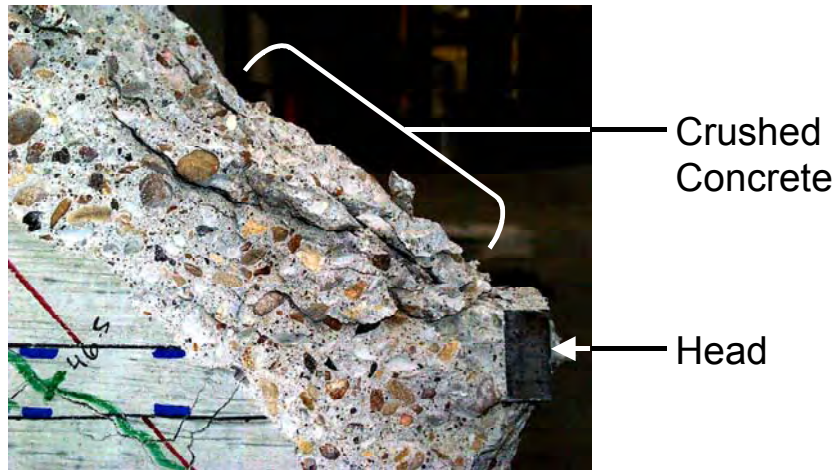
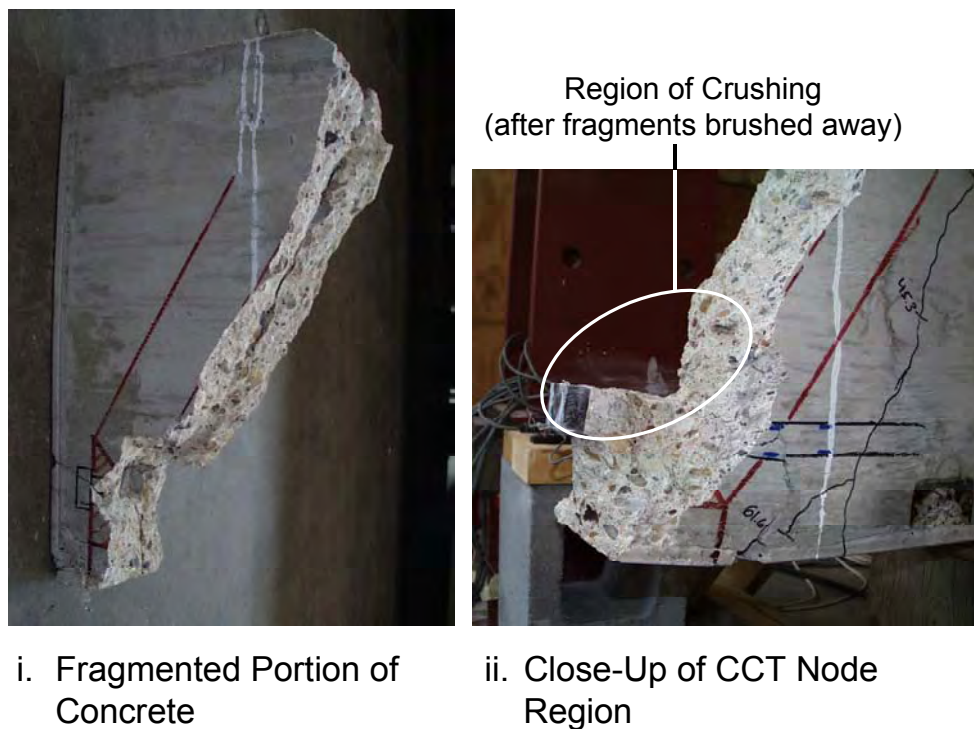


Figure 3-28: Zone of crushed concrete in a specimen with a horizontally oriented head (CCT-11-45-04.13(H)-1) after failure (side view)



i. Fragmented Portion of Concrete

ii. Close-Up of CCT Node Region

Figure 3-29: Specimen CCT-08-55-02.80(H)-1 after failure

Though the hooked bar specimens did not suffer the same explosive rupture as the examples listed above, bulging of the concrete along the strut and vertical cracking along the front face of the specimen suggested a splitting failure also occurred in the hooked bar tests. This would be consistent with the behavior of the headed bar specimens that had vertical head orientation. Such heads provided a tall and narrow bearing profile for the anchorage of the tie bar similar to the profile provided by the hooked bars.

The final mode of failure, yielding, was achieved with many of the largest head sizes that were studied. When testing first began, yielding was judged by strain gage readings taken during the test. Later, it was realized that strain gage readings might indicate yielding, yet the specimen would continue to gain capacity, as was discussed in the proceeding section. In some cases this could result in a failure at or just past the yield point. Once this was realized, testing was continued past the yield point until deflection data indicated a satisfactory yield plateau had occurred in the behavior. Some of the earlier tests unfortunately have an ambiguous yield failure because the tests were prematurely stopped at a point in which strain data indicated yielding, but the deflection data had not yet done so. Tables 3-1a and 3-1b list the failure modes of all of the unconfined CCT node tests excluding those from the first and second casts (the early trial specimens). Failure modes are categorized as pullout, splitting (rupture), crushing (rupture), or yield. Additional notes are provided for some specimens. A more complete list of failure modes and ultimate capacities is provided in Appendix C.

Table 3-3a: Failure modes of unconfined CCT node specimens

Specimen Identification	f'_c	Failure Mode - Notes
CCT-08-45-00.00-1-B6	4000	Pullout
CCT-08-45-00.00-1	4000	Pullout
CCT-08-45-01.18-1	4000	Splitting
CCT-08-45-01.85-1	4000	Splitting
CCT-08-45-01.85-2	3100	Splitting
CCT-08-45-02.80(H)-1	4000	Yield - Unconfirmed; test stopped early
CCT-08-45-02.80(H)-2	3100	Splitting
CCT-08-45-02.80(V)-1	3900	Splitting
CCT-08-45-04.04-1	4000	Yield - Bar $f_y = 61$ ksi; lower than most bars
CCT-08-45-04.06-1	3100	Crushing
CCT-08-45-04.70(H)-1	3100	Crushing
CCT-08-45-04.70(V)-1	3900	Splitting
CCT-08-45-10.39-1	3100	Crushing - Very poor concrete quality
CCT-08-45-10.39-2	3800	Crushing
CCT-08-45-Hook1-1	4000	Splitting
CCT-08-45-Hook2-1	4000	Splitting
CCT-08-30-00.00-1	4100	Pullout
CCT-08-30-01.18-1	4100	Splitting
CCT-08-30-01.85-1	4100	Yield
CCT-08-30-04.04-1	4100	Yield
CCT-08-30-04.06-1	4100	Yield
CCT-08-30-10.39-1	4100	Yield
CCT-08-55-00.00-1	3900	Pullout
CCT-08-55-01.18-1	3900	Splitting
CCT-08-55-01.85-1	3900	Splitting
CCT-08-55-02.80(H)-1	3900	Splitting
CCT-08-55-02.80(V)-1	3900	Splitting
CCT-08-55-04.04-1	3100	Crushing
CCT-08-55-04.06-1	3100	Crushing
CCT-08-55-04.70(H)-1	4000	Yield - Unconfirmed; test stopped early
CCT-08-55-04.70(H)-2	3100	Crushing
CCT-08-55-04.70(V)-1	3900	Splitting
CCT-08-55-10.39-1	4000	Yield

Table 3-3b: Failure modes of unconfined CCT node specimens (continued)

Specimen Identification	f'_c	Failure Mode - Notes
CCT-11-45-00.00-1	4100	Pullout
CCT-11-45-01.10-1	4100	Splitting
CCT-11-45-01.56-1	4100	Splitting
CCT-11-45-02.85(H)-1	4100	Splitting
CCT-11-45-02.85(V)-1	4100	Crushing
CCT-11-45-03.53-1	4000	Crushing
CCT-11-45-04.13(H)-1	4100	Crushing
CCT-11-45-04.13(V)-1	4000	Splitting
CCT-11-45-04.77-1	4000	Crushing
CCT-11-45-06.69(H)-1	4000	Yield
CCT-11-45-06.69(V)-1	4000	Yield
CCT-11-45-09.26-1	4000	Yield

3.1.7 Special Test Results

Though analysis of the rupture patterns of failed specimens provided some interesting insight into the behavior, one question still persisted: Does splitting initiate at the bottom of the strut, the middle, or the top? In order to answer this question, two special specimens were fabricated. Each of these specimens was built with special instrumented details aligned along the axis of the diagonal strut. The strain gages along the special details provided insight about the behavior of tensile strains within the struts.

3.1.7.1 Specimen CCT-08-45-04.70(V)-1-S2 (Transverse Splitting)

Specimen CCT-08-45-04.70(V)-1-S2 was detailed with gages oriented transversely along the length of the strut. A reinforcing detail resembling a ladder was built out of $\frac{3}{16}$ " diameter plain wire. Gages were placed along each rung of the ladder. This detail was then tied into the specimen reinforcing cage such that the gages on the rungs of the ladder would measure transverse splitting strains at every 2" up the length of the diagonal strut. Figure 3-30 illustrates the layout of this ladder detail. A vertically oriented rectangular head was chosen specifically to create a transverse splitting situation along the strut. The measured concrete compressive strength of the specimen was 4100 psi and the tensile strength was 420 psi.

Data from the ladder detail in specimen CCT-08-45-04.70(V)-1-S2 are shown in Figure 3-31. The gage on the lower-most rung of the ladder was damaged during the casting process. Transverse tensile strain developed very slowly in the strut. At a load of 40 kips, the maximum measured strain was just over $200\mu\epsilon$ (0.0002 in/in), less than the cracking strain of concrete which can be estimated at $300\mu\epsilon$. The maximum strain occurred at the top of the strut next to the CCC node. Some tensile strains were developed at the bottom of the strut as well. From load levels of 40 kips to 55 kips, strain increased rapidly at the top and bottom of the strut. The length from 8"-14" (directly in the middle of the strut) developed very little tensile strain even up to failure. Maximum tensile strain at the top of the strut occurred slightly outside of the CCC node. These results do not indicate if transverse splitting begins at the top or bottom of the strut, only that it does not occur in the middle. Beyond a load of 50 kips, tensile strains at the top and bottom of the strut exceeded $300\mu\epsilon$ indicating that the concrete had begun to split. At that point, the rungs of the ladder detail had begun to act as transverse reinforcement for the strut. The specimen reached a maximum capacity of 54.8 kips, then split along a plane parallel to the rungs of the ladder detail and perpendicular to the transverse splitting plane.

Transverse strains measured along the strut in specimen CCT-08-45-04.70(V)-1-S2 match a shape similar to concrete cylinders subjected to a double-punch tensile test. The head at the lower end of the strut formed a concrete wedge that subjected the immediate concrete to large tensile stress. A similar event occurred at the top of the strut where it met the CCC node and the load plate. Based on these test results,

transverse splitting can be characterized as the cleaving of the strut laterally by naturally forming wedges at one or both ends of the strut. It does not conform to the expected stress distribution envisioned for bottle shaped struts in which splitting is caused by spreading of the compression forces such that maximum tension results in the middle of the strut.

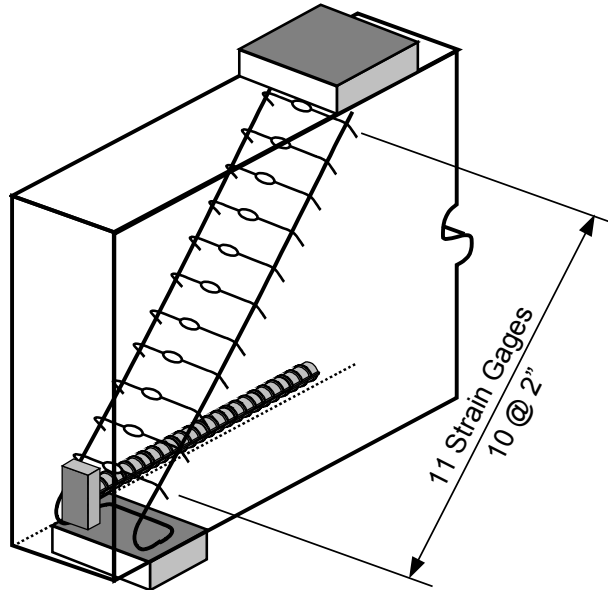


Figure 3-30: Special instrumentation in Specimen CCT-08-45-04.70(V)-1-S2

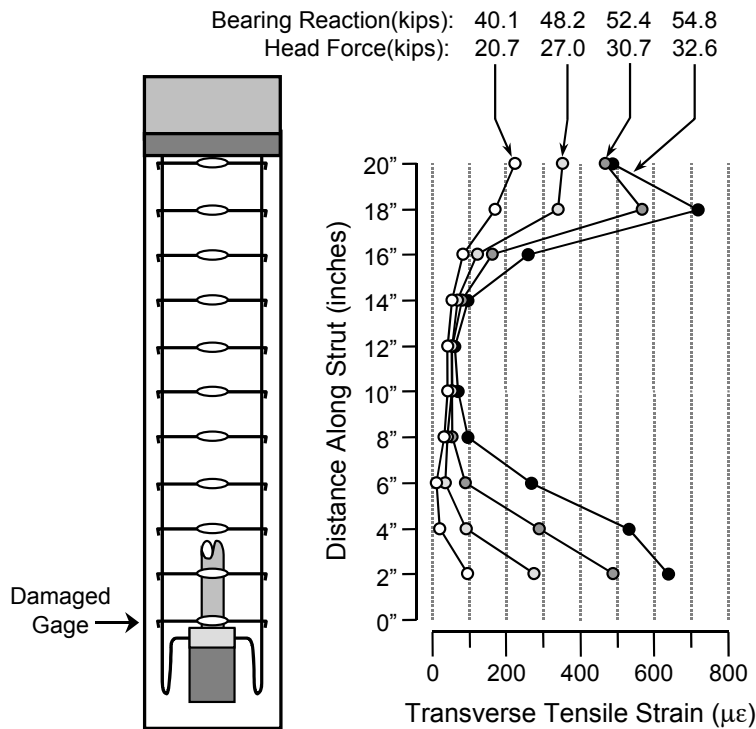


Figure 3-31: Transverse splitting strains in specimen CCT-08-45-04.70(V)-1-S2

Results from specimen CCT-08-45-04.70(V)-1-S2 are compared to a companion specimen with no special reinforcement along the strut, CCT-08-45-04.70(V)-1, in Table 3-4. One would expect the presence of the special detail to enhance the capacity of the specimen because it adds reinforcement to the strut. In fact, the capacity of the reinforced specimen (CCT-08-45-04.70(V)-1-S2) was lower than the unconfined specimen. Both the bearing reaction, P_{max} , and the bar stress at the head, $f_{s,head}$, were lower in the specimen with the ladder detail. Though counterintuitive, this behavior can be explained. First, reinforcement in the strut may not necessarily affect the capacity if the failure is controlled by anchorage at the node. The reinforcement provided by the ladder detail was provided for the wrong element of the specimen, the strut rather than the node. Secondly, the concrete placed in the node region of the specimen with the ladder detail was probably not vibrated as well as the specimen without the ladder detail. The specimen with the ladder detail had a number of strain gages placed in the nodal zone and strut region that had to be protected from damage during the casting process. The researchers had to be more careful during the casting process and had to avoid excessive vibration in the nodal region of the specimen. Additionally, the presence of the ladder detail made it harder to place concrete in the nodal region. Thus, not only did the ladder detail fail to add confining reinforcement to the critical nodal zone of the specimen, but it also hindered the quality of the concrete at the node. Hence, the reasons that the CCT node specimen with the special detail had a lower capacity than the CCT node specimen without any confining reinforcement.

Table 3-4: Capacities of companion CCT node specimens with and without the ladder detail

Specimen	f'_c (ksi)	P_{max} (kip)	$f_{s,head}$ (ksi)
CCT-08-45-04.70(V)-1 (<i>no confinement</i>)	3.9	63.9	48.8
CCT-08-45-04.70(V)-1-S2 (<i>ladder detail</i>)	4.2	54.8	41.3

3.1.7.2 Specimen CCT-08-45-04.70(H)-1-S3 (In-Plane Splitting)

Specimen CCT-08-45-04.70(H)-1-S3 was detailed with gages perpendicular to the plane instrumented in the ladder detail test. Figure 3-32 shows the detailing of specimen CCT-08-45-04.70(H)-1-S3. The strut detail consisted of $3/16$ " diameter plain wire pieces bent up to form the pattern shown in Figure 3-32. The wires were in a single plane centered along the strut transversely. Because the special detail did not fit correctly into the formwork when tied (due to fabrication errors), a 1.5" plinth was added to the top of specimen. Strain gages were placed on the rungs of the detail, perpendicular to the axis of the strut, but within the plane of the specimen. Ten strain gages were placed at 2" spacing. The lower-most gage and the sixth one from the bottom were damaged during the casting process (the electrical connections of the gages were severed). In order to help initiate splitting perpendicular to the axis of the strut gages, a horizontally-oriented head was used. The measured concrete compressive strength was 3800 psi and the split cylinder tensile strength was 360 psi.

Figure 3-33 is a plot of the data collected from specimen CCT-08-45-04.70(H)-1-S3. Data from two load levels is presented. At a bearing reaction of 58.8 kips, the maximum load measured for the specimen, very little tensile stress had developed along the strut. The maximum measured strain was just over $300\mu\epsilon$ indicating that the concrete in the strut was close to splitting or had just begun to split along a short length. Tensile stress was higher at the bottom of the strut, next to the head. There was a small amount of compression at the top of the strut close to the CCC node. During the process of applying the next increment of load, a splitting crack formed along the length of the strut right along the path of the strain gages (see photo in Figure 3-33). Though the load capacity remained high, capacity was lost and never again reached the prior level. Once the splitting crack formed, larger tensile strains were measured in the middle of the strut. This is the conventional strain distribution expected for strut splitting. However, it only occurred once cracking had initiated and capacity was lost. Before the maximum capacity had been

reached, tensile stresses were greatest next to the anchorage of the tie bar, at the head. The measured strains tend to indicate that the splitting crack initiated at the CCT node and spread upward. The special detail restrained complete failure of the strut after the splitting crack had formed, however, the splitting crack continued to open and the capacity decreased once the crack had formed.

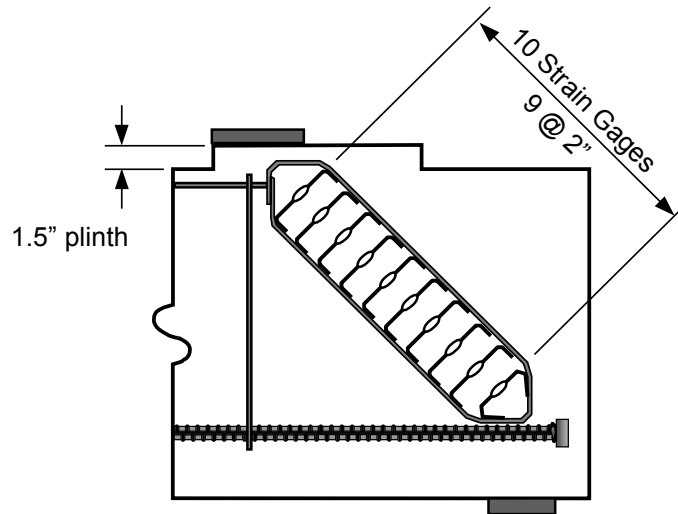


Figure 3-32: Special instrumentation in Specimen CCT-08-45-04.70(H)-1-S3

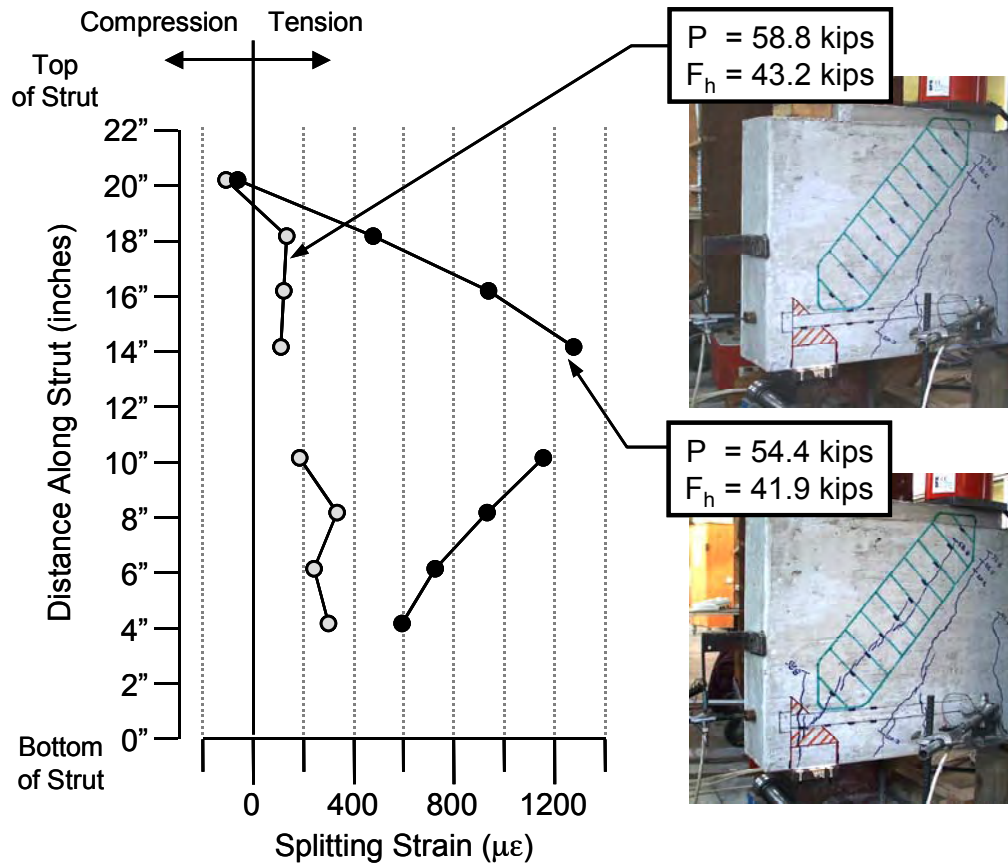


Figure 3-33: In-plane splitting strains in specimen CCT-08-45-04.70(H)-1-S3

Results from specimen CCT-08-45-04.70(H)-1-S3 are compared to a companion specimen with no special reinforcement along the strut, CCT-08-45-04.70(H)-1, in Table 3-5. The specimen with the strut detail had a slightly higher capacity than the specimen with no reinforcement along the strut, however, when differences in the concrete strengths of the two specimens are taken into account, there is very little influence of the special reinforcement evident. As with the companion specimens with and without the ladder detail (see the previous section), the difference in performance is most likely accounted for by two reasons. First, the special detail along the strut of the specimen did not contribute reinforcement to the critical location of the node. Second, the presence of the detail along the strut most likely hindered placement of concrete in the nodal zone.

Table 3-5: Capacities of companion CCT node specimens with and without the strut detail

Specimen	f'_c (ksi)	P_{max} (kip)	$f_{s,head}$ (ksi)
CCT-08-45-04.70(H)-1 (<i>no confinement</i>)	3.1	51.5	53.6
CCT-08-45-04.70(H)-1-S3 (<i>strut detail</i>)	3.8	58.8	54.7

3.2 CONFINED SPECIMEN BEHAVIOR

Confining reinforcement was provided for the CCT node in the form of vertical stirrups. Five specimens with vertical stirrups were cast. One other confining detail was attempted prior to the use of stirrups. Specimen CCT-08-45-04.70(V)-1-S1 was cast with a spiral made of $\frac{3}{16}$ " diameter plain wire around the end of the bar in the CCT node region (Figure 3-34). The spiral idea was conceived because of the resemblance of the headed bars to post-tensioned anchors and the evidence that failure of the strut initiates at the headed anchor. A spiral was envisioned as the ideal method of reinforcing the anchor region of the CCT node. However, while theoretically an ideal placement of tensile reinforcement, in practice the spiral prevented concrete from properly consolidating around the head. A large void was trapped inside of the spiral. Thus, specimen CCT-08-45-04.70(V)-1-S1 failed prematurely due to poor concrete consolidation and the spiral detail proved to be a hindrance to the performance of the node rather than an enhancement. This section thus deals only with the performance of the specimens with stirrups.

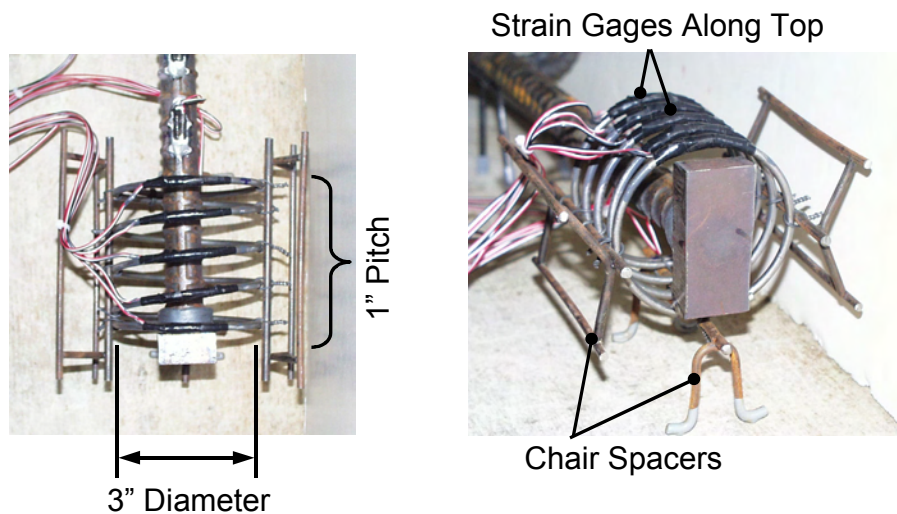


Figure 3-34: Spiral confinement detail attempted in specimen CCT-08-45-04.70(V)-1-S1

3.2.1 Cracking Behavior

Cracking behavior for the confined specimens differed from that of the unconfined ones. Figure 3-35a and 3-35b show the progression of crack development for specimen CCT-08-45-04.70(V)-1-C0.012, a heavily confined headed bar specimen. The north face of the specimen is shown in these figures unlike the south face that was used in all previous crack development figures because the cracking was more interesting on the north face. This specimen contained #3 hoop stirrups at 3" spacing in the node and strut region. The measured concrete compression strength was 3800 psi and the measured tensile strength was 360 psi. A vertically oriented rectangular head was used to anchor the tie bar in order to encourage a transverse splitting failure of the strut.

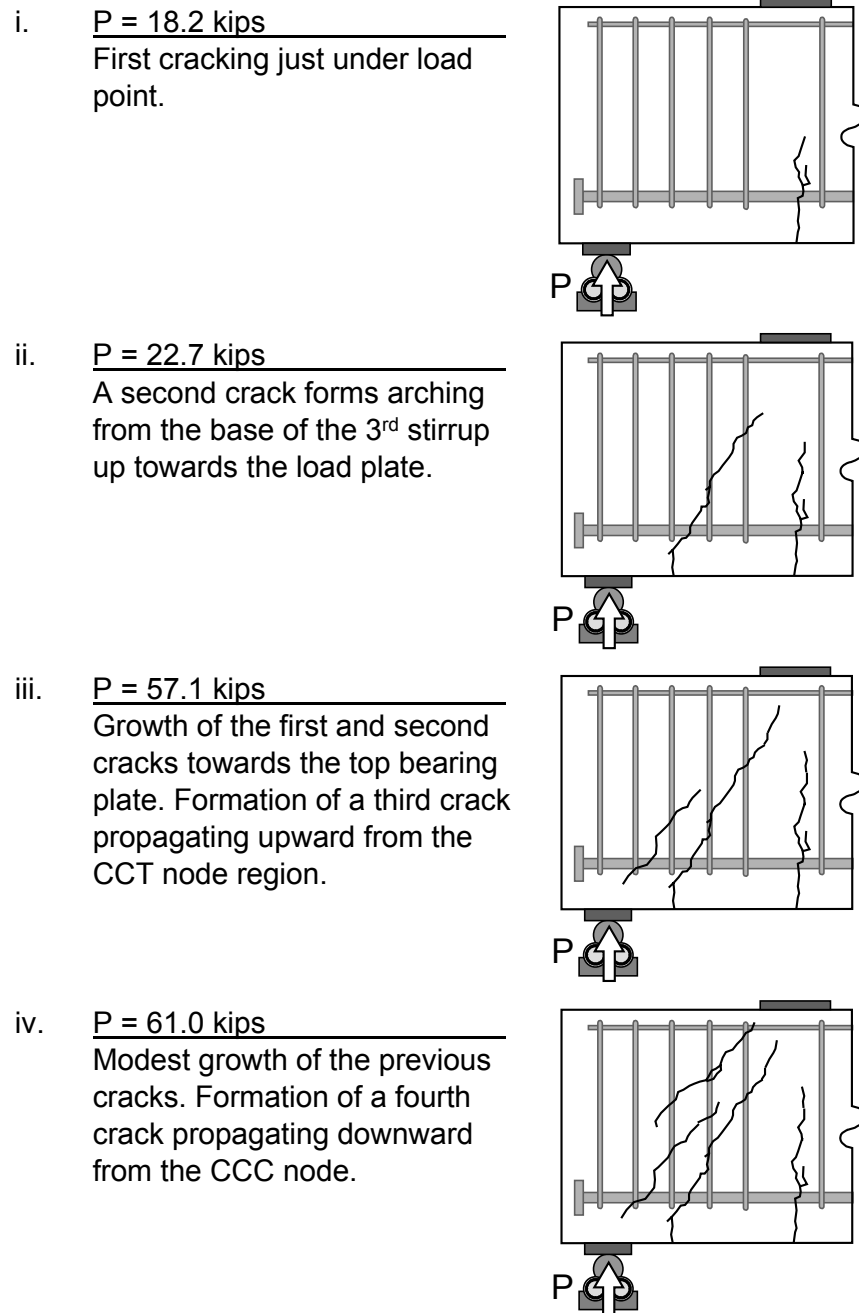


Figure 3-35a: Development of cracks in a heavily confined, headed bar specimen (CCT-08-45-04.70(V)-1-C0.012)

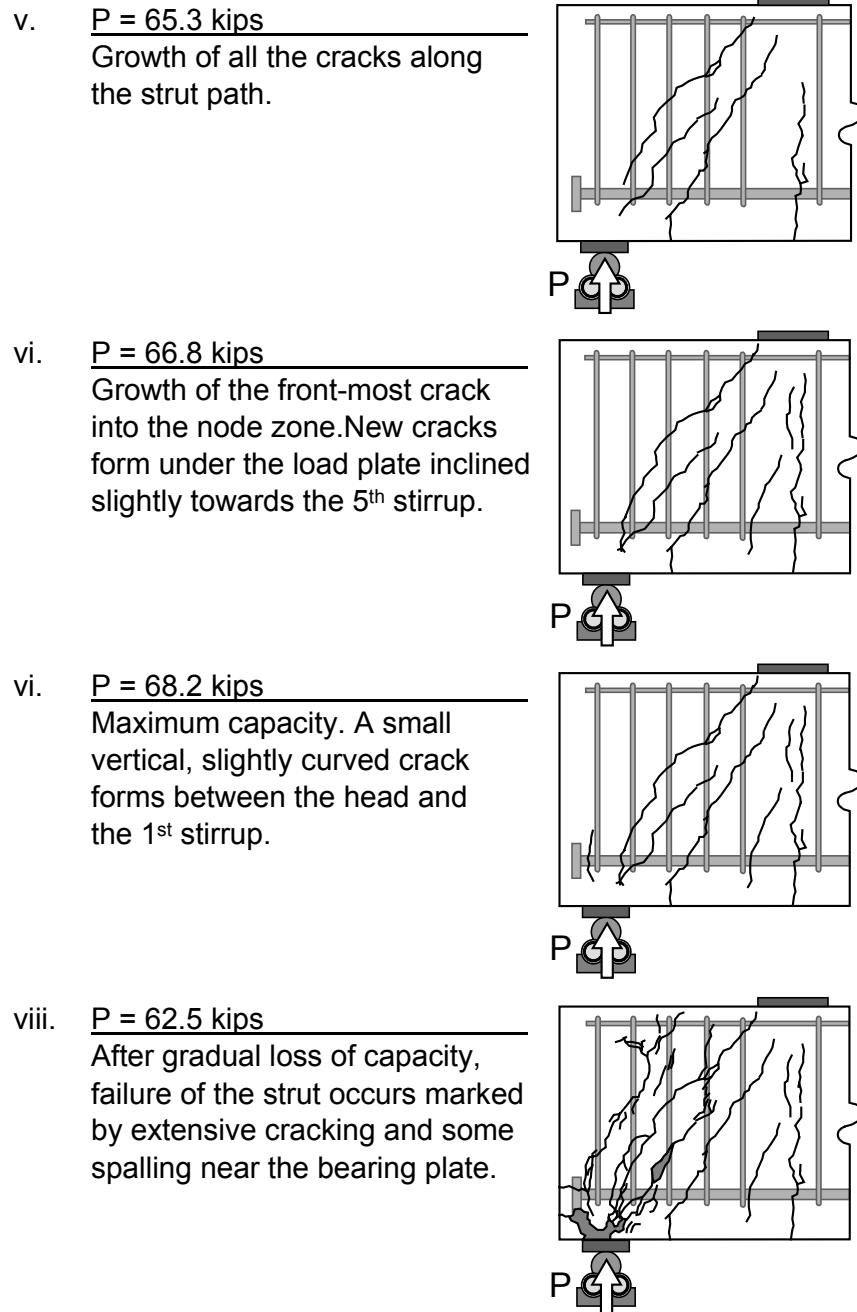


Figure 3-35b: Development of cracks in a heavily confined, headed bar specimen (CCT-08-45-04.70(V)-1-C0.012) (continued)

First cracking in the heavily confined headed bar specimen occurred in the same manner as most unconfined specimens with vertical cracking underneath the top load plate when the bearing reaction reached 18 kips (part i). The formation of the first diagonal crack was consistent with the behavior of the unconfined specimens. A diagonal crack formed midway between the load point and the CCT node at a reaction of 22 kips (part ii). After the formation of that diagonal crack, no additional cracking occurred for some time. Between a bearing reaction of 22 kips and 57 kips, there was only modest growth of the two existing cracks. At 57 kips, a third crack formed parallel to the second one, propagating upwards

from the nodal zone towards the top CCC region (part iii). Following the formation of that crack, deterioration of the specimen was rapid. At 61 kips, a fourth crack formed along the top of the primary strut path (part iv). As load was increased, these cracks grew quickly along the strut path (part v). At 66.8 kips, a fifth crack formed next to the first, along a path from the CCC node to the base of the fifth stirrup (part vi). Maximum capacity was reached at 68.2 kips. At this load level, a small vertical crack appeared next to the head of the tie bar (part vii). The appearance of the crack gave the impression of a breakout cone projecting from the head to the surface of the concrete. The specimen then began to lose capacity. Extensive cracking occurred across a broad area from the CCT node to the CCC node (part viii).

Prior to reaching maximum load, cracking of the heavily confined, headed bar specimen was similar to that seen in the unconfined specimens with cracking limited to the strut region or below the strut. After the peak capacity was reached, the specimen underwent extensive cracking and continued to hold 90% of its peak load. The nature of the cracking suggested that the specimen initially developed a truss behavior similar to the unconfined specimens, then shifted to a truss mechanism that utilized the stirrups in the transfer of the strut force (Figure 3-36).

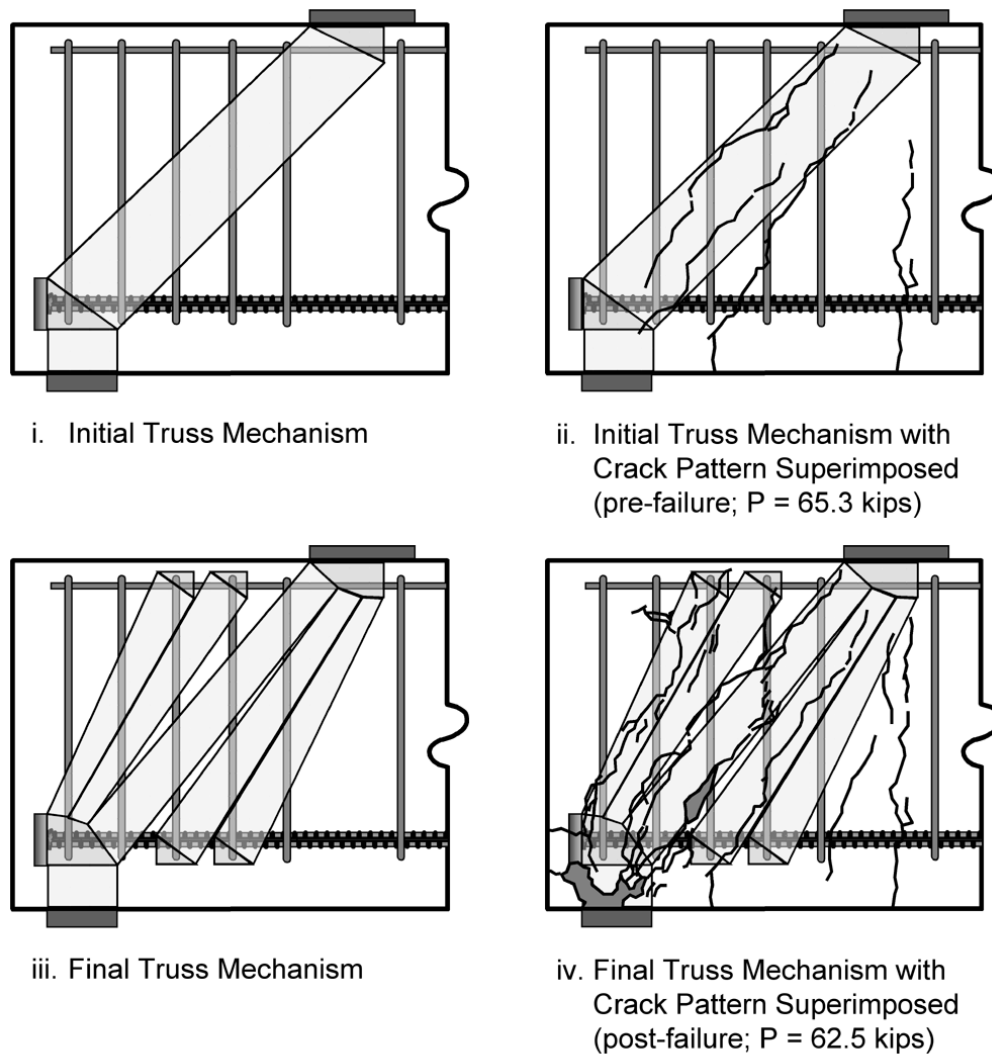


Figure 3-36: Crack patterns overlaid onto probable truss mechanisms for the heavily confined, headed bar specimen (CCT-08-45-04.70(V)-1-C0.012)

Measurements of the crack widths also indicated differences in behavior between specimens with and without stirrups; with stirrups, cracking tended to follow the pattern shown in Figure 3-37. After the formation of the first diagonal crack, no further diagonal cracks formed during a large increase in load. Thus, the first diagonal crack to form showed the greatest widening rather than the latter diagonal cracks (see Figure 3-3 and related discussion).

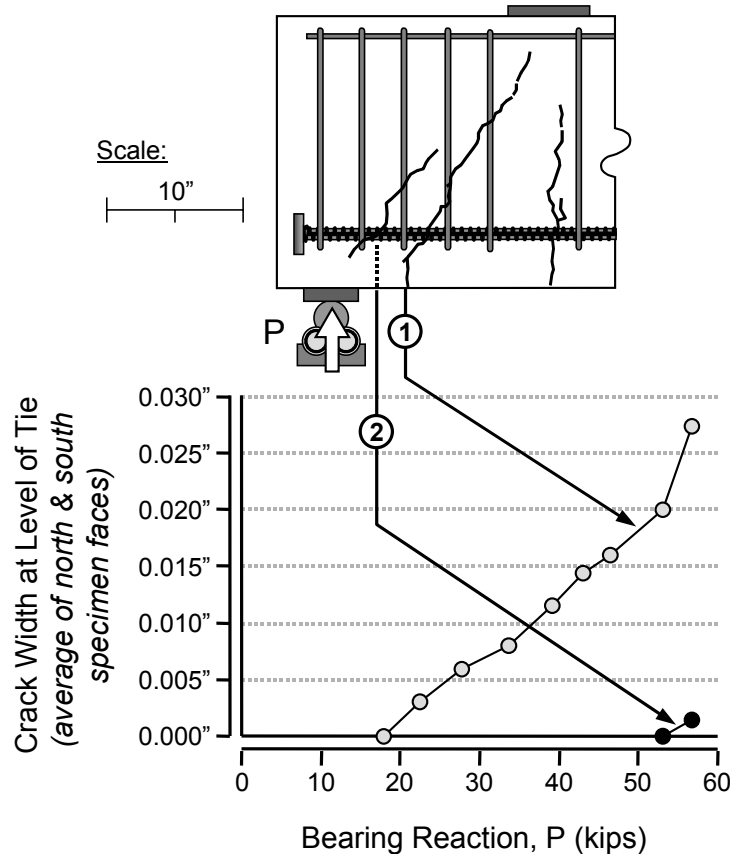


Figure 3-37: Crack width measurements from the heavily confined, headed bar specimen (CCT-08-45-04.70(V)-1-C0.012)

Specimen CCT-08-45-04.70(V)-1-C0.006 had half the transverse steel as the previous specimen, but was the same in all other aspects. Figure 3-38 shows the development of cracks in this lightly confined, headed bar specimen. Cracking in this specimen showed tendencies between that similar to specimens without stirrups and that of the more heavily reinforced one discussed earlier. Cracking followed the common patterns discussed earlier with vertical cracking under the load point (part i) and the development and growth of cracks along the diagonal strut (parts ii and iii). At failure, there was extensive cracking along and next to the primary strut path (part iv). The cracking was less extensive than the more heavily reinforced specimen, but more extensive than the unreinforced case.

Figure 3-39 shows the development of cracks in specimen CCT-08-45-Hook2-1-C0.012. This specimen is similar to the heavily confined, headed bar specimen except that a hooked bar was used as a tie rather than a headed bar. This specimen can also be compared to the unconfined hooked bar specimen shown in Figure 3-5. Diagonal cracking in the heavily confined, hooked bar specimen developed much closer to the CCT node and tended to occur through the center of the primary diagonal strut. The specimen had a lower ultimate capacity than the companion unreinforced specimen, though the differences can probably be

attributed to differences in concrete material properties. At failure, there was extensive cracking along the strut path (in the unreinforced case, cracking occurred only along the top and bottom edges of the diagonal strut). Bulging of the concrete along the strut path indicated a splitting failure.

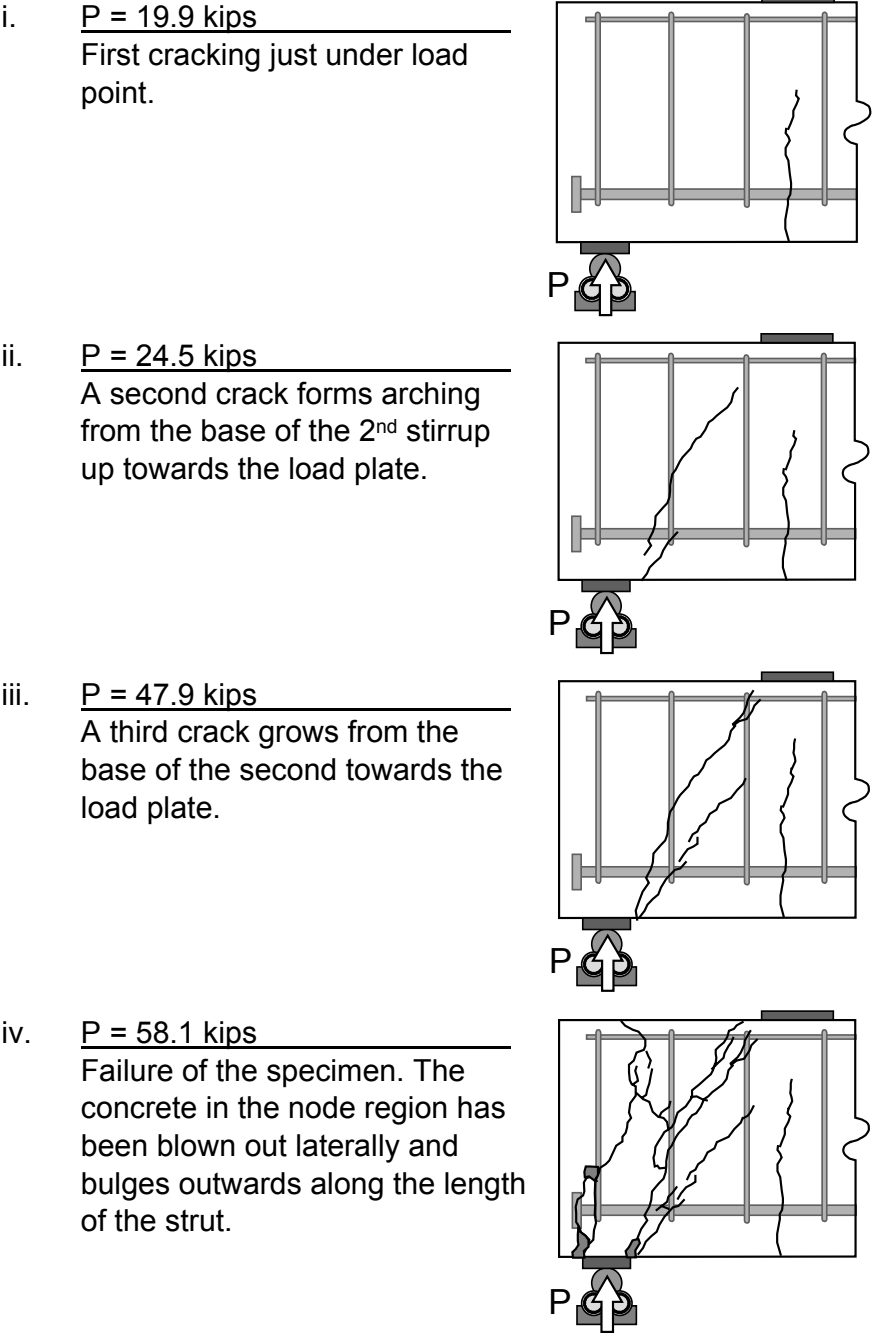


Figure 3-38: Development of cracks in a lightly confined, headed bar specimen (CCT-08-45-04.70(V)-1-C0.006)

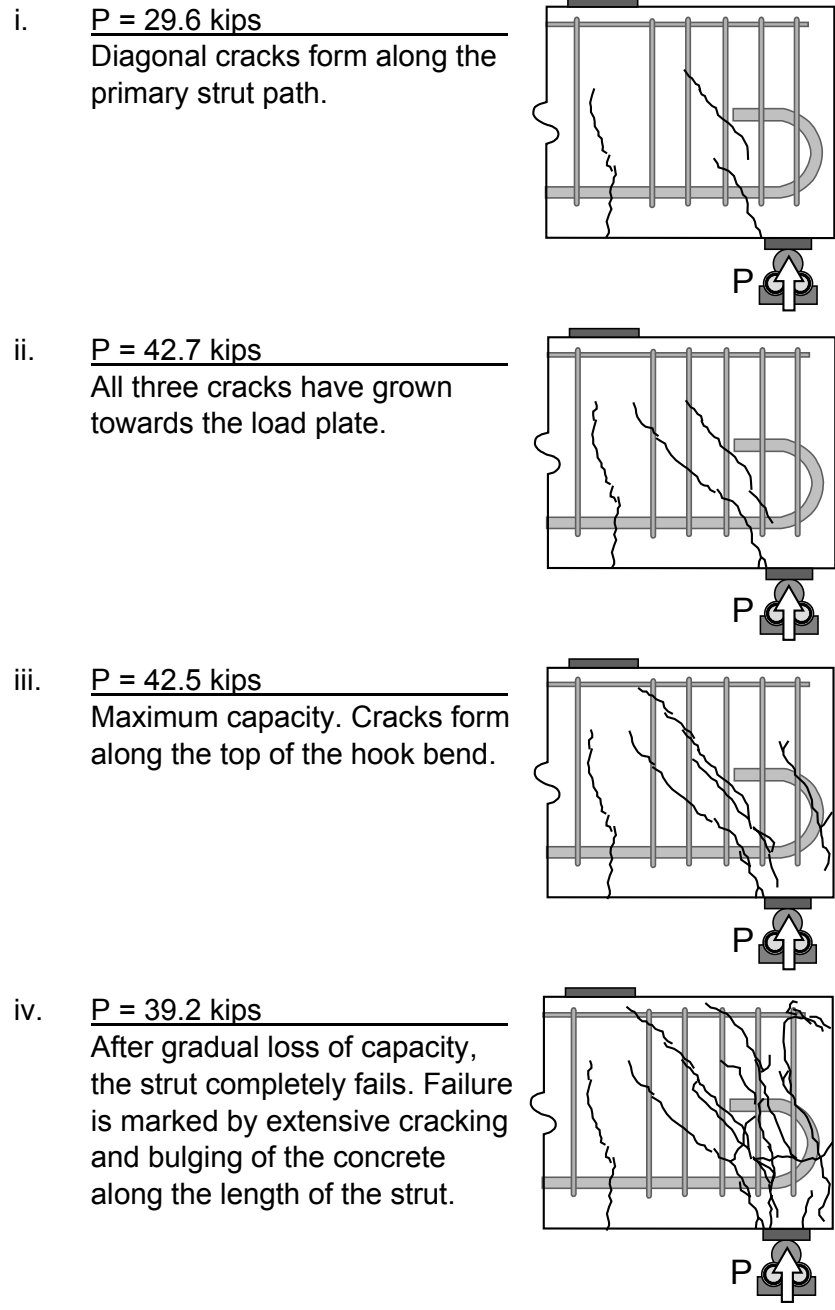


Figure 3-39: Development of cracks in a heavily confined, hooked bar specimen (CCT-08-45-Hook2-1-C0.012)

3.2.2 Stress/Strain Development in the Bar

Measurements of strain along the tie bar indicated that there was a lower strain gradient in the confined condition over the unconfined condition. In Figure 3-40, strain development in unconfined and heavily confined specimens (CCT-08-45-04.70(H)-1-C0.000 and CCT-08-45-04.70(H)-1-C0.012 with concrete compressive strengths of 3900 psi and 3800 psi respectively) is shown by plotting the bar strains at 5" from the head against bearing load, P. The slopes of the plots show that with stirrups, the strain at 5" increased at a slower rate than in the unconfined specimen. This indicates that development of the bar

occurred closer to the head in the unconfined specimen than in the confined specimen. In the confined specimen, fan-like strut behavior (as in the strut mechanism depicted in Figure 3-36 part iii) was made possible by stirrups in the nodal zone. This strut behavior allowed for transfer of diagonal forces by multiple paths that extended away from the nodal zone, thus reducing the strain gradient along the bar.

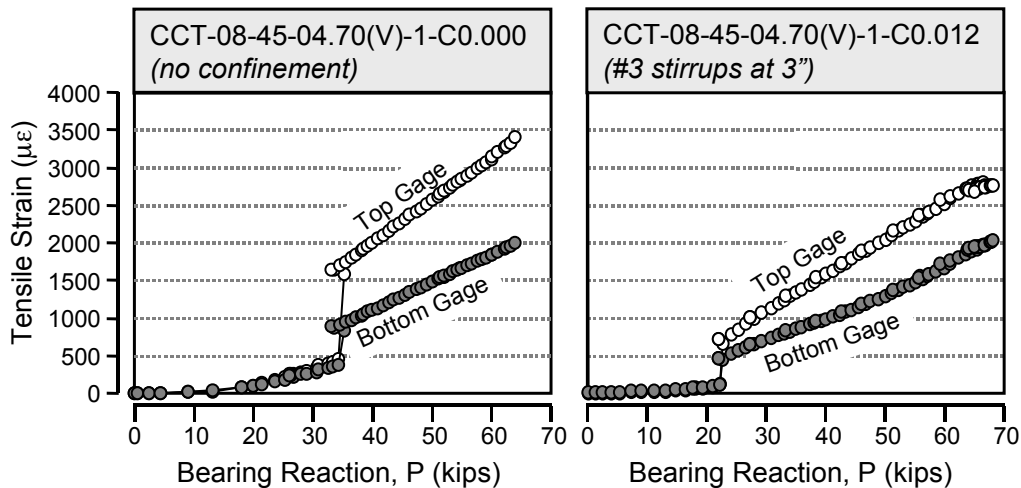


Figure 3-40: Strain at 5" vs. bearing reaction in unconfined and confined specimens

Examination of the difference between the top and bottom fiber bar strains showed that kinking of the tie bar across diagonal cracks was reduced in the confined specimen. There was much less separation between the magnitudes of the top and bottom strain gage measurements in the confined specimen, than in the unconfined case. As expected, the stirrups reduced shear deformation after cracking. As a result, dowel action of the tie bar was also reduced.

Figure 3-41 shows the relative components of bar stress that were provided by bond and head bearing in specimen CCT-08-45-04.70(V)-1-C0.012. This specimen displayed behavior similar to the unconfined specimen shown in Figure 3-14. The presence of heavy confinement did not improve the peak bond capacity, however the confinement did maintain the level of the bond stress until failure of the head occurred.

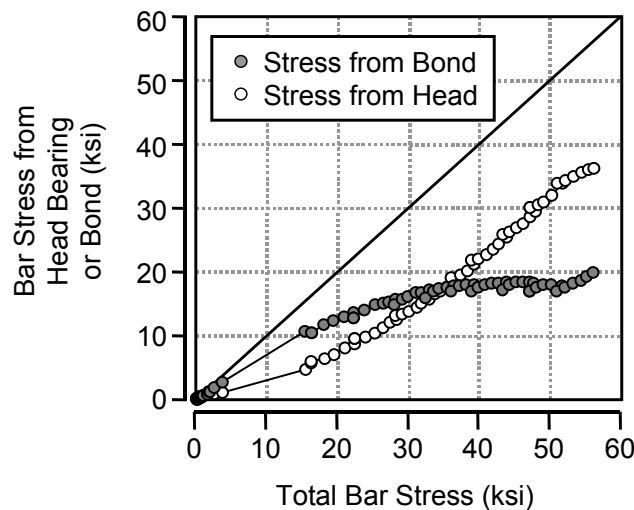


Figure 3-41: Components of bar stress provided by bond and head bearing in CCT-08-45-04.70(V)-1-C0.012

3.2.3 *Stress/Strain Development in the Stirrups*

Strain gages were placed on the vertical legs of each nodal zone stirrup and on the horizontal leg underneath the tie bar.

3.2.3.1 **Vertical Splitting Strains along the Tie Bar**

Vertical strains were measured at a point just above the tie bar to determine the role of the stirrups as: (1) shear cracking developed in the member and (2) bond splitting occurred along the bar and bearing on the head increased. Figure 3-42 shows the development of tensile strain in the stirrups of the heavily confined, headed bar specimen (CCT-08-45-04.70(V)-1-C0.012). Strain increased most rapidly in stirrup 4, located furthest from the CCT node, when the first crack formed. Stirrup 1 was in compression through most of the test. Initially, the diagonal strut and reaction forces placed stirrup 1 in compression. As tie force was transferred from the bar to the head, a concrete wedge formed in front of the head. This wedge created splitting stresses near the head. Near peak capacity splitting forces from the head began to counteract vertical compression in the node region. Once splitting from the head initiated, tensile strain in stirrup 1 quickly exceeded that of the other stirrups and peak capacity of the specimen was reached. Figure 3-43 shows the development of vertical tensile strains in the stirrups of the lightly confined, headed bar specimen (CCT-08-45-04.70(V)-1-C0.006) in which the stirrup spacing was doubled. The plot shows much higher strains in stirrup 2 because fewer bars crossed the diagonal crack. Strain in stirrup 2 reached the yield at peak capacity of the specimen.

The vertical stirrup strain along the length of the tie bar for the heavily confined, headed, non-headed, and hooked bar specimens (CCT-08-45-04.70(V)-1-C0.012, CCT-08-45-00.00-1-C0.012, and CCT-08-45-Hook2-1-C0.012) is shown in Figures 3-44 through 3-46. All three specimens had the same confinement, strut angle, and concrete properties and differed only in anchorage detail.

The headed bar specimen (Figure 3-44) showed a linear distribution of strain until the peak capacity was approached. Then large splitting strains began to develop at the head. At 61 kips, the third crack had just formed along the upper part of the diagonal strut. By 66.4 kips, that crack had propagated down to the bottom of the strut. At both of these load stages, the vertical tensile strains were nearly linear along the tie bar. At the final load stage, 68.2 kips, crack 4 formed near the head, and large vertical tensile strains appeared in stirrup 1.

The non-headed specimen (Figure 3-45) also showed a linear profile of vertical tensile strains at low load levels. At 35.8 kips, only the first and second diagonal cracks had formed. By 41.6 kips, the maximum capacity, a third crack had branched off of the second. During post failure loading, this crack turned horizontally and propagated to the front face of the specimen. The corresponding vertical tension plots show that considerable strain developed in the first stirrup as this occurred. However, the strains were higher further along the bar.

The hooked bar specimen (Figure 3-46) again showed a non-linear though generally increasing profile of vertical tensile strain. At a load of 42.7 kips, cracks 1 and 2 had formed and stirrups 2-4 were in tension. No new cracks had formed by a load of 52.4 kips. At 52.5 kips, cracks 3 and 4 formed and the maximum capacity of the specimen was reached. The profile of the vertical tensile strains did not change significantly throughout the cracking process. The gages on stirrup 4 were lost at the peak load. Stirrup 1 never developed significant tension indicating that, unlike headed bars, the hook does not create vertical splitting in the bend region.

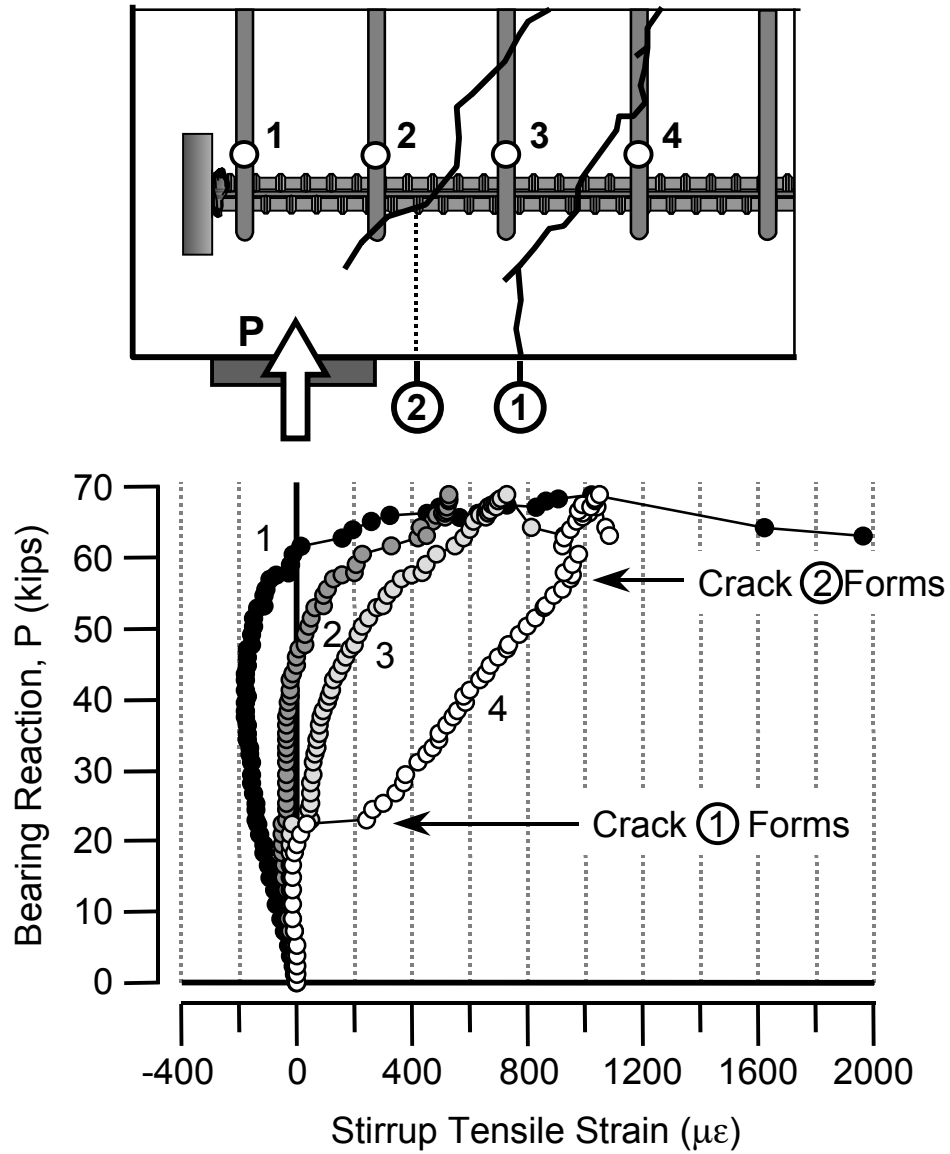


Figure 3-42: Development of vertical tensile strain in the stirrup confinement of the heavily confined, headed bar specimen (CCT-08-45-04.70(V)-1-C0.012)

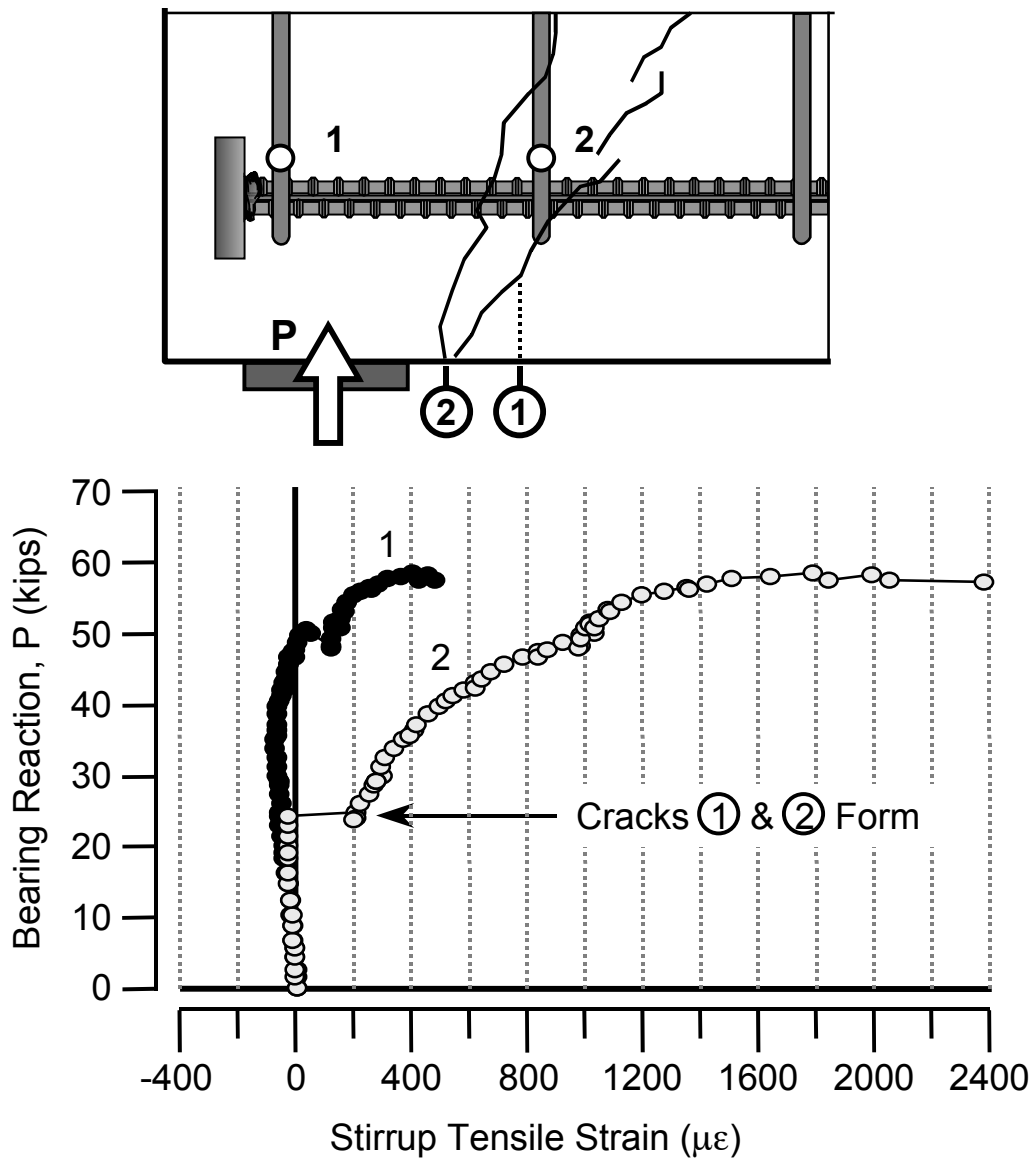


Figure 3-43: Development of vertical tensile strain in the stirrup confinement of the lightly confined, headed bar specimen (CCT-08-45-04.70(V)-1-C0.006)

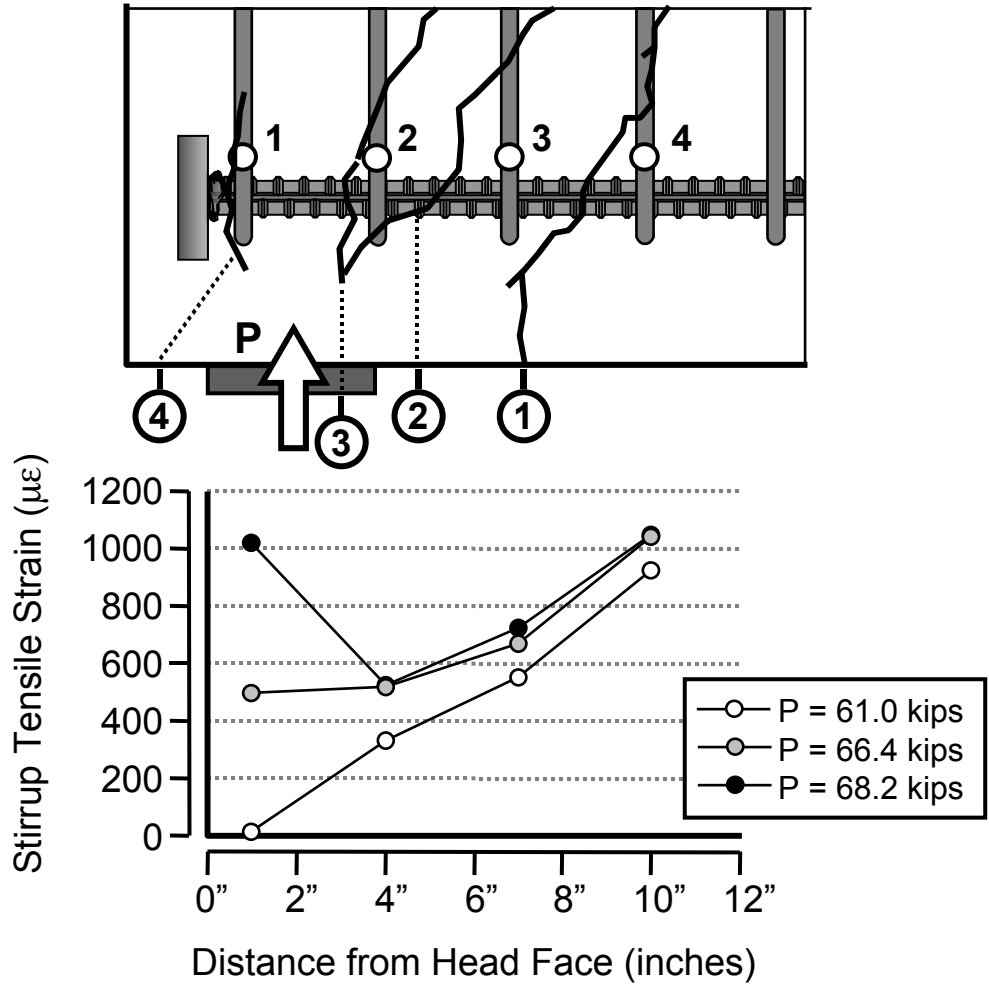


Figure 3-44: Vertical tensile strains along the tie in the heavily confined, headed bar specimen (CCT-08-45-04.70(V)-1-C0.012)

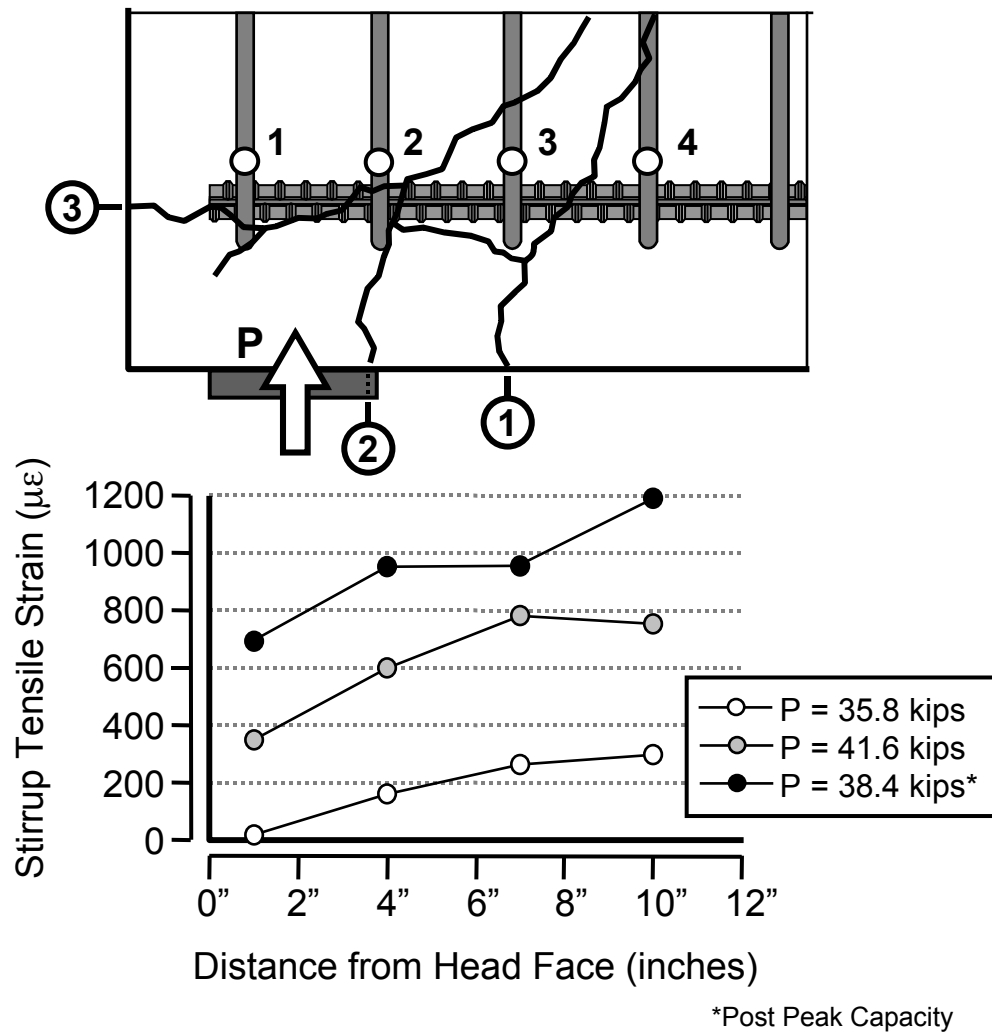


Figure 3-45: Vertical tensile strains along the tie in the heavily confined, non-headed bar specimen (CCT-08-45-00.00-1-C0.012)

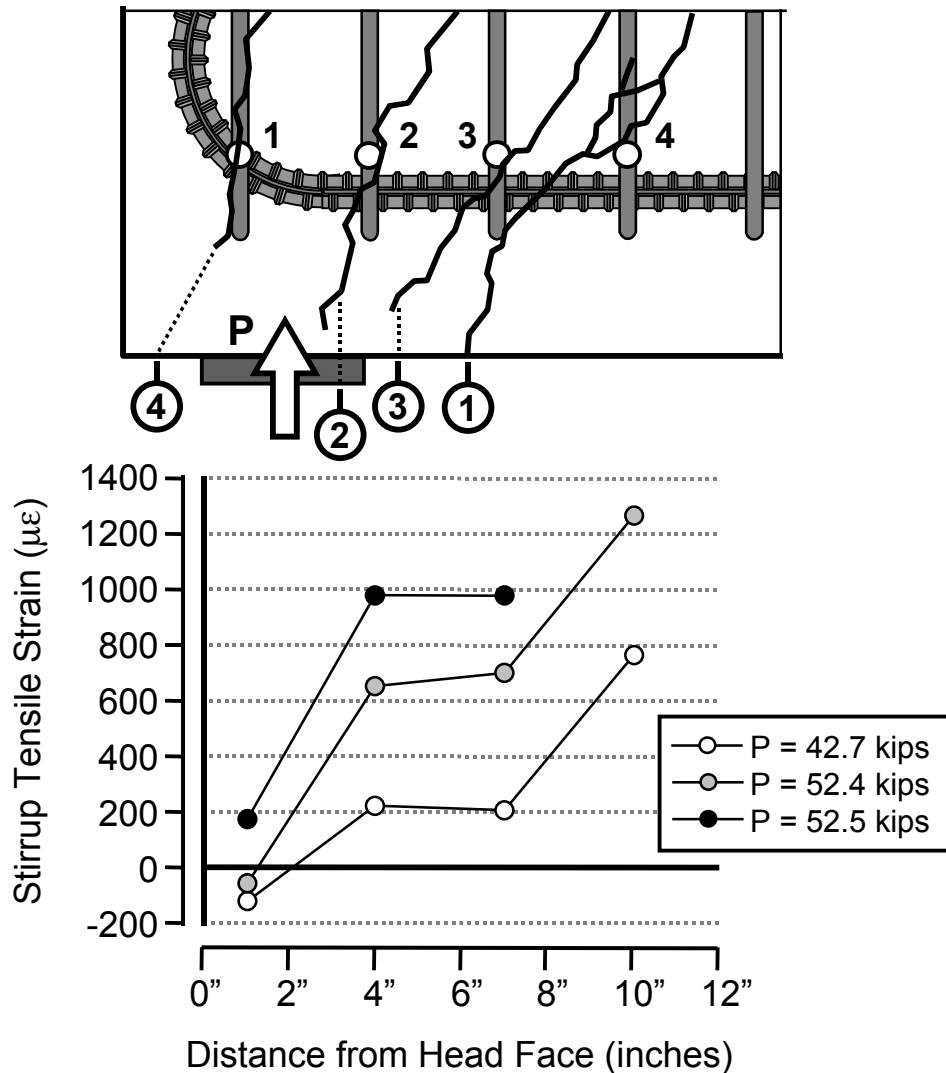


Figure 3-46: Vertical tensile strains along the tie in the heavily confined, hooked bar specimen (CCT-08-45-Hook2-1-C0.012)

3.2.3.2 Transverse Splitting Strains underneath the Tie Bar

Gages on the bottom of the hoop stirrups provided data on the transverse tensile strains along the underside of the tie bars. Transverse tensile strain was caused by bond splitting along the bar and wedging action at the head. Tensile strain was counteracted by compression between the bottom bearing plate and the head in the CCT node region. The full width of the beam at the CCT node was subject to compression by the bottom bearing plate. At the CCT node, these compression stresses must neck inward to equilibrate with the compression stresses at the head of the tie bar. This creates transverse compression on the underside of the CCT node. These effects are illustrated in Figure 3-47.

The transverse strain is plotted as a function of bearing load for the four instrumented stirrups of the heavily confined, headed bar specimen (CCT-08-45-04.70(V)-1-C0.012) in Figure 3-48. From the earliest stages of load to the final stages, stirrups 1 and 2 remain in compression and stirrups 3 and 4 remain in tension. The two sets of stirrups are divided by their placement inside (stirrups 1 and 2) or outside

(stirrups 3 and 4) of the CCT node/strut compression region. Outside of the node/strut zone, bond along the tie bar creates radial splitting stress and produces tension in the stirrups. Inside the node/strut zone, the radial tension stress is counteracted by the transverse compression within the CCT node. Similar behavior is seen in the lightly confined, headed bar specimen (CCT-08-45-04.70(V)-1-C0.006). Figure 3-49 shows the behavior of this specimen. Near peak capacity, the radial tension stress from bond splitting forced stirrup 2 to yield.

In Figure 3-50 through 3-52, the transverse strain profiles for specimens the heavily confined, headed, non-headed, and hooked bar specimens (CCT-08-45-04.70(V)-1-C0.012, CCT-08-45-00.00-1-C0.012, and CCT-08-45-Hook2-1-C0.012) are presented. All three of these specimens contained similar concrete properties, confinement, and load geometry. They differed only the anchorage condition of the tie bar in the CCT node.

The headed bar specimen (Figure 3-50) demonstrated a transverse strain profile with very distinct regions of compression and tension strain. Inside of the node region, the stirrup gages were in compression. Outside of the node region, the stirrup gages were in tension. At the peak load, 68.2 kips, the measured tension strain exceeded $300\mu\epsilon$ indicating that the concrete was probably cracked. Longitudinal cracking along the underside of the specimen was witnessed in many tests and is consistent with the results from these stirrup gages.

The non-headed specimen (Figure 3-51) demonstrated a more linear distribution of transverse splitting strain. While the first stirrup gage went into compression, the second and third stirrup gages were in tension at higher load levels. The fourth gage was damaged during the casting process. This transverse strain profile differed from the profile for the headed bar in the readings from the second and third gages. Not only was the second gage in tension rather than compression, but the third gage exceeded the level of tensile strain that was seen for the headed bar specimen at the same location. The reason that the non-headed bar exhibited much more transverse tension than the headed bar is most likely due to higher bond stresses along the non-headed bar. Because the bar had no head, it relied more on bond for anchorage. This greater reliance on bond resulted in greater radial splitting stresses and thus a greater reliance on the stirrups to resist those splitting stresses. Hence, the higher tensile strains.

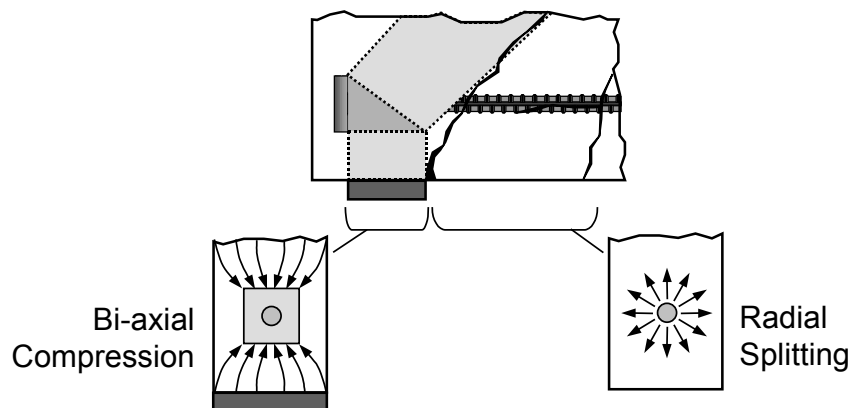


Figure 3-47: State of stress around the CCT node

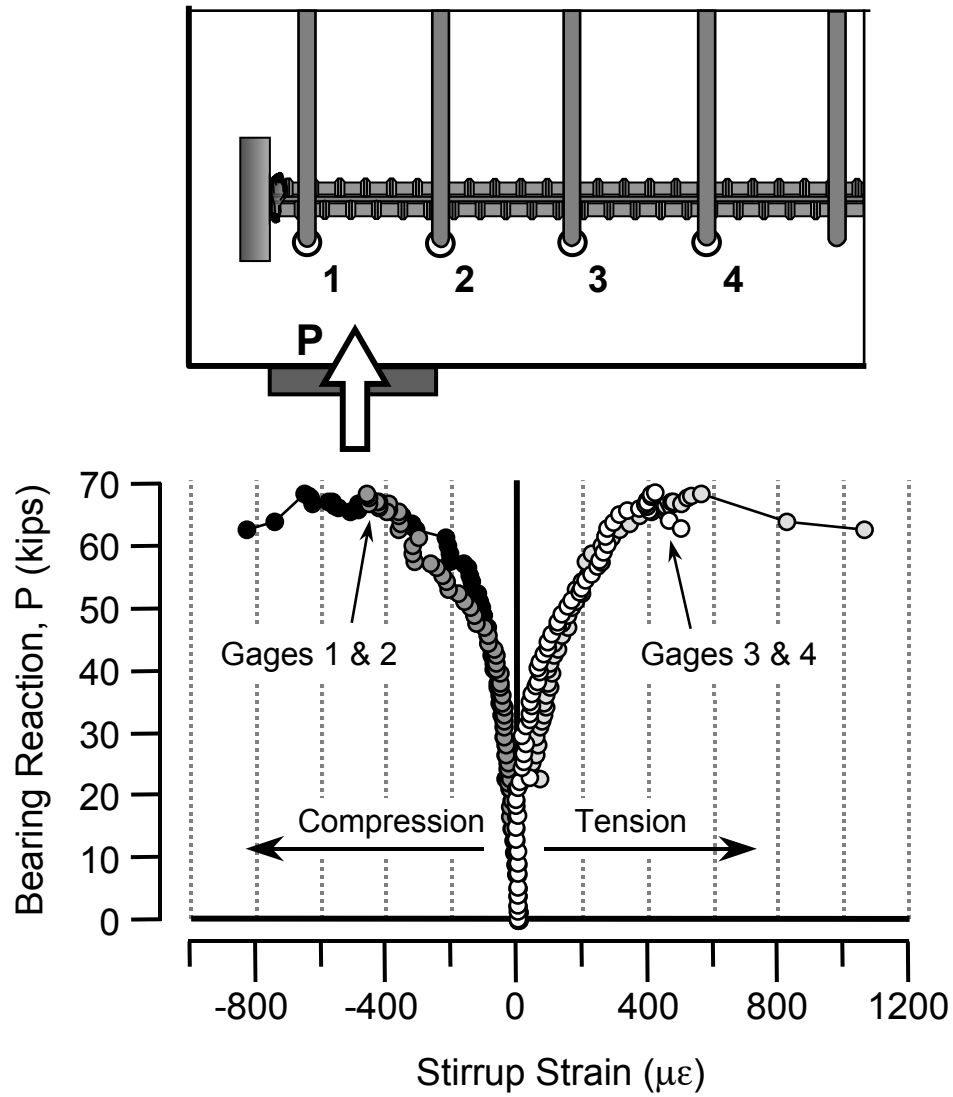


Figure 3-48: Development of transverse tensile strain in the stirrup confinement of the heavily confined, headed bar specimen (CCT-08-45-04.70(V)-1-C0.012)

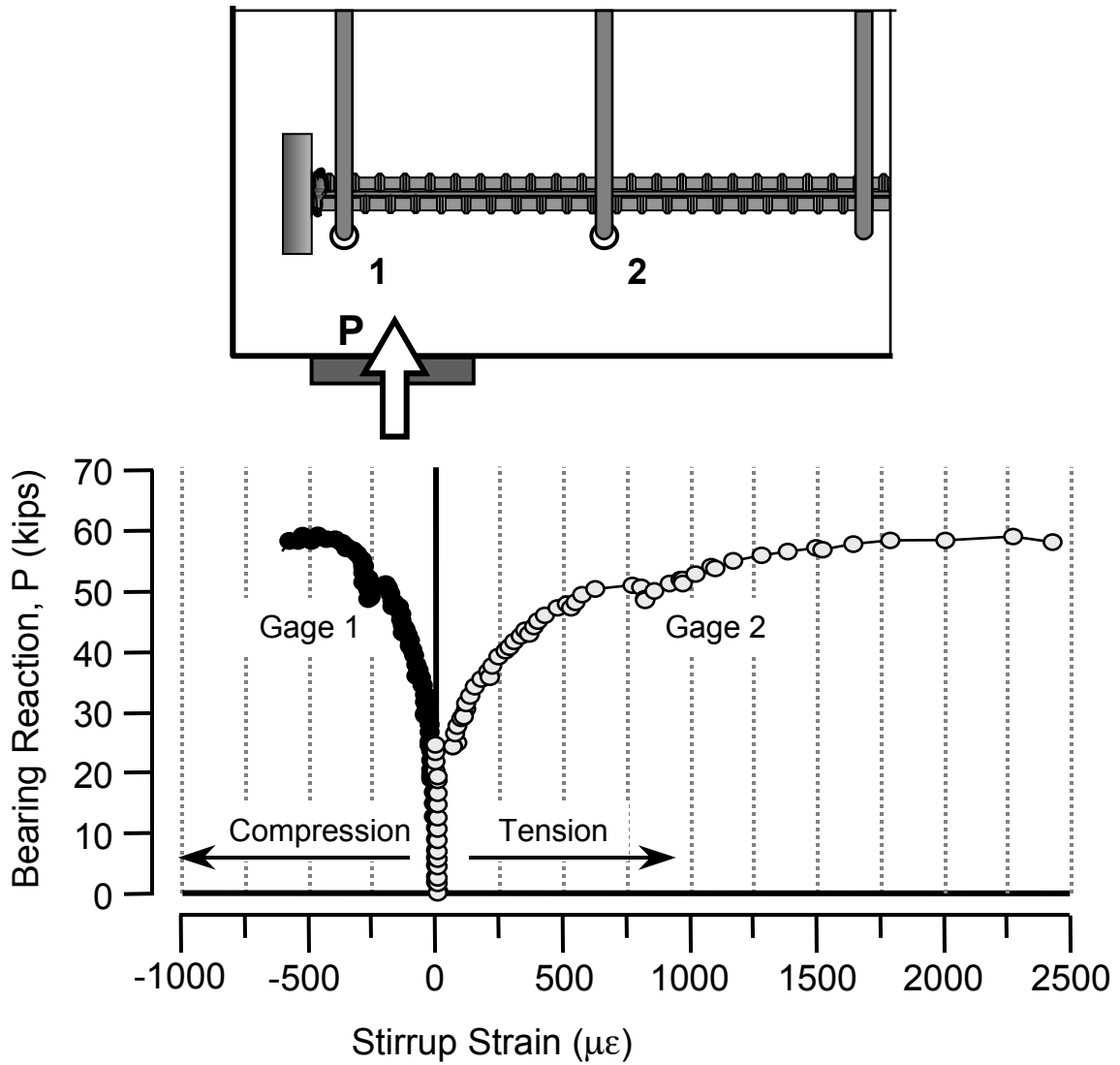


Figure 3-49: Development of transverse tensile strain in the stirrup confinement of the lightly confined, headed bar specimen (CCT-08-45-04.70(V)-1-C0.006)

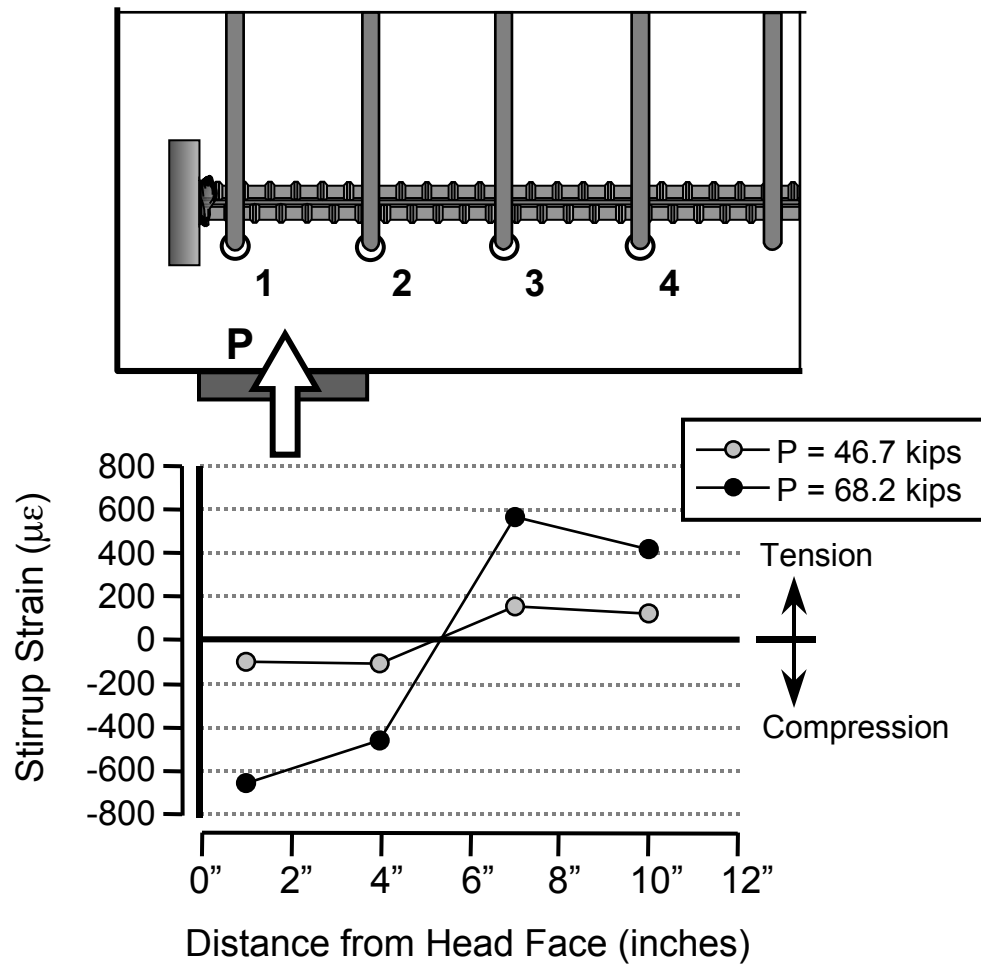


Figure 3-50: Transverse strains along the underside of the tie in the heavily confined, headed bar specimen (CCT-08-45-04.70(V)-1-C0.012)

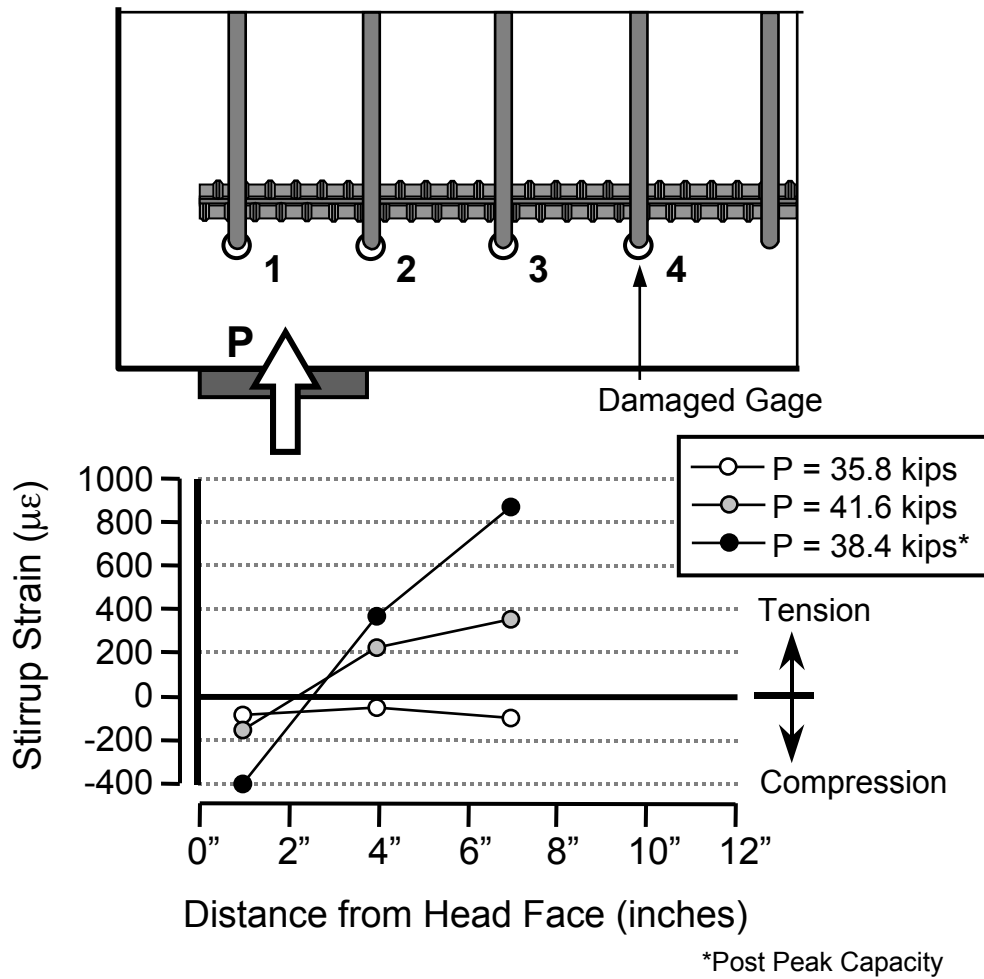


Figure 3-51: Transverse strains along the underside of the tie in the heavily confined, non-headed bar specimen (CCT-08-45-00.00-1-C0.012)

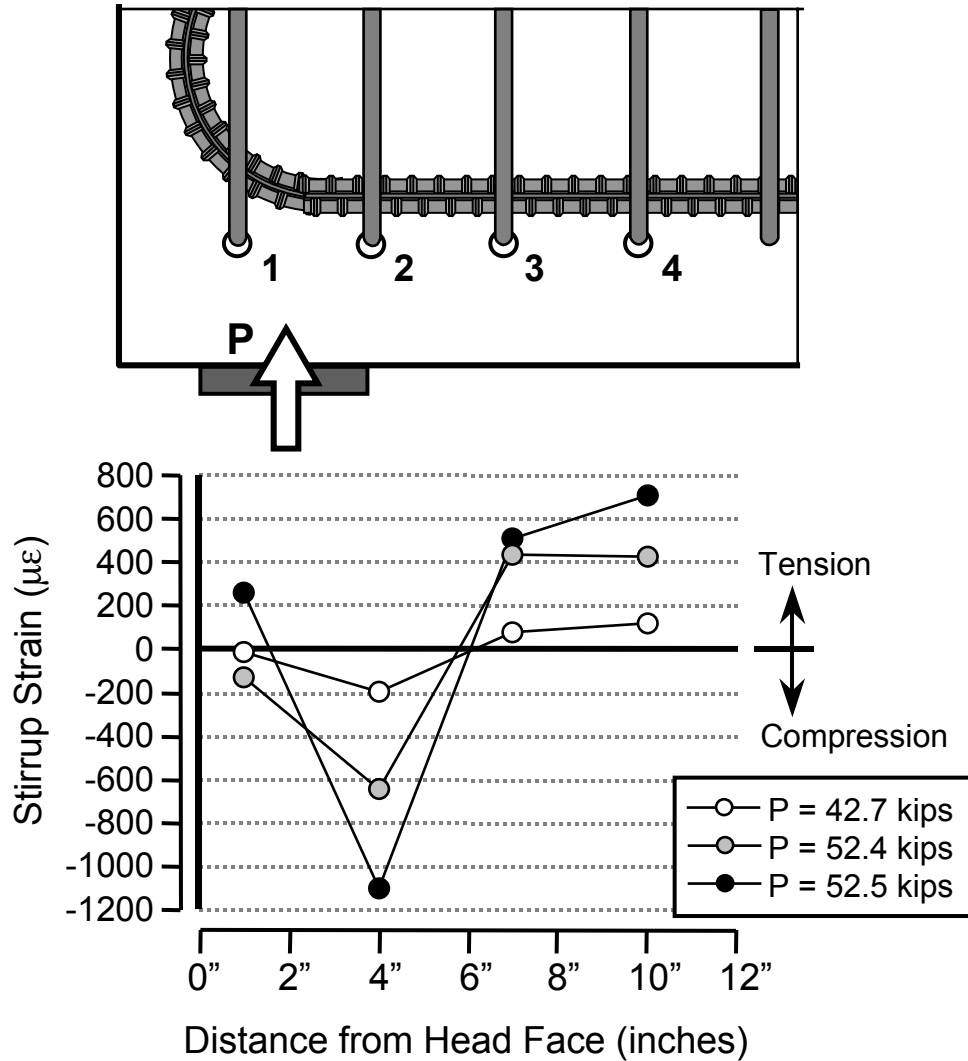


Figure 3-52: Transverse strains along the underside of the tie in the heavily confined, hooked bar specimen (CCT-08-45-Hook2-1-C0.012)

The hooked bar specimen (Figure 3-52) demonstrated similar transverse strains outside of the CCT node region. The tensile strain levels in the third and fourth stirrups were slightly higher at lower load levels than the headed bar case indicating that the hooked bar was slightly more reliant on bond at that location similar to the behavior of the headed bar test. Within the CCT node however (stirrups 1 and 2), the results of the hooked bar vary from the headed bar. Transverse strain in stirrup 1 was initially in compression and eventually shifted into tension. However, the strains were low indicating that virtually no stress transfer was occurring within the node at that location. At stirrup 2, the compression strain was much greater than was the case for the headed bar. The bend of the hook shifts the point of bearing back and upward from the location at which the headed bar bears on the concrete. Thus stirrup 1 was less effective and more demand was placed on the stirrup 2. These results, coupled with the vertical strain data from the previous section (Figure 3-46), show that the optimum location for stirrup confinement of a hooked bar is closer to the start of the bend than the end of the bend. As shown by the data plotted in Figures 3-46 and 3-52, Stirrup 1 was ineffective and merely hampered the ability to place concrete around the hook.

3.2.4 Head Slip

Head slip in the confined specimens is presented in Figure 3-53. Data from the unconfined companion specimen were not available due to instrumentation errors during that test. The behavior of the two confined specimens followed expected behavior. The specimen with more confinement demonstrated a stiffer slip resistance than the specimen with less confinement. The slip response of the two specimens is generally less stiff than that of similar head sizes of unconfined specimens shown in Figure 3-18, however, the test results come from specimens with different concrete properties and the stiffness responses may not be directly comparable.

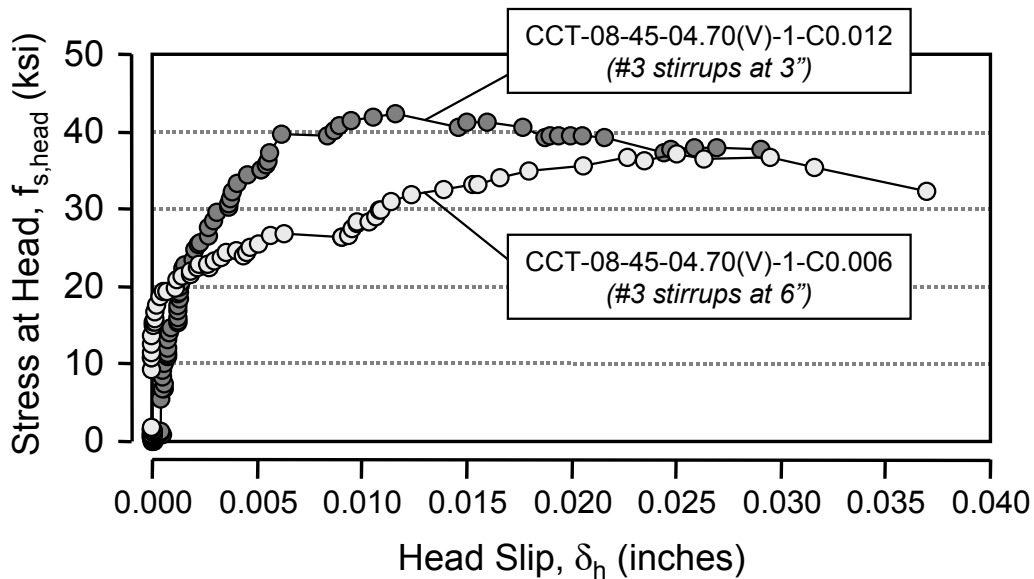


Figure 3-53: Bar stress versus head slip for unconfined and confined specimens

3.2.5 Load-Deflection Response

Load-deflection data for an unconfined and a confined specimen (CCT-08-45-04.70(V)-1-C0.000 and CCT-08-45-04.70(V)-1-C0.012) are shown in Figure 3-54. The load-deflection responses of these two specimens were very similar. The two plots align on top of one another up until a load of 64 kips when the unconfined specimen failed. The similarity of the data also suggest that there must have been little difference in the head slip behavior of the two specimens which would have affected the overall stiffness of the specimens. For the confined specimen, a definite yield plateau was achieved. Nevertheless, the confined specimen could not sustain the ductility demand placed on it and eventually failed at the node.

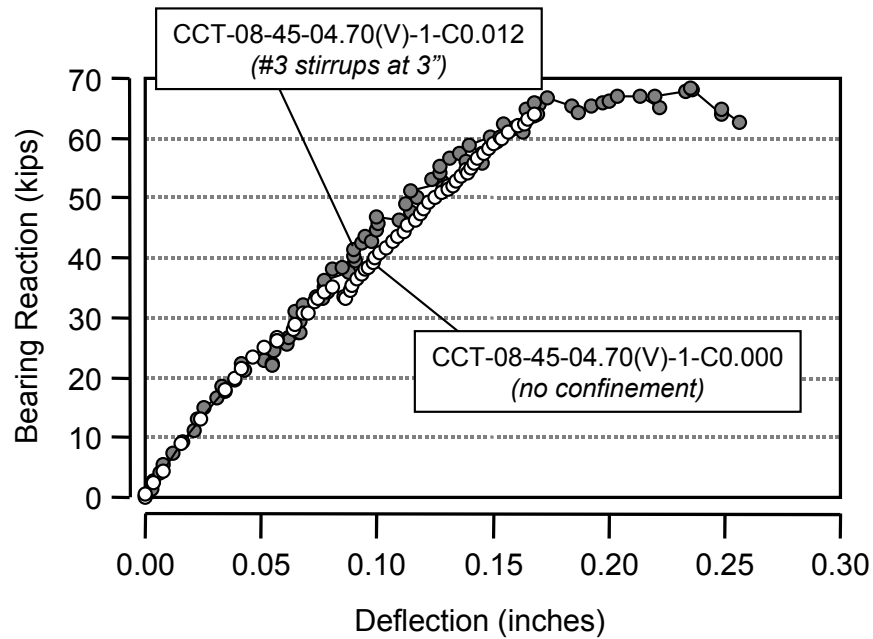


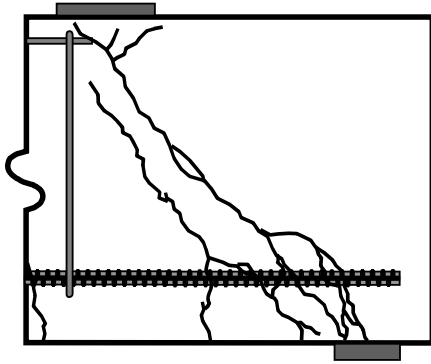
Figure 3-54: Load-deflection data for specimens unconfined and confined specimens

3.2.6 Modes of Failure

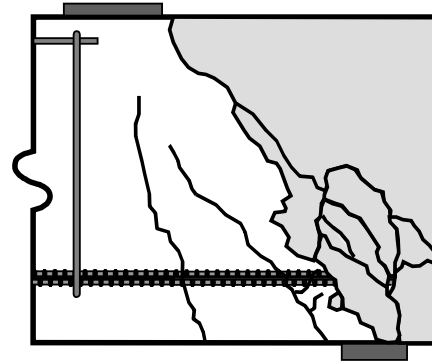
The failure modes of the five confined specimens resembled those of the unconfined specimens. The non-headed bars failed by pullout. The headed bars and the hooked bar failures involved strut rupture and transverse splitting. The one exception was the heavily confined, headed bar specimen (CCT-08-45-04.70(V)-1-C0.012), the most successful of the confined tests with the highest capacity. The specimen exhibited some ductility prior to failure, which did not occur in any of the previous specimens. Post-yield failure occurred because the node could no longer sustain the degree of deformation placed on it or because of continued development of the confined strut-and-tie mechanism. The confined mechanism (shown in Figure 3-36) involved the utilization of not just the bottom horizontal bar, but also the vertical stirrup bars as ties. This type of truss mechanism reaches its ultimate capacity when all the ties have yielded or until a strut or node fails. In the heavily confined, headed bar specimen, though the main horizontal tie may have begun to yield, redistribution of forces to alternative strut paths continued until one of the struts or nodes failed.

Figure 3-55 shows the cracking patterns at failure for non-headed and headed bar specimens with varying degrees of confinement. The cracking at failure of the non-headed bar specimens did not change significantly with the addition of confinement. The headed bar specimens did show some changes in behavior at failure. When unconfined, the specimen failed by splitting at the bottom of the strut and cleaving off of the top-front corner of the specimen. In the confined specimens, this dramatic cleaving off of large portions of the concrete was restrained. However, after failure, the confined specimens were left with large chunks of concrete bulging out from the sides along the length of the primary strut. This behavior tended to indicate that transverse splitting was significant.

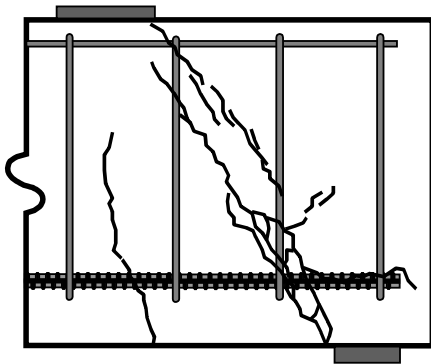
Table 3-6 summarizes the failure modes for the confined specimens. Failure modes conform to the categories discussed in Section 3.1.6.



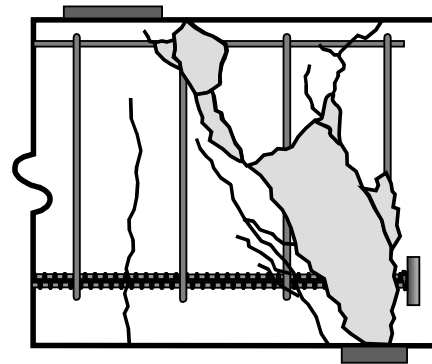
i. CCT-08-45-00.00-1-C0.000
(no head, no confinement)



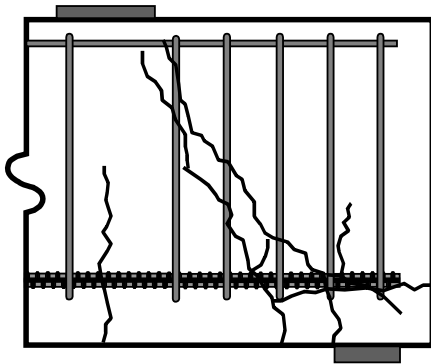
ii. CCT-08-45-04.70(V)-1-C0.000
(headed, no confinement)



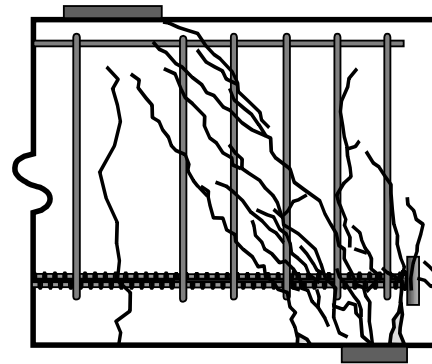
iii. CCT-08-45-00.00-1-C0.006
(no head, stirrups at 6")



iv. CCT-08-45-04.70(V)-1-C0.006
(headed, stirrups at 6")



v. CCT-08-45-00.00-1-C0.012
(no head, stirrups at 3")



vi. CCT-08-45-04.70(V)-1-C0.012
(headed, stirrups at 3")

Figure 3-55: Failure cracking patterns for non-headed and headed specimens with varying degrees of confinement

Table 3-6: Failure modes of confined CCT node specimens

Specimen Identification	f'_c	Failure Mode - Notes
CCT-08-45-00.00-1-C0.006	3800	Pullout
CCT-08-45-00.00-1-C0.012	3800	Pullout
CCT-08-45-04.70(V)-1-C0.006	3800	Splitting
CCT-08-45-04.70(V)-1-C0.012	3800	Yield then Splitting
CCT-08-45-Hook2-1-C0.012	3800	Splitting

3.3 SUMMARY OF BEHAVIORAL OBSERVATIONS

The various observations from the confined and unconfined specimens add together like pieces of a jigsaw puzzle to form a picture of the whole mechanism of force transfer in the CCT node specimens. Strain gage data from the confined, unconfined and special detail specimens provided information on the development of the tie bar and the locations of compression and tension regions within the CCT node panel. Combined strain data with the observations of cracking and failure modes provides an overall picture of the CCT node behavior.

Data from the special detail tests have shown that splitting tension along the diagonal strut begins at the ends of the strut. The behavior of the strut resembles the behavior of a concrete cylinder subjected to a double punch test. A wedge of concrete forms in front of the bearing face of the head and acts to cleave the strut in two. Splitting may occur in the plane of the truss model or transverse to the plane of the truss model depending on the orientation and size of the head. Failure most likely initiates at the CCT node.

Anchorage of the headed bars consists of two stages: the first in which load is primarily anchored by bond. This stage continues until maximum bond is reached, past which the bond stress gradually declines. This point begins the start of the second stage in which anchorage force is transferred to the head. This stage continues until the head reaches its maximum capacity or bar yield occurs. Final anchorage capacity is the sum of the maximum head capacity plus the residual bond left after the decline in bond begins.

Strain readings from gages on the tie bar indicate that the critical section at which the tie bar must fully develop occurs at the front-most diagonal crack. This crack forms along the lower edge of the diagonal compression strut and propagates downward to the edge of the bearing plate. The critical section can thus be estimated as the location at which the tie bar passes out of the path of the diagonal compression strut. Shear deformation across this crack can cause severe kinking of the tie bar.

Strain readings from stirrups in the confined specimen indicate that beneath the CCT node, compression stresses from the lower bearing plate must neck inward to equilibrate spatially with the bearing face of the head. This creates a region of vertical and transverse compression. This region begins at the bearing face of the head and extends to the surface of the critical diagonal crack. On the other side of the crack, radial splitting stresses created by bond of the reinforcing bar cause the reverse stress state.

Load-deflection data suggest that the top CCC node undergoes severe contraction during loading of the specimen. The CCC node is under a state of biaxial compression and can potentially sustain compression stresses up to 1.5 times the uniaxial concrete compression strength, f'_c . As the CCC node becomes highly stressed, the top of the strut can also become a critical location for the initiation of failure.

The truss mechanism forms after a succession of cracks develop. Cracks form first underneath the load point (the CCC node), then closer and closer to the CCT node. The cracks closest to the CCT node propagate diagonally and follow the lower edge of the diagonal strut path. Even in confined specimens, the initial truss mechanism to form begins with a single diagonal strut connecting the CCT node directly to the CCC node. This is the stiffest and most direct path for force transfer. As this strut begins to weaken due to cracking, secondary strut paths may form to mobilize the stirrups.

Crack width measurements indicate that the primary diagonal crack, closest to the strut and the CCT node, undergoes the most opening during loading.

Finally, head slip measurements demonstrate the enhanced resistance provided with increased head size. Head slip was shown to have a detrimental affect on the overall stiffness of the specimen. Slip was very often a precursor to failure. However, the amount of slip was also related to the amount of total bar stress transferred to the head. For longer development lengths, less bar stress would be transferred to the head before yielding and smaller heads could be used without concern for slip.

CHAPTER 4: CCT NODES: COMPARISON TO FAILURE MODELS AND FORMULATION OF DESIGN METHODOLOGY

4.1 INTRODUCTION

In this chapter the CCT node data are examined for trends then compared to existing theories of head capacity. This analysis leads towards the development of a design formula for headed bar anchorage. The existing theories to which the CCT node data are compared include: the ACI STM design procedures for nodes and struts [2], the modified CCD methods developed by DeVries [9] for headed bars, the ACI bearing capacity equations [2], and the ACI development length equations [2].

4.2 TRENDS IN THE DATA

The variables studied in the CCT node study included relative head area, strut angle, head shape and orientation, bar size, and confinement. The effects of these variables on the trends in the data are examined in this section.

4.2.1 Effect of Relative Head Area

Figure 4-1 shows the effect of increases in relative head area on the ultimate bar stress carried by the head. Values of ultimate bar stress have been adjusted by a ratio of $4\text{ksi}/f'_c$ to normalize the effects of differences in concrete strength. Only data from specimens that did not yield are plotted. Figure 4-1 shows that the ultimate capacity of the head generally increased with increasing relative head area.

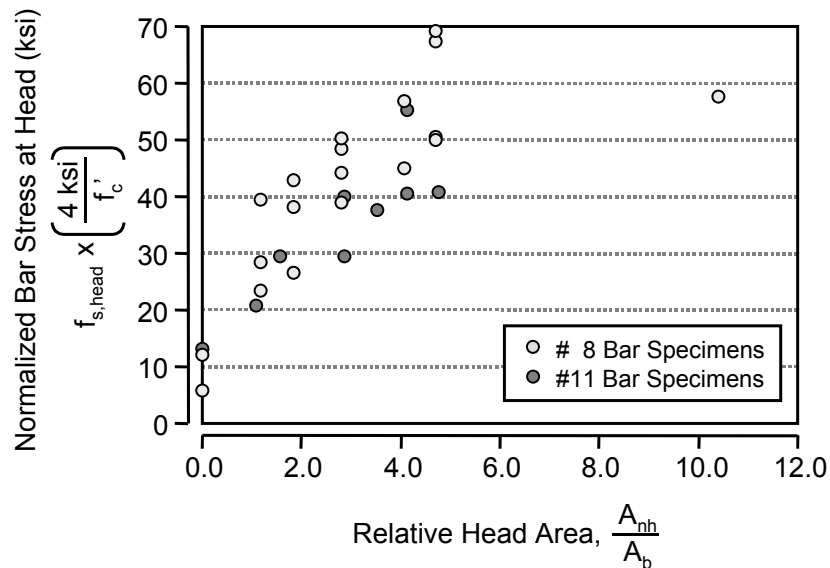


Figure 4-1: Effect of relative head area on head capacity

4.2.2 Effect of Strut Angle

Figure 4-1 included data from specimens with different strut angles. The head capacity was not influenced by the strut angle. However, the strut angle did affect the bond component of the anchorage. As the strut angle was decreased, more of the length of the tie bar was included in the path of the strut as shown in

Figure 4-2. As a result, the development length of the tie bar was increased and bond became a larger component of the anchorage. Thus smaller head sizes were able to achieve full development of the tie bar. In Figure 4-3, the minimum head sizes that achieved yield of the tie bar are plotted for the three different strut angles studied. The plot shows that decreases in the strut angle allowed smaller head sizes to successfully anchor the tie bar.

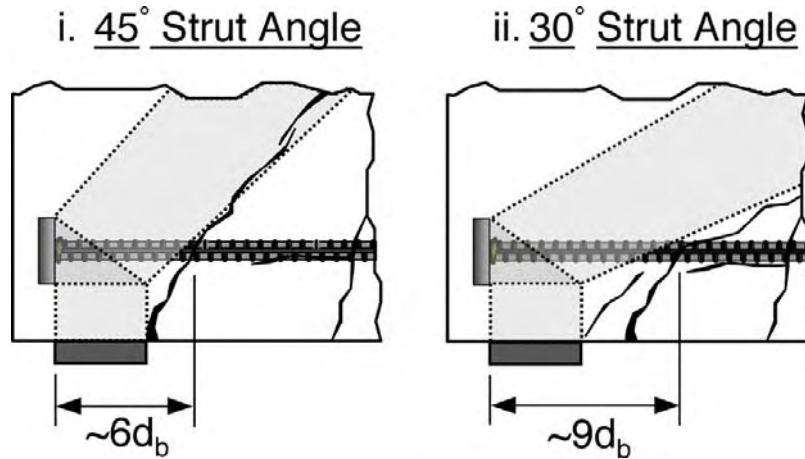


Figure 4-2: Approximate development lengths for 45° and 30° strut angles

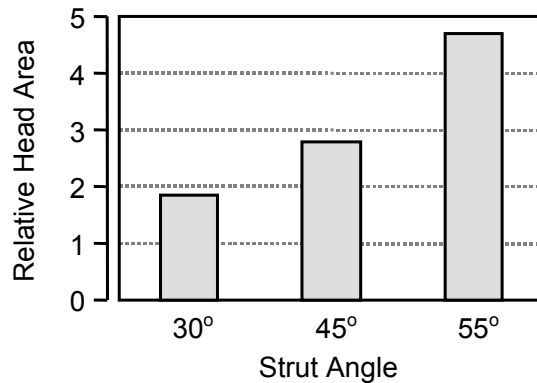


Figure 4-3: Minimum head size necessary to achieve yield of the tie bar

4.2.3 Effect of Head Shape and Orientation

Three basic head shapes were studied in the research: circular, square, and rectangular. For the rectangular head shapes, the affect of the orientation of the head was also studied. Three pairs of specimens used circular and square heads of almost exactly the same relative head area (Table 4-1). Of these three pairs, however, only one provided two specimens that both failed to yield and thus provided data that could be used to study the affects of head shape. Head slip plots for specimens CCT-08-55-04.04-1 and CCT-08-55-04.06-1 are presented in Figure 4-4. The data show that the square head performed slightly better than the circular one, but not significantly. DeVries [9] also studied head shape. He concluded that it was not a significant variable and excluded it from his design equations.

Table 4-1: Companion specimens for effect of head shape

Specimen Pair	Head Shape	f'_c (ksi)	$f_{s,head}$ (ksi)	Failure Mode
CCT-08-30-04.04-1	Circular	4.2	27.5	Yield
CCT-08-30-04.06-1	Square	4.2	33.5	Yield
CCT-08-45-04.04-1	Circular	4.0	32.7	Yield
CCT-08-45-04.06-1	Square	3.1	34.8	Crushing
CCT-08-55-04.04-1	Circular	3.1	25.1	Crushing
CCT-08-55-04.06-1	Square	3.1	27.5	Crushing

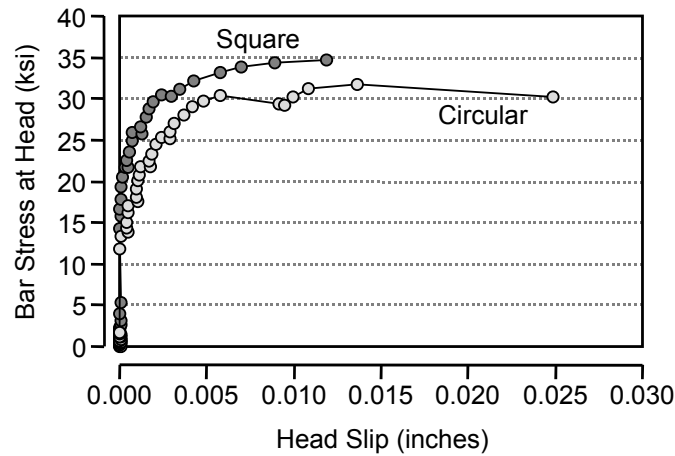


Figure 4-4: Head slip plots for circular and square heads

Seven pairs of specimens provided information on the effect of rectangular head orientation (Table 4-2). One pair of specimens (CCT-11-45-06.69(H)-1 and CCT-11-45-06.69(V)-1) both yielded. Thus, the bar stress sustained by the heads at a slip of 0.005” was used instead of ultimate stress data. Ratios of the horizontal head capacity to vertical head capacity were then calculated for each pair of specimens and plotted against the aspect ratio (long dimension / short dimension) of the head (Figure 4-5). This plot shows that the head orientation did have an effect on the capacity for heads with larger aspect ratios. The data for slightly rectangular heads (long/short \approx 1.3-1.5) were inconsistent. Some head capacities were greater with a horizontal orientation and some greater with a vertical orientation. However when the aspect ratio of the head approached 2, the horizontal orientation of the head consistently provided a capacity 30-40% greater than the vertical orientation.

The effect of head orientation can be explained by examining the angles of the forces produced by the head. As a concrete wedge forms in front of a rectangular head, the orthogonal faces of the wedge form at steep and shallow angles relative to the axis of the bar (Figure 4-6). As this wedge bears against the concrete, the shallow faces of the wedge produce greater transverse splitting stresses than the steep faces (Figure 4-7). Thus for a rectangular head, transverse splitting stresses are greater along the axis perpendicular to the long head dimension. In a CCT node, the larger transverse splitting stress are counteracted by vertical compression stresses when a head is oriented horizontally (Figure 4-8, part i). Thus, a head with a horizontal orientation should have a greater capacity than a head with a vertical capacity as the data in Figure 4-5 suggest. From a practical point of view, however, it is unrealistic to dictate what the orientation of the heads should be when a reinforcement cage is assembled. It is likely

that heads will be oriented randomly. For design, limits should be placed on the aspect ratio of head shapes to prevent undue influence from head orientation. Thus head orientation can be dropped as a factor in capacity equations.

Table 4-2: Companion specimens for effect of head orientation

Specimen Pair	Head Dimensions	Aspect Ratio	Horizontal Test		Vertical Test		$\frac{(f_s/f_c)_{\text{Horiz.}}}{(f_s/f_c)_{\text{Vert.}}}$
			$f_{s,\text{head}}$ (ksi)	f'_c (ksi)	$f_{s,\text{head}}$ (ksi)	f'_c (ksi)	
CCT-08-45-02.80(H)-2 CCT-08-45-02.80(V)-1	1.5" x 2.0"	1.33	37.6	3.1	49.1	3.9	0.96
CCT-08-45-04.70(H)-1 CCT-08-45-04.70(V)-1	1.5" x 3.0"	2.00	53.7	3.1	48.7	3.9	1.39
CCT-08-55-02.80(H)-1 CCT-08-55-02.80(V)-1	1.5" x 2.0"	1.33	38.0	3.9	43.2	3.9	0.88
CCT-08-55-04.70(H)-2 CCT-08-55-04.70(V)-1	1.5" x 3.0"	2.00	52.2	3.1	49.2	3.9	1.33
CCT-11-45-02.85(H)-1 CCT-11-45-02.85(V)-1	2.0" x 3.0"	1.50	30.3	4.1	40.9	4.1	0.74
CCT-11-45-04.13(H)-1 CCT-11-45-04.13(V)-1	2.0" x 4.0"	2.00	56.5	4.1	39.6	3.9	1.36
CCT-11-45-06.69(H)-1 CCT-11-45-06.69(V)-1	3.0" x 4.0"	1.33	42.6*	3.9	39.3*	3.9	1.08

* Stress at 0.005" slip.

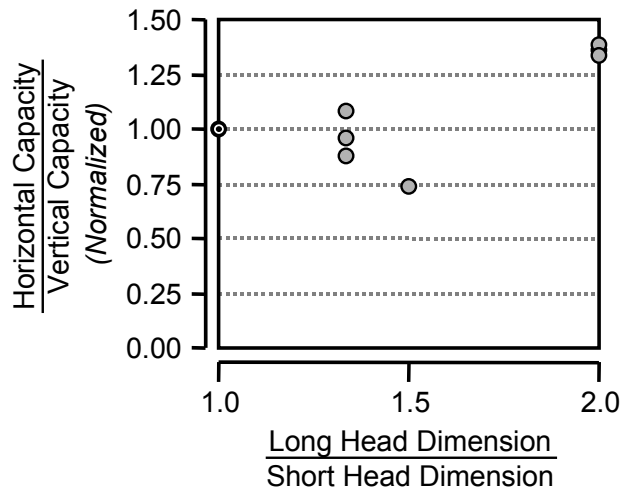


Figure 4-5: Effect of head orientation and aspect ratio on head capacity

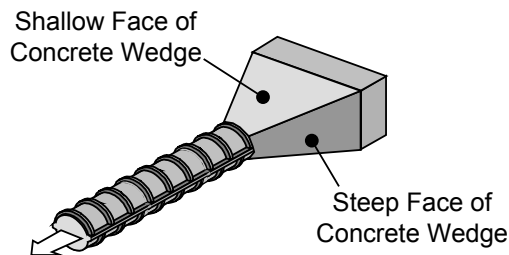


Figure 4-6: Shallow and steep faces of the wedge for a rectangular head

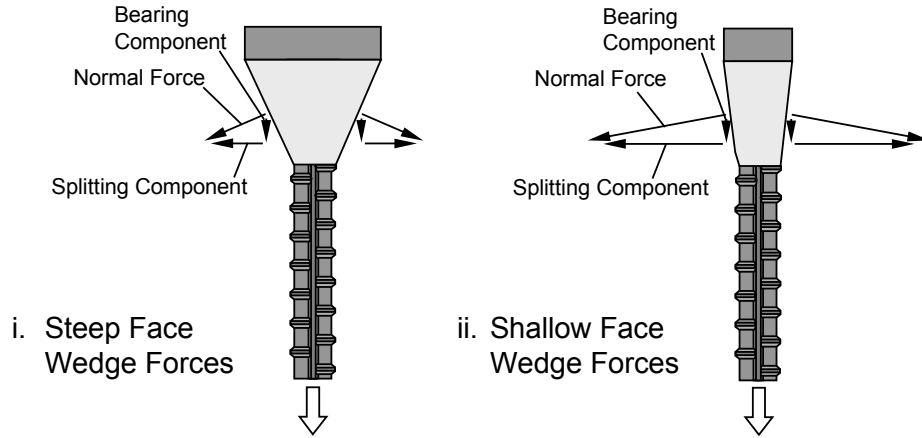


Figure 4-7: Transverse splitting components of shallow and steep wedge face bearing

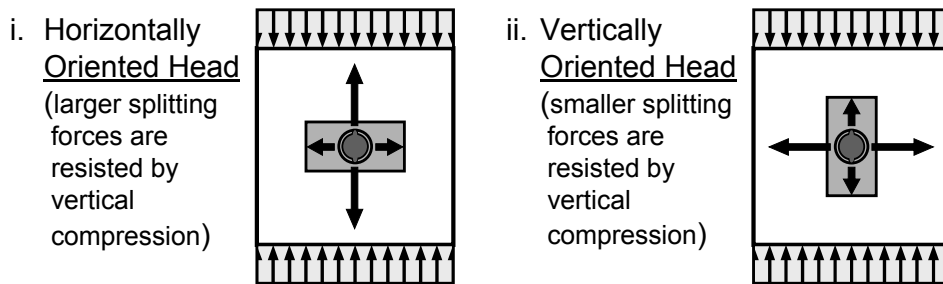


Figure 4-8: Horizontal versus vertical head orientation in a CCT node

4.2.4 Effect of Bar Size

Two bar sizes were tested in the CCT node study: #8's and #11's. The side cover and bottom bearing plate length were scaled to the bar diameter to maintain the proportionality of the CCT node. However, bottom cover remained constant. The data from the #8 and #11 tests with 45° strut angles are plotted in Figure 4-9. The #11 bar data points generally lay below the #8 bar data points. The decreased capacity of the #11's may be due to the smaller relative bottom cover in those specimens.

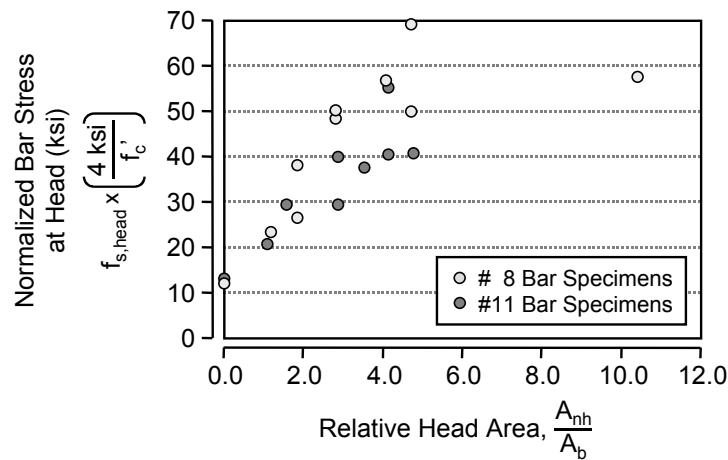


Figure 4-9: Effect of bar size on head capacity

4.2.5 Effect of Confinement

Tests were performed on non-headed, headed, and hooked bars with transverse reinforcement (stirrups) in the anchorage region. Confinement enhances the bond when the cover provided over the bar is small. However, in the CCT node specimen configuration, the tie bar always had large cover. Analysis of the effect of confinement on bond showed that the confinement provided no discernible improvement in bond stress. However, confinement had an effect similar to that of strut angle. The presence of the stirrups changed the manner in which the diagonal strut intersected the tie bar. The result was that the development length of the bar was increased. This allowed for a greater contribution of bond to anchorage capacity.

The effect of confinement on the head capacity is shown in Figure 4-10. The plot shows that the head anchorage carried about 20% less capacity when confinement steel was added. This could have been due to two factors. First, the unconfined specimen was cast separately from the confined specimens. The drop off in capacity might be an effect of variations in the concrete mixes and curing conditions. The compressive strengths of the concrete batches were not greatly different, though the tensile strength was lower in the batch used for the confined specimens. Secondly, the presence of the confining steel may have affected the ability of the fresh concrete to consolidate properly around the head. This would have resulted in the drop in capacity. It should also be noted that the configuration of the confining steel was not ideal for restraining the critical splitting stresses produced by the anchorage of the head. As the results of the specially detailed specimens showed, the critical location of tensile splitting stresses occurs at the upper portion of the head. The stirrup confining steel passed along the sides and bottom of the head, but not along the top of the head through the critical section where maximum tensile stresses developed. Though consistent with typical detailing, the confinement that was studied was not ideal for enhancing the capacity of the head anchorage. Furthermore, whatever the cause of the decreased capacity in the confined specimens, the results come from only three tests which is not enough to provide compelling evidence that a trend exists. This issue requires further study.

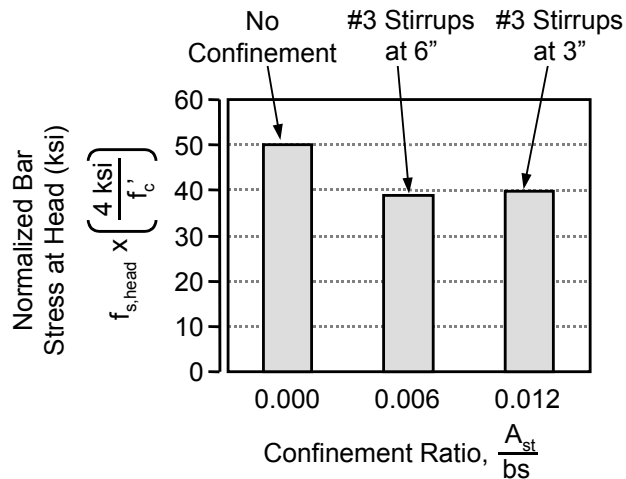


Figure 4-10: Effect of confinement on head capacity

4.2.6 Comparison to Hooked Bars

Results of the two unconfined hook tests are compared to the headed bar results in Figure 4-11. The stress data in Figure 4-11 is from the strain gages at the edge of the nodal region ($7d_b$ from the face of the head). Hook 1 refers to standard hook detail 1 and hook 2 refers to standard hook detail 2 (see Figure 2-10). All of the data are for #8 bar tests. The figure shows that both hooks and headed bars are substantial improvements over straight, non-headed bars ($A_{nh}/A_b = 0$). The plot also shows that the for relative head

areas greater than 2, all but two of the headed bars had greater than or equal anchorage capacities than comparable hooked bars. The data show the feasibility of using headed bars in place of hooks.

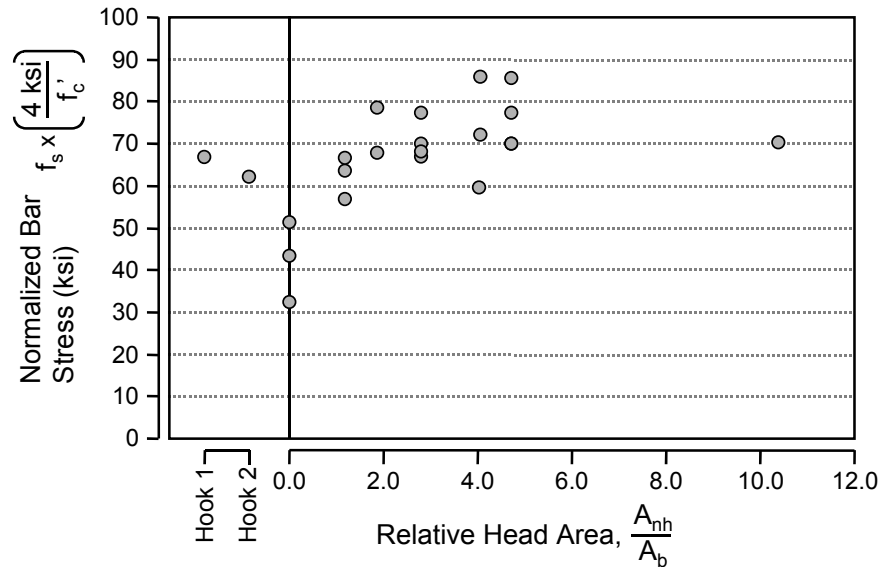


Figure 4-11: Bar stress from hooked bars compared with headed bars (#8 sizes)

4.3 COMPARISON OF HEAD CAPACITY TO THEORETICAL MODELS

4.3.1 Comparison to ACI STM Procedures

The ACI STM procedures [2], like the other existing STM procedures, base the capacity of nodes and struts on allowable stresses limits at the faces of the nodes and struts [19]. In this section, the ACI stress limits are compared with the data from the CCT node specimens. The strength of the node was checked at the forward face of the node, where it abuts against the bearing face of the head and the strength of the strut was checked at the face that adjoins against the CCT node (Figure 4-12).

Bearing of the CCT node was most critical at the face that contacted the bearing area of the head. At that face, the geometry of the node was rigidly defined by the boundaries of the head and the face area was equivalent to the net bearing area of the head. The force at the head was determined from strain gage measurements close to the head. Bearing stresses at failure were calculated for all specimens that failed by rupture of the strut and node region. Efficiency factors for each test were then determined as a fraction of f_c' . Figure 4-13 shows these values plotted against the relative head area for the 26 CCT node specimens that failed by rupture.

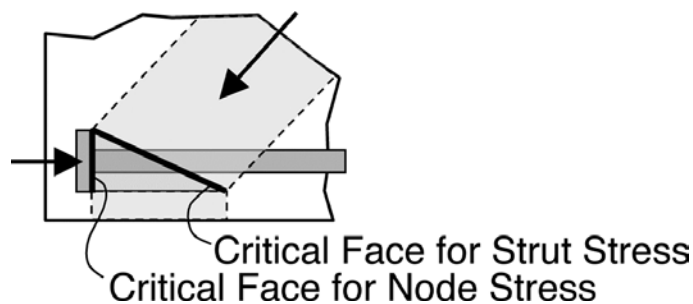


Figure 4-12: Critical node faces for STM stresses

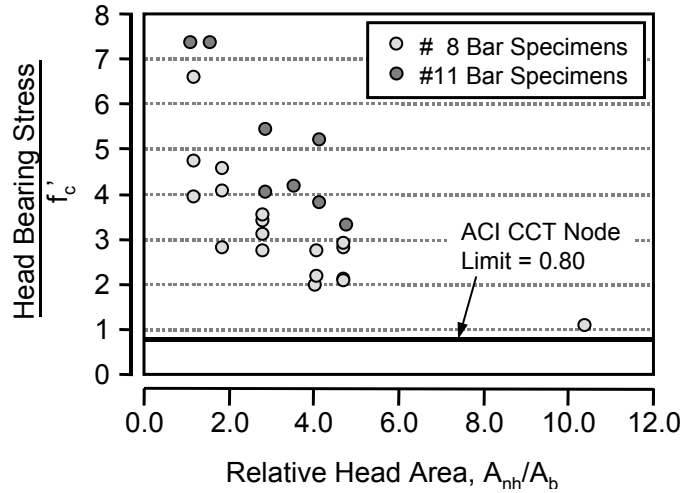


Figure 4-13: Efficiency factors for node bearing at the face adjacent to the head

Figure 4-13 shows that the bearing capacity of the concrete at the head was much greater than the uniaxial compression strength of the concrete. There was a trend of decreasing bearing strength with increasing relative head area. For the smallest heads, the efficiency factor of the concrete was between 4.0 and 7.5. The efficiency factor dropped off with increasing head size. A single data point at the far right indicates that the efficiency factor dropped off to 1.0 at a relative head area of 10.4. There was no apparent difference between the data points from #8 bar tests with different strut angles. However, there was a significant difference between the data from #8 bar tests and #11 bar tests. The data for the #11 bar tests were greater than analogous data from #8 bar tests. All of the calculated efficiency factors were greater than the maximum ACI limit of $0.80f'_c$ for CCT nodes.

Figure 4-14 shows the distribution of the efficiency factors for the 26 specimens. The distribution had an average value of 3.8 with a standard deviation of 1.6. The distribution shape was not normal.

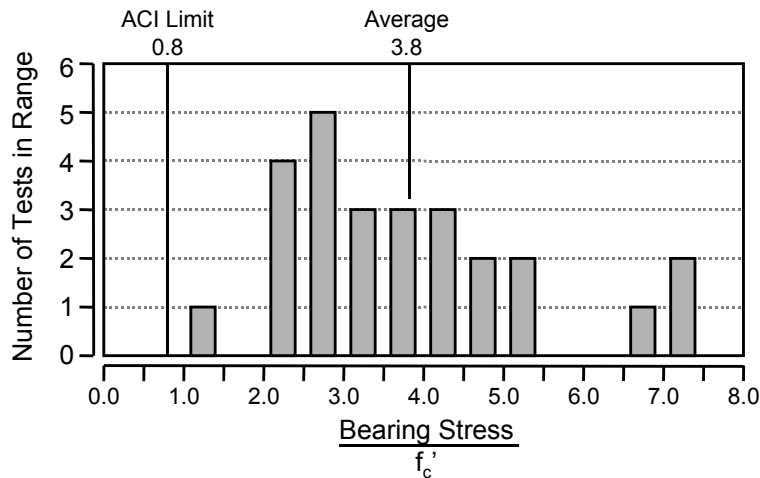
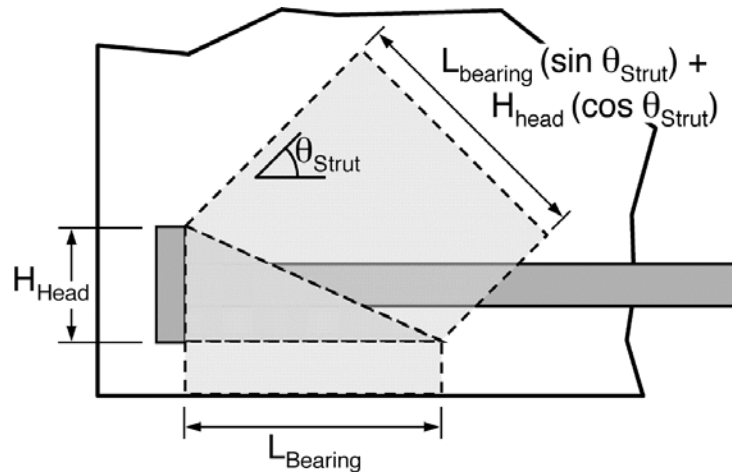


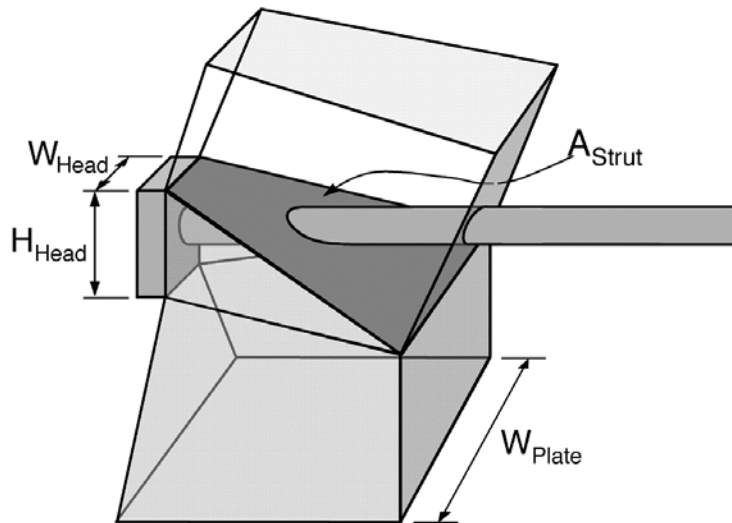
Figure 4-14: Distribution of efficiency factors for CCT node bearing results

The bearing capacity of the strut was analyzed. The face area of the strut was determined by the boundary conditions at the CCT node. The bottom bearing plate and the geometry of the head define the shape and dimensions of the lower strut face. Figure 4-15 illustrates the geometry that can be reasonably assumed

for the node/strut intersection. The assumed shape was trapezoidal. The depth of the trapezoid was dictated by the height of the head, H_{head} , and the length of the bearing plate, L_{bearing} . The top width of the trapezoid was assumed to match the width of the head, W_{head} , and the bottom width to match the width of the bearing plate, W_{plate} . The actual cross-sectional shape of the strut may have been different, but given the geometry of the conditions that defined the node, the bearing plate and head plate, the trapezoidal assumption was reasonable within the dictates of STM analysis.



i. Side view of strut and node geometry



ii. Oblique view of strut and node geometry

Figure 4-15: Geometry of the strut/node intersection at the CCT node

The area of the strut, A_{strut} , was calculated as described above and the force in the strut was determined from the measured bar force and the measured bearing reaction. Using this data, bearing stresses at failure were calculated for 25 CCT specimens that failed by rupture. One specimen, CCT-08-45-01.18-1 was omitted because data for the bar force were lacking. This specimen had a damaged strain gage at a critical location and the total bar force could not be calculated properly. The calculated strut bearing stresses were divided by f_c' to determine efficiency factors. The distribution of these efficiency factors is plotted in

Figure 4-16. Figure 4-16 shows that there were distinct differences between the #11 bar tests and the #8 bar tests. The lowest efficiency factor was 0.87. All of the data were greater than the ACI maximum strut limit of $0.85f'_c$ for uniaxial struts. The struts in the CCT node specimens would most likely be assumed to be bottle shaped in an analysis and subject to a maximum efficiency factor of 0.51 because they were unreinforced. The distribution of all specimens was non-normal because of the distinct differences between the #8 and #11 bar results. The average efficiency factor for the #11 bar tests was 0.95 and the average efficiency factor of the #8 bar tests was 1.37. The overall average was 1.24.

The proceeding analyses suggest that a single efficiency factor cannot be applied to the design of the CCT nodes. The bearing stress that can be supported by the head was not constant but seemed to vary inversely with relative head area (Figure 4-13). The bearing stress that could be supported by the strut seemed to be affected by bar size or the geometric variations between the larger and smaller bar size tests. In both analyses, the estimated bearing stresses were always greater than the ACI allowable. The ACI STM procedure provided an extremely conservative estimate of capacity.

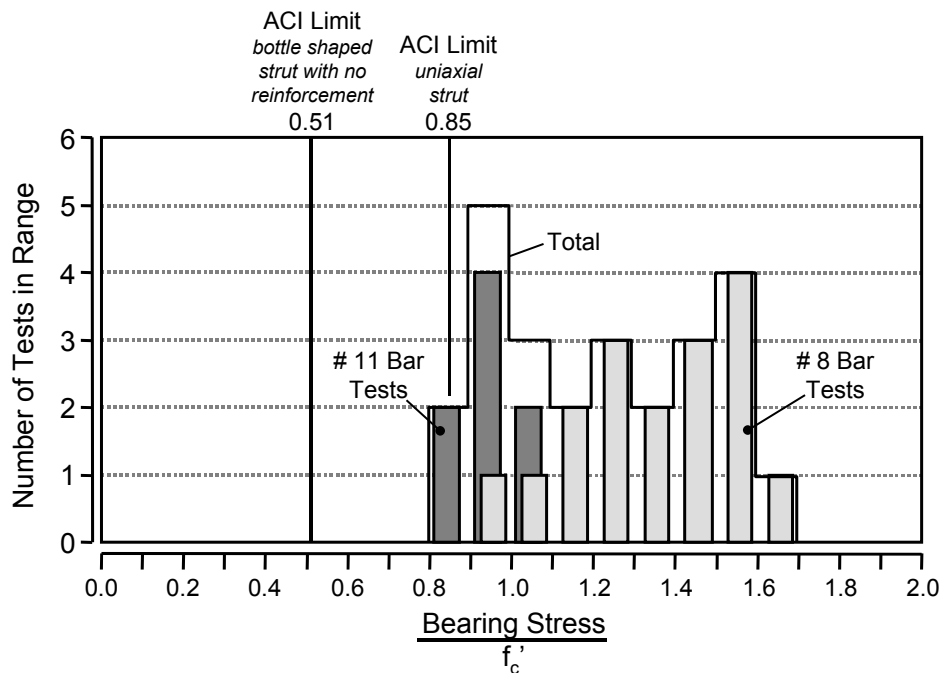


Figure 4-16: Distribution of efficiency factors for strut bearing at the face adjacent to the CCT node

4.3.2 Comparison to Modified CCD Approach

DeVries [9] developed modified Concrete Capacity Design (CCD) formulas for calculating the anchorage capacity of headed bars in mass concrete. Data from the CCT nodes were compared to the two models recommended by DeVries: concrete breakout and side blow-out. [19]

4.3.2.1 Comparison to Concrete Breakout Model

The concrete breakout failure mode applies to headed bars with very shallow embedment lengths. The anchorage lengths of the headed bars tested in the CCT nodes (measured from the head to the critical crack location) were generally in the $5-9d_b$ range which should normally qualify as shallow embedment. The model neglects contributions from bond of the bar. The concrete breakout model is most dependent on the embedment depth, the concrete strength, and the cover conditions which affect the projected

breakout area, A_N . Figure 4-17 shows how the embedment depth and projected breakout area were defined for capacity calculations. The definition of the projected breakout area was modified to accommodate the slanted failure surface of the CCT node specimens.

Calculated concrete breakout capacities were very low and did not vary with increases in relative head area. The model does not recognize changes in capacity with increased head area except in the manner in which head dimensions affect the breakout surface, which is a very slight effect. In Figure 4-18, measured bar stress at the head is plotted against the calculated values. There was no correlation between the concrete breakout model and the measured results. The failure behavior of the CCT node specimens did not resemble the failure behavior that the breakout model is based on, so the lack of correlation is unsurprising.

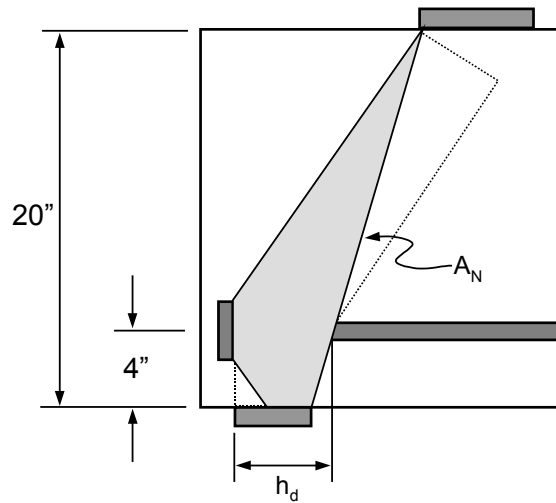


Figure 4-17: Definition of embedment depth and project breakout area for application of concrete breakout model

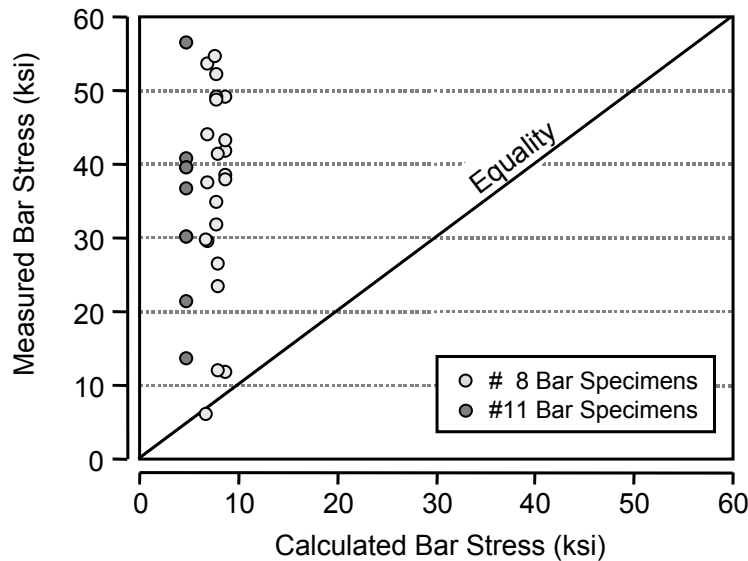


Figure 4-18: Correlation of measured and calculated values for concrete breakout model

4.3.2.2 Comparison to Side Blow-Out Model

Many of the CCT node specimens failed by splitting the strut transversely. The lateral rupture of the concrete caused by the splitting was similar to the side blow-out blowout failures observed by DeVries for deeply embedded bars. DeVries' side blow-out model is primarily dependent on concrete strength, head area, concrete cover, and the projected side blow-out area, A_{Nsb} . Figure 4-19 shows the projected side blow-out areas used for the different specimen series. The portion of the projected side blow-out area that crossed beyond the critical crack location (assumed at the lower-back boundary of the diagonal compression strut) was subtracted from the area. The side blow-out capacity was calculated for all of the CCT specimens that failed by rupture. In Figure 4-20, measured bar stresses at the heads are plotted against the calculated stresses.

Figure 4-20 shows that the side blow-out model appreciably underestimated the results of the CCT nodes. Mean and standard deviation were calculated for the ranges of measured/calculated ratios for the side blow-out model (Table 4-3). The mean values of the #8's and #11's were close showing that the model accounted for the differences between bar sizes that was observed in the raw data (Figure 4-9). The overall coefficient of variation was 19% which compares favorably to the coefficient of variation of 30% reported by DeVries for his data [9]. However, the method provided a very poor overall average of 2.6. The form of the side blow-out equation is promising and could be adapted for design purposes by manipulating the coefficients of the equation.

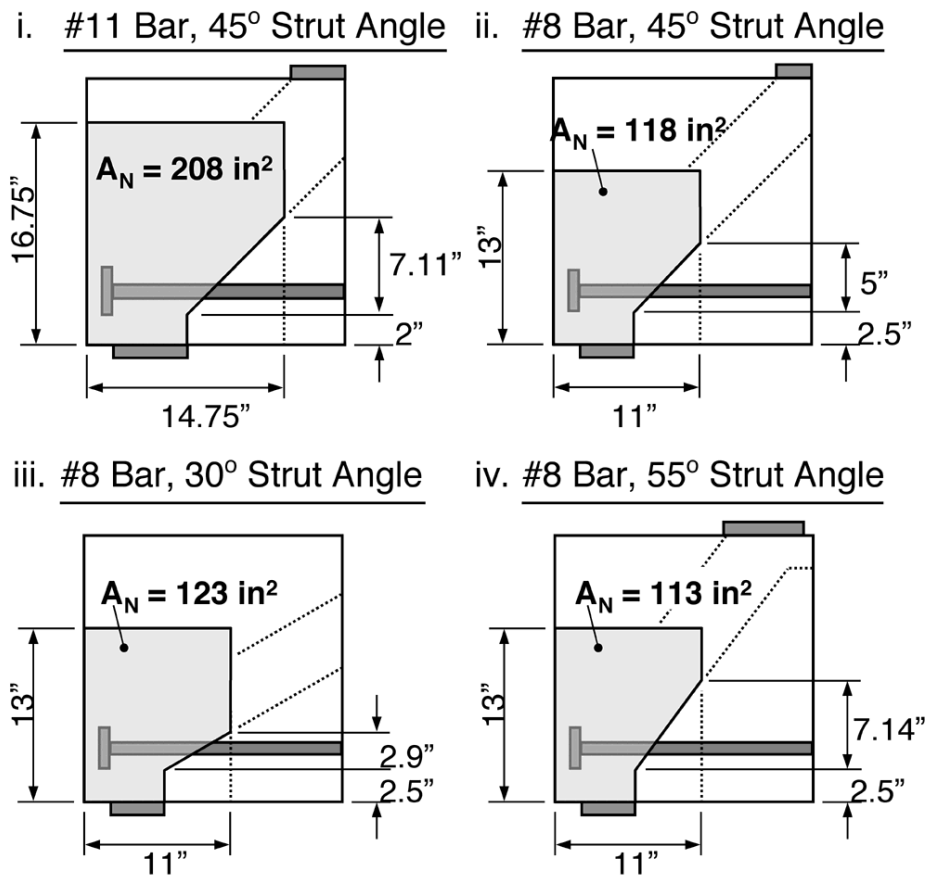


Figure 4-19: Projected side blow-out areas for various CCT specimen series

Table 4-3: Statistical data for accuracy of side blow-out model

Bar Size	Number of Specimens	Measured/Calculated Values		
		Range	Mean	Standard Deviation
#8	8	1.87 - 4.02	2.67	0.53
#11	19	2.08 - 3.24	2.52	0.40
All	27	1.87 - 4.02	2.63	0.49

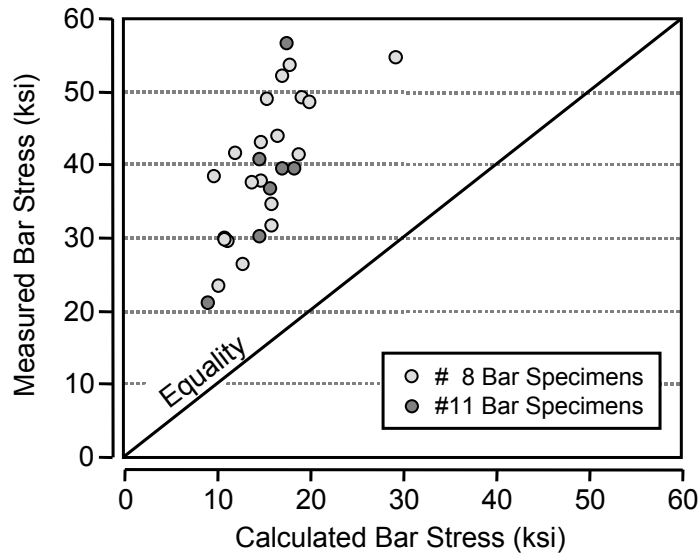


Figure 4-20: Correlation of measured and calculated values for side blow-out model

4.3.3 Comparison to ACI Bearing Capacity Model

The ACI bearing capacity model (Section 10.17 of the ACI code [2] and Section 5.7.5 of the AASHTO code [1]) was used to calculate the contribution of the head to the tie bar anchorage. The bearing capacity equation depends on three main variables: the bearing area (or in this case, the net head area), A_{nh} , the concrete compressive strength, f'_c , and the notional area projected beneath the surface of the loaded plate, A_2 . Reference CTR report 1855-1 "Anchorage Behavior of Headed Reinforcement: Literature Review" [19], Section 3.6.4 for additional information on the ACI bearing strength model.

The notional area, A_2 , is primarily dependent on the cover conditions and is limited to four times the bearing area by the ACI provisions. This limitation is very severe [19]. Research by Niyogi [16] and Hawkins [13] has shown that the limit should be much higher, around 40 times the bearing area. For the following analysis, the effect of a limitation on notional area was examined, and the bearing model was found to fit the measured data much better without it. Furthermore, the notional area was simply defined as the largest square that fit within the cover limitations provided by the CCT node specimen even for rectangular heads. Vertically oriented heads would typically project a larger notional area than other heads because their proportions fit the shape of the CCT specimen better. However, in keeping with the assumption that head orientation will likely be random in actual construction, it is recommended that the notional area should generally be assumed to be square for single heads attached to single bars. This

removed many complications associated with head shape in the analysis of the CCT nodes and from foreseeable design approaches using bearing as a failure model for headed bars. Figure 4-21 shows the notional areas that were used.

Figure 4-22 presents the measured and calculated values for the heads using the bearing model and shows that the model performed better than the previous models. Except for one point, the data are well distributed around the equality line.

Mean and standard deviation were calculated for the range of measured/calculated ratios for the bearing model (Table 4-4). The mean was 0.92 and the standard deviation was 0.18 giving a coefficient of variation of 20% similar to the side blow-out model. Figure 4-23 shows the distribution of the measured/calculated ratios. The distribution was slightly skewed towards low values.

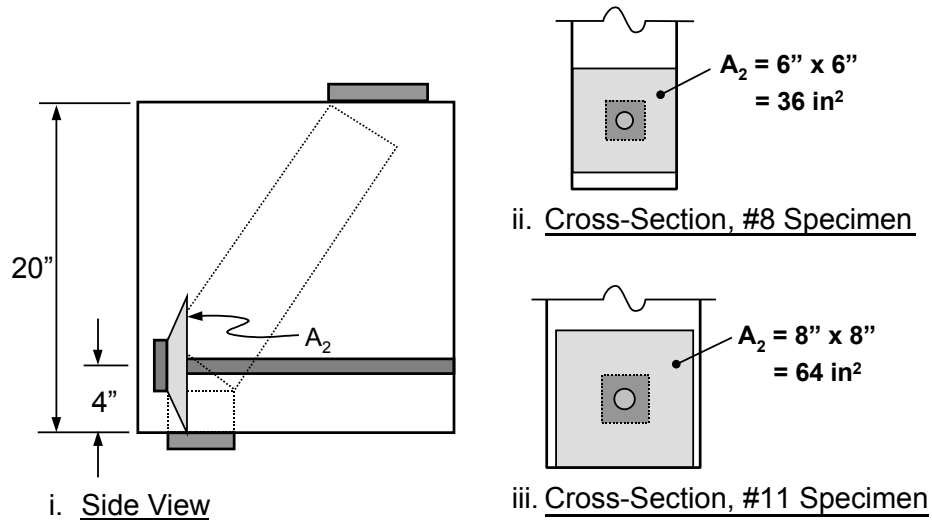


Figure 4-21: Notional areas for bearing analysis of CCT nodes

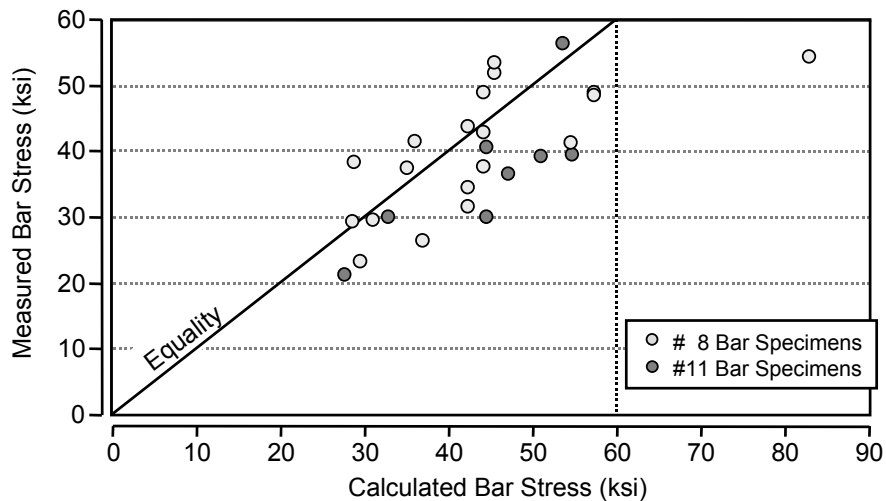


Figure 4-22: Correlation of measured and calculated values for bearing model

Table 4-4: Statistical data for accuracy of ACI bearing model

Bar Size	Number of Specimens	Measured/Calculated Values		
		Range	Mean	Standard Deviation
#8	8	0.66 - 1.35	0.96	0.19
#11	19	0.68 - 1.06	0.83	0.13
All	27	0.64 - 1.35	0.92	0.18

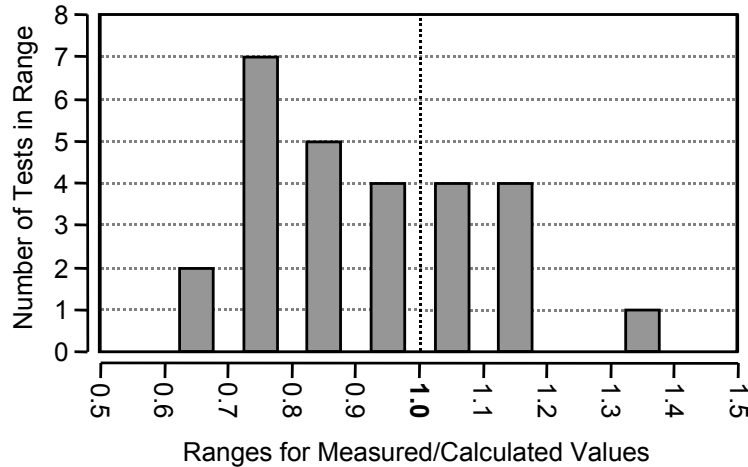


Figure 4-23: Distribution plot of measured/calculated ratios for bearing model

4.4 DEVELOPMENT OF A CAPACITY MODEL FOR HEAD BEARING

Both the side blow-out and the bearing models discussed in the previous section provided reasonable models for the anchorage capacity provided by the head. However, an investigation was performed to determine if a better model could be developed [19]. The similarities between the behavior of headed bars, anchor bolts, and bearing plates was emphasized.

The side blow-out model developed from research performed on anchor bolts and headed bars. The bearing model developed from studies of bearing plates on concrete blocks. Though developed to describe different phenomena, these models depend on a number of the same variables: bearing area (A_{nh}), concrete cover (c_1 or $\sqrt{A_2}$), and the concrete strength (f'_c). The primary differences between the models are the exponent applied to the concrete strength and the radial stress disturbance factor (Ψ_1) which is applied to anchor bolts and headed bars, but not bearing plates. The radial disturbance factor is dependent on the ratio of maximum and minimum cover (c_2/c_1). These variables are illustrated in Figure 4-24. In this section, the collected data base of headed bar tests, deeply embedded anchor bolt tests, and bearing plate tests are analyzed to produce one model that adequately predicts the capacity in all three situations.

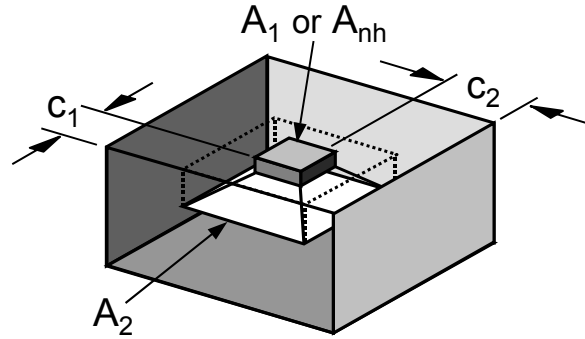


Figure 4-24: Important dimensions in bearing capacity models

A variety of literature sources was reviewed to collect a sizable database of test data that could be used in a regression analysis. Table 4-5 lists the sources that were collected. The following criteria were used to select appropriate test results for the database:

- Headed bar tests in which the capacity provided solely by the head could be determined. Thus only the deep embedment tests from the University of Texas in which the deformed bar portion was sheathed with PVC were used because the published capacity data reflected anchorage provided by the head alone without any contribution from bond. The CCT test data of this study could also be used because strain gage instrumentation allowed for the head capacity to be separated from the total bar capacity.
- Anchor bolt tests in which the embedment depth to side cover ratio was greater than or equal to five. This criteria was used in the University of Texas headed bar pullout tests to separate deeply embedded bars from shallow embedded bars.
- Bearing block tests in which the side cover to block depth ratio was at least two. This included all concentrically loaded cube tests. This ratio was selected because it represented the majority of the available data. Furthermore, only tests in which the bottom surface of the block was fully supported by a rigid medium were included.
- Tests in which the aspect ratio of the head or bearing plate was less than 2.1. This restriction is examined in Section 4.4.4.
- Tests in which no confinement was provided near the head or bearing plate.

Within the restrictions imposed by the above criteria, 544 test results were selected for the database. This number included 100 results from headed bar tests (18.4% of the total), 69 results from anchor bolt tests (12.7% of the total), and 375 results from bearing plate tests on concrete (68.9% of the total). Though the database was heavily loaded with bearing capacity tests on concrete blocks, the results presented in this section show that the headed bar and anchor bolt tests are well calculated by the proposed models, and the behavior of those tests can be treated in the same fashion as the behavior of the bearing tests.

The three test types are shown in Figure 4-25. The deeply embedded anchor bolts and bearing block tests represent similar conditions of CCC nodes. The CCT node tests from this study are very similar. Except for the fact that the bond along the deformed portion of the bar causes tensile stress within the nodal zone, the nodes of this study could be considered CCC nodes. In fact, the similar trends seen between the tests from this study and the other tests from the database suggest that headed bar anchorage at a CCT node should rightly be considered a CCC node condition.

The bearing pad of the CCT node tests of this study provides a clamping force perpendicular to the axis of the tie bar. This clamping force does not make the CCT node tests from this study greatly different from the CCC nodes of the bearing block and deeply embedded anchor bolt tests. Note that in the bearing block and deeply embedded anchor bolt studies, the compression struts that resist the force of the bearing plate or anchor bolt head must necessarily neck inward towards the CCC node in order to satisfy compatibility with the node. As the compressive struts neck inward, they will intersect the node at an angle which will have a lateral component of force, a clamping force. In fact, unless the CCC node occupies the full width of the member, lateral force will be a necessary component of the state of stress at the node. Thus, the fact that the CCT node tests from this study have an obvious clamping force should not be viewed as a reason to exclude these tests from the overall database. Furthermore, the models developed from examination of this database are not dependent on the condition of a clamping force from a bearing reaction lateral to the tie bar.

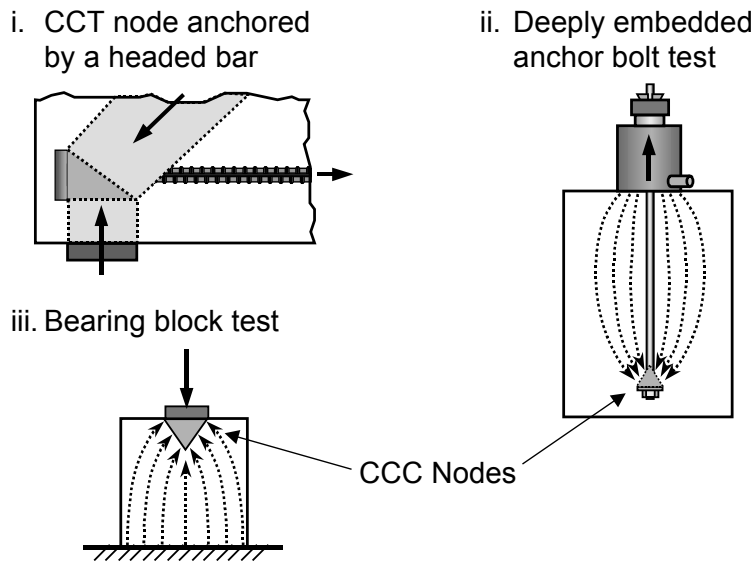


Figure 4-25: Node states of the test types used in the bearing database

Table 4-5: Summary of sources for collected database of headed bar, anchor bolt, and bearing tests

Source	Type of Test	Number of Data Values	Ranges for Variables		
			f'_c (ksi)*	$\frac{2c_1}{\sqrt{A_{nh}}}$	$\frac{c_2}{c_1}$
UT Deep Embedment [9]	Headed Bar	73	2.8 - 6.4	1.0 - 3.8	1.0 - 15.2
UT CCT Node Tests (present study)	"	27	3.1 - 4.2	2.1 - 6.2	1.1 - 1.3
Breen [8]	Anchor Bolt	17	3.2 - 5.5	2.0 - 3.7	3.1 - 4.0
Lee & Breen [15]	"	7	2.2 - 5.4	2.6 - 3.5	4.0 - 6.4
Lo [12]	"	16	3.0 - 5.5	1.3 - 3.6	3.0 - 6.0
Hasselwander [12]	"	9	2.6 - 5.5	1.5 - 4.1	3.4 - 12.0
Furche & Elgehausen [11]	"	20	3.8	2.9 - 7.4	3.8 - 7.5
Shelson [18]	Bearing Block	12	5.6 - 6.7	2.8 - 8.0	1.0
Au & Baird [7]	"	12	4.5 - 8.1	1.4 - 4.0	1.0
Hawkins [12]	"	73	1.7 - 7.6	1.0 - 6.8	1.0 - 6.0
Niyogi [16, 17]	"	119	1.4 - 7.3	1.0 - 8.0	1.0 - 4.0
Williams [23]	"	159	2.6 - 9.8	1.0 - 10.2	1.0 - 9.4
All Headed Bar Tests		100	2.8 - 6.4	1.0 - 6.2	1.0 - 15.2
All Anchor Bolt Tests		69	2.2 - 5.5	1.3 - 7.4	3.0 - 12.0
All Bearing Block Tests		375	1.4 - 9.8	1.0 - 10.2	1.0 - 9.4
All Tests		544	1.4 - 9.8	1.0 - 10.2	1.0 - 15.2

*Equivalent Cylinder Strength Values

Table 4-6 lists the dependency of the bearing and side blow-out models to the primary variables that have been shown to be the most significant factors affecting capacity. Both models are proportional to side cover, c_1 , and the square root of bearing area, $(A_{nh})^{0.5}$. They are also related to concrete strength, but differ in the power assigned to the concrete strength. Bearing is directly proportional to compression strength, f'_c , while the side blow-out model is directly proportional to concrete tensile strength represented by the square root of compression strength, $(f'_c)^{0.5}$. Furthermore, the side blow-out model allows for an increase in capacity due to the influence of the secondary side cover, c_2 . In developing a new model for head capacity, these variables (f'_c , A_{nh} , c_1 , and c_2) were selected as the most important factors influencing capacity. The form of the new model was selected to be a product of three factors:

- A factor for bearing area and side cover, $A_{nh}(2c_1/\sqrt{A_{nh}})$. This factor is expressed in a form similar to that of the bearing model, as a product of bearing area and the square root of the ratio of supporting area to bearing area, $\sqrt{A_2/A_1}$. If the supporting area is taken as square in shape, then A_2 is equal to $4c_1^2$. The bearing area notation is changed from A_1 to A_{nh} . Thus the term $\sqrt{A_2/A_1}$ translates to $2c_1/\sqrt{A_{nh}}$, the form used in the proposed model.
- A factor for concrete strength. Two possible forms were examined: one in which the power of the concrete strength was constant and one in which the power of concrete strength varied based on the $2c_1/\sqrt{A_{nh}}$ ratio. Niyogi [17] noted that the dependency of bearing strength on concrete strength changed as the bearing plate size shrunk relative to the bearing block size. As the bearing plate size was decreased, the capacity was no longer directly proportional to f'_c , but some lesser power of f'_c . Hawkin's [13] formula for bearing capacity was related to terms that contained both

f'_c and $\sqrt{f'_c}$. The relative contributions of these terms in Hawkin's formula are dependant on values of A_1 and $\sqrt{A_2/A_1}$. Thus the contribution from concrete strength was related to the relative sizes of the bearing area and the supporting area. These two previous investigations noted a dependency of the concrete strength contribution on geometric considerations. This dependency is explained in Figure 4-26. When the ratio of bearing area to supporting area is near 1.0, loading is primarily uniaxial (like a cylinder test) and capacity is proportional to compression strength. As the ratio of bearing area to supporting area shrinks, failure of the bearing plate is governed by resistance in the surrounding concrete to the splitting caused by wedging action of the plate. Thus capacity is proportional to tensile strength or $\sqrt{f'_c}$.

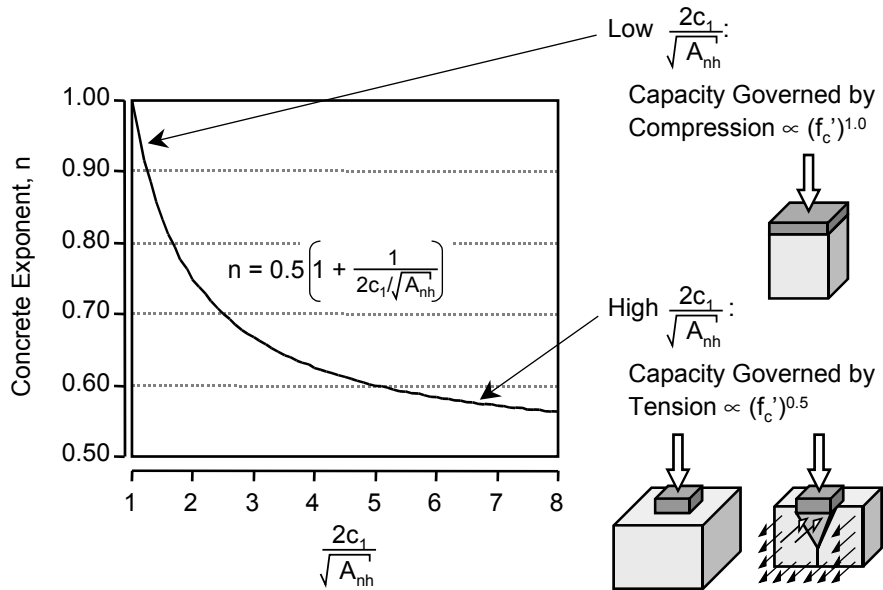


Figure 4-26: Relation of concrete power to $2c_1/\sqrt{A_{nh}}$ ratio

- A factor recognizing the contribution provided by the secondary cover dimension, c_2 . A form similar to that used in the side blow-out model was examined in which this factor is linearly dependent on the ratio of secondary cover to minimum cover. The factor equals 1.0 when the c_2/c_1 ratio equals 1.0 and rises as the c_2/c_1 ratio increases. Upper limits were examined for this factor as well.

These factors were examined in regression analyses to develop best-fit models that calculated bearing capacity for the collected database listed in Table 4-5. After an extensive investigation, which is not detailed in this report, two potential models were developed. These models are listed below and justified by the discussion contained in the subsequent subsections. Table 4-6 lists the relation of these models to the significant variables discussed previously.

Model #1:

$$\text{Bearing Capacity, } P = A_{nh} \left(2.6\Psi \left(\frac{2c_1}{\sqrt{A_{nh}}} \right) \left(\frac{f'_c}{2.4} \right)^{0.5 \left(1 + \frac{\sqrt{A_{nh}}}{2c_1} \right)} \right) \quad (4-1)$$

$$\text{with } \Psi = 0.7 + 0.3 \frac{c_2}{c_1} \leq 1.8 \quad (4-2)$$

Model #2:

$$\text{Bearing Capacity, } P = A_{nh} \left(0.9\Psi \left(\frac{2c_1}{\sqrt{A_{nh}}} \right) (f'_c) \right) \quad (4-3)$$

$$\text{with } \Psi = 0.6 + 0.4 \frac{c_2}{c_1} \leq 2.0 \quad (4-4)$$

P = head capacity (kips)

Ψ = radial disturbance factor

A_{nh} = net head area (in²)

c_1 = minimum cover dimension (in)

c_2 = secondary cover dimension (the smallest cover dimension measured perpendicular to the minimum cover) (in)

f'_c = concrete cylinder strength (ksi)

Table 4-6: Various models for head capacity

Failure Model	Relation to Significant Variables:			
	Concrete Strength	Head Bearing Area	Minimum Side Cover	Secondary Side Cover
Bearing	f'_c	$(A_{nh})^{0.5}$	$(A_2)^{0.5} \propto c_1$	-
Side Blow-Out	$(f'_c)^{0.5}$	$(A_{nh})^{0.5}$	c_1	$0.7 + 0.1(c_2/c_1)$
Proposed # 1	$(f'_c)^{0.5(1+\sqrt{A_1/A_2})}$	$(A_{nh})^{0.5}$	c_1	$0.7 + 0.3(c_2/c_1)$
Proposed # 2	f'_c	$(A_{nh})^{0.5}$	c_1	$0.6 + 0.4(c_2/c_1)$

4.4.1 Effect of Cover/Head Bearing Area Ratio

Normalized bearing capacity is plotted against the ratio $2c_1/\sqrt{A_{nh}}$ in Figure 4-27 for the collected database. Bearing capacities were normalized against f'_c , Ψ , and A_{nh} . The plot shows that a linear relationship exists between the normalized capacities and the $2c_1/\sqrt{A_{nh}}$ ratio. The plot also shows that this relationship is unlimited up to values of $2c_1/\sqrt{A_{nh}} = 10$, the upper limit within the database. This

trend justifies the inclusion of the $2c_1/\sqrt{A_{nh}}$ term in Equations 4-1 and 4-3. Furthermore, no limits were placed on the contribution to capacity provided by $2c_1/\sqrt{A_{nh}}$ as is the case in the bearing capacity equation provided in the ACI code [2].

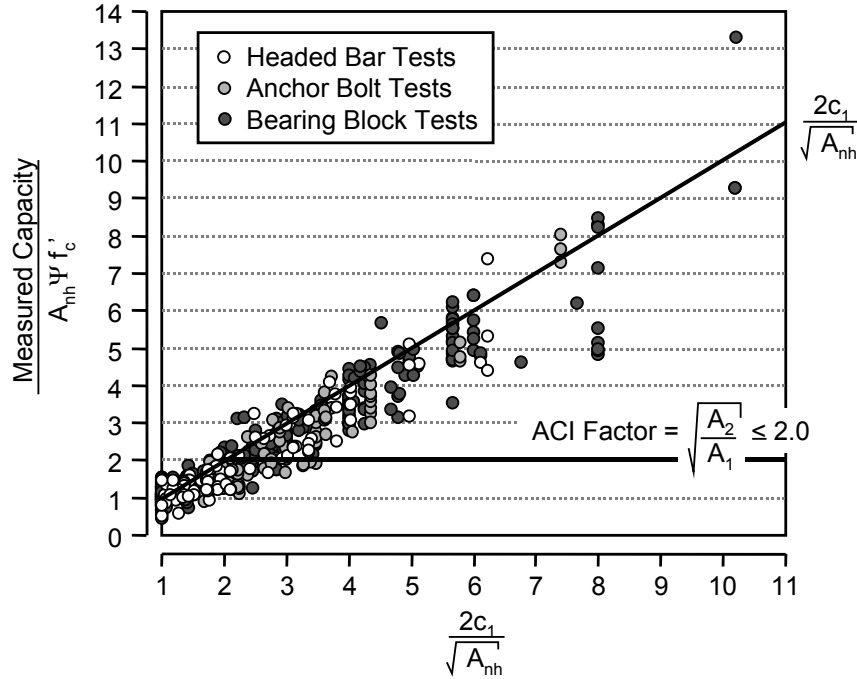


Figure 4-27: Normalized bearing capacity versus $2c_1/\sqrt{A_{nh}}$ ratio

4.4.2 Effect of the Secondary Cover

DeVries [9] accounted for the effect of second cover dimension in the form of a radial disturbance factor, Ψ . Similar factors were included in the proposed models, however, the proposed factors allow for greater increases to capacity from the secondary cover. DeVries' Ψ factor was designed to equal 1.0 when a headed bar was close to only one edge and to decrease to 0.8 as a corner condition was approached. The proposed Ψ factors were designed to do the opposite. They equal 1.0 under the corner condition and increase as the headed bar is moved away from the corner. In order to compare the two equations for Ψ , they must both be normalized to reflect the same boundary limits. Normalized bearing capacity is plotted against the c_2/c_1 ratio in Figure 4-28. The three equations for Ψ have been plotted against the data in order to compare their predictive capacities. DeVries' Ψ factor has been normalized to equal 1.0 when the c_2/c_1 ratio is equal to 1.0. Equations 4-2 and 4-4 have also been adjusted to normalize the differences between coefficients in Equations 4-1 and 4-3. The plot demonstrates there is a clear increase in capacity as the secondary cover dimension is increased. This increase ceases after the non-critical cover dimension begins to exceed about 4 times the minimum cover dimension ($c_2/c_1 = 4$). The increase to capacity is significant and is underestimated by DeVries' Ψ factor.

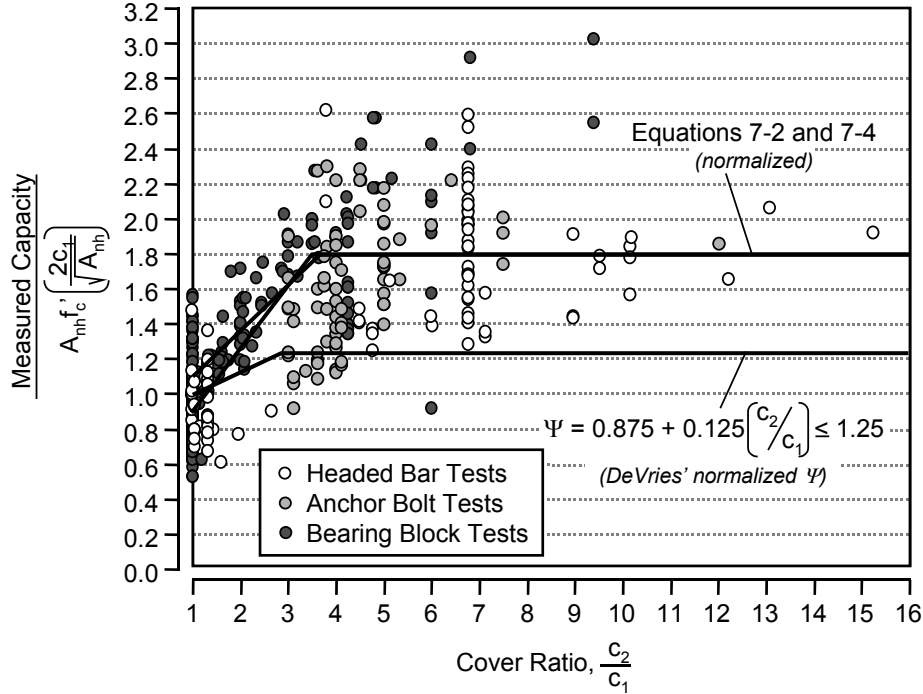


Figure 4-28: Normalized bearing capacity versus cover ratio, c_2/c_1

4.4.3 Effect of Concrete Strength

Normalized bearing capacity is plotted against concrete strength in Figure 4-29. Best-fit trend lines based on linear relationships to f'_c and $\sqrt{f'_c}$ are plotted against the data. Figure 4-29 shows that, between the two fixed powers of concrete strength, the capacity is best predicted with an exponent of 1.0. The bearing data are divided into two groups: data with $2c_1/\sqrt{A_{nh}}$ ratios less than or equal to 2.0 and data with $2c_1/\sqrt{A_{nh}}$ ratios greater than 2.0. At low concrete strengths (less than 6 ksi), the data from these two groups are fairly well intermixed. However, at higher concrete strengths, there is some indication of divergence between the two groups. The data with lower $2c_1/\sqrt{A_{nh}}$ ratios are generally higher than the data with $2c_1/\sqrt{A_{nh}}$ ratios greater than 2.0, but the trend is slight.

The data are plotted against the proposed model with the variable concrete exponent in Figure 4-30. The data are divided into two plots for clarity. The top plot presents data with $2c_1/\sqrt{A_{nh}}$ ratios between 1.0 and 2.0. The bottom plot presents data with $2c_1/\sqrt{A_{nh}}$ ratios greater than 2.0. The proposed model does not have a single trend line within a given range of $2c_1/\sqrt{A_{nh}}$ values, therefore, the bounds of the proposed model are presented in each plot for the appropriate ranges. The best fit of the proposed model was provided by:

$$\text{Concrete Factor} = 2.6 \left(\frac{f'_c}{2.4} \right)^{0.5(1+\sqrt{A_{nh}}/2c_1)} \quad (4-5)$$

with variables as defined previously.

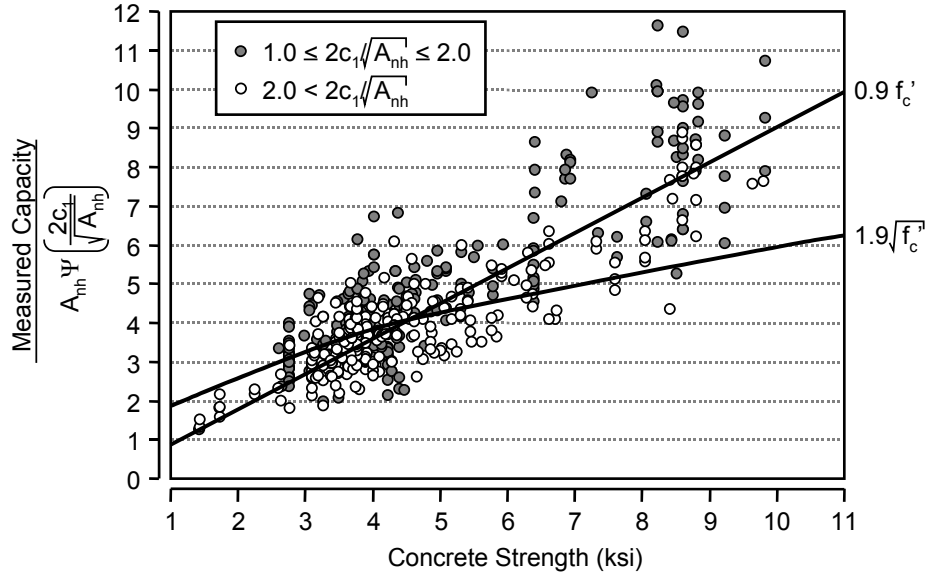


Figure 4-29: Normalized bearing capacity versus concrete strength, f'_c , with trend lines for relationships to f'_c and $\sqrt{f'_c}$

The proposed model fits the data slightly better than the relationship provided by f'_c with an exponent of 1.0. However, the improvement may not be significant enough to justify the use of the complex concrete exponent. A simple, single exponent of 1.0 would be preferable for design purposes. The best fit provided by a concrete strength factor with an exponent of 1.0 provides a maximum bearing pressure of $0.9f'_c$ when $2c_1/\sqrt{A_{nh}}$ is equal to 1.0. The variable exponent provides a maximum bearing pressure of $1.1f'_c$ when $2c_1/\sqrt{A_{nh}}$ is equal to 1.0. Which model makes more sense? For the most part, the experimental data were provided by cube tests. The concrete strength used in the model is based on cylinder strengths however. When $2c_1/\sqrt{A_{nh}}$ is equal to 1.0, the model is providing a conversion from cylinder strength to cube strength which should equal about $1.1f'_c$ to $1.2f'_c$. The other extreme of $2c_1/\sqrt{A_{nh}}$ values corresponds with the bearing of a deformed bar lug which has a very small dimensions compared with the surrounding concrete. This situation corresponds to bond stress, which is related to $\sqrt{f'_c}$. Thus, at the extremes of $2c_1/\sqrt{A_{nh}}$, the variable exponent model fits the considerations of mechanics better than the simple model based on f'_c with a constant exponent of 1.0.

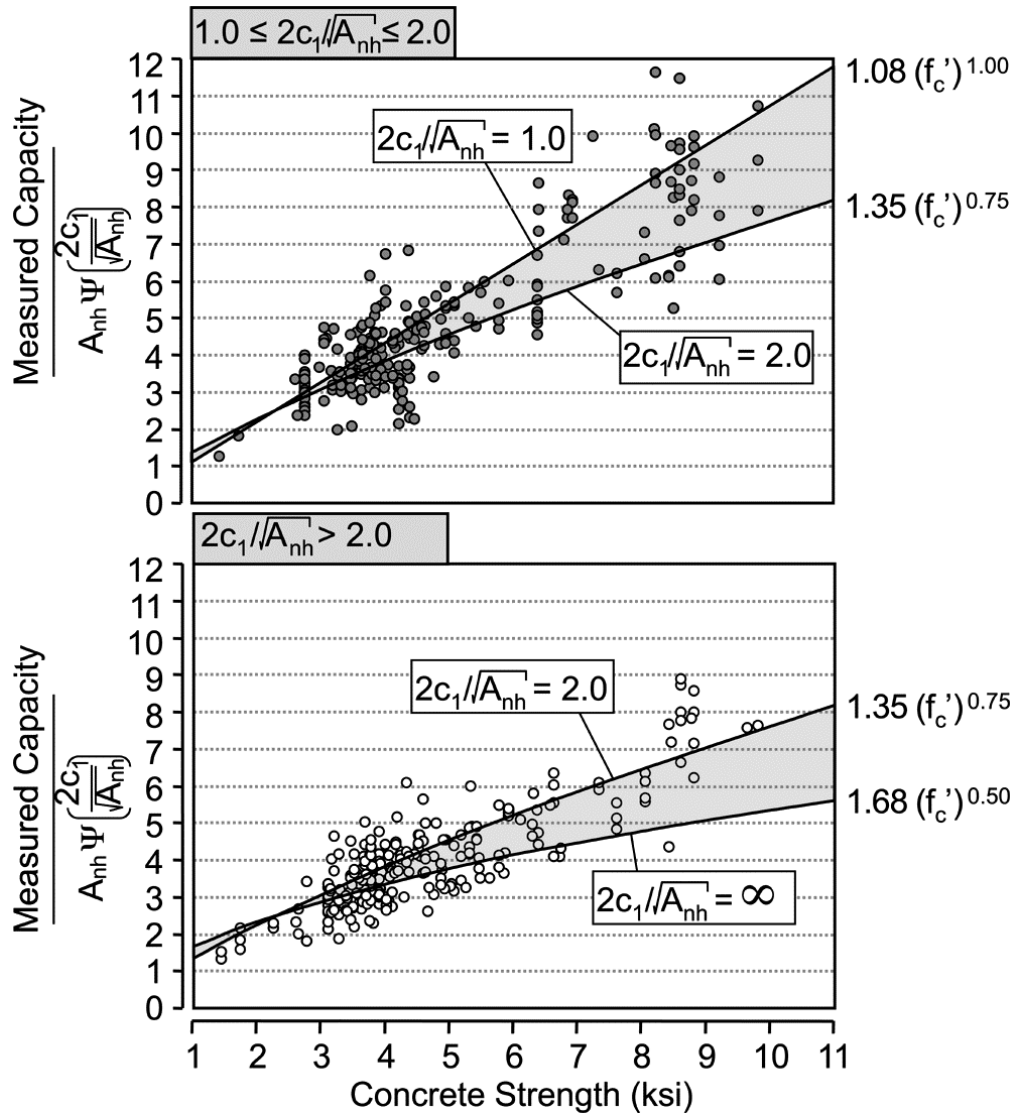


Figure 4-30: Normalized bearing capacity versus concrete strength, f_c' , with trend lines for the proposed concrete exponent term

4.4.4 Effect of Aspect Ratio

Though the aspect ratio of the bearing plates and heads was restricted for the data used in the database, a number of additional tests from outside of the database were accessed in order to examine the effect of aspect ratio. 82 additional tests from among the sources listed in Table 4-5 fit the criteria used to select the database, yet had aspect ratios greater than 2.1. Almost all of these tests were bearing block tests. The data points with large aspect ratios were from strip load tests on concrete blocks. Figure 4-31 plots the measured/calculated values against aspect ratio. Model 1 (Equation 4-1) was used to calculate capacity values. A similar analysis using model 2 was conducted and produced similar results.

Figure 4-31 shows that much scatter exists in the data. However, there is a slight trend of decreasing capacity with increasing aspect ratio. This reduction in capacity is most likely due to the neglect of head shape in the proposed models. Both models treat the unloaded area, A_2 , as being square and equal to $4c_1^2$ rather than using an area geometrically similar to the loading area, A_1 . For larger aspect ratios this

simplification becomes unrealistic and results in lower capacities. A trend of the data suggests an adjustment to capacity equal to:

$$\text{Aspect Ratio Factor} = (45 - \text{Aspect Ratio})/44 \quad (4-6)$$

This reduction is only 2.5% for the largest aspect ratio used in the database, 2.1. This difference is smaller than the scatter seen in the data indicating the models are reasonable for large aspect ratios and that a limit larger than 2 could be recommended for the model. A limit of 4 would result in an average reduction of only 7% according to the trend line.

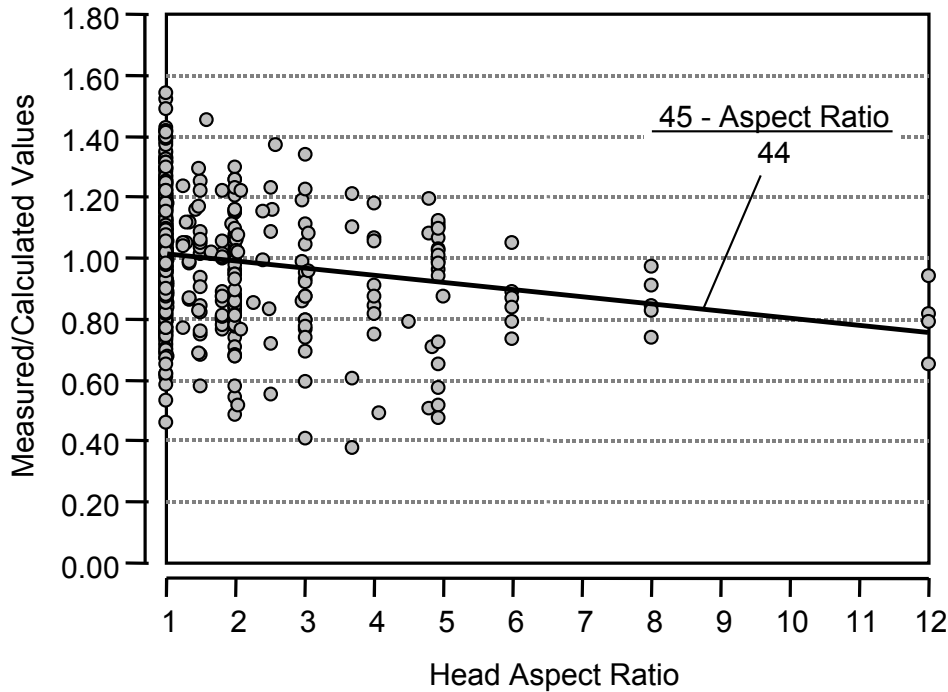


Figure 4-31: Effect of head aspect ratio on capacity

4.4.5 Aggregate Size Effect

No consideration was given to differences in aggregate size among the tests included in the database. Differences in the relative size of the specimen dimensions to the maximum aggregate size have been shown to affect the capacity of tests when all other variables are similar [6]. In general, a decrease in capacity is expected as the maximum aggregate size becomes smaller relative to the specimen dimensions. The cover/aggregate size ratio was determined for 524 of the 544 tests included in the database. Aggregate size was not reported in the study by Furche and Eligehausen [11]. The measured/calculated ratios of the specimens are plotted against the cover/aggregate size ratio in Figure 4-32. Calculated capacities were determined using model 1 (Equation 4-1), however, the trends were the same when calculations were performed using model 2.

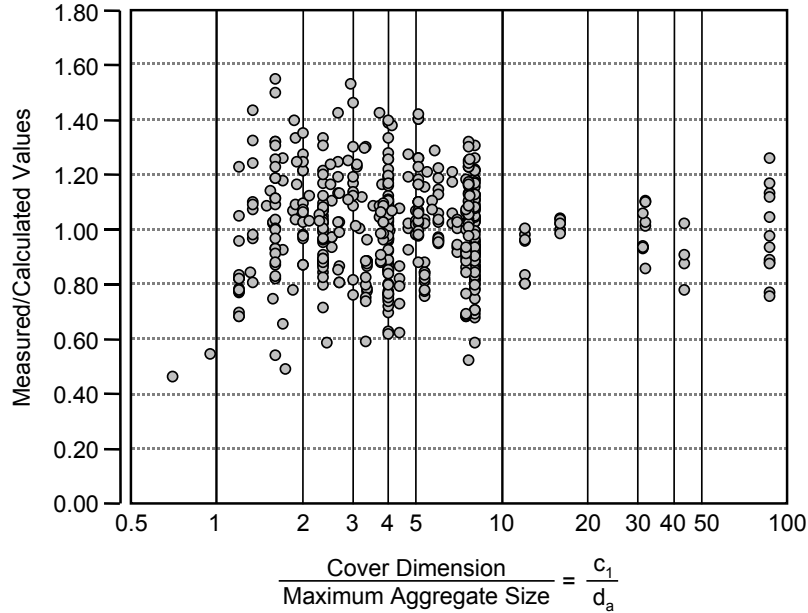


Figure 4-32: Size effect on capacity

Figure 4-32 shows that reductions in the aggregate size had no significant effect on capacity. The analysis plotted in Figure 4-32 used the cover as the critical dimension for analysis of size effect. The data were also analyzed using bearing plate dimensions (estimated by $\sqrt{A_{nh}}$) as the critical dimension. Again, no trend was found related to relative aggregate size. Niyogi [17] noted a size effect in his study, however, over the collected database, which includes test specimens cast and cured under a variety of environmental conditions, the scatter in the data is more significant than any trend that may exist related to size effect.

4.4.6 Regression Analysis of Proposed Models

The proceeding sections have been presented to justify the selection of variables chosen for the proposed models. Two models were proposed: Equation 4-1 and Equation 4-3. The first model contains a variable exponent for concrete strength. The second model uses a constant exponent of 1.0 for the concrete strength. Both models fit the data well, but the second was much simpler. Statistical analysis was performed for each model. The results of those analyses are presented in this section.

Table 4-7 presents the statistical information for the two models of bearing. The first model (Equation 4-1) performed better than the second (Equation 4-3) among each subgroup of the data (headed bars, anchor bolts, and bearing tests) and over the entire database. However, the difference was not great. Model 1 had an overall coefficient of variation of 17.5% and model 2 had an overall coefficient of variation of 19.6%. Model 1 provided a closer agreement between the mean values of the three test types than model 2 (0.95 – 1.03 versus 0.90 – 1.04). This indicates that model 1 does a slightly better job of representing each test type equally than model 2 does.

Figures 4-33 and 4-34 present the distributions of measured/calculated values for both models. Model 1 has a more normal distribution than model 2, which is slightly skewed towards low values. The plots also show that the distributions of the headed bars and anchor bolts line up better with the total distribution for model 1. It is evident that model 1 works better than model 2, however, model 2 uses a much simpler equation. A final recommendation must consider the performance of the model and the ease by which it can be used. Model 2 works reasonably and is much more simple than model 1 and is thus recommended.

Table 4-7: Statistical data for proposed models of bearing capacity

Model	Measured/Calculated Values			
	Range	Mean	Standard Deviation	Coefficient of Variation
# 1 (Equation 8-1)				
Headed Bars	0.49 - 1.46	0.95	0.17	18.1%
Anchor Bolts	0.59 - 1.40	0.98	0.20	20.2%
Bearing Blocks	0.46 - 1.55	1.03	0.17	16.5%
All Tests	0.46 - 1.55	1.00	0.18	17.5%
# 2 (Equation 8-3)				
Headed Bars	0.53 - 1.63	0.97	0.20	20.7%
Anchor Bolts	0.55 - 1.27	0.90	0.19	21.3%
Bearing Blocks	0.50 - 1.73	1.04	0.19	18.2%
All Tests	0.50 - 1.73	1.01	0.20	19.6%

$$P_{\text{Head}} = 2.6 A_{\text{nh}} \Psi \left(\frac{2c_1}{\sqrt{A_{\text{nh}}}} \right) \left(\frac{f'_c}{2.4} \right)^{0.5(1+\sqrt{A_{\text{nh}}}/2c_1)} \quad \text{with } \Psi = 0.7 + 0.3 \left(\frac{c_2}{c_1} \right) \leq 1.8$$

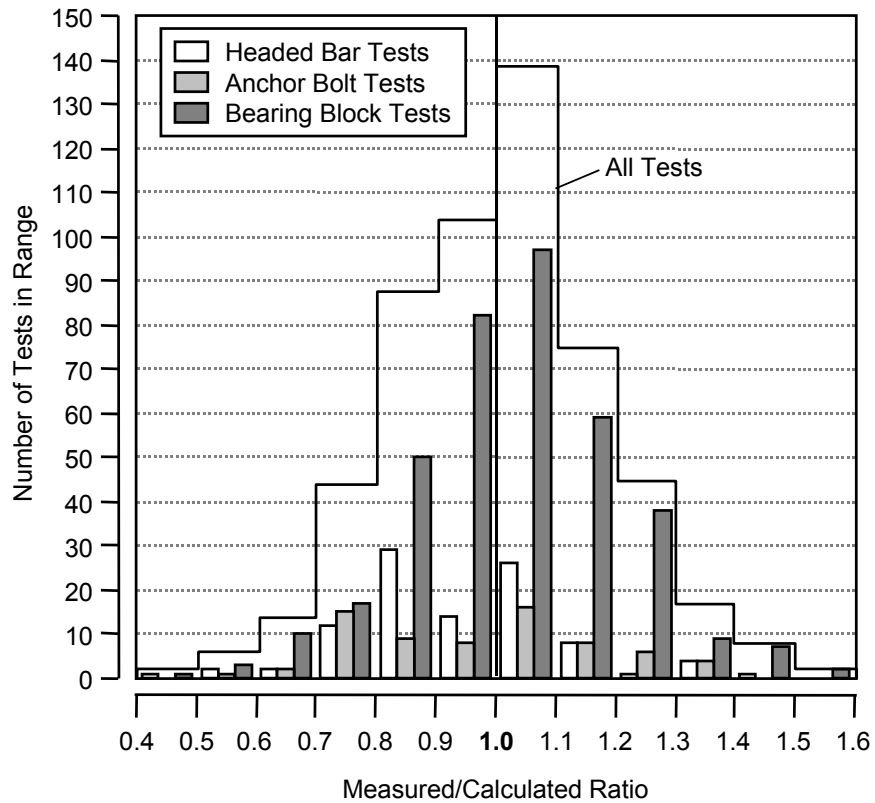


Figure 4-33: Distribution of measured/calculated values for bearing model 1

$$P_{\text{Head}} = 0.9 A_{\text{nh}} \Psi \left(\frac{2c_1}{\sqrt{A_{\text{nh}}}} \right) f'_c \quad \text{with } \Psi = 0.6 + 0.4 \left(\frac{c_2}{c_1} \right) \leq 2.0$$

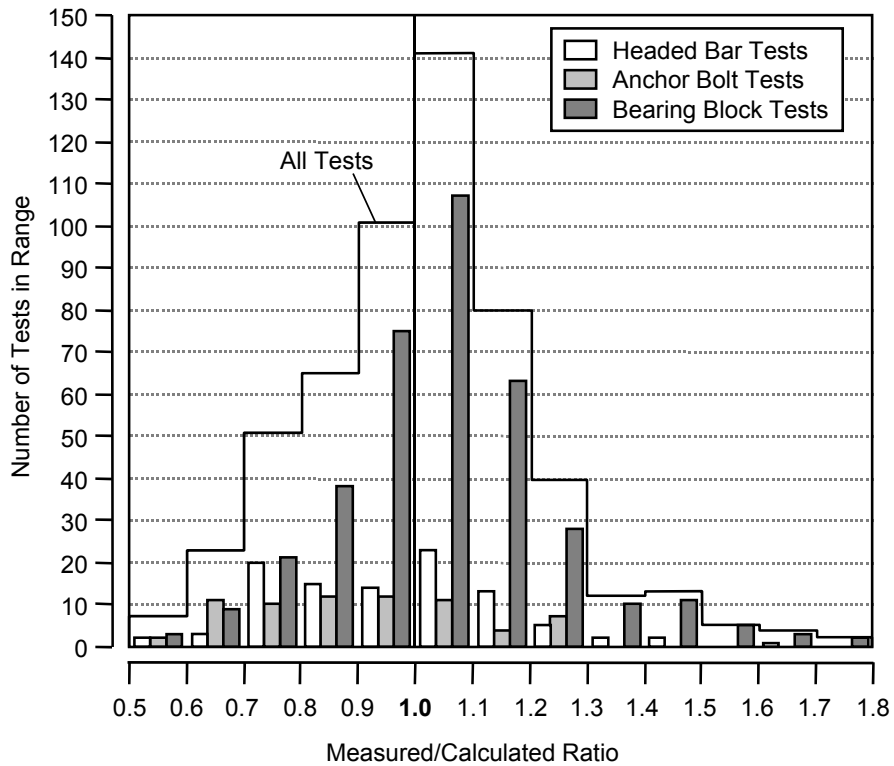


Figure 4-34: Distribution of measured/calculated values for bearing model 2

The preceding analysis has been based on mean capacity. An exclusion factor must be applied to provide a lower bound to the test results. A 5% exclusion was chosen as an acceptable lower bound. The probability of an unsafe test outcome is plotted against exclusion factor in Figure 4-35. The probability that an unsafe test would occur was determined by integrating the distribution plots in Figures 4-33 and 4-34 and plotting those results against the measured/calculated ratio. To produce a 5% exclusion of test results, models 1 and 2 require factors, $n_{5\%}$, of 0.72 and 0.68 respectively. A 5% exclusion factor of 0.7 would be appropriate for both models. In addition to the 5% exclusion factor, a strength reduction (ϕ) factor that accounts for potential understrength of materials and deviations from tolerable dimensions should also be applied. The recommendation of an acceptable ϕ factor is not made at this time.

Table 4-8 lists the ranges, averages, and standard deviations of the CCT node data under proposed model 1. The distribution of measured/calculated ratios for model 1 is plotted in Figure 4-36. The data show that the new model predicts capacity much better than the side blow-out and bearing models did. The average measured/calculated ratios are closer to 1.0 with less variation. The distribution of the data was more normal than the distribution was for the ACI bearing model.

Table 4-9 lists the ranges, averages, and standard deviations of the CCT node data under proposed model 2. The distribution of measured/calculated ratios for model 2 is plotted in 4-37. The data show that models 1 and 2 produced very similar results to one another. The mean of measured/calculated ratios was the same under each model. Model 2 had a slightly better coefficient of variation than model 1 for the CCT node data: 18.2% versus 18.6%. The distributions of the two models were similar in shape. Appendix B summarizes the statistical data for proposed models 1 and 2 for all of the test series listed in Table 4-5.

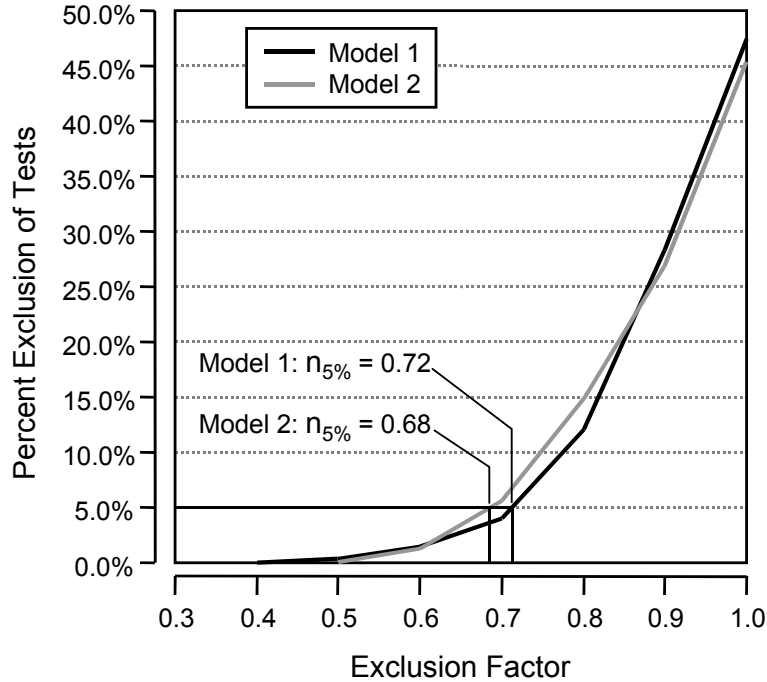


Figure 4-35: Probability of unsafe test outcome as a function of exclusion factor

Table 4-8: Statistical data for accuracy of model 1 (CCT node tests)

Bar Size	Number of Specimens	Measured/Calculated Values		
		Range	Mean	Standard Deviation
#8	8	0.63 - 1.39	0.93	0.19
#11	19	0.75 - 1.15	0.91	0.14
All	27	0.63 - 1.39	0.93	0.17

Table 4-9: Statistical data for accuracy of model 2 (CCT node tests)

Bar Size	Number of Specimens	Measured/Calculated Values		
		Range	Mean	Standard Deviation
#8	8	0.65 - 1.32	0.94	0.18
#11	19	0.74 - 1.15	0.90	0.14
All	27	0.65 - 1.32	0.93	0.17

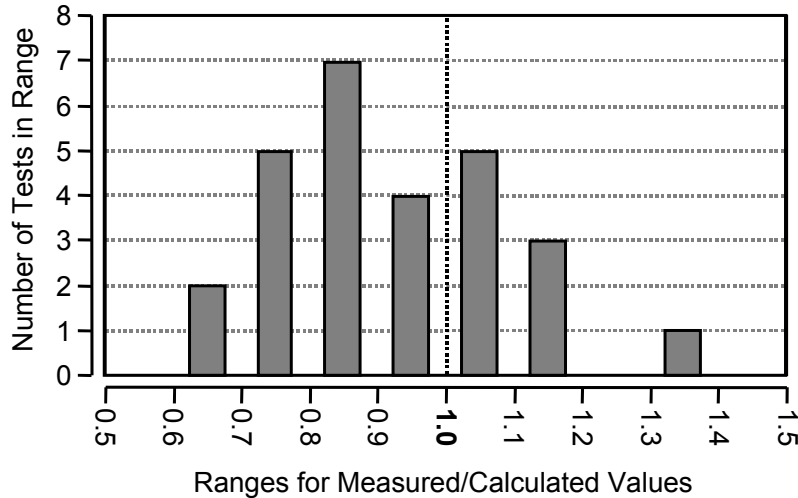


Figure 4-36: Distribution plot of measured/calculated ratios for model 1 (CCT node tests)

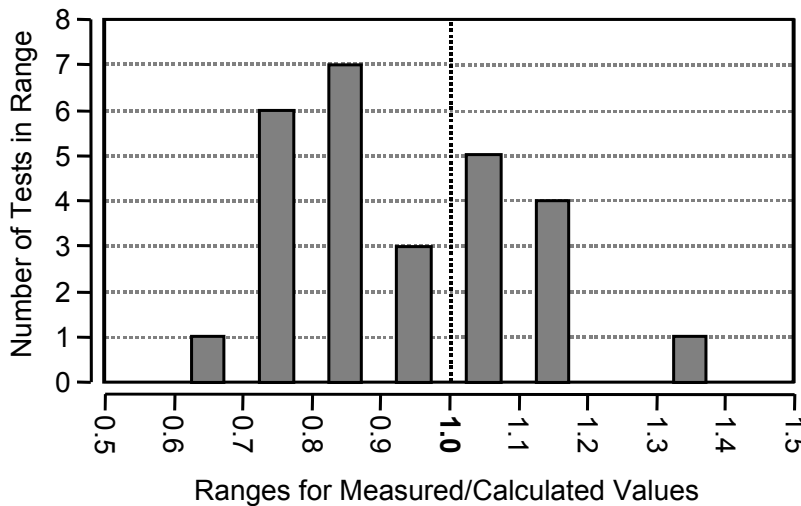


Figure 4-37: Distribution plot of measured/predicted ratios for model 2 (CCT node tests)

4.5 CONTRIBUTION FROM BOND

The development length equation from ACI 12.2.3 (equation 2-1 in Chapter 2 of CTR 1855-1 [19]) was used to calculate the contribution to anchorage from bond that would occur over the deformed bar length. Calculated bar stresses were then compared to the measured stress data collected from strain gages on the headed bars. The contribution to bar stress from bond was determined by the difference in strain readings between the strain gages at $1d_b$ (immediately behind the head) and $7d_b$ (approximately the location of maximum development for most of the CCT node test bars) along the length of the bar. The difference in bar stress over the $6d_b$ length was then used to determine average bond stress over that length. A total of 30 tests were used in the CCT node database for bond analysis.

Measured bond stress (normalized to a concrete strength of 4 ksi) at failure is plotted against relative head area in Figure 4-38. It is clear from the plot that the bond stress at failure decreased as the relative head

area was increased. As discussed in the last chapter (Section 3.1.2), development of the headed bars was a two stage process: bar force was first resisted by bond which would then break down allowing the head to carry a greater component of the bar force. Final capacity tended to consist of head bearing plus some residual bond resistance. Peak bond stresses occurred and then began to decrease before the maximum capacity of the tie bar was reached. The degree to which bond stress declined before failure of the specimen depended on the size of the head. A non-headed bar failed once bond stress reached its peak capacity. A bar with a small head would experience only a slight loss in bond before the head reached its ultimate capacity and failure occurred. A bar with a large head experienced a large loss of bond before the head achieved its peak capacity and failure occurred. This trend is demonstrated by the data in Figure 4-38. Bond stresses at failure decreased as the head size increased.

The bond stress determined by the ACI development length equation is also plotted in Figure 4-38. The calculated bond stress was determined by rearranging the ACI development length equation to determine bar stress, then converting that bar stress into bond stress:

$$u_{\text{bond}} = \frac{f_s A_b}{\pi d_b L_d} = \frac{40}{3} \cdot \frac{L_d}{d_b} \cdot \sqrt{f'_c} \cdot \left(\frac{c + K_{tr}}{d_b} \right) \cdot \frac{A_b}{\pi d_b L_d} \quad (4-7)$$

$$u_{\text{bond}} = \frac{10}{3} \cdot \sqrt{f'_c} \cdot \left(\frac{c + K_{tr}}{d_b} \right) \quad (4-8)$$

For the bond analysis of the CCT node specimens, $(c + K_{tr})/d_b$ was equal to its maximum limit, 2.5. Concrete strength was normalized to 4 ksi. Additionally, the calculated bond stress was divided by 0.9 to remove the built-in safety reduction factor from the ACI equation.

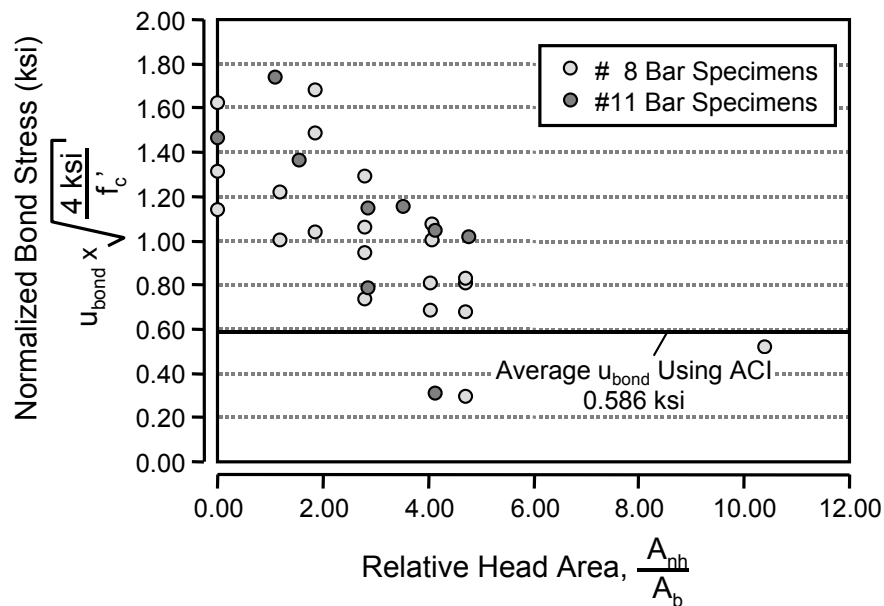


Figure 4-38: Measured failure bond stress versus relative head area

Figure 4-38 shows that most of the measured bond stresses were greater than the ACI calculated bond stress. The four non-headed bars had an average bond stress of about 1.4 ksi which is more than twice the calculated value. The high bond stresses may be due to the confinement provided by the reaction (vertical compression at the CCT node) or by lateral confinement from the bearing plate (friction force developed between the concrete and the rigid bearing plate). If the compression stress played a role in enhancing

bond, then differences should be seen between the specimens with different strut angles. The magnitude of the compression stress at the front support was a function of the strut angle of the CCT node configuration. Such a trend would be hard to discern from Figure 4-38 because the data in that figure are also affected by head size. In order to determine if compression at the support played a role in enhancing the bond stress, peak bond stresses were determined from each CCT node test. Rather than using the bond stress measured when the specimen achieved its ultimate capacity, the peak bond stress that occurred during the entire loading sequence was determined.

In Figure 4-39, peak measured bond stress is plotted against the support compression stress that was present at the time of the peak bond. Support compression stress was determined by the load cell measurement of the bearing reaction at the CCT node. The bearing reaction was simply divided by the area of the bearing plate to determine support compression stress at the node. Between compression stresses of $0.1f_c'$ and $0.7f_c'$, no clear trend is apparent in the data, and there is much scatter. All of the measured bond stresses were greater than the bond stress calculated using the ACI equation. However, the lack of a clear trend in the relationship between bond stress and support compression stress suggests that compression stress may not be the cause of the enhanced bond stress. Rather, the restraint provided by the rigid bearing plate may have a more significant effect on bond.

Two studies have proposed models for increases in bond stress with increasing lateral compression: Untrauer and Henry [22] and Thrö [21]. These models were applied to the ACI calculated bond stress to determine if they fit the data measured from the CCT node tests. They are plotted in Figure 4-39. The Thrö model fits the data better than the Untrauer and Henry model, however, the data are so scattered, that no definite conclusion of behavior can be asserted.

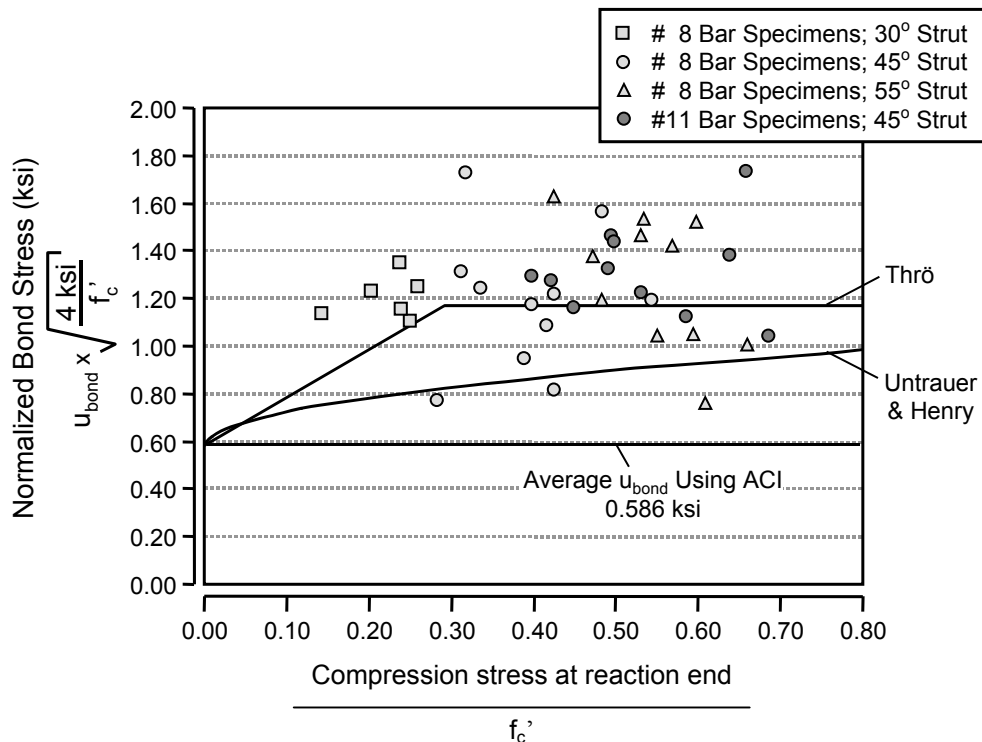


Figure 4-39: Measured peak bond stress versus vertical compression stress

In Figure 4-40, peak bond stress is plotted against relative head area. The peak bond stresses are much more constant than the failure bond stresses, but there still seemed to be a trend of decreasing capacity

with increasing head size. This trend may be due to changes in the relative anchorage stiffness between the head and the deformed bar as the head size become larger. Larger head sizes experienced less slip than did the smaller head sizes. This increase in the stiffness of the end anchorage of the bar may have prevented optimum bond from occurring. As the head became larger, it becomes a stiffer component of the bar anchorage, thus attracting more of the anchorage force, possibly away from the bond. This would account for the decrease in peak bond stress as the relative head area was increased.

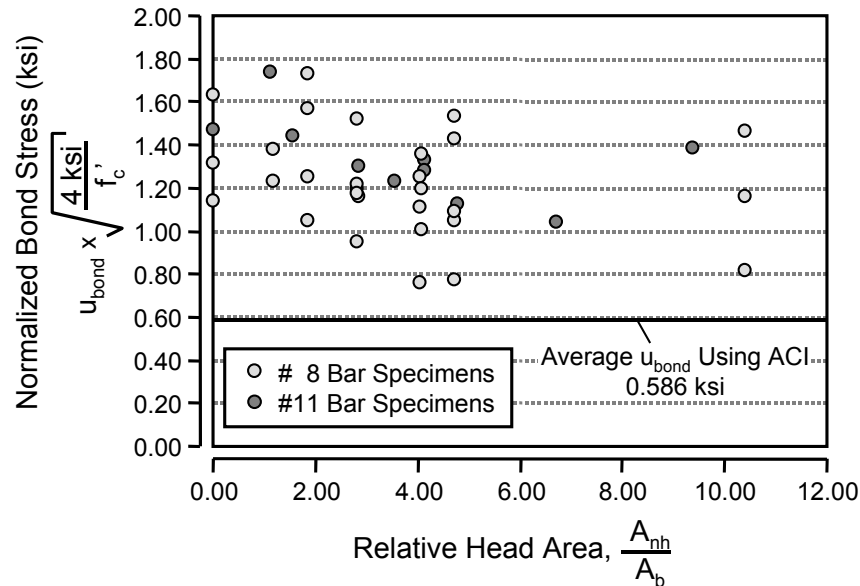


Figure 4-40: Measured peak bond stress versus relative head area

Statistical analysis was performed of the failure bond and the peak bond stresses. Tables 4-10 and 4-11 present the statistical data for the sets of peak and failure data. Figures 4-41 and 4-42 present the distributions of measured/calculated values. The ACI bond stress equation was very poor for calculating the failure bond stress, though it was conservative for most tests. The ACI equation was even more conservative for peak bond. The average peak bond was nearly twice the predicted bond stress. The vertical compression model proposed by Thrö would account for the high peak bond values. However, the effect could also be due to platen restraint. Furthermore, it is the bond at failure that matters, not the peak bond. The bond at failure is the product of two effects. First, it is increased by the compression stresses at the support bearing plate and/or restraint (through friction between the concrete and bearing plate resisting lateral expansion) of the CCT node. Second, it is diminished by the nature of the anchorage failure, which necessitates that bond deteriorates before bar force can be transferred to the head. These two actions counter each other and the final bond that results does not fit the existing models of bond stress.

Table 4-10: Statistical data for accuracy of ACI bond equation in predicting the failure bond

Bar Size	Number of Specimens	Measured/Calculated Values		
		Range	Mean	Standard Deviation
#8	9	0.50 - 2.86	1.72	0.55
#11	21	0.38 - 2.11	1.35	0.47
All	30	0.38 - 2.86	1.61	0.58

Table 4-11: Statistical data for accuracy of ACI bond equation in predicting the peak bond

Bar Size	Number of Specimens	Measured/Calculated Values		
		Range	Mean	Standard Deviation
#8	11	1.27 - 2.11	1.60	0.23
#11	28	1.30 - 2.94	2.08	0.43
All	39	1.27 - 2.94	1.95	0.44

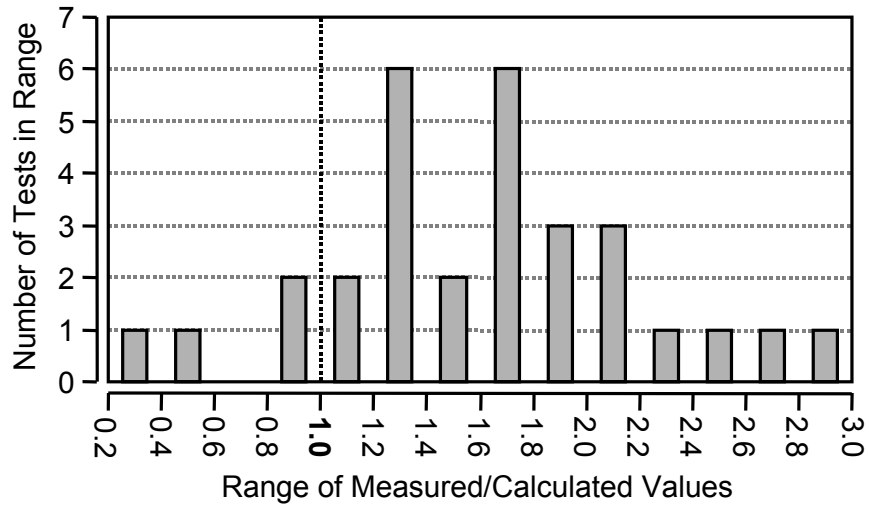


Figure 4-41: Distribution plot of measured/calculated ratios for failure bond

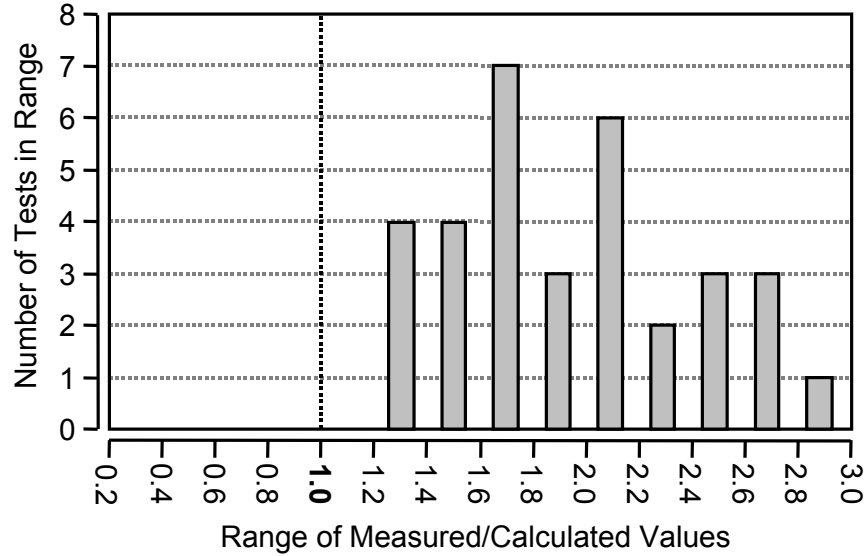


Figure 4-42: Distribution plot of measured/calculated ratios for peak bond

4.6 SUMMARY

Headed bar anchorage is achieved through contributions from bond and bearing on the head. These behavior of these two components are not independent of each other (head capacity affects the magnitude of bond stress at failure). However, the capacities provided by each can be determined separately and added to find the total anchorage capacity. The data for these two components from the CCT node tests were analyzed separately in this chapter. The combination of these two components is dealt with in CTR 1855-3 "The Anchorage Behavior of Headed Reinforcement in Lap Splices" [20].

Two models for the capacity of head bearing were recommended. These models were shown to adequately model the behavior of the measured head capacities from the CCT node tests as well a variety of additional headed bar tests, anchor bolt tests, and bearing plate tests on concrete blocks. The following model was recommended:

$$\text{Bearing Capacity, } P = A_{nh} \left(0.9\Psi \left(\frac{2c_1}{\sqrt{A_{nh}}} \right) (f'_c) \right) \quad (4-9)$$

$$\text{with } \Psi = 0.6 + 0.4 \frac{c_2}{c_1} \leq 2.0 \quad (4-10)$$

P = head capacity (kips)

Ψ = radial disturbance factor

A_{nh} = net head area (in²)

c_1 = minimum cover dimension (in)

c_2 = secondary cover dimension (the smallest cover dimension measured perpendicular to the minimum cover) (in)

f'_c = concrete cylinder strength (ksi)

The ACI model for bond stress was examined as a possible candidate for the bond data measured from the CCT node tests. This model was found to provide very poor, though conservative results. Bond stress at

failure was influenced by compression and/or restraint of the CCT node produced by the support bearing plate and the breakdown in bond that occurs as bar stress is transferred to the head. These two influences greatly affected the bond behavior and prevented the ACI model from working. This model must be modified in order to work under the conditions of CCT node confinement and the effect of head bearing.

Additionally, the following observations were noted:

- Bearing pressure at the head increased linearly with increases in the ratio $2c_1/\sqrt{A_{nh}}$. There was no limit to the increase in head capacity up to $2c_1/\sqrt{A_{nh}} = 10$, the upper limit of available test data. This limit is 5 times the current ACI limit of 2.
- Head capacity increased linearly with increases in the ratio c_2/c_1 with an upper limit on the c_2/c_1 ratio between 3 and 4.
- Head capacity increased with increasing concrete strength. The order of the relationship seemed to be variable with exponents between 0.5 and 1.0. The value of this exponent was inversely proportional to the $2c_1/\sqrt{A_{nh}}$ ratio. The exponent was 1.0 when $2c_1/\sqrt{A_{nh}}$ equaled 1.0 and dropped off to 0.5 as $2c_1/\sqrt{A_{nh}}$ approached infinity. However, a reasonable model of head capacity could be achieved using a single exponent of 1.0 for the concrete strength.
- The peak bond stress achieved by the headed bars averaged twice the ACI predicted bond stress most likely due to the active confinement provided by vertical compression and/or platen restraint in the CCT node. This increase was best modeled by the recommendations of Thrö [21]. However, the peak bond stress was not as important to capacity as the bond stress at failure.
- There was some indication that peak bond stress was affected by the head size and decreased slightly as the relative head area became larger.
- The bond stress at failure was less than or equal to the peak bond stress. The failure bond stress was equal to peak bond stress for non-headed bars but decreased as the head size became larger.
- Final anchorage was achieved by a combination of peak head capacity and diminished bond capacity.
- In the CCT nodes, head orientation had a small effect on capacity. Optimal head performance in these tests was developed when the head was oriented such that the long axis was normal to the plane in which the strut-and-tie model is represented. For all other tests, the head capacity was not significantly affected up to an aspect ratio of 3. Within this limit, the decrease in capacity fell within the limits of scatter.
- Decreases in strut angle resulted in a longer development length for the bar. The longer development length provided a greater contribution from bond and allowed for smaller head sizes to achieve yield.
- Limited test data showed that confinement in the form of stirrups did not improve the capacity of the head. However, stirrup confinement did change the behavior of the strut-and-tie model allowing for a longer development length, thus enhancing the total anchorage capacity of the bar.

A summary of all CCT node test results is provided in Appendix C.

CHAPTER 5: SUMMARY AND CONCLUSIONS

5.1 SUMMARY

A test program was conducted to study the anchorage behavior of headed bars in CCT nodes. The goal of the testing was to determine the viability of headed bars to shorten development lengths and alleviate congestion in complex structural details. The CCT node specimen was selected to simulate a commonly occurring anchorage situation where development length and congestion are important factors.

Sixty-four CCT node specimens were tested. The nodes in the specimens were anchored by a single tie bar (Figure 5-1). The variables in the study were: anchorage type (straight, headed, or hooked bar), relative head area ($A_{nh}/A_b = 0.0$ to 10.4), strut angle ($\theta_{strut} = 30^\circ, 45^\circ, \text{ or } 55^\circ$), tie bar size (#8 or #11), and the level of confinement (none or #3 closed hoop stirrups placed at 6" or 3"). Specimens were instrumented to measure the bearing reaction at the CCT node, strain along the anchorage portion of the tie bar, and head slip. The cracking behavior was also observed and recorded.

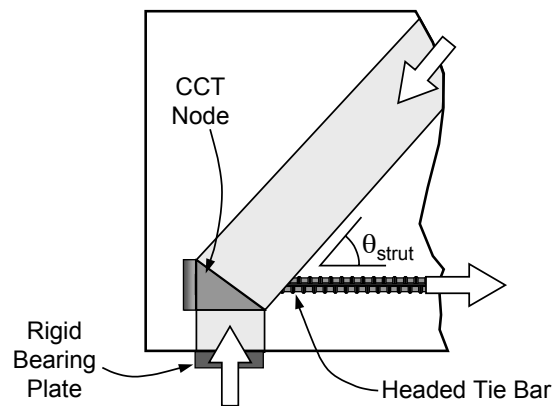


Figure 5-1: Typical CCT node from the test program

5.2 CONCLUSIONS

The conclusions from the CCT node tests are divided into two categories: behavior of headed bars and behavior of CCT nodes.

5.2.1 Anchorage Behavior of Headed Reinforcement

The following conclusions about headed bars were drawn from the CCT node tests:

- **The anchorage process of headed bars consists of two stages.** In the first stage, anchorage was carried almost entirely by bond stress, which peaks as the first stage ends. In the second stage, the bond began to deteriorate allowing bar stress to be transferred to the head. Throughout the second stage, bond declined and head bearing increased. The second stage ended with yield of the bar or bearing failure of the concrete at the head. As a result of this behavior, peak bond and peak head bearing did not occur simultaneously. The capacity of the bar at failure was determined by the peak bearing capacity plus some contribution from reduced bond along the bar between the head and the point of peak bar stress.
- **The bearing capacity of the heads** was similar to the side blow-out capacity of deeply embedded anchor bolts and the bearing capacity of rigid plates on concrete. The bearing behavior

of these three elements (headed bars, anchor bolts, and bearing plates) can be treated similarly in analysis. A formula was developed to determine the bearing capacity of rigid heads and plates which is dependent on four variables: the net bearing area (A_{nh}), the cover dimensions (c_1 and c_2), and the concrete cylinder strength (f_c'). The equations for calculating nominal bearing capacity for a rigid head are reproduced below:

$$\text{Nominal Bearing Capacity (kips)} = \phi \cdot n_{5\%}(A_{nh}) \cdot \left(\frac{2c_1}{\sqrt{A_{nh}}} \right) \cdot \Psi \cdot f_c' \quad (12-1)$$

$$\Psi = 0.6 + 0.4 \left(\frac{c_2}{c_1} \right) \leq 2.0 \quad (12-2)$$

A_{nh} = net bearing area of the head (in²)

c_1 = minimum cover dimension over the bar (in)

c_2 = minimum cover dimension over the bar measured orthogonal to c_1 (in)

f_c' = concrete cylinder strength (ksi)

ϕ = resistance factor, unknown at this time

$n_{5\%}$ = 5% exclusion factor, 0.7

Ψ = radial disturbance factor (a function of the cover dimensions)

This model was used to compute capacities obtained from bearing, anchor bolt, and headed bar studies. The average calculated strength (omitting $n_{5\%}$) was equal to the average measured strength with a coefficient of variation of 20%. The exclusion factor is a statistical factor that corrects for the fact that the above equation was derived to correspond to mean behavior rather than lower bound behavior (see Section 4.4.6 for more information).

- **The failure bond stress can be directly related to head size.** The larger the relative size of the head, the smaller the bond stress sustained at failure.
- **The bearing capacity of the head was not significantly improved by confinement in the form of hoop stirrups.** Previous studies have shown that it is very difficult to improve the anchorage of a headed bar with confining steel. It is far more economical to improve the bearing capacity by simply increasing the size of the head.
- **Confinement appeared to help sustain bond stresses** during the second stage of headed bar anchorage when bar stress is transferred to the head. The effect of confinement on the bond stress of headed bars requires further study.
- **Slip of the head** was decreased as head size was increased for a given anchorage length. Slip occurred in two stages: insignificant head slip occurred before the head attained most of its capacity. Once the capacity in bearing was reached, slip initiated and the head provided little resistance to movement with failure occurring quickly thereafter.
- **Head shape and aspect ratio** had no significant effect on capacity. Because head orientation cannot be controlled under field conditions, circular heads provide the most reliable means of avoiding violation of cover requirements due to fabrication and placement of reinforcement and assembled bars. Ideally, the choice of head shape should be based on detailing considerations such as clearance and congestion.
- **Headed bars provide a feasible substitute for hooks.** Headed bars can achieve equal or superior performance to comparable hooked bars depending on head size.

5.2.2 CCT Node Behavior

The following conclusions about the behavior of CCT nodes were drawn from the data collected in the study:

- **CCT nodes failed by mechanisms related to anchorage.** Non-headed bars failed by pullout from the node. Headed bars failed when bearing stress at the head exceeded the bearing capacity of the concrete. Failure of a CCT node anchored by a headed bar was explosive, resulting in rupture of the node and struts. Rupture was characterized by crushing just above the head and lateral splitting of the diagonal strut. The extent to which these two characteristics occur depends on head size and orientation.
- **The development of the truss mechanism is a staged process.** The strut-and-tie mechanism has a preference to transfer force along the most direct path between loads or reactions. In a D-region with stirrups or other reinforcement capable of acting as tension ties, force is initially transferred along a straight path from the point of load application to the CCT node. Only after extensive cracking and softening of the primary strut, are stirrups utilized to form secondary strut paths. The formation of secondary strut paths may not occur until after the peak capacity of the member has been reached.
- **The critical development point** of the tie bar in a CCT node can be estimated as the intersection of the tie bar and the edge of the diagonal compression strut that is anchored by that tie bar (Figure 5-2).

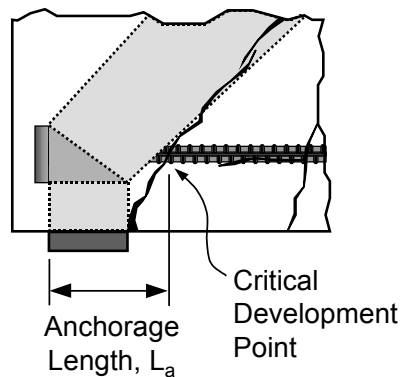


Figure 5-2: Critical development point for a CCT node

- **The state of stress at a CCT node** reversed on either side of the critical crack. Beneath the CCT node, compression stresses from the lower bearing plate necked inward to equilibrate spatially with the bearing face of the headed bar. This created a region of vertical and transverse compression. This region began at the bearing face of the head and extended to the surface of the critical diagonal crack where development of the bar began. On the other side of the crack, radial splitting stresses created by bond of the reinforcing bar caused a state of tension within the concrete (Figure 5-3).

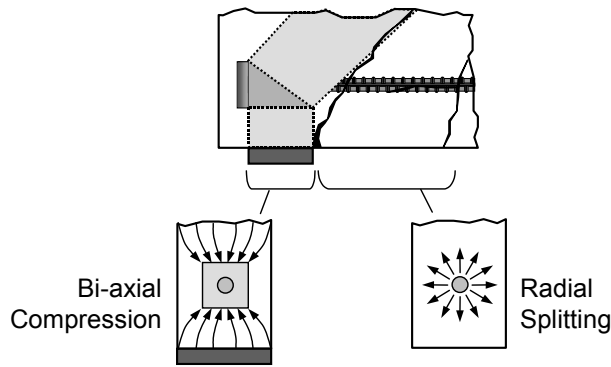


Figure 5-3: The state of stress at the CCT node

- **Bond stress within a CCT node** was significantly improved by lateral compression and platen restraint. Lateral compression is the bearing stress on the platen/reaction area. Platen restraint is the confinement provided by the platen/reaction to expansion of the concrete parallel to the plane of bearing surface. If a bearing material such as neoprene is used, lateral compression will be provided but platen restraint may be reduced considerably. Lateral compression and platen restraint both provided compression stress perpendicular to the axis of the reinforcing bar. Such compression tended to counteract splitting stress from bond. In the current study and in tests reported in the literature, little change in bond stress has been observed with changes in lateral compression, which tends to indicate that lateral compression was not as influential as platen restraint. Platen restraint may provide significant increases in bond stress and should be a subject for future study.
- **The anchorage length in the CCT node zone can be increased by confinement.** Changes in the strut-and-tie mechanism (provided by adding vertical stirrups) allowed the critical development point of the headed bar to move away from the primary CCT node. Due to the increases in anchorage length, bond stress acted over a longer portion of the bar, increasing the total anchorage capacity.
- **Variations in strut angle** did not affect the bearing capacity of the head or the bond stress developed by the bar. However, strut angle did affect the anchorage length of the bar. Shallow strut angles allowed a longer length of bar to be included within the bounds of the diagonal strut, moving the critical development point away from the head and increasing anchorage length. The increase in the anchorage length of the tie bar resulted in higher anchorage capacity for the tie. However, decreases in strut angle also made the tie much less efficient at resisting the loads placed on the specimen.
- **CCT nodes anchored by bars with 180° hooks** are taller than analogous nodes anchored by headed or non-headed bars if the height of the node is increased to the full height of the hook. However, in the tests, the centroid where the strut and tie forces intersect seemed to occur just inside the bend of the hook. Hooked bar anchorages failed by splitting the node and struts along the plane corresponding to the plane of the hooked bar.
- **The dimensions of CCT and CCC nodes** were much smaller than the dimensions suggested in the ACI and AASHTO code provisions [1, 2] for all the configurations tested — headed, non-headed, or hooked. Furthermore, the stresses sustained by these nodes were much higher than the stresses allowed under the current code provisions. The ultimate strength of nodes may be completely controlled by anchorage considerations. The allowable stress requirements for nodes and struts require further experimental investigation.
- **The philosophy of the current code provisions** for determining the capacity of CCT nodes may require reconsideration. The evidence from the tests shows that the failure of these nodes was primarily related to anchorage and that the current stress limits for nodes were unrealistic. It is possible that CCT nodes cannot fail in compression if anchorage of the tie bars is sufficient. The stress limits imposed by the code provisions may be unnecessary.

APPENDIX A: INSTRUMENTATION AND MECHANICAL PROPERTIES OF REINFORCING BARS

Tensile and flexural properties were measured for the different stocks of deformed bars used in the research. Much of the data for the performance of the headed bars were determined from strain gages placed on the surface of the deformed bars. Because this type of instrumentation was so pervasive in the research, it is important to discuss it in detail. Mechanical property tests of bar samples were always calibrated with regard to strain gage measurements.

A.1 INSTRUMENTATION OF REINFORCING BARS

Reinforcing bars were instrumented by adhering foil strain gages to the surface of the bars. The strain gages were used to determine strain data for the bars and thus calculate stress and force values for the bars. Gages placed on the surface of the bars interfere with bond by covering the ribs of the deformed bar. In order to reduce any such effect, gages were placed over the main ribs of the bar (Figure A-1). Since the main rib already interferes with direct bearing on the transverse ribs, it was reasoned that placement there would produce the least interference from the gages.

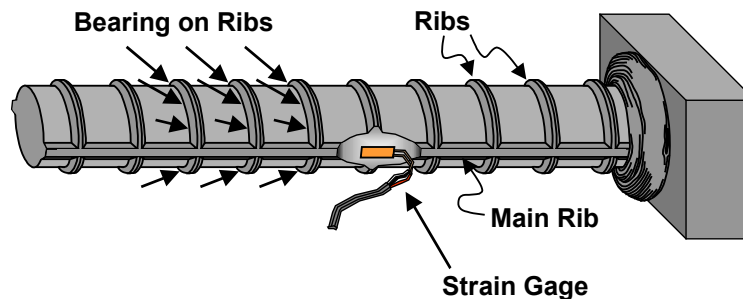


Figure A-1: Placement of strain gage on main rib of bar

Figure A-2 shows photos of a bar in the progress of being instrumented. First, a section of the main rib is ground down to a flat, level surface. This grinding was done with a hand-held grinder. Because the grinding was done by hand, the surface the gage was adhered to was not always precisely machined. Some misalignment and non-flatness could occur for each gage. This imprecision causes the gage data to have some error that will be discussed in the next section. Once the surface was cleaned, electronic foil gages were then adhered to the bar as per the instructions provided by the manufacturer (All of the gages used in the project were purchased from Measurements Group, Inc.). Once the gages had been attached and soldered to insulated three-wire leads, the gage was covered by a quick setting epoxy. The epoxy coating provided a hard, waterproof armor for the gage that protected it during the casting process.

Two different gage sizes were used. A $\frac{1}{8}$ " gage length was used for bars #4 and smaller (Measurements Group product EA-06-125BT-120). A $\frac{1}{4}$ " gage length was used for bars #8 and larger (Measurements Group product EA-06-250BG-120).

A.2 TENSILE PROPERTIES

The instrumentation placed on the tie bars used in the test specimens provides data on strain values only. In order to convert the strain data into the more useful stress and force equivalents, one must have previously measured several mechanical properties of the bars: the area (A) and first moment of inertia (I) properties of the bar cross-section and the modulus of elasticity of the steel (E). Pure tension tests of instrumented bar specimens were designed to provide values for the product AE.

- i. A flat smooth surface is ground onto the main rib of the rebar.



- ii. Electronic foil strain gages are adhered to the ground surfaces.



- iii. Insulated 3-wire leads are soldered onto the strain gages (covered by a white water-proof acrylic lacquer in this photo).



- iv. A clear epoxy coating is placed over the gages and the leads to protect them during the casting process.



Figure A-2: Steps in the bar instrumentation process

Short lengths of sample bars were instrumented with strain gages and pulled in tension in a universal load machine. Data from the gages provided information on the bar strain (ϵ). Data from the load machine provided information on the tensile force in the bar (F_{bar}). The two values are related by Hook's Law:

$$\sigma = \epsilon \cdot E \quad (\text{A-1})$$

$$F_{\text{bar}}/A = \epsilon \cdot E \quad (\text{A-2})$$

$$F_{\text{bar}}/\epsilon = AE \quad (\text{A-3})$$

These tests also provided values for the yield stress (f_y) of the bars.

Figure A-3 shows the typical layout of a tensile test specimen for a larger bar size. Between 3 to 6 strain gages were placed on each tensile specimen. No two gages will provide the exact same reading, therefore multiple gages were used on multiple bar samples to provide values for the mean bar stiffness (AE) and the standard distribution (σ). Samples of $3/16$ " diameter plain round bar and #2, #3, #4, #5, #8, and #11 deformed bar sizes were tested. Bars used in the project came from a variety of suppliers. At least one bar sample was tested for each supplier.

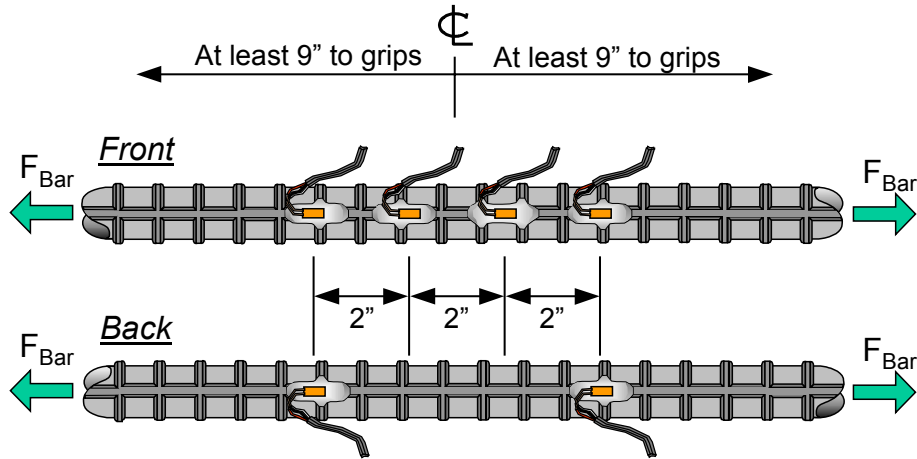


Figure A-3: Layout of strain gages for #8 and #11 tensile specimens

Figure A-4 shows typical from a tensile bar test. The data come from a #8 bar provided by ERICO. The top plot shows the force-strain relationship measured during the test. The bottom plot shows the slopes calculated from the data in the top plot. A range of slope points from $400\mu\epsilon$ to $1900\mu\epsilon$ was averaged to determine the stiffness associated with each gage.

The individual gage stiffnesses from all of the bars of the same size from a given supplier were averaged to determine the mean stiffness for that bar group. The data range of stiffnesses for each group was also analyzed to determine standard deviations. The standard deviation was calculated using the following formula:

$$\text{Mean Stiffness, } \overline{AE} = \frac{1}{n} \sum_{i=1}^n (AE)_i \quad (\text{A-4})$$

$$\text{Gage Variance, } \text{Var}_i = \left(\overline{AE} - (AE)_i \right)^2 \quad (\text{A-5})$$

$$\text{Standard Deviation, } \sigma = \sqrt{\frac{1}{n-1} \sum_{i=1}^n \text{Var}_i} \quad (\text{A-6})$$

n = number of working strain gages for a group

$(AE)_i$ = stiffness value for a given gage i

Note that a denominator of $n-1$ is used in equation (A-6) rather than n . The subtraction of one from the number of samples acts as a penalty for smaller sample sizes.

Table A-1 summarizes the stiffness values and standard deviations for all bar groups. Bar groups are sorted by bar size and supplier. Standard deviations are also expressed as percentages for each group. The bar group with the best (in this case smallest) standard deviation was the $3/16$ " diameter plain wire. This is

most likely due to the fact that no grinding was required to prepare the bar surface for gage installation. Only a light sanding was needed to prepare the surface for epoxy adherence to the metal. The uniformity of the manufacture of the plain wire bars was very good. The worst standard deviations are found in the #8 bar groups. Most of the #8 bars were tested early in the research when that bar size was the predominant one used in specimens. At that time, the skill of the researchers in placing the gages on the bars was not that good. Later tests of #5 and #11 bars showed improvement of gaging skills. A good indication of the improvement of the researchers' skills in placing gages is demonstrated by comparing two #8 bar groups: ERICO⁽¹⁾ and ERICO⁽²⁾. There are two #8 ERICO groups because the limited supply of #8 bars from ERICO was depleted and additional bars were ordered. Two samples were taken from each shipment of bars. Samples from the first shipment were tested from 2/10/2000 to 2/11/2000 along with most of the other #8 bars. Samples from the second shipment were tested on 2/27/2001, one year later. After a year of practice, the standard deviation of 10 gages placed by the researchers dropped from 10.6% to 3.4%, a significant improvement. Some of the groups have large standard deviations because of the imposed penalty for small sample sizes.

Histograms of the stiffness data ranges for each bar size are presented in Figures A-5 through A-11. The histograms are presented as indications of the normalness of each distribution of bar group data. They also give a graphical indication of the scatter.

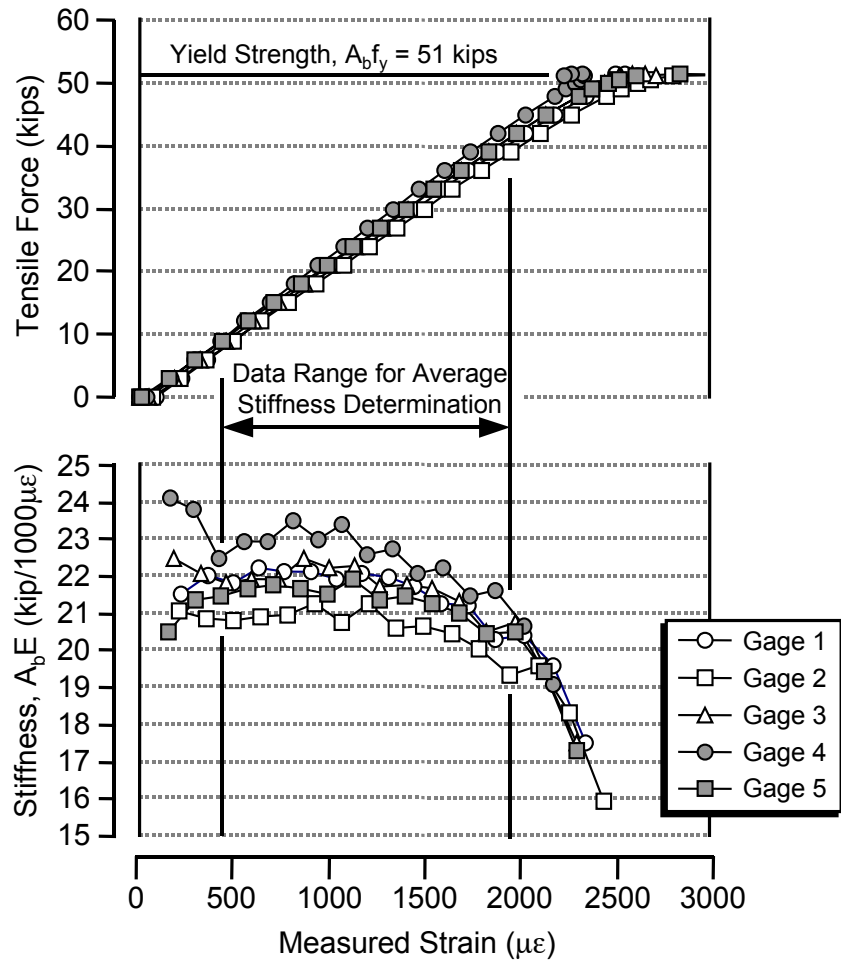


Figure A-4: Typical load-strain data from a tensile test (# 8 ERICO⁽²⁾ bar group)

Table A-1: Stiffness, A_bE , and yield stress, f_y , for all specimen bar sizes

	Bar Size	Supplier	Number of Bars Sampled	Total Working Gages	Mean Bar Stiffness $A_{bar}E_s (\pm \sigma)$ (kip/1000 $\mu\epsilon$)	$\frac{\sigma}{AE}$ (%)	Yield Stress (ksi)
Confinement Bars	Plain Wire ($\frac{3}{16}$ " ϕ)	L. Stock*	4	16	0.831 ± 0.007	0.9%	82
	# 2	Mexican†	4	12	1.13 ± 0.10	8.4%	80
	# 3	A.I.W.‡	3	8	2.61 ± 0.21	7.9%	63
	# 4	A.I.W.‡	3	9	4.88 ± 0.26	5.4%	60
Headed Bar Samples	# 5	HRC	4	16	7.46 ± 0.44	5.9%	60
		ERICO	3	12	7.50 ± 0.31	4.2%	74
	# 8	HRC	4	17	21.3 ± 1.8	8.4%	68
		ERICO ⁽¹⁾	2	10	19.9 ± 2.1	10.6%	61
		ERICO ⁽²⁾	2	10	21.3 ± 0.7	3.4%	65
		All ERICO	4	20	20.6 ± 1.7	8.2%	-
		A.I.W.‡	1	4	21.6 ± 2.4	11.0%	68
		All Bars	9	41	21.0 ± 1.8	8.5%	-
	# 11	HRC	4	19	39.1 ± 2.6	6.6%	63
		ERICO	2	11	42.3 ± 2.3	5.5%	67

* Lab Stock

† Lab Stock, Mexican Supplier

‡ Alamo Iron Works

(Standard Hook sample for # 8's)

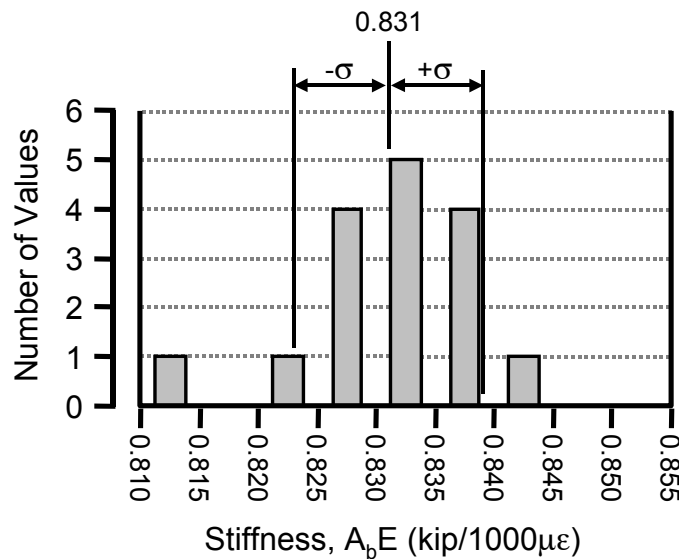


Figure A-5: Histogram of $\frac{3}{16}$ " diameter plain wire tensile test data

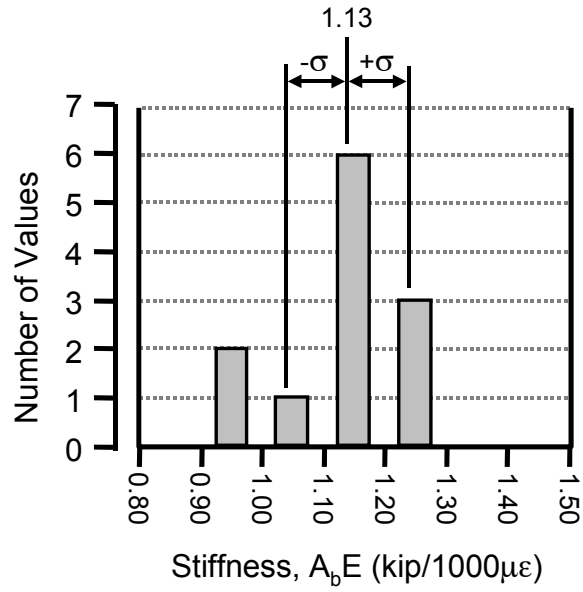


Figure A-6: Histogram of # 2 bar tensile test data

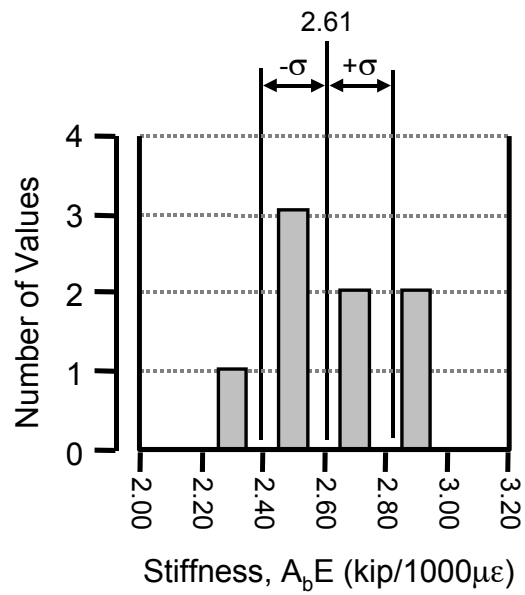


Figure A-7: Histogram of # 3 bar tensile test data

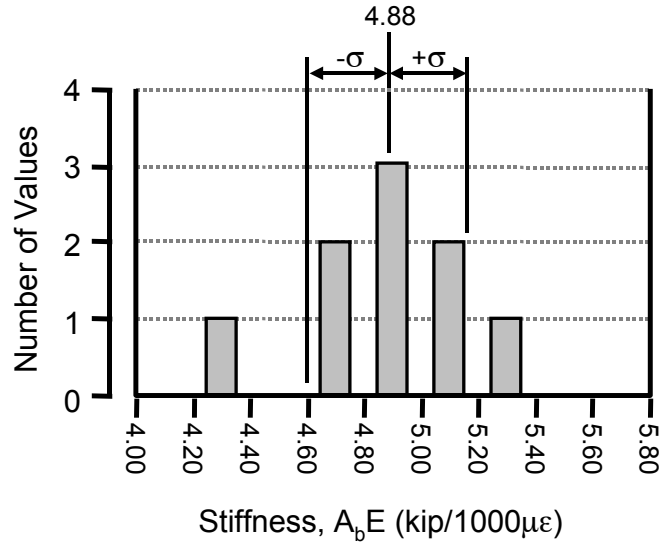


Figure A-8: Histogram of # 4 bar tensile test data

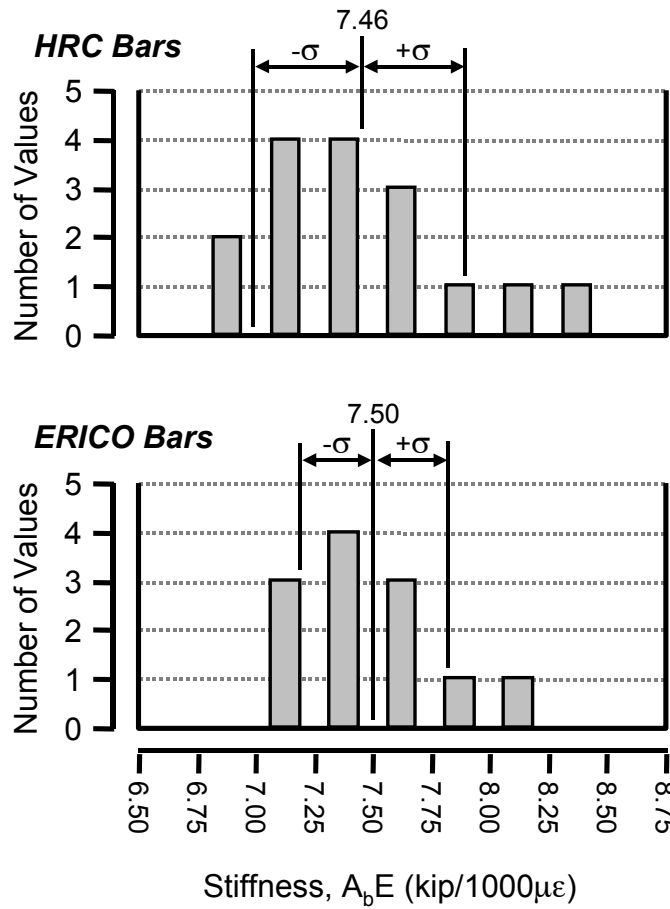
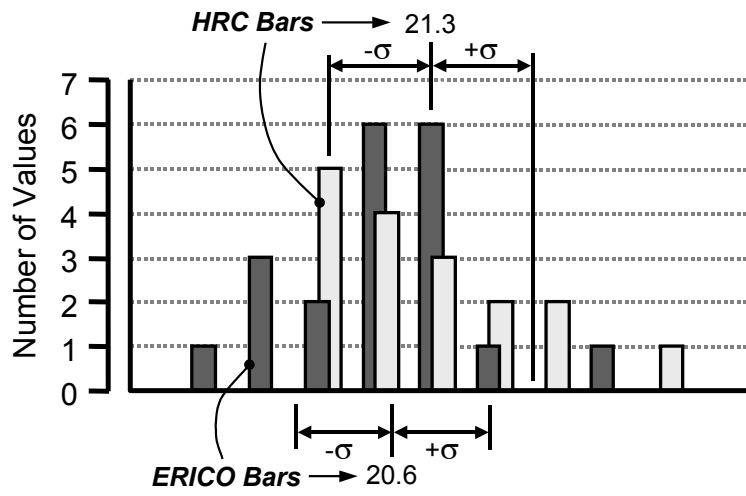


Figure A-9: Histogram of # 5 bar tensile test data

HRC & ERICO Bars



All # 8 Bars

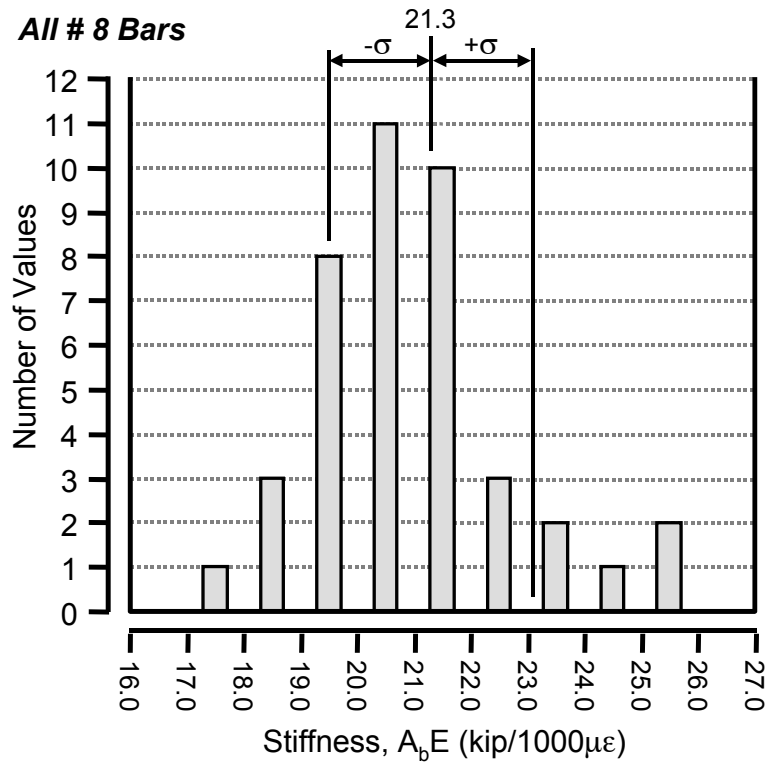


Figure A-10: Histogram of # 8 bar tensile test data

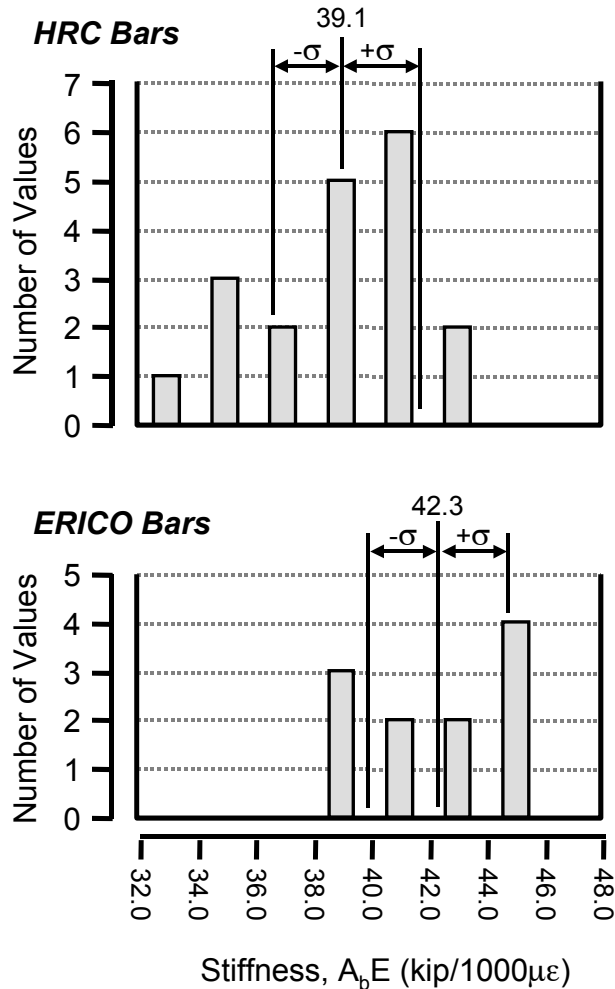


Figure A-11: Histogram of # 11 bar tensile test data

A.3 FLEXURAL PROPERTIES

The data from the bending tests were necessary in analyzing the information gathered from CCT node tests where kinking forces produced large bending strains in the specimen bars. The tensile tests of the bars provided values only for the axial stiffness of the bars. For complete analysis of the data measured in the test specimens, information was also need on the flexural stiffness properties of the bars. Bending tests of #8 and #11 bar samples were performed to measure the flexural stiffness values, IE/t , of the various bar groups in those size ranges. Figure A-12 shows the basic configuration of a bending test for bar samples. The moment was calculated from the load placed on the bar multiplied by the shear span. Strain was measured by two strain gages placed in the constant moment region at the midspan of the bar specimen: one on the compression side of the bar, the other on the tension side.

Once specimens were tested, the data were plotted and the flexural stiffness of each gage was determined. Figure A-13 shows data from a typical test. Once a strain of about $2400\mu\epsilon$ was reached, the outer fibers began to yield and the stiffness of the bar dropped towards zero. Flexural stiffness values were determined by averaging over a range from $400\mu\epsilon$ to $2400\mu\epsilon$.

Data from tensile and bending tests were used to determine the physical properties for the bars that could be used to analyze strain data for elastic and plastic behavior. The bar is assumed to have a circular cross-

section and the stress-moment relationship is used to determine the radius of the bar from the axial and flexural stiffness values derived in the bar tests:

$$\text{Moment, } M = \frac{\sigma I}{r} \quad (\text{A-7})$$

$$\text{Moment, } M = (\text{Strain, } \epsilon) \frac{IE}{r} \quad (\text{A-8})$$

Substitute $I = \frac{\pi r^4}{4}$ for circular sections:

$$\frac{\text{Moment}}{\text{Strain}} = \frac{\pi r^4 E}{4r} \quad (\text{A-9})$$

$$\frac{\text{Moment}}{\text{Strain}} = \frac{(\pi r^2 E) \cdot r}{4} \quad (\text{A-10})$$

$$\frac{\text{Moment}}{\text{Strain}} = \frac{(AE) \cdot r}{4} \quad (\text{A-11})$$

r = bar radius (inches)

A = bar area (in²)

I = first moment of inertia (in⁴)

E = modulus of elasticity (ksi)

Table A-2 lists the flexural stiffness values measured from the bending tests. Calculated bar radii are also listed.

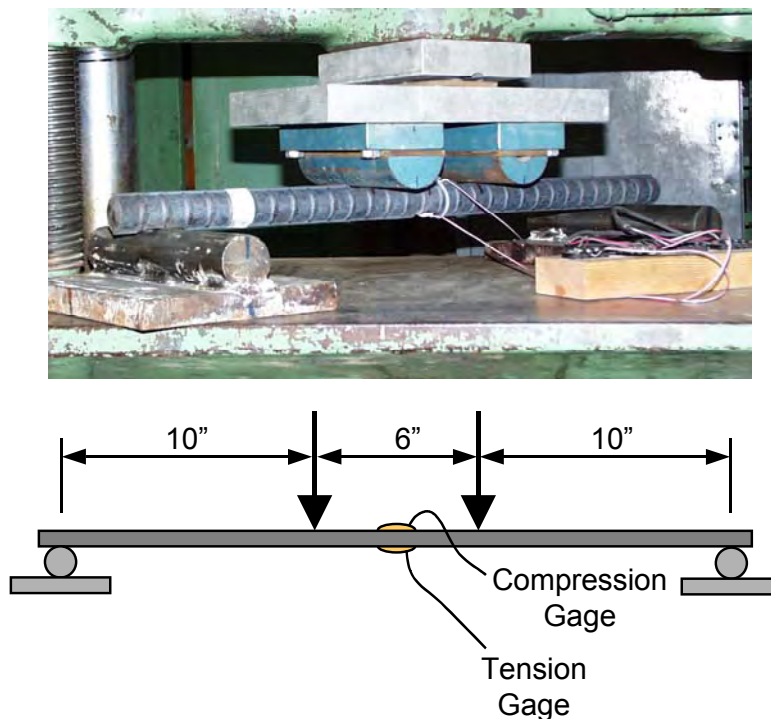


Figure A-12: Test setup for bending tests of bars

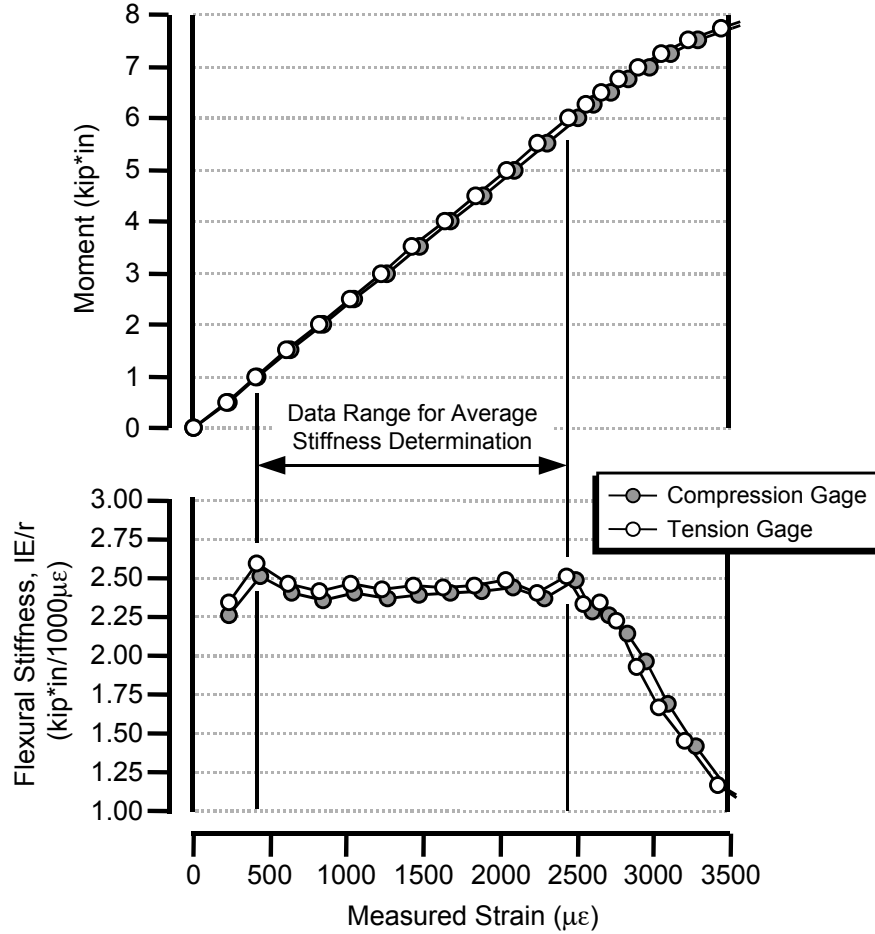


Figure A-13: Typical moment-strain data from a bending test (# 8 ERICO⁽²⁾ bar group)

Table A-2: Flexural stiffness, IE/r , and radii, r , for all specimen bar sizes

Bar Size	Supplier	Num. of Bars	AE (kip/1000 $\mu\epsilon$)	IE/r (kip·in/1000 $\mu\epsilon$)	Radius r ($\pm \sigma$) (inches)	$\frac{\sigma}{r}$ (%)
# 8	HRC	2	21.3	2.61	0.490 ± 0.024	4.8%
	ERICO ⁽²⁾	2	21.3	2.43	0.457 ± 0.007	1.6%
	All Bars	4	21.0	2.52	0.480 ± 0.034	7.0%
# 11	HRC	2	39.1	7.03	0.719 ± 0.016	2.2%
	ERICO	2	42.3	7.03	0.664 ± 0.014	2.1%

A.4 CALCULATION OF BAR FORCES

Given the flexural and tensile properties of the bar, the bar force can be calculated by using the extreme fiber strain data. Figure A-14 shows a bar instrumented with strain gages 1 and 2 located on the top and bottom fibers of the bar. The instrumented section of bar was located near a crack across which shear and tensile forces are transmitted. The bar was placed in both tension and flexure at this location (this was typical of a bar anchored in a CCT node specimen). Figure A-14 shows the cross-section strain and stress

distribution of the bar. Because the stress distribution was non-uniform and the bar was only partially yielded, it was unrealistic to characterize the bar by its average strain. Instead, plastic analysis of the section must be performed to determine resultant axial forces and moments. If the section is assumed to be approximately circular and the strain distribution linear, then the force on the section can be determined by formulas using the top and bottom steel strains (ϵ_1 and ϵ_2 respectively) and the cross-section and material properties (area: A , radius: r , modulus: E , and yield strain: ϵ_y) determined from the bar sample tests described in the previous sections. The applicable equations are listed on the following pages.

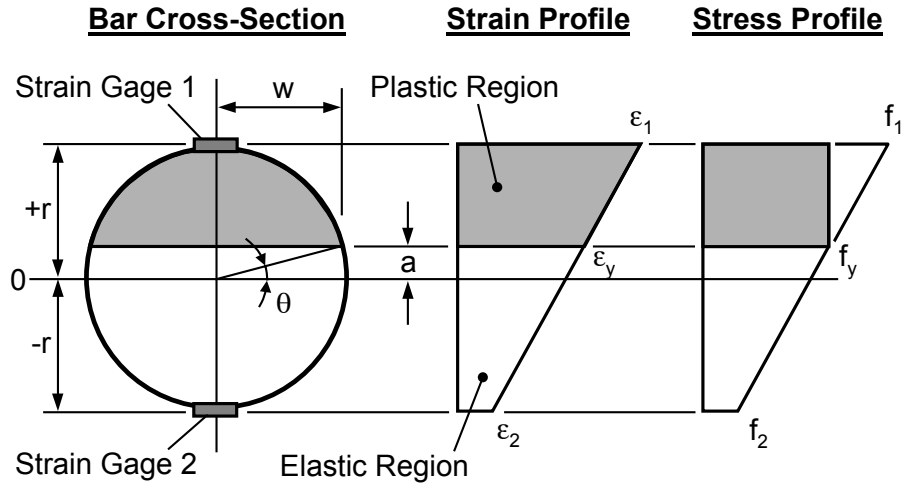


Figure A-14: Bar cross-section strains and stresses

Axial Force in Bar, P:

- Fully elastic behavior:

$$P = E\epsilon_{\text{avg}}\pi r^2 \tag{A-12}$$

- Partially plastic behavior:

$$P = E\left\{-\frac{2}{3}mw^3 + \left(\left(\frac{\pi}{2} + \theta\right)r^2 + wa\right)\epsilon_{\text{avg}} + \left(\left(\frac{\pi}{2} + \theta\right)r^2 - wa\right)\epsilon_y\right\} \tag{A-13}$$

- Fully plastic behavior:

$$P = E\epsilon_y\pi r^2 \tag{A-14}$$

Moment in Bar, M:

- Fully elastic behavior:

$$M = E\left(\frac{1}{4}m\pi r^4\right) \tag{A-15}$$

- Partially plastic behavior:

$$M = E \left\{ \frac{2}{3} w^3 (\epsilon_y - \epsilon_{\text{avg}}) + m \left[\frac{1}{4} \left(\frac{\pi}{2} + \theta \right) r^4 + aw \left(\frac{1}{4} r^2 - \frac{1}{2} w^2 \right) \right] \right\} \quad (\text{A-16})$$

- Fully plastic behavior:

$$M = 0 \quad (\text{A-17})$$

$$m = \text{strain gradient, } \frac{\epsilon_1 - \epsilon_2}{2r}$$

$$\epsilon_{\text{avg}} = \text{average strain, } \frac{\epsilon_1 + \epsilon_2}{2}$$

$$a = \text{plastic boundary, } \frac{\epsilon_y - \epsilon_2}{m} - r \quad (\text{see Figure A-14})$$

$$w = \text{plastic width, } \sqrt{(r^2 - a^2)} \quad (\text{see Figure A-14})$$

$$\theta = \text{plastic angle, } \sin^{-1} \left(\frac{a}{r} \right) \quad (\text{see Figure A-14})$$

The above equations are very complex for partially plastic bar behavior, however, they can be programmed into a spreadsheet and performed automatically. Note also that “fully plastic behavior” refers to tension yielding of the section. Thus the moment when the section is fully plastic is zero. The necessity of these complex calculations arose from the curvature induced into the tensile reinforcement in CCT tests which is discussed in Chapter 3.

APPENDIX B: DISTRIBUTION PLOTS FOR BEARING CAPACITY DATABASE

B.1 PROPOSED BEARING CAPACITY MODEL 1

Distribution plots for proposed bearing capacity model 1 are presented in Figures B-1 through B-14. Model 1 is presented below:

$$\text{Bearing Capacity, } P = A_{nh} \left(2.6\Psi \left(\frac{2c_1}{\sqrt{A_{nh}}} \right) \left(\frac{f'_c}{2.4} \right)^{0.5 \left(1 + \sqrt{A_{nh}} / 2c_1 \right)} \right) \quad (\text{B-1})$$

$$\Psi = 0.7 + 0.3 \frac{c_2}{c_1} \leq 1.8 \quad (\text{B-2})$$

with

All variables are as defined in Chapter 4.

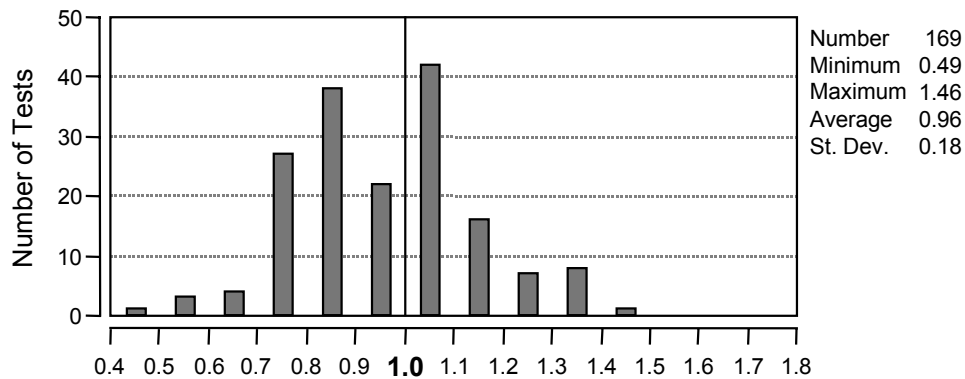


Figure B-1: All headed bar and anchor bolt tests listed in database (model 1)

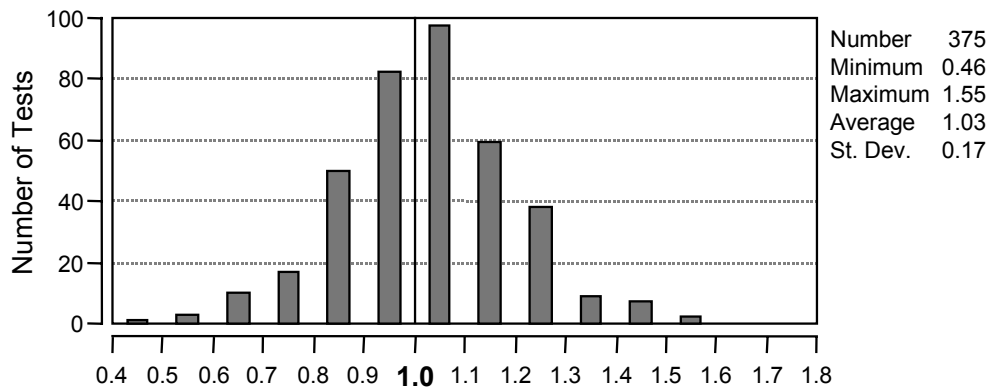


Figure B-2: All bearing block tests listed in database (model 1)

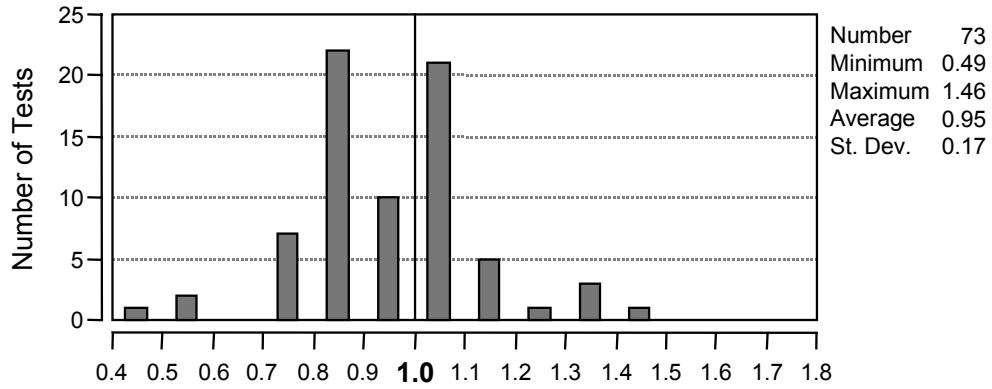


Figure B-3: University of Texas Deep Embedment Tests (model 1)

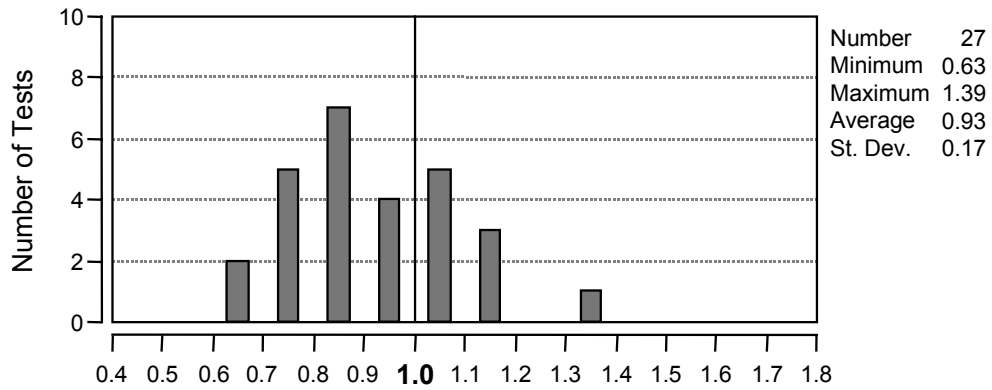


Figure B-4: University of Texas CCT node tests (current study) (model 1)

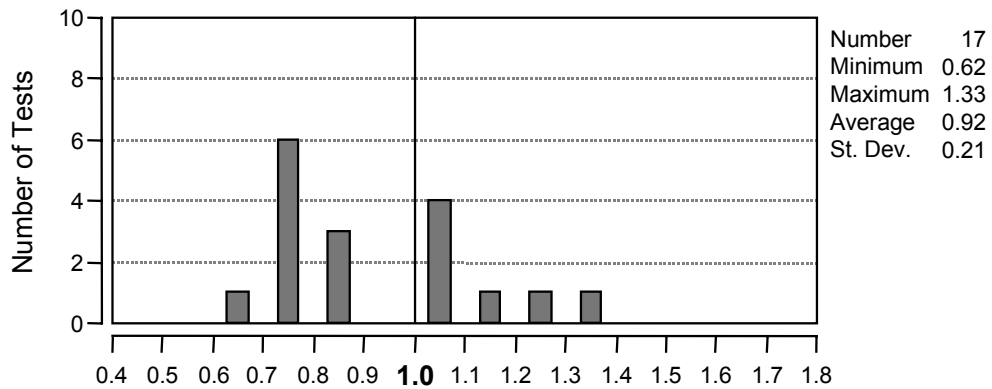


Figure B-5: Breen, 1964 (model 1)

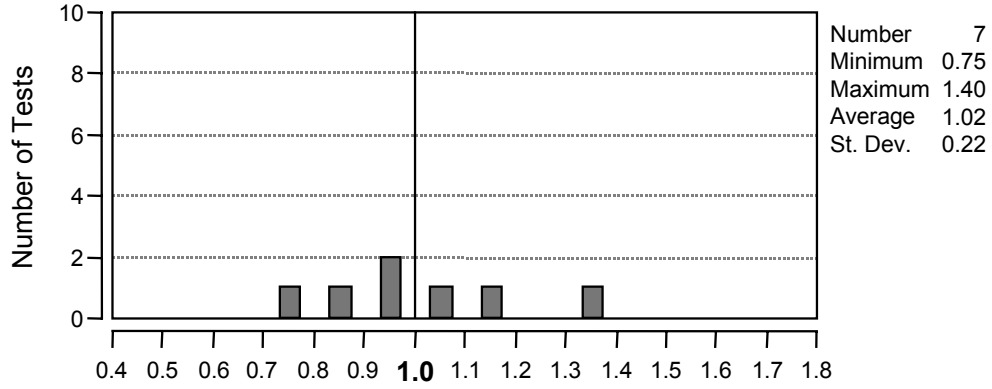


Figure B-6: Lee and Breen, 1966 (model 1)

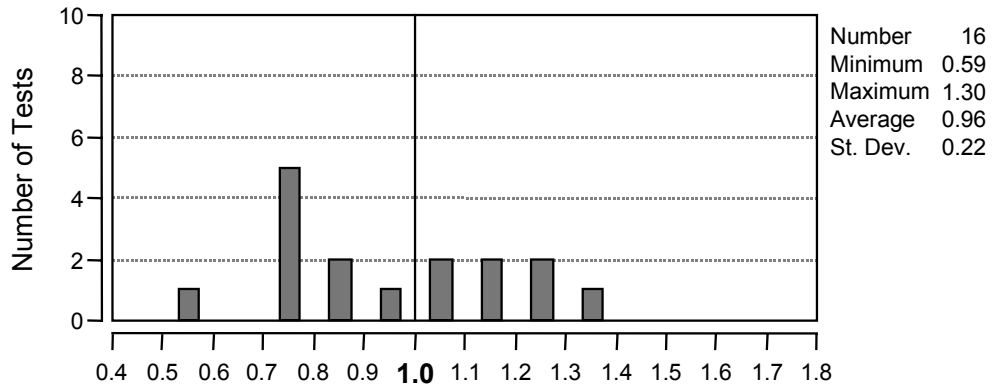


Figure B-7: Lo, 1975 (model 1)

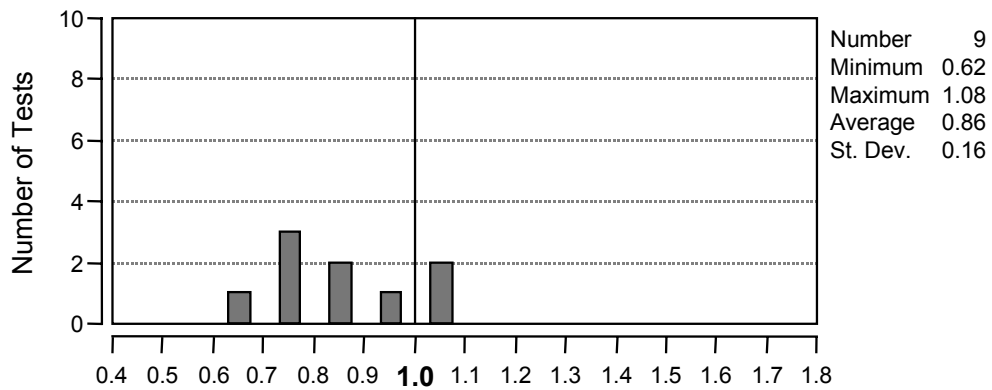


Figure B-8: Hasselwander, 1977 (model 1)

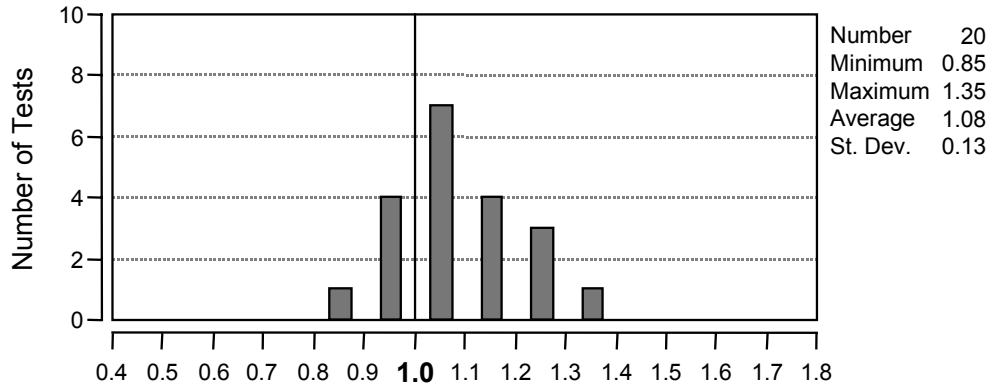


Figure B-9: Furche and Eligehausen, 1991 (model 1)

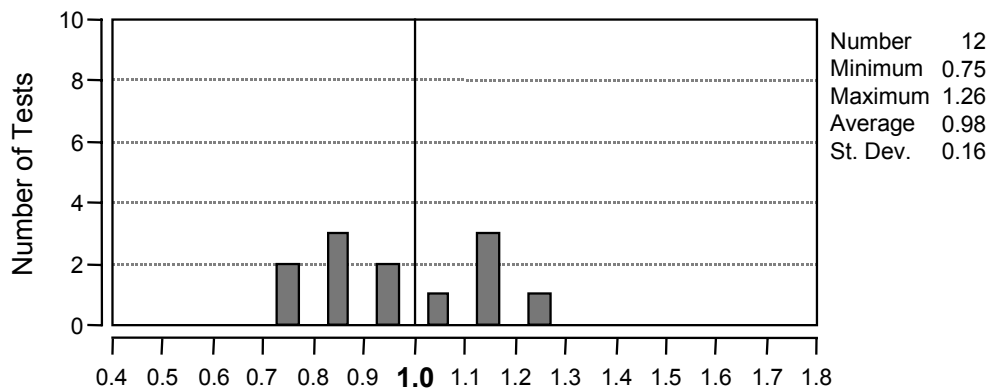


Figure B-10: Shelson, 1957 (model 1)

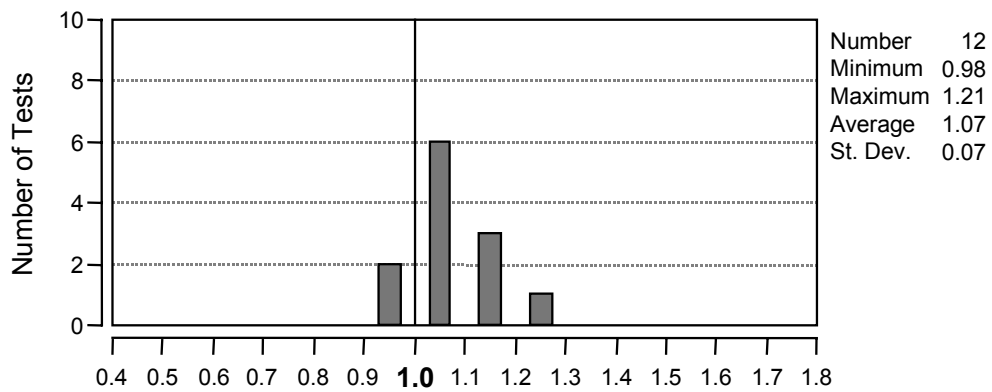


Figure B-11: Au and Baird, 1960 (model 1)

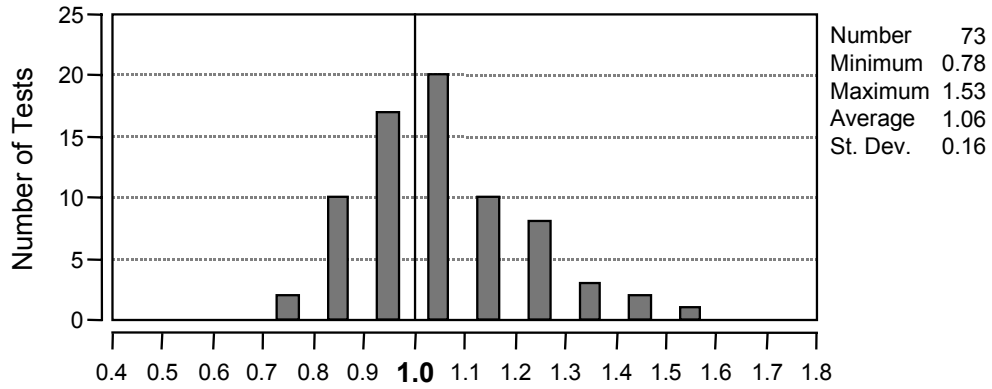


Figure B-12: Hawkins, 1968 (model 1)

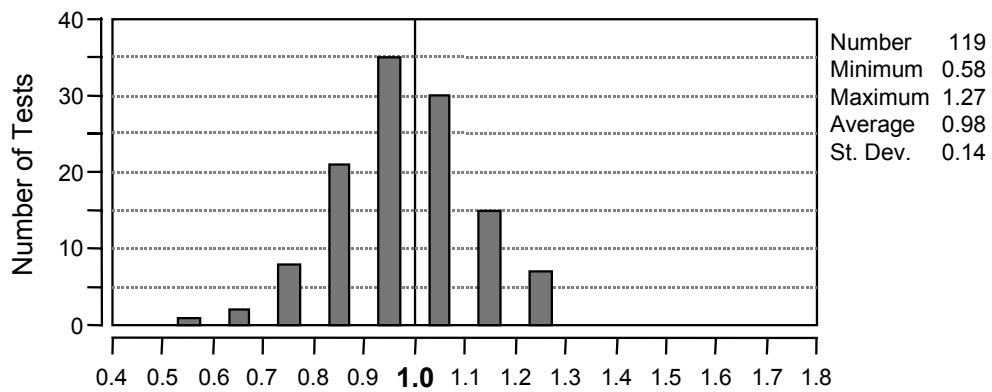


Figure B-13: Niyogi, 1973 (model 1)

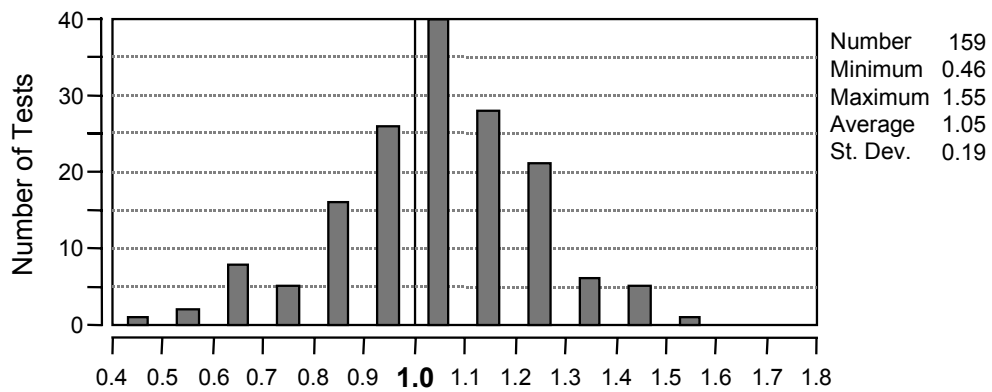


Figure B-14: Williams, 1979 (model 1)

B.2 PROPOSED BEARING CAPACITY MODEL 2

Distribution plots for proposed bearing capacity model 2 are presented in Figures B-15 through B-28. Model 2 is presented below:

$$\text{Bearing Capacity, } P = A_{nh} \left(0.9 \Psi \left(\frac{2c_1}{\sqrt{A_{nh}}} \right) f'_c \right) \quad (\text{B-3})$$

with
$$\Psi = 0.6 + 0.4 \frac{c_2}{c_1} \leq 2.0 \quad (\text{B-4})$$

All variables are as defined in Chapter 4.

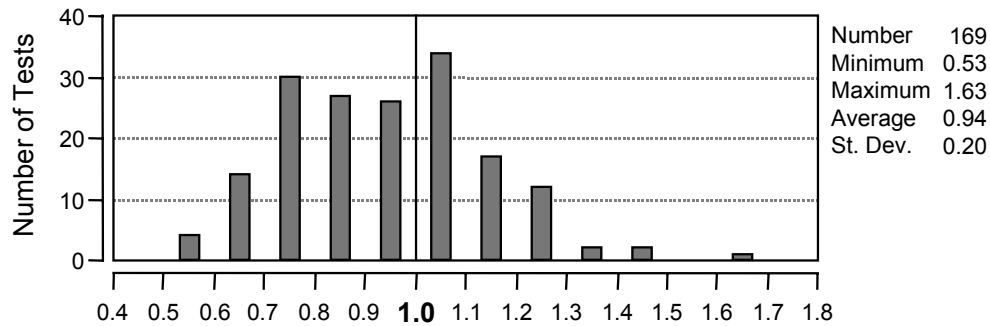


Figure B-15: All headed bar and anchor bolt tests listed in database (model 2)

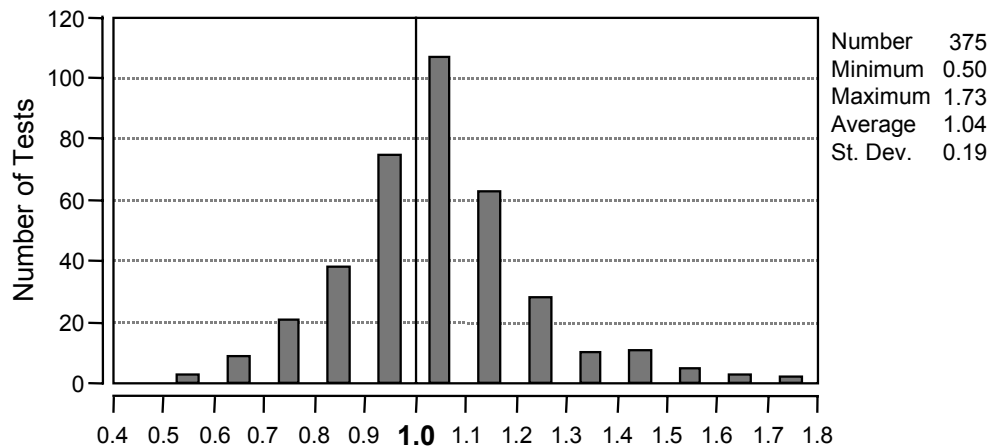


Figure B-16: All bearing block tests listed in database (model 2)

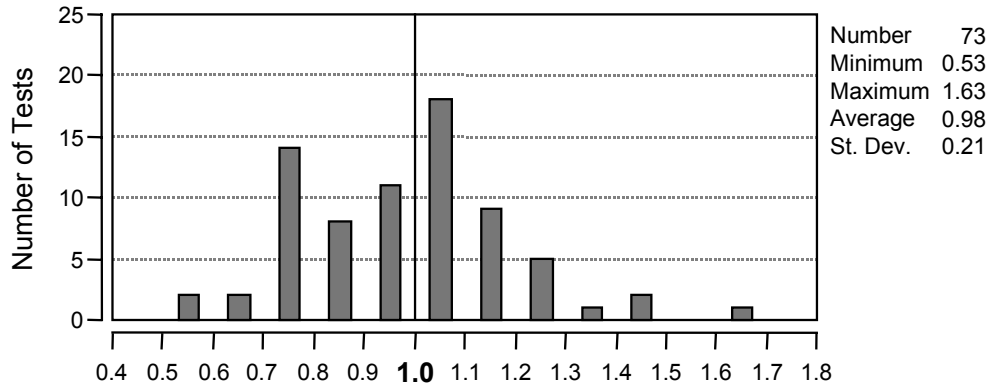


Figure B-17: University of Texas Deep Embedment Tests (model 2)

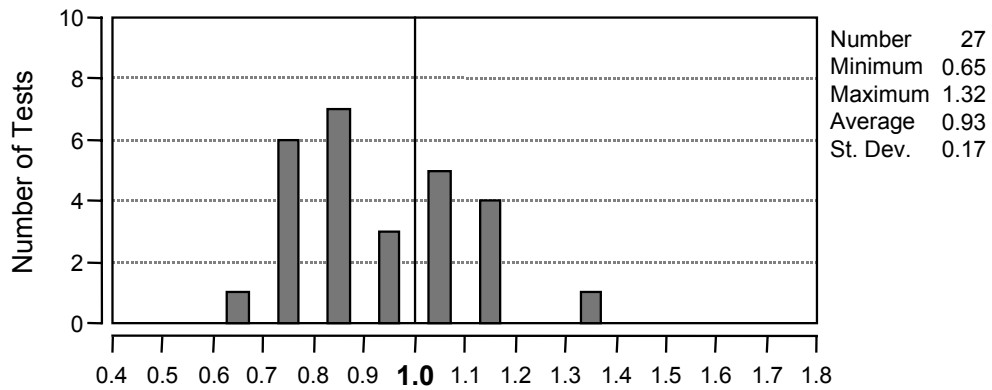


Figure B-18: University of Texas CCT node tests (current study) (model 2)

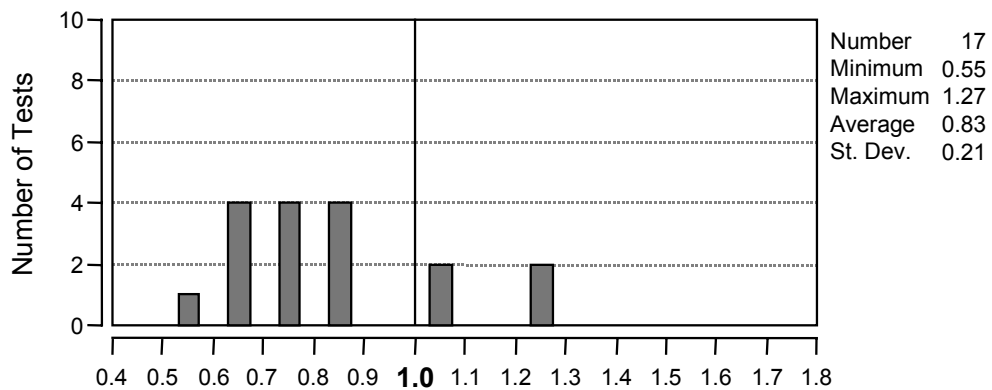


Figure B-19: Breen, 1964 (model 2)

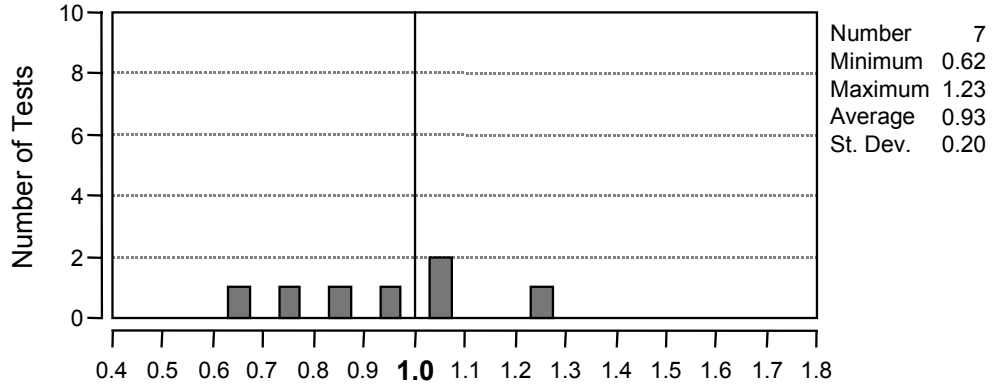


Figure B-20: Lee and Breen, 1966 (model 2)

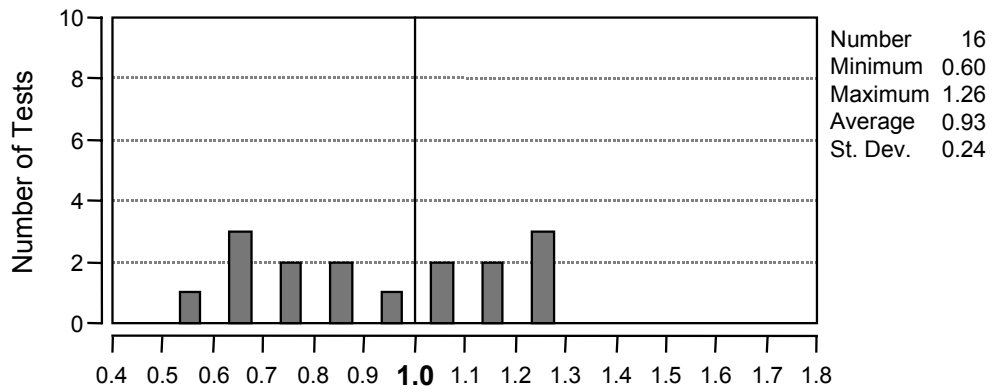


Figure B-21: Lo, 1975 (model 2)

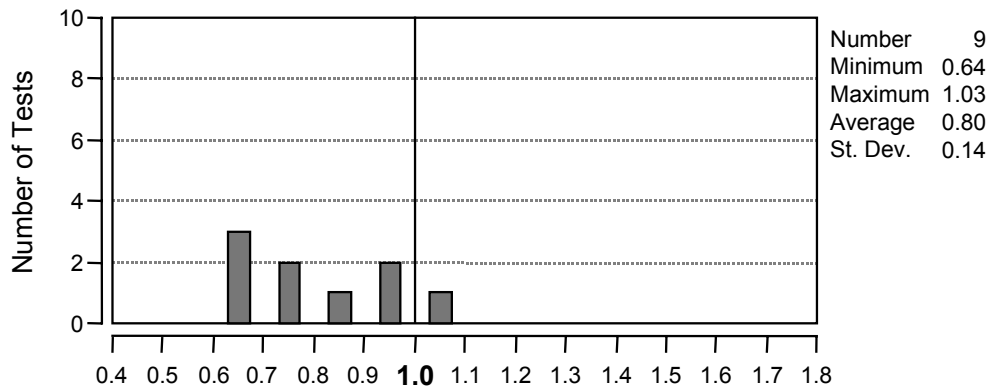


Figure B-22: Hasselwander, 1977 (model 2)

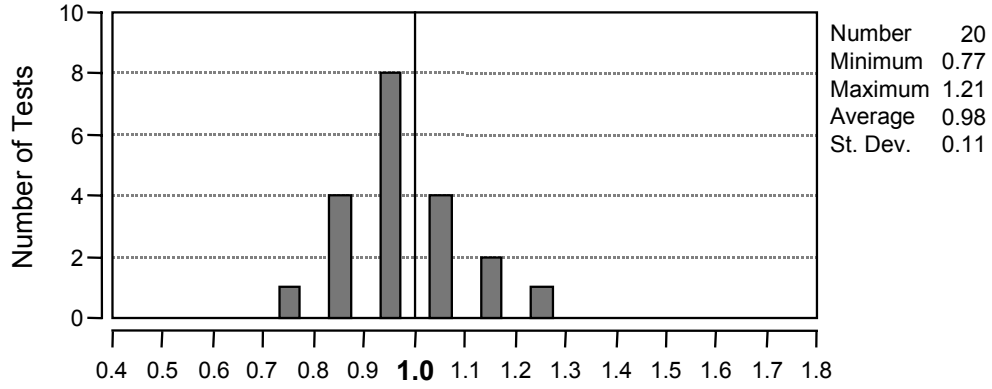


Figure B-23: Furche and Eligehausen, 1991 (model 2)

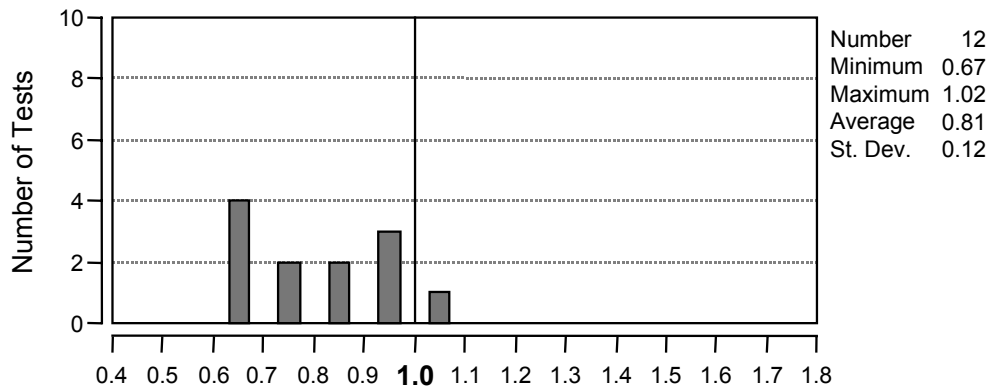


Figure B-24: Shelson, 1957 (model 2)

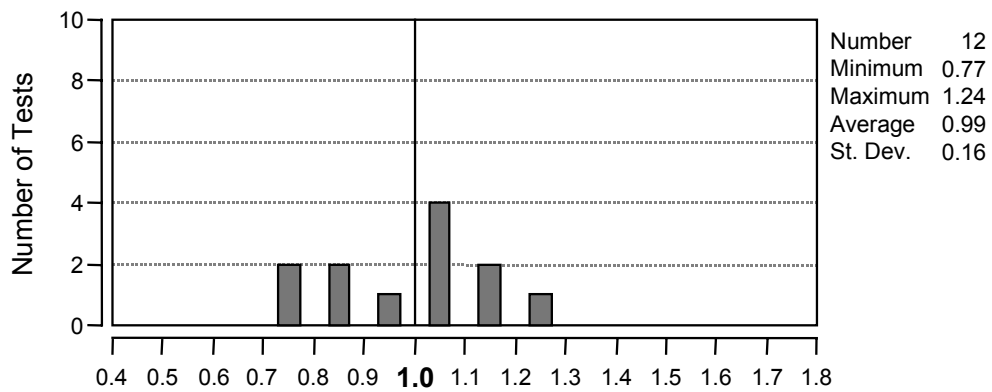


Figure B-25: Au and Baird, 1960 (model 2)

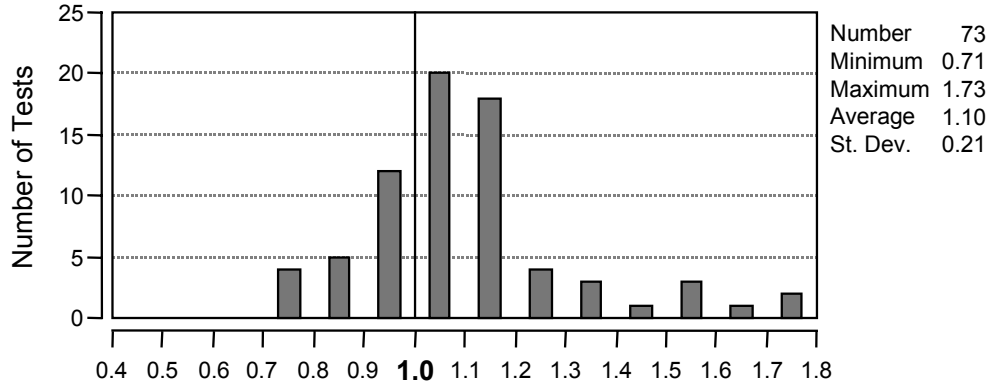


Figure B-26: Hawkins, 1968 (model 2)

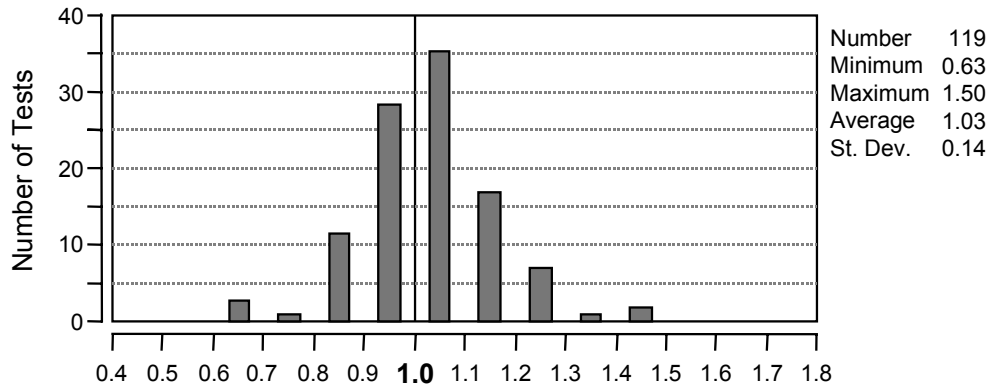


Figure B-27: Niyogi, 1973 (model 2)

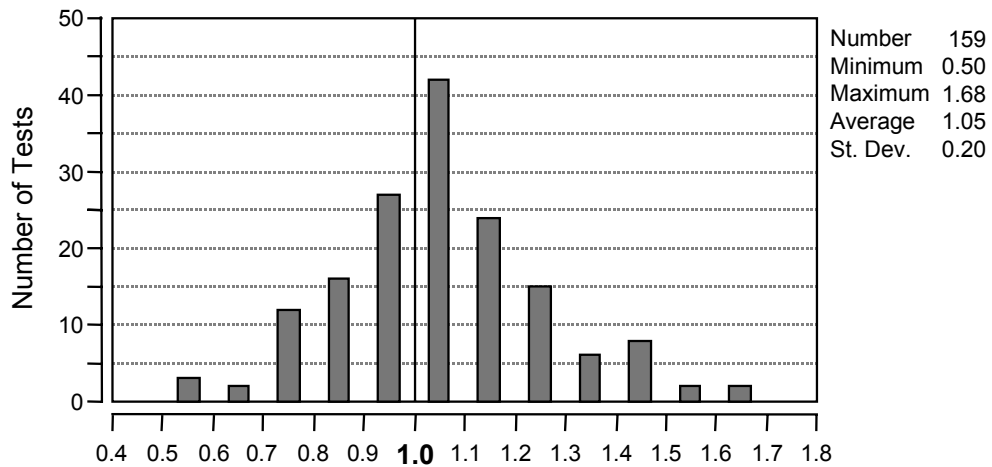


Figure B-28: Williams, 1979 (model 2)

APPENDIX C: SUMMARY OF CCT NODE DATA

CCT test results are summarized in Tables C-1a through C-1c. The tables report the maximum bar stresses at $1d_b$ (next to the head) and $7d_b$ (close to the critical crack) and the maximum bearing reaction, P (see Figure C-1). Important parameters from the specimens are also reported.

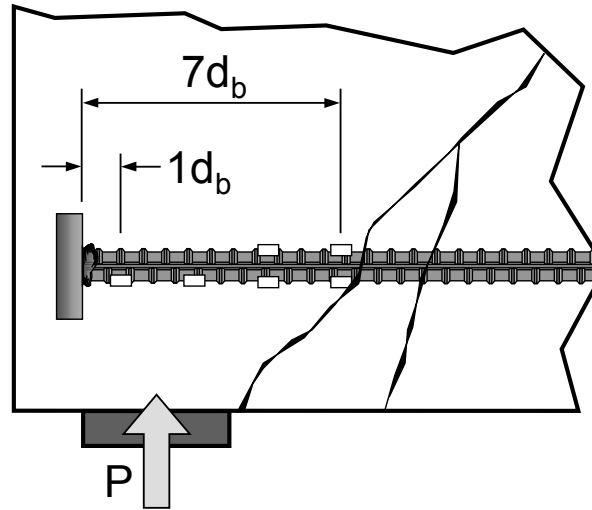


Figure C-1: Close-up of CCT node

Table C-1a: Summary of CCT node test results

Specimen Identification	Head Type	θ_{strut}	$\frac{L_{\text{plate}}}{d_b}$	$\frac{A_{\text{nh}}}{A_b}$	$\frac{C_1}{d_b}$	$\frac{C_2}{d_b}$	f'_c (ksi)	f_s at $1d_b$ (ksi)	f_s at $7d_b$ (ksi)	P_{max} (kip)	Failure Mode
CCT-08-45-00.00-1-E1,W8	no head	45°	6.0	0.00	4.0	4.0	5.7	-	-	-	shear†
CCT-08-45-01.18-1-E1,W8	$d_h = 1.48"$	45°	6.0	1.18	4.0	4.0	5.7	-	-	64.1	shear†
CCT-08-45-04.70(H)-1-E1,W8	$1.5" \times 3.0"$	45°	6.0	4.70	4.0	4.0	5.7	-	-	53.8	shear†
CCT-08-45-10.39-1-E1,W8	$3.0" \times 3.0"$	45°	6.0	10.39	4.0	4.0	5.7	-	-	75.0	shear†
CCT-08-45-00.00-1-E2,W8	no head	45°	6.0	0.00	4.0	4.0	3.0	-	-	45.3	pullout
CCT-08-45-01.18-1-E2,W8	$d_h = 1.48"$	45°	6.0	1.18	4.0	4.0	3.0	-	-	51.7	splitting
CCT-08-45-04.70(H)-1-E2,W8	$1.5" \times 3.0"$	45°	6.0	4.70	4.0	4.0	3.0	-	-	76.0	crushing
CCT-08-45-10.39-1-E2,W8	$3.0" \times 3.0"$	45°	6.0	10.39	4.0	4.0	3.0	-	-	72.5	crushing
CCT-08-45-00.00-1-E2,W6	no head	45°	6.0	0.00	3.0	4.0	3.0	-	-	48.7	pullout
CCT-08-45-04.70(H)-1-E2,W6	$1.5" \times 3.0"$	45°	6.0	4.70	3.0	4.0	3.0	-	-	66.7	crushing
CCT-08-45-10.39-1-E2,W6	$3.0" \times 3.0"$	45°	6.0	10.39	3.0	4.0	3.0	-	-	57.8	crushing
CCT-08-45-00.00-1-B6	no head	45°	6.0	0.00	3.0	4.0	4.0	16.3	55.9	53.7	pullout
CCT-08-55-00.00-1	no head	55°	4.0	0.00	3.0	4.0	3.9	11.7	50.2	56.1	pullout
CCT-08-55-01.18-1	$d_h = 1.48"$	55°	4.0	1.18	3.0	4.0	3.9	37.9	61.8	67.7	splitting
CCT-08-55-01.85-1	$1.5" \times 1.5"$	55°	4.0	1.85	3.0	4.0	3.9	41.8	66.3	80.7	splitting
CCT-08-55-02.80(H)-1	$1.5" \times 2.0"$	55°	4.0	2.80	3.0	4.0	3.9	38.0	68.4†	86.4	splitting
CCT-08-55-02.80(V)-1	$1.5" \times 2.0"$	55°	4.0	2.80	3.0	4.0	3.9	43.2	65.4	78.3	splitting
CCT-08-55-04.04-1	$d_h = 2.25"$	55°	4.0	4.04	3.0	4.0	3.1	30.3	46.3	63.9	crushing
CCT-08-55-04.06-1	$2.0" \times 2.0"$	55°	4.0	4.06	3.0	4.0	3.1	34.8	55.9	69.2	crushing
CCT-08-55-04.70(H)-1	$1.5" \times 3.0"$	55°	4.0	4.70	3.0	4.0	4.0	46.6	68.4†	88.7	yield
CCT-08-55-04.70(H)-2	$1.5" \times 3.0"$	55°	4.0	4.70	3.0	4.0	3.1	52.1	66.5	82.3	crushing
CCT-08-55-04.70(V)-1	$1.5" \times 3.0"$	55°	4.0	4.70	3.0	4.0	3.9	48.6	68.4†	85.4	splitting
CCT-08-55-10.39-1	$3.0" \times 3.0"$	55°	4.0	10.39	3.0	4.0	4.0	59.0	68.4†	91.9	yield

Table C-2a: Summary of CCT node test results (continued)

Specimen Identification	Head Type	θ_{strut}	$\frac{L_{\text{plate}}}{d_b}$	$\frac{A_{\text{nh}}}{A_b}$	$\frac{C_1}{d_b}$	$\frac{C_2}{d_b}$	f'_c (ksi)	f_s at $1d_b$ (ksi)	f_s at $7d_b$ (ksi)	P_{max} (kip)	Failure Mode
CCT-08-45-00.00-1	no head	45°	4.0	0.00	3.0	4.0	4.0	12.0	43.5	42.3	pullout
CCT-08-45-01.18-1	$d_h = 1.48"$	45°	4.0	1.18	3.0	4.0	4.0	18.7	-	46.3	splitting
CCT-08-45-01.85-1	$1.5" \times 1.5"$	45°	4.0	1.85	3.0	4.0	4.0	26.6	66.7*	43.4	splitting
CCT-08-45-01.85-2	$1.5" \times 1.5"$	45°	4.0	1.85	3.0	4.0	3.1	29.6	60.9	52.0	splitting
CCT-08-45-02.80(H)-1	$1.5" \times 2.0"$	45°	4.0	2.80	3.0	4.0	4.0	46.5	68.4	62.2	yield
CCT-08-45-02.80(H)-2	$1.5" \times 2.0"$	45°	4.0	2.80	3.0	4.0	3.1	37.6	59.8	53.1	splitting
CCT-08-45-02.80(V)-1	$1.5" \times 2.0"$	45°	4.0	2.80	3.0	4.0	3.9	49.1	66.5	59.8	splitting
CCT-08-45-04.04-1	$d_h = 2.25"$	45°	4.0	4.04	3.0	4.0	4.0	41.4	61.0	54.7	yield
CCT-08-45-04.06-1	$2.0" \times 2.0"$	45°	4.0	4.06	3.0	4.0	3.1	44.1	66.6	62.7	crushing
CCT-08-45-04.70(H)-1	$1.5" \times 3.0"$	45°	4.0	4.70	3.0	4.0	3.1	53.6	59.9	51.5	crushing
CCT-08-45-04.70(V)-1	$1.5" \times 3.0"$	45°	4.0	4.70	3.0	4.0	3.9	48.8	68.4	63.9	splitting
CCT-08-45-10.39-1	$3.0" \times 3.0"$	45°	4.0	10.39	3.0	4.0	3.1	-	54.6	45.8	crushing
CCT-08-45-10.39-2	$3.0" \times 3.0"$	45°	4.0	10.39	3.0	4.0	3.8	54.7	68.4	59.5	crushing
CCT-08-45-Hook1-1	Hook 1	45°	4.0	-	3.0	4.0	4.0	-	-	49.0	splitting
CCT-08-45-Hook2-1	Hook 2	45°	4.0	-	3.0	4.0	4.0	-	-	52.8	splitting
CCT-08-30-00.00-1	no head	30°	4.0	0.00	3.0	4.0	4.1	6.1	34.0	20.2	pullout
CCT-08-30-01.18-1	$d_h = 1.48"$	30°	4.0	1.18	3.0	4.0	4.1	29.9	59.8	31.1	splitting
CCT-08-30-01.85-1	$1.5" \times 1.5"$	30°	4.0	1.85	3.0	4.0	4.1	40.5	68.4†	41.5	yield
CCT-08-30-04.04-1	$d_h = 2.25"$	30°	4.0	4.04	3.0	4.0	4.1	34.8	61.0†	37.8	yield
CCT-08-30-04.06-1	$2.0" \times 2.0"$	30°	4.0	4.06	3.0	4.0	4.1	49.2	68.4†	40.6	yield
CCT-08-30-10.39-1	$3.0" \times 3.0"$	30°	4.0	10.39	3.0	4.0	4.1	46.0	68.4†	39.0	yield
CCT-08-45-04.70(V)-1-S1	$1.5" \times 3.0"$	45°	4.0	4.70	3.0	4.0	4.1	-	-	-	pullout
CCT-08-45-04.70(V)-1-S2	$1.5" \times 3.0"$	45°	4.0	4.70	3.0	4.0	4.1	41.3	58.0	54.8	crushing
CCT-08-45-04.70(H)-1-S3	$1.5" \times 3.0"$	45°	4.0	4.70	3.0	4.0	3.8	54.7	66.0	58.8	splitting

Table C-3a: Summary of CCT node test results (continued)

Specimen Identification	Head Type	θ_{strut}	$\frac{L_{\text{plate}}}{d_b}$	$\frac{A_{nh}}{A_b}$	$\frac{C_1}{d_b}$	$\frac{C_2}{d_b}$	f'_c (ksi)	f_s at $1d_b$ (ksi)	f_s at $7d_b$ (ksi)	P_{max} (kip)	Failure Mode
CCT-08-45-00.00-1-C0.006	no head	45°	4.0	0.00	3.0	4.0	3.8	2.1	43.1	40.6	pullout
CCT-08-45-00.00-1-C0.012	no head	45°	4.0	0.00	3.0	4.0	3.8	7.2	41.2	41.6	pullout
CCT-08-45-04.70(V)-1-C0.006	1.5" x 3.0"	45°	4.0	4.70	3.0	4.0	3.8	36.5	64.1	58.1	splitting
CCT-08-45-04.70(V)-1-C0.012	1.5" x 3.0"	45°	4.0	4.70	3.0	4.0	3.8	39.2	65.6	66.8	splitting
CCT-08-45-Hook2-1-C0.012	Hook 2	45°	4.0	-	3.0	4.0	3.8	-	59.6	52.5	splitting
CCT-11-45-00.00-1	no head	45°	4.0	0.00	2.8	3.0	4.1	13.6	38.9	68.4	pullout
CCT-11-45-01.10-1	$d_h = 2.04"$	45°	4.0	1.10	2.8	3.0	4.1	21.4	51.3	91.4	splitting
CCT-11-45-01.56-1	2.0" x 2.0"	45°	4.0	1.56	2.8	3.0	4.1	30.2	53.7	90.0	splitting
CCT-11-45-02.85(H)-1	2.0" x 3.0"	45°	4.0	2.85	2.8	3.0	4.1	30.3	50.1	78.4	splitting
CCT-11-45-02.85(V)-1	2.0" x 3.0"	45°	4.0	2.85	2.8	3.0	4.1	40.9	54.4	89.6	crushing
CCT-11-45-03.53-1	$d_h = 3.00"$	45°	4.0	3.53	2.8	3.0	4.0	36.7	55.9	93.7	crushing
CCT-11-45-04.13(H)-1	2.0" x 4.0"	45°	4.0	4.13	2.8	3.0	4.1	56.5	61.9	96.2	crushing
CCT-11-45-04.13(V)-1	2.0" x 4.0"	45°	4.0	4.13	2.8	3.0	4.0	39.1	57.0	88.9	splitting
CCT-11-45-04.77-1	3.0" x 3.0"	45°	4.0	4.77	2.8	3.0	4.0	39.7	56.8	84.0	crushing
CCT-11-45-06.69(H)-1	3.0" x 4.0"	45°	4.0	6.69	2.8	3.0	4.0	54.9	62.8 [†]	95.8	yield
CCT-11-45-06.69(V)-1	3.0" x 4.0"	45°	4.0	6.69	2.8	3.0	4.0	40.0	62.8 [†]	99.1	yield
CCT-11-45-09.26-1	4.0" x 4.0"	45°	4.0	9.26	2.8	3.0	4.0	50.5	62.8 [†]	107.7	yield

- data not available or not applicable

* questionable data point

† stress equal to f_y

‡ shear failure on back portion of specimen

REFERENCES

1. "AASHTO LRFD Bridge Design Specifications, 2nd ed.," American Association of State Highway and Transportation Officials, Washington, DC, 1998.
2. ACI 318-02, "Building Code Requirements for Structural Concrete and Commentary," American Concrete Institute, Farmington Hills, Michigan, October 2002.
3. ASTM C39/C39M-99, "Standard Test Method for Compressive Strength of Cylindrical Concrete Specimens," American Society for Testing and Materials, West Conshohocken, Pennsylvania, September 1999.
4. ASTM C496-96, "Standard Test Method for Splitting Tensile Strength of Cylindrical Concrete Specimens," American Society for Testing and Materials, West Conshohocken, Pennsylvania, September 1996.
5. ASTM C469-94, "Standard Test Method for Static Modulus of Elasticity and Poisson's Ratio of Concrete in Compression," American Society for Testing and Materials, West Conshohocken, Pennsylvania, September 1994.
6. "Fracture Mechanics of Concrete: Concepts, Models and Determination of Material Properties," Report by ACI 446, Fracture Mechanics (Z. P. Bazant, Chairman), Detroit, Michigan, December 1989.
7. Au, T. and Baird, D.L., "Bearing Capacity of Concrete Blocks," Journal of the American Concrete Institute, Proceedings Vol. 56, No. 9, pgs. 869-879, Detroit, Michigan, March 1960.
8. Breen, J.E., "Development Length for Anchor Bolts," Center for Transportation Research Report CTR-55-1F, Austin, Texas, April 1964.
9. DeVries, R.A., "Anchorage of Headed Reinforcement in Concrete," PhD Dissertation, The University of Texas at Austin, Austin, Texas, December 1996.
10. Eibl, J. and Zeller, W., "Untersuchungen zur Traglast der Druckdiagonalen in Konsolen," Bericht, Institut für Massivbau und Baustofftechnologie, University of Karlsruhe, Germany, 1991.
11. Furche, J. and Eligehausen, R., "Lateral Blow-Out Failure of Headed Studs Near a Free Edge," Proceedings of International Symposium "Anchors in Concrete – Design and Behavior," ACI International, SP-130, pg. 235-252, Farmington Hills, Michigan, 1991.
12. Hasselwander, G.B., Jirsa, J.O., Breen, J.E., and Lo, K., "Strength and Behavior of Anchor Bolts Embedded Near Edges of Concrete Piers," Center for Transportation Research Report CTR-29-2F, Austin, Texas, May 1977.
13. Hawkins, N.M., "The Bearing Strength of Concrete: 1. Loading Through Rigid Plates Covering Part of the Full Supporting Area," The University of Sydney, Research Report No. 54, Sydney, Australia, March 1967.
14. Kupfer, H., Hilsdorf, H.K., and Rusch, H., "Behavior of Concrete Under Biaxial Stresses," Journal of the American Concrete Institute, Proceedings Vol. 66, No. 8, pg. 656-666, Detroit, Michigan, August 1969.
15. Lee, D.W. and Breen, J.E., "Factors Affecting Anchor Bolt Development," Center for Transportation Research Report CTR-88-1F, Austin, Texas, August 1966.
16. Niyogi, S.K., "Bearing Strength of Concrete – Geometric Variations," ASCE Journal of Structural Engineering, Vol. 99, No. 7, pgs. 1471-1490, New York, New York, July 1973.
17. Niyogi, S.K., "Concrete Bearing Strength – Support, Mix, Size Effect," ASCE Journal of Structural Engineering, Vol. 100, No. 8, pgs. 1685-1702, New York, New York, August 1974.
18. Shelton, W., "Bearing Capacity of Concrete," Journal of the American Concrete Institute, Proceedings Vol. 54, No. 5, pgs. 405-414, Detroit, Michigan, November 1957.
19. Thompson, M.K., Jirsa, J.O., Breen, J.E., and Klingner, R.E., "Anchorage Behavior of Headed Reinforcement: Literature Review," Center for Transportation Research Report 1855-1, Austin, Texas, May 2002.

20. Thompson, M.K., Ledesma, A. L., Jirsa, J.O., Breen, J.E., and Klingner, R.E., "Anchorage of Headed Reinforcement in Lap Splices," Center for Transportation Research Report 1855-3, Austin, Texas, May 2002.
21. Thrö, Gerfried Schmidt, Stöckl, Siegfried, and Kupfer, Herbert, "Verankerung der Bewehrung am Endauflager bei einachsiger Querpressung" ("Anchorage of Reinforcement at an End Bearing with Uni-Axial Lateral Pressure"), Deutscher Ausschus für Stahlbeton, Heft 389, pg. 11-98, Berlin, Germany, 1988.
22. Untrauer, R.E. and Henry, R.L., "Influence of Normal Pressure on Bond Strength," Journal of the American Concrete Institute, Proceedings Vol. 62, No. 5, Detroit, Michigan, May 1965.
23. Williams, A., "The Bearing Capacity of Concrete Loaded Over a Limited Area," Cement and Concrete Association, Technical Report 526, Wexham Springs, Slough, The United Kingdom, August 1979.
24. Young, M.J., "Performance of Headed Reinforcing Bars in CCT Nodal Regions," Master's Thesis, The University of Texas at Austin, Austin, Texas, August 2000.
25. Zeller, W., "Conclusions from Tests on Corbels," IASBE Colloquium on Structural Concrete (Stuttgart 1991), IABSE Reports Vol. 62, pg. 577-582, Zurich, Switzerland, 1991.